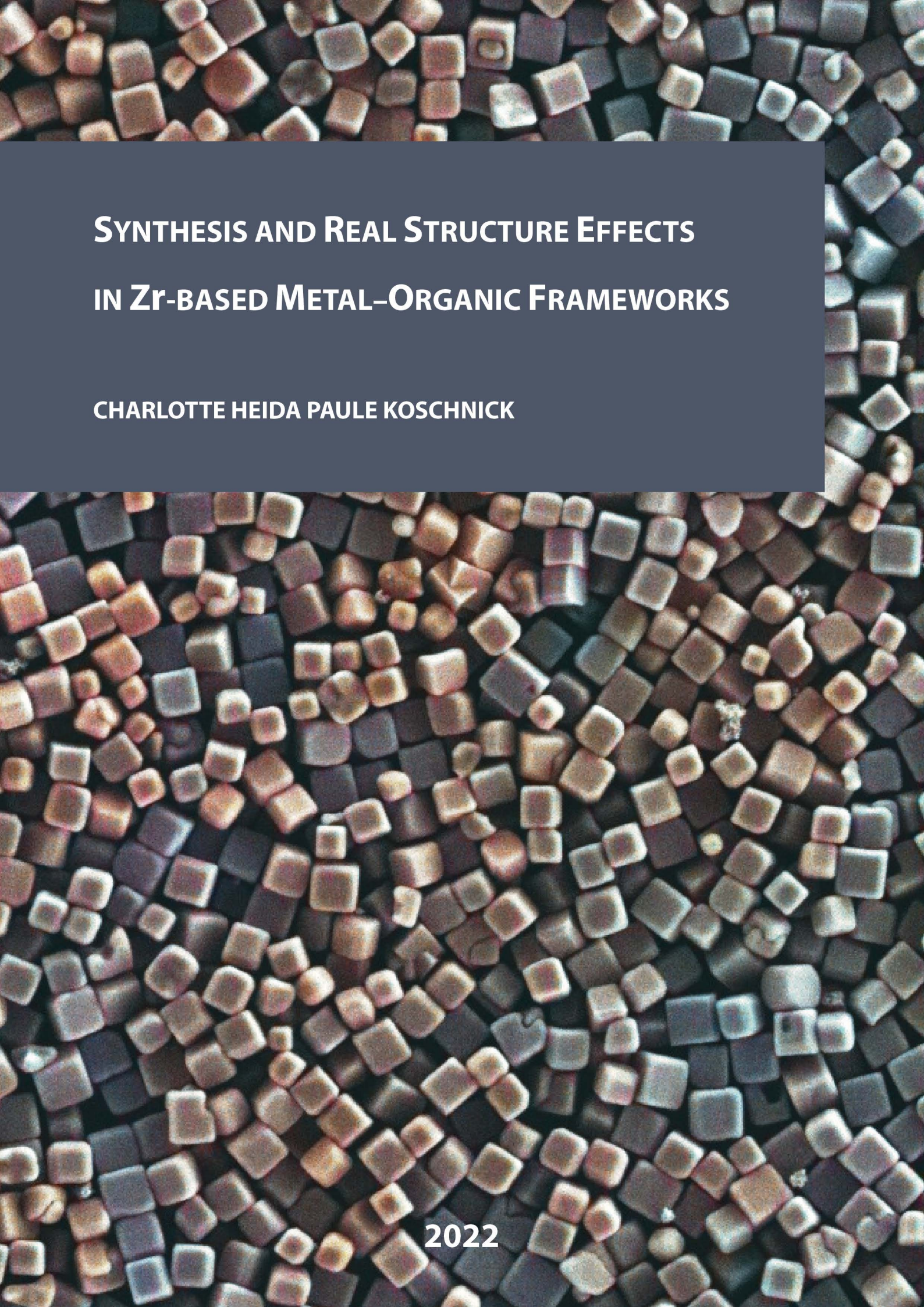

Synthesis and Real Structure Effects in Zr-based Metal–Organic Frameworks

Charlotte Heida Paule Koschnick

2022

Dissertation zur Erlangung des Doktorgrades

der Fakultät für Chemie und Pharmazie

der Ludwig-Maximilians-Universität München

Synthesis and Real Structure Effects in Zr-based Metal–Organic Frameworks

Charlotte Heida Paule Koschnick

aus

München, Deutschland

2022

ERKLÄRUNG

Diese Dissertation wurde im Sinne von §7 der Promotionsordnung vom 28. November 2011 von Frau Prof. Dr. Bettina V. Lotsch betreut.

EIDESSTATTLICHE VERSICHERUNG

Diese Dissertation wurde eigenhändig und ohne unerlaubte Hilfe erarbeitet.

München, den 07.10.2022

_____

Charlotte Heida Paule Koschnick

Dissertation eingereicht am:	12.10.2022
Erstgutachterin:	Prof. Dr. Bettina V. Lotsch
Zweitgutachter:	Prof. Dr. Konstantin Karaghiosoff
Mündliche Prüfung am:	14.11.2022

DANKSAGUNG

Mein erster Dank gilt meiner Doktormutter Bettina Lotsch, für die Betreuung meiner Arbeit und die Möglichkeit an MOFs zu forschen. Danke für Dein Vertrauen in meine Forschung, die Freiheiten eigene Ideen zu verfolgen und die produktiven Diskussionen, die mir beim anfertigen dieser Doktorarbeit geholfen haben.

Prof. Dr. Konstantin Karaghiosoff danke ich für die Übernahme des Zweitgutachtens und der immerwährenden Unterstützung bei Fragen zum Studium und zur Promotion. Prof. Dr. Roland Fischer, Prof. Dr. Knut Müller-Caspery, Prof. Dr. Ivana Ivanović-Burmazović, und Prof. Dr. Jürgen Senker danke ich für ihren Beisitz in meiner Prüfungskommission.

Mein besonderer Dank geht an meine Kooperationspartner, die maßgeblich zum Erfolg der Projekte beigetragen haben. Danke an Alberto von Mankowski, der mich in die Welt der MOFs eingeführt hat und an Robert Stäglich für die stundenlangen Telefongespräche, in denen wir zu vielen (nützlichen) Erkenntnissen gekommen sind. Des Weiteren gilt mein Dank Maxwell Terban für seine fortwährende Unterstützung bei allen Projekten und Stefano Canossa und Tanja Scholz für ihre Expertise und die vielen Diskussionen.

Außerdem möchte ich mich bei Viola Duppel, Fabian Heck, Daniel Zink und Marie-Luise Schreiber für ihre Hilfe bei der Charakterisierung der vielen Proben, bei Gökcen Savasci für die theoretischen Berechnungen und bei Konstantin Epp und Anna Lisa Semrau für ihre Hilfestellung zu Beginn meiner Doktorarbeit bedanken. Danke auch an Hagen Klauk für die externe Betreuung am MPI und an Hanna Boström und Simon Krause für Eure Unterstützung, die vielen Gespräche und das Korrekturlesen meiner Dissertation.

Natürlich gilt mein Dank auch meinen fleißigen Forschungspraktikanten Natalie Fehn, Jessica Wulfes, Lina Beisswenger, Florian Binder, Ana Mateos, Julia Römer, Felix Böhm und Stefan Clewing. Die Zusammenarbeit mit Euch hat Spaß gemacht und mich motiviert an scheinbar unlösbaren Fragestellungen dran zu bleiben.

Ganz besonders möchte ich meinen wunderbaren Kollegen und Freunden danken, sowohl in München als auch in Stuttgart. Vom Herzen Danke an Marie, Christian, Lars, Alex, Sebastian, Andi, Max, Kerstin und Katalin. Ihr habt mit mir die Erfolge gefeiert und mir bei den Herausforderungen geholfen—ohne Eure Unterstützung wäre ich nicht so weit gekommen!

Mein größter Dank gebührt meinen Eltern und Chris, die mich jederzeit und bedingungslos unterstützt haben.

Life is nothing without a little chaos to make it interesting.

— Amelia Atwater-Rhodes

ABSTRACT

After more than two decades of research in the field of metal–organic frameworks (MOFs), a plethora of structures has been reported and used for a variety of applications including catalysis, gas adsorption, and drug delivery. Zr-based MOFs have emerged as pioneering materials due to their outstanding stability and structural flexibility. Although new Zr-based MOFs are published frequently, systematic investigations on disorder and vacancies in the structures, which are known to affect the materials' properties, remain sparse. In addition, synthetic reports are often irreproducible, leading to phase mixtures of two or more MOFs limiting their utility in targeted applications. This thesis investigates the structural complexity of Zr-based MOFs, in particular cluster disorder and vacancies, and explores the link between synthesis parameters and product outcome.

Combination of Zr-oxo clusters with the chromophore tetrakis(4-carboxyphenyl)porphyrin gives rise to a series of porphyrinic MOFs with interesting (opto)electronic properties. Chapter 2 explores the structures of the cubic representatives PCN-221, MOF-525, and PCN-224. Based on a comprehensive synthetic and structural analysis spanning the local- and long-range, it was found that PCN-221 consists of octahedral $Zr_6O_4(OH)_4$ clusters tilted in four directions, rather than cubic Zr_8O_6 clusters as previously reported in literature. A new structure model—*disordered PCN-224* (dPCN-224)—was established to understand cubic porphyrinic Zr-based MOFs with varying degrees of orientational cluster disorder, linker vacancies, and cluster–linker coordination. In a further step, Chapter 3 evaluates the complexities of synthesising porphyrinic Zr-based MOFs, specifically dPCN-224. A detailed step-by-step formation pathway of dPCN-224 was characterized, revealing that the MOF formed *via* an intermediate. Importantly, it was shown that the Zr source and water content in the reaction influenced the formation of the inorganic building unit and with this the resultant product.

Additionally, Chapter 4 explores the structural complexity of Zr-based MOFs with methane-tetrakis(*p*-biphenylcarboxylate) (MTBC) linkers. Two new MTBC-based structures are presented, namely c-(4,12)MTBC-Zr_6 and t-(4,12)MTBC-Zr_6, that show unexpectedly high structural versatility. The 12-fold cluster coordination found in both structures is enabled by a combination of cluster disorder and linker flexibility. Importantly, Hf analogues were also obtained for both structures revealing that the structural flexibility is not limited to Zr–MTBC compounds.

TABLE OF CONTENTS

CHAPTER 1

INTRODUCTION

Porosity is a fundamental structural feature in nature, found in both living organisms and inorganic materials.[1] Compared to their non-porous counterparts, porous materials are characterized by their high internal surface area, which drives a variety of surface-based interactions such as gas adsorption, gas exchange, and catalysis.[2] For example, the small alveoli in our lungs have a combined surface area larger than a tennis court allowing for efficient gas exchange between the lungs and blood. Likewise, activated charcoal, a form of carbon with surface areas exceeding 3000 m^2 g^{-1}, is often used in medicine for the adsorption of ingested toxins.[3-4]

Porous materials are generally classified by the size of the void space—the pores—into microporous (pore diameter < 2 nm), mesoporous (2 nm < pore diameter < 50 nm), or macroporous (pore diameter > 50 nm) regimes.[5] While the size and shape of the pores can be random in some instances, there are countless examples where the pore size, shape, and volume drive a particular function and thus require a high level of definition. For example, zeolites are well established microporous inorganic materials used as ion exchangers in detergents, adsorbent materials, or for gas separation and purification.[6] In such uses, high control over the pore size is needed; otherwise the target molecule will not interact with the pores. This is analogous to size exclusion chromatography, which uses microbeads to control the retention time of molecules passing through. From a chemistry and engineering perspective, porous materials are playing a transformative role in solving many real-world challenges including environmental remediation, heterogeneous catalysis, medicine, and energy generation and storage.[7-9] The high surface area of these materials is being utilized to improve reaction rates in heterogeneous catalysis, for CO_2 adsorption to reduce carbon emission, or to produce hydrogen for hydrogen-based fuel cells, to give only a few examples.[10-13]

In particular, research into micro- and mesoporous materials has garnered considerable attention, and spans a wide array of materials including inorganic zeolites, organic covalent organic frameworks, and hybrid metal–organic frameworks (MOFs).[7] Importantly, efforts have focused on controlling the properties of these materials to improve the functionality. When developing materials with a specific application in mind, it is important to understand the structure–property

relationships, and therefore, the structure of the material. While long-range order and controlled pore size distributions are important in defining a material's property, short-range disorder and defects may also strongly influence the performance of the material. For instance, the addition of defects is a common strategy to tune or introduce new functionality into a material.[7] When synthesizing functional materials it is therefore essential to have a full understanding of both the short- and long-range features of the material, and how synthetic parameters affect those. As materials become more complex in terms of the number of components used, understanding these features becomes increasingly difficult and requires analysis of the material on several length scales.

This thesis investigates certain types of underexplored disorder and defects that occur in MOFs, specifically in Zr-based MOFs. Although it is clear that properties of Zr-based MOFs depend on the structure, control over phase purity and topological ordering remain poorly understood, and will be the focus of this work. Throughout, the structural complexity arising in Zr-based MOFs built from tetrakis(4-carboxyphenyl) porphyrin and methane-tetrakis(*p*-biphenylcarboxylate) linkers will be investigated, and the link between synthesis conditions and phase selectivity will be examined.

This introductory chapter commences by an overview of MOFs, their tunable structures, and the typical defects found in MOFs. Following this, the challenges in MOF synthesis towards controlled phases will be discussed as well as the common techniques used to characterize these materials. Lastly, an overview of the goals and scope of this thesis will be given.

1.1 Metal–organic frameworks

1.1.1 A brief introduction to MOFs

MOFs are a particularly exciting class of porous materials that consist of extended networks built from inorganic metal cations and clusters linked by polytopic organic linker molecules (Figure 1.1).[14-15] Compared to inorganic zeolites, MOFs are hybrid materials in which organic molecules link the inorganic nodes *via* coordinative bonds. Therefore, MOFs belong to the class of coordination compounds, in which a central atom, usually a metal cation, is coordinated by a surrounding array of ligands.[16] More specifically, MOFs belong to the sub-class of coordination networks, which are defined as coordination compounds extending through repeating coordination entities.[17]

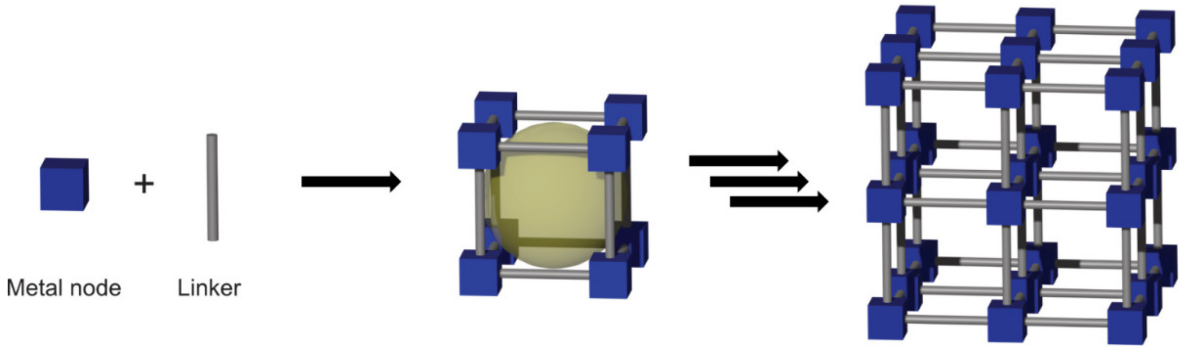

Figure 1.1: Schematic representation of 8-fold coordinated metal nodes (blue) and ditopic linker molecules (grey) that assemble to a three-dimensional MOF structure containing pores (yellow).

In another definition by IUPAC in 2005, MOFs are defined as "*coordination networks with organic ligands containing potential voids*".[17] In many instances, these voids, or pores, result in extremely high porosities and surface areas—in some cases, specific pore volumes of 5.03 $cm^3\ g^{-1}$ and Brunauer-Emmett-Teller (BET) specific surface areas of up to 7920 $m^2\ g^{-1}$ have been reported.[18-19] The outstanding porosity accompanied by high surface areas make the materials exciting for a variety of applications including gas storage and separation, catalysis, and drug delivery.[20-23]

Reports of porous coordination networks (PCNs) first emerged in the 50's. A notable example is the work from Yukio *et al.*, who described a three-dimensional (3D) network of copper atoms linked by adiponitril linkers.[24] However, it was not until the early 1990s that research on PCNs became more mainstream, when Hoskins and Robson's introduced a new class of solid polymeric materials built from metal centers with a tetrahedral or octahedral coordination arrays linked by rod-like connecting units.[25-26] The resulting infinite, ordered frameworks had large cavities, which were suitable for ion exchange and catalytic applications.[27] In 1995, Yaghi *et al*. coined the term *metal–organic framework* with the introduction of a Co-trimesate-based framework.[14] In this work, a microporous, thermally stable material was prepared from symmetric organic molecules bound by metal ions forming layers of open and rigid metal–organic compounds.[14]

In 1999, the single crystal structures obtained from HKUST-1 (HKUST = Hong Kong University of Science and Technology) and MOF-5 represented a major breakthrough in the field of MOF chemistry.[15,28] While HKUST-1 was still referred to as nanoporous material at the time, MOF-5 was the first compound described as a MOF at the time of publication.[15] To date, both materials remain among the most studied frameworks.[29-30] MOF-5 is built of zinc-oxo (Zn_4O) cluster nodes bridged by 1,4-benzodicarboxylate (BDC) linkers coordinating the Zn_4O tetrahedra along the six edges (Figure 1.2a). In contrast, HKUST-1 is comprised of dimeric copper nodes coordinated by four carboxylate groups from four benzene-1,3,5-tricarboxylic acids (BTC) linker molecules

(Figure 1.2b). Both structures feature a 3D connected network of pores with approximately 1 nm wide channels allowing pore accessibility for guest molecules throughout the frameworks. The unit cell of HKUST-1 contains small pore diameters of 5 Å and larger pore diameters of 11 and 13.5 Å, whereas the unit cell of MOF-5 features small pore diameters of 14.2 Å and larger pore diameters of 19 Å depending on the rotation of the phenyl rings, which illustrates how the pore sizes depend on the framework structure.[15,28,31] Since then the MOF field literally exploded, with more than 110,000 MOF structures in the *Cambridge Structural Database*.[32] The hybrid nature of the materials allows for the individual tuning of both the inorganic and organic building units, which opens opportunities for the rational design of pore geometries and framework properties towards specific applications.[33]

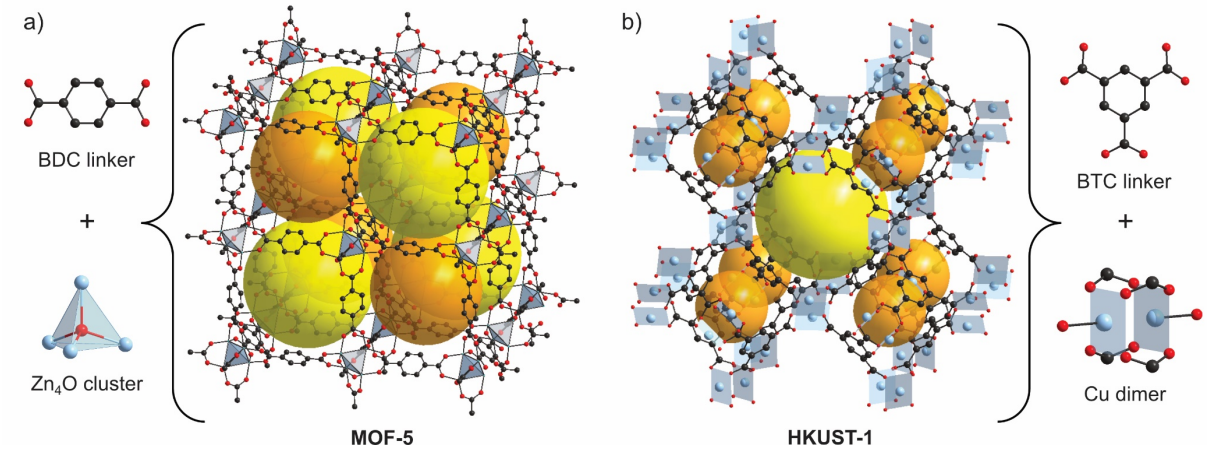

Figure 1.2: a) MOF-5 structure, which has a combination of small and large pore diameters of 14.2 Å (orange) and 19 Å (yellow), respectively, built from tetrahedral Zn_4O clusters and ditopic 1,4-benzodicarboxylate (BDC) linkers. b) Structure of HKUST-1 with small and large pore diameters of 5 Å (orange) and 11–13.5 Å (yellow), respectively, built from dimeric copper nodes and tritopic 1,3,5-tricarboxylic acid (BTC) linkers. Each copper dimer is coordinated by two water molecules and four carboxylate groups from four BTC linkers that bridge the two metal centers.

1.1.2 Design of MOFs towards specific applications

In early coordination polymer chemistry, the networks were built of single nodes and neutral organic linkers with weak and non-directional bonds. In contrast, MOFs consist of metal ions or clusters that are connected by charged linkers to form strong directional bonds with increased stability.[15,34-35] The metal center or cluster and the coordinating functional groups on the linker constitute the secondary building unit (SBU).[35] In MOF-5, for example, carboxylate linkers aggregate the Zn_4O cluster into $Zn_4O(CO_2)_6$ SBUs in which the Zn tetrahedra are capped by six carboxylate groups along the six edges (Figure 1.3a).[15] The metal centers are held in place by strong interactions within the clusters, which promotes rigidity of the SBU and ultimately affords

outstanding architectural stability and permanent porosity. In addition to their mechanical properties, the directional bonding of vertices and linkers assists the prediction of framework topologies of new MOFs.[35]

The design of new MOFs typically involves the selection of symmetrically complementary SBUs and linkers, which will predetermine the network structure and topology that is formed, a concept known as reticular chemistry.[35-37] The judicious choice of molecular building units (namely the metal cation or cluster, and ligand) allows engineering of complex new MOFs structures with desired properties such as pore size, or specific framework functionalities.

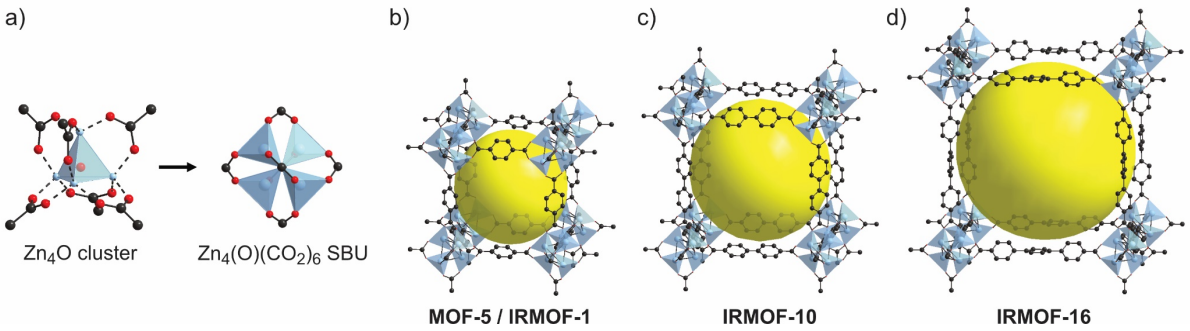

Figure 1.3: a) Each Zn_4O cluster in MOF-5 is coordinated by six 1,4-benzodicarboxylate (BDC) linkers along the six edges of the tetrahedron forming the secondary building unit (SBU) $Zn_4O(CO_2)_6$. b) Structure of MOF-5 (IRMOF-1) built from $Zn_4O(CO_2)_6$ SBU and the BDC linker. c) and d) Isoreticular MOFs IRMOF-10 and IRMOF-16 built from bi- and triphenyldicarbocylate linkers, respectively. The MOF's pore size (yellow) increases with the length of the linker.[38]

The organic linker plays an important role in determining the properties of the MOF. By adjusting the size and geometry of linkers, the pore sizes and shape of the MOF can be tuned. For example, combination of Zn_4O cluster with bidentate BDC linker yields MOF-5, whereas the longer bi- or triphenyldicarbocylate linkers results in the isoreticular MOF (IRMOF) IRMOF-10 and IRMOF-16, respectively. These MOFs feature an increase in pore size by up to 50 %; a phenomenon referred to as isoreticular expansion (Figure 1.3b-d).[38] In addition, the properties of MOFs can be modulated by modifying the ligand. For example, replacing the BDC linker in MOF-5 with tridentate biphenyl-3,4,5-tricarboxylic acid yields complex 3D frameworks with luminescent properties.[39-40] On the other hand, thiolate-based linkers with conjugated organic cores and high charge delocalization, or azolate-based ligands with σ-donating and π-accepting character allowing for electronic coupling, are two common inclusions in MOF design to promote electrical conductivity.[41] Introducing functional groups on the linker can direct the specific surface chemistry as well. Hydrocarbon chains on the linker, for example, will increase the hydrophobicity and were shown to favour methane uptake.[38,42] On the other hand, catalytically active groups can be attached

to linkers in order to introduce single-site catalysts into the framework. This is seen in the case of cobaloxime-based linkers, which can yield a MOF that is active towards electrocatalytic hydrogen evolution.[43]

Using different metals to construct the SBU can also have a dramatic impact on the structure and properties of the resulting MOF. For example, MIL-53 (MIL= Matériaux de l'Institut Lavoisier), first published with Cr(III), is built of infinite chains of metal cations that are cross-linked by 1,4-benzodicarboxylate linkers and is known for its unique structural flexibility.[44] Upon heating, the inorganic chains are reversibly displaced due to water loss, and form expanded channels (Figure 1.4). Rehydration upon cooling reverses the process.[45] However, the responsive flexible behaviour depends on the nature of the metal. For example, the V(IV) derivative MIL-47 with oxidised metal and bridging oxides in the inorganic chains, compared to hydroxides in MIL-53(Cr), remains in the large-pore form and does not show the so-called breathing behaviour.[46-47] This example highlights the importance of the metal cation as a design element for MOFs.

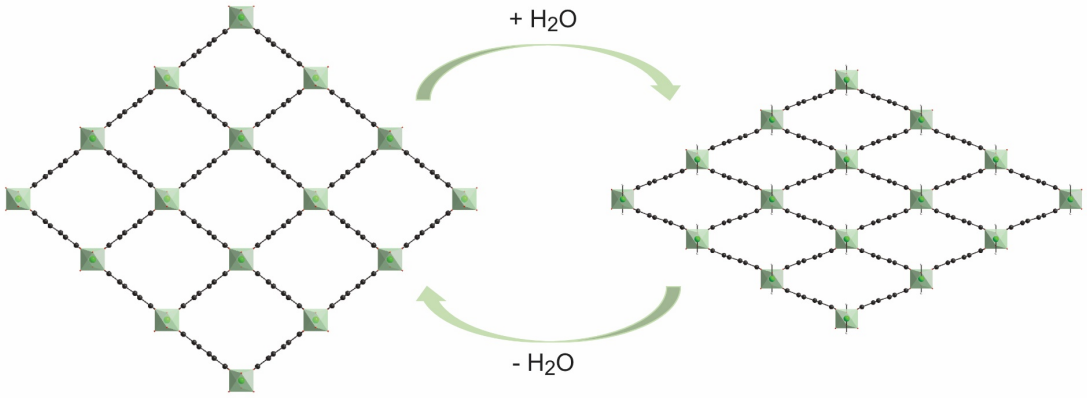

Figure 1.4: The MIL-53(Cr) structure built from inorganic [Cr-OH] chains (green) and 1,4-benzodicarboxylate linkers in its dehydrated large-pore form (left) and hydrated closed-pore form (right).

Changing the chemical nature of SBUs can further help to specify host-guest interactions. MOF-74(Fe) built of iron oxide chains and 2,5-dioxido-1,4-benzenedicarboxylate linkers, for example, shows a strong affinity towards unsaturated hydrocarbons while the analogue MOF-74(Mn) has a higher affinity towards aromatic molecules.[48-49] On the other hand, introducing SBUs with open metal sites can improve the gas sorption properties of the MOF. This is exemplified by HKUST-1 which features free coordination sites on its dimeric copper nodes and is among the best performing materials for methane storage.[50] In addition, MOFs with Lewis acidic open metal sites on their nodes such as Ni-based Ni_2(DHTP) (DHTP = 2,5-dihydroxyterephthalic acid) interact well with Lewis bases like carboxylates and are useful for CO_2 capture.[34,51]

All together, the geometric and chemical variety of both SBUs and linkers gives rise to a plethora of possible MOF structures, which has led to MOFs becoming a widely used and important material for chemists over the last three decades.

1.2 Zr-based MOFs

Zr-based MOFs are of particular interest owing to their high chemical and thermal stability when compared to other MOFs.[52-53] Generally, the weakest part in MOFs are the coordination bonds between cluster and linker.[36] Beside metal–ligand coordination geometry, the ionic radius of the metal ion and the pK_a of ligands determine the strength of the bond and, therefore, greatly affect the stability of the framework.[54-55] Following the hard/soft acid/base (HSAB) concept, the high charge density of hard Lewis-acid Zr(IV)-ions and the associated affinity towards hard Lewis-bases such as oxide anions bestows Zr-based MOFs with increased stability.[36,56] While Zr-based MOFs readily decompose in basic conditions, the frameworks remain stable in most organic solvents and water, and show exceptional stability in acidic conditions.[36,52] Furthermore, the high abundance of Zr and its low toxicity motivates the study and applications of Zr-based MOFs, especially for applications such as waste water treatment and drug delivery.[57-61]

UiO-66 (UiO = University of Oslo) was the first Zr-based MOF to be synthesized and published in 2008 by Lillerud and co-workers.[52] The framework consists of $[Zr_6(\mu_3\text{-}O)_4(\mu_3\text{-}OH)_4]^{12+}$ clusters, where the six Zr(IV) cations are octahedrally arranged and bridged by four $\mu_3\text{-}O^{2-}$ and four $\mu_3\text{-}OH^-$ that alternate on the triangular faces of the octahedra (Figure 1.5). The ditopic, linear 1,4-benzenedicarboxylate (BDC) linker connects the Zr-clusters to yield a 3D porous framework with a sum formula of $Zr_6O_4(OH)_4(BDC)_6$. Here, the 12 edges of the octahedral Zr-oxo clusters are coordinated by 12 carboxylate groups from the BDC linkers forming robust $Zr_6O_4(OH)_4(CO_2)_{12}$ SBUs which lead to a high network stability (Figure 1.5).

Since the discovery of UiO-66, more than 2,000 publications on Zr-based MOFs have been reported, owing to the uniquely variable connectivity of the hexanuclear node.[36,62-65] In addition to the $Zr_6O_4(OH)_4(CO_2)_{12}$ SBU, which has a coordination number (CN) of 12, SBUs from $Zr_6O_4(OH)_4$ clusters with 4, 6, 8, 10, and 11 linker carboxylate groups (CN = 4, 6, 8, 10, and 11, respectively) have been reported in MOFs (Figure 1.6).[36,66-67] Here, OH^-/H_2O pairs and terminal monocarboxylate ligands occupy the vacant coordination sites on the cluster in order to balance the charge.[68] These sites are of particular interest for introducing new ligands *via* solvent-assisted ligand incorporation (SALI) in order to modify MOFs postsynthetically.[69-70]

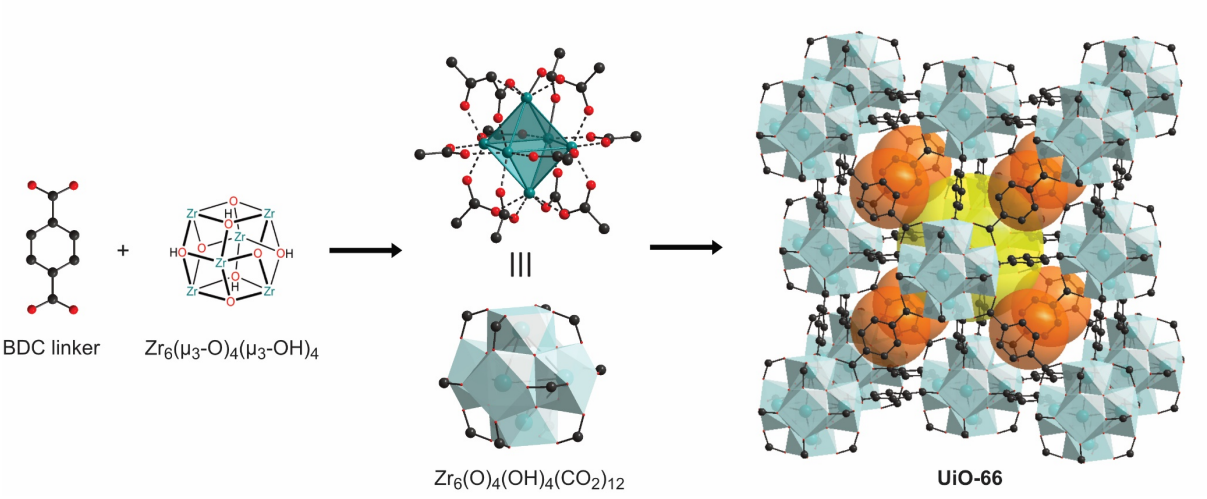

Figure 1.5: UiO-66 structure containing small and large pore diameters of 9 Å (orange) and 11 Å (yellow), respectively. The framework is built from $Zr_6(\mu_3\text{-}O)_4(\mu_3\text{-}OH)_4$ clusters coordinated by 12 1,4-benzodicarboxylate (BDC) linkers along the edges of the Zr octahedron forming the $Zr_6(\mu_3\text{-}O)_4(\mu_3\text{-}OH)_4(CO_2)_{12}$ secondary building units (SBUs).

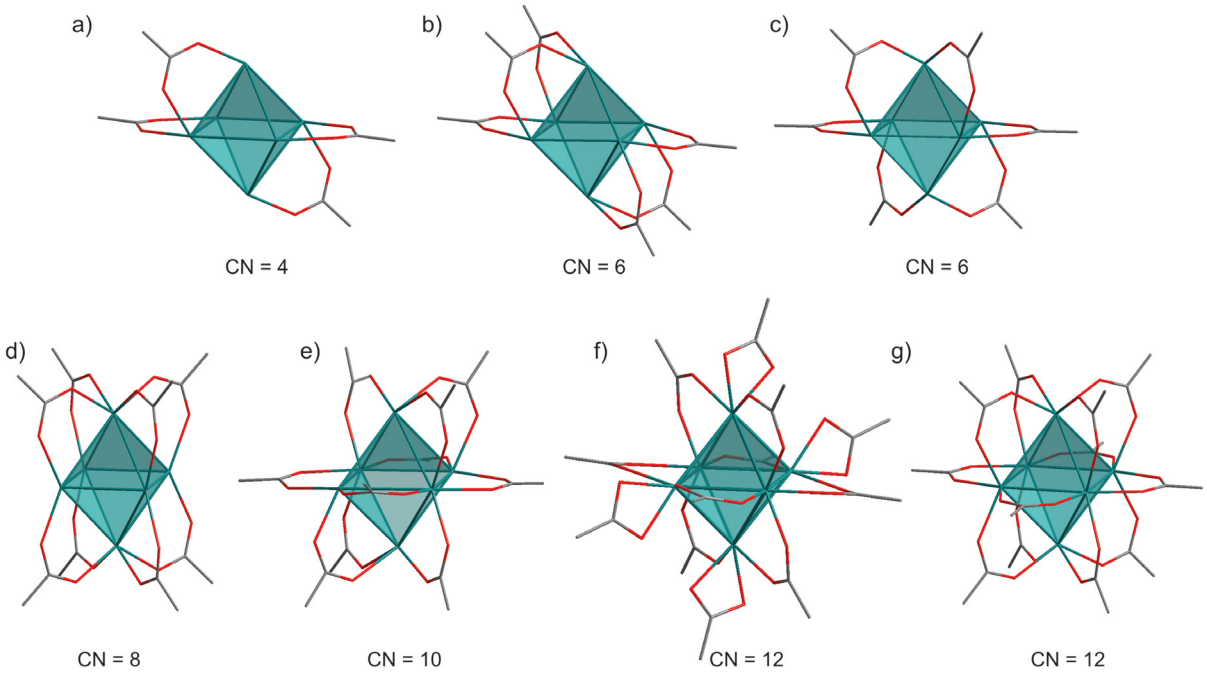

Figure 1.6: Schematic representation of a) 4-fold, b) and c) 6-fold, d) 8-fold, e) 10-fold, and f) and g) 12-fold coordination of octahedral $Zr_6O_4(OH)_4$ cluster by carboxylate groups found in Zr-based MOFs.

The versatile coordination capability of the $Zr_6O_4(OH)_4$ cluster allows for a wide array of MOF topologies, generally defined by three-letter codes, with variable densities and pore sizes depending on the geometric properties of the selected linkers.[36,62-64] In 2014, the Snurr group performed a computational analysis of hypothetical network topologies taking into account $Zr_6O_4(OH)_4$ cluster connectivities and linker symmetries, and identified 204 compatible MOF topologies.[71] The topology of the networks is guided by the symmetry of the employed linker. The combination of a Zr-cluster and a linear linker, for example, allows for **dia** (CN = 4), **bcu** (CN = 6), **reo** (CN = 8), **bct** (CN = 10), and **fcu** (CN = 12) topologies. Tritopic linkers in turn permit **spn** and **kgd** topologies, both with 6-connected $Zr_6O_4(OH)_4$ clusters. When expanding to tetratopic linkers, even more topologies are possible, including **she** with 6-fold coordination, **csq**, **scu**, and **sqc** with 8-fold coordination, and **ftw** and **shp** with 12-fold cluster coordination.[36,72] Some representative network topologies that occur in Zr-based MOFs are shown in Figure 1.7.

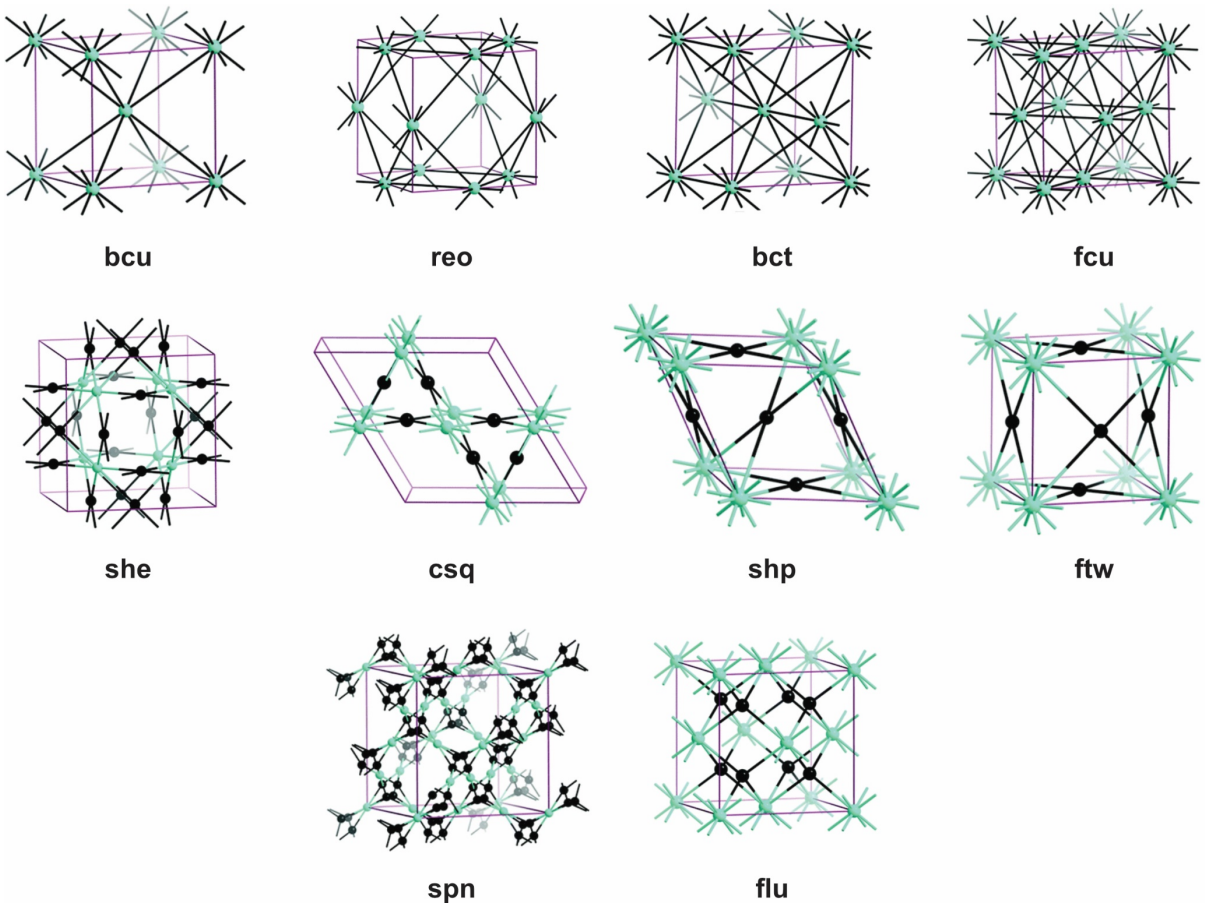

Figure 1.7: Adapted figure from Bai *et al.*[36] showing representative topologies for linear linkers (**bcu**, **reo**, **bct**, and **fcu**), tetratropic planar linkers (**she**, **csq**, **shp**, and **ftw**), trigonal linkers (**spn**), and tetrahedral linkers (**flu**). Adapted with permission from Royal Society of Chemistry (Great Britain), Copyright 2016.

In addition to octahedral $Zr_6O_4(OH)_4$ clusters, Zr-based MOFs have also been reported with isolated Zr(IV)-ions, Zr(IV)-oxo-chain structures, chains of condensed Zr_6O_8 clusters, or ZrO_6, ZrO_7, ZrO_8, Zr_8O_6, $Zr_8O_8(OH)_4$, and $Zr_{12}O_8(OH)_8$ metal nodes, further extending the library of MOF structures formed from Zr-based SBUs.[73-74] Among these, octanuclear Zr-oxo clusters are of particular interest in this work due to their intriguing geometries (Figure 1.8). MOFs reported with these clusters include PCN-221 and Zr-MTBC, which are built from tetrakis(4-carboxyphenyl)porphyrin (TCPP) and methane-tetrakis(*p*-biphenylcarboxylate) (MTBC) linkers, respectively.[75-76] In PCN-221, the eight Zr(IV) cations form a Zr_8 cube that is connected by six μ_4-O^{2-} on the six faces of the cube. The 12 edges of the cubic cluster are bridged by 12 carboxylate groups from the TCPP linker resulting in a $Zr_8(\mu_4\text{-}O)_6(CO_2)_{12}$ SBU (Figure 1.8a). To balance the charge, each Zr further coordinates one hydroxy group. Zr-MTBC in turn contains $Zr_8(\mu_2\text{-}O)_8(\mu_2\text{-}OH)_4$ clusters, in which eight μ_2-O^{2-} and four μ_2-OH^- connect the eight Zr(IV) cations on the 12 edges of the Zr cube. Similar to PCN-221, 12 carboxylate groups from the MTBC linker coordinate the cluster along the 12 edges of the Zr_8O_6 cluster to form $Zr_8(\mu_2\text{-}O)_8(\mu_2\text{-}OH)_4(CO_2)_{12}$ SBUs (Figure 1.8b). Interestingly, both the $Zr_8(\mu_4\text{-}O)_6$ cluster and the $Zr_8(\mu_2\text{-}O)_8(\mu_2\text{-}OH)_4$ cluster feature very short Zr–Zr distances of 2.69 Å and 2.75 Å, respectively, compared to 3.51 Å in the $Zr_6(\mu_3\text{-}O)_4(\mu_3\text{-}OH)_4$ cluster of UiO-66, for example.[52,75-76] In fact, the Zr–Zr distances are much shorter than in all inorganic Zr-based compounds from the Inorganic Crystal Structure Database (ICSD).[77] Such short distances suggest that the cubic arrangement of Zr atoms found from single crystal (SC) refinements of PCN-221 and Zr-MTBC is erroneous. Therefore, elucidating the true structures of these MOFs is the basis of this thesis.

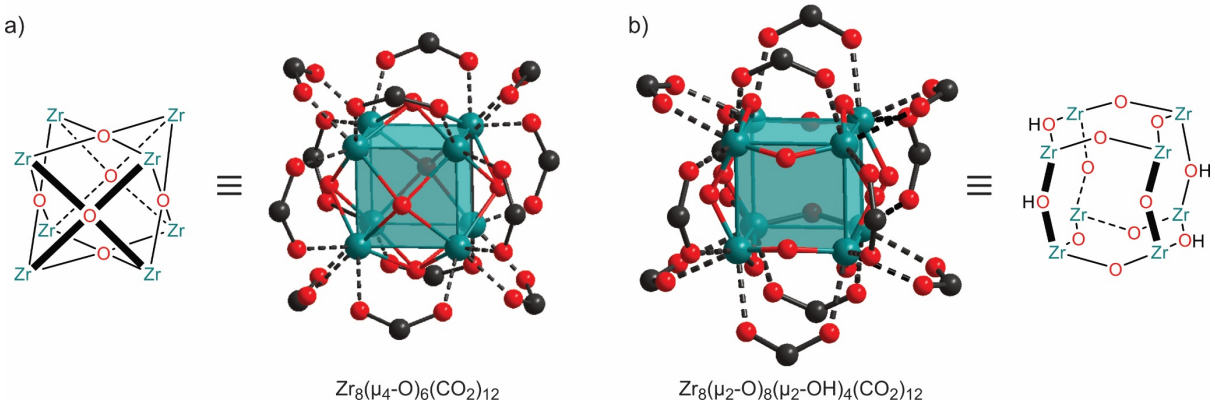

Figure 1.8: a) $Zr_8(\mu_4\text{-}O)_6(CO_2)_{12}$ SBU found in PCN-221. The SBU is built from a Zr_8 cube connected by six μ_4-O^{2-} on the six faces of the cube and coordinated by 12 carboxylate groups from 12 tetrakis(4-carboxyphenyl)porphyrin linkers. b) $Zr_8(\mu_2\text{-}O)_8(\mu_2\text{-}OH)_4(CO_2)_{12}$ SBU reported in Zr-MTBC. The SBU is built from Zr_8 cubes connected by eight μ_2-O^{2-} and four μ_2-OH^- and coordinated by 12 carboxylate groups from methane-tetrakis(*p*-biphenylcarboxylate) linkers.

1.2.1 Zr-porphyrin-based MOFs

MOFs based on porphyrin linkers have become very popular due to the chromophoric properties of these molecules.[78] Stemming from the Greek porphyra ("like purple"), the free-base porphyrin, H_2-P, appears intensely purple. Indeed, porphyrins show high absorbance in the visible light region originating from their highly conjugated π-electron system.[78] In addition, the porphyrin core is capable of complexing metal cations in a stable and often irreversible manner (Figure 1.9a).[79] In fact, complexation with porphyrins is possible for most transition metals and leads to metalloporphyrins, which are excellent catalysts and play a fundamental role in living organisms. For example, a Fe(II) complexed porphyrin unit is found in the haeme blood protein where it plays a crucial role in dioxygen fixation.[80] Likewise, chlorophyll, which is essential for photosynthesis, contains an aromatic porphyrin core with a sequestered magnesium atom, which aids in the adsorption of sunlight.[79] From a chemistry perspective, porphyrins are particularly interesting since they can be readily substituted at the *β*- and *meso*-position of the macrocycle.[81] Reaction of pyrrole and benzaldehyde yields *meso*-tetraphenyl porphyrin, which can easily be metallated and is widely employed as a photosensitizer or redox catalyst.[82-84]

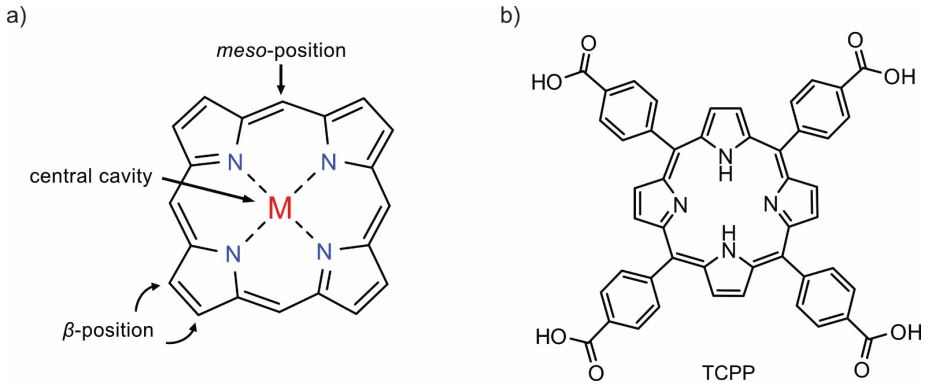

Figure 1.9: Chemical structures of a) the porphyrin core coordinating a metal in the central cavity indicating the *β*- and *meso*-position of the macrocycle and b) the tetratopic linker tetrakis(4-carboxyphenyl)porphyrin (TCPP).

Immobilization of the porphyrin unit on a rigid support such as MOFs prevents the aggregation of molecules, thereby increasing the optical performance of the chromophore and improving the accessibility of active sites for catalysis and adsorption, for example.[85-87] In the last decade, vast research efforts have been made on the synthesis of MOFs from carboxy-based porphyrins, especially in combination with Zr-oxo clusters due to the stable Zr–carboxylate coordination. The high stability combined with light absorbing properties yields frameworks with excellent optoelectronic properties utilized in photocatalytic CO_2 reduction and hydrogen evolution.[88-90]

Among the various possible porphyrin-based linkers, considerable attention has been devoted to porphyrinic MOFs built of tetrakis(4-carboxyphenyl)porphyrin (TCPP) (Figure 1.9b). The tetratopic linker exhibits D_{2h} symmetry as a free base and D_{4h} symmetry when metallated, allowing for a wide array of MOF topologies.[78] So far, six MOFs have been reported from TCPP in combination with $Zr_6O_4(OH)_4$ clusters: 6-connected PCN-224[91] (**she**), 8-connected MOF-545/PCN-222[85,92] (**csq**), PCN-225[86] (**sqc**), and NU-902[93] (**scu**), as well as 12-connected MOF-525[92] (**ftw**) and PCN-223[94] (**shp**) (Figure 1.10).

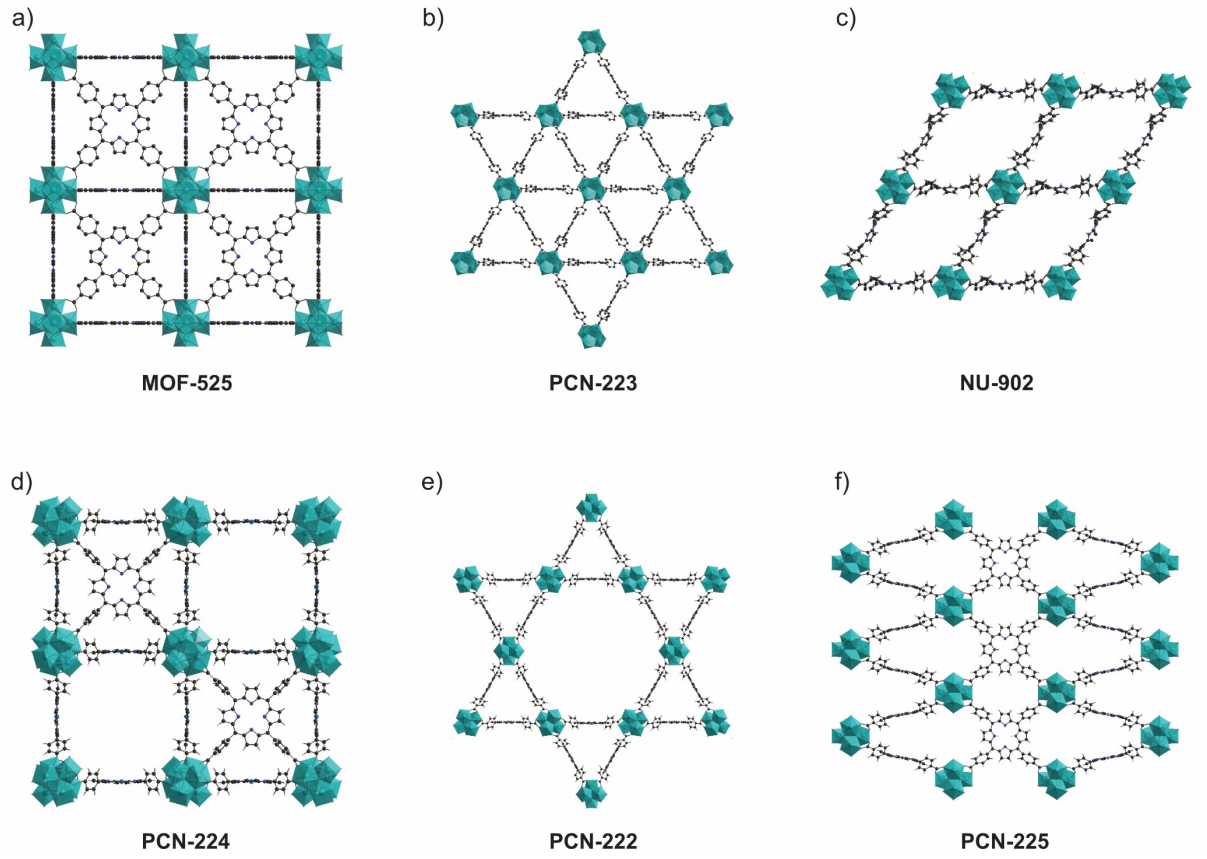

Figure 1.10: Structures of a) MOF-525, b) PCN-223, c) NU-902, d) PCN-224, e) PCN-222, and f) PCN-225. All MOFs are built from $Zr_6O_4(OH)_4$ clusters and tetrakis (4-carboxyphenyl)porphyrin linkers.

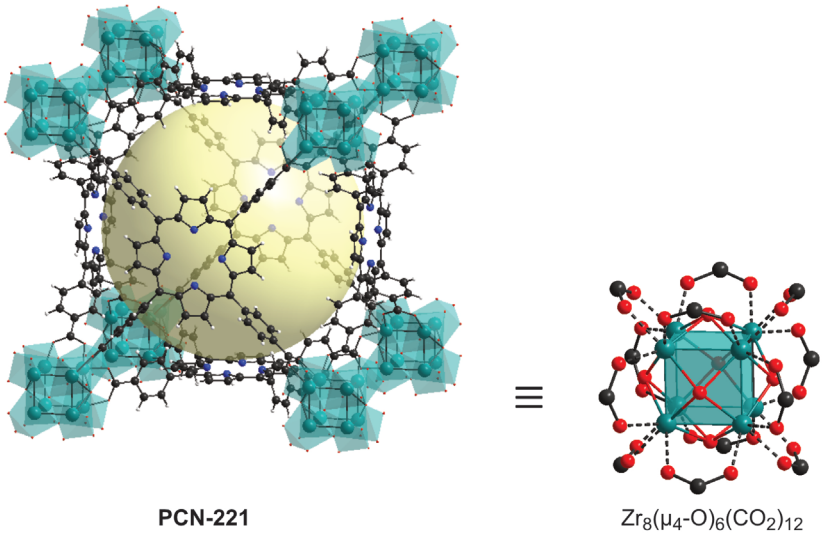

Figure 1.11: The PCN-221 structure built from Zr_8O_6 clusters and tetrakis(4-carboxyphenyl)porphyrin linkers. The Zr_8O_6 clusters are coordinated by 12 linkers along the 12 edges of the Zr_8 cube thereby forming a $Zr_8(\mu_4\text{-}O)_6(CO_2)_{12}$ SBU.

Besides MOF-525 and PCN-224, an additional cubic TCPP-based MOF, PCN-221, was published featuring cubic Zr_8O_6 clusters instead of octahedral $Zr_6O_4(OH)_4$ clusters (Figure 1.11).[75] Both MOF-525 and PCN-221 are described with 12-fold coordination of the respective $Zr_6O_4(OH)_4$ and Zr_8O_6 clusters and feature similar unit cells—19.39 Å and 19.51 Å, respectively.[75,92] Even though MOF-525 and PCN-221 are widely studied, the structure reported for both MOFs are disputed.[72] As previously discussed, the Zr_8O_6 clusters in PCN-221 feature short Zr–Zr distances of only 2.69 Å, which bring into question the MOF's structure. On the other hand, MOF-525 features co-planar phenyl rings in the TCPP linkers, which are energetically demanding.[95] As the properties of MOFs depend on their structure, it is of vital importance that the structure and characterization of these materials be well understood to inform their application.[96] Exploring these structures is the subject of this work.

1.2.2 Zr-MTBC-based MOFs

The use of tetratopic linkers with tetrahedral symmetry expands the array of possible Zr-MOF topologies. In 2014, Zhou *et al.* synthesized PCN-521, the first Zr-MOF from a tetrahedral linker, methane-tetrakis(*p*-biphenylcarboxylate) (MTBC), which was also the first Zr-based MOF with **flu** topology (Figure 1.12 and Figure 1.13a).[97] PCN-521 consists of $Zr_6O_4(OH)_4$ clusters that are coordinated by eight linker carboxylate groups from MTBC linkers thereby forming large tetrahedral cavities. While PCN-521 consists of $Zr_6O_4(OH)_4$ clusters only, another MOF based on MTBC linkers, Zr-MTBC, with a mixture of $Zr_8O_8(OH)_4$ and $Zr_6O_4(OH)_4$ clusters in a 1:3 ratio

was reported two years later (Figure 1.13b).[76] Zr-MTBC has a cubic structure, where both the $Zr_8O_8(OH)_4$ and $Zr_6O_4(OH)_4$ clusters are coordinated by 12 carboxylate groups from MTBC linkers along the edges of the Zr-cube and Zr-octahedra, respectively. Curiously, both tetragonal PCN-521 and cubic Zr-MTBC are synthesized under strikingly similar reaction conditions, raising the question of whether both MOFs are actually formed from different Zr clusters.[76,97] In addition, the Zr–Zr distances of $Zr_8O_8(OH)_4$ clusters reported in cubic Zr-MTBC are quite short (2.75 Å), which draws parallels to porphyrinic PCN-221 which has Zr_8O_6 clusters.[75-76] This highlights the need for a deeper examination of the structures and compositions of these MOFs.

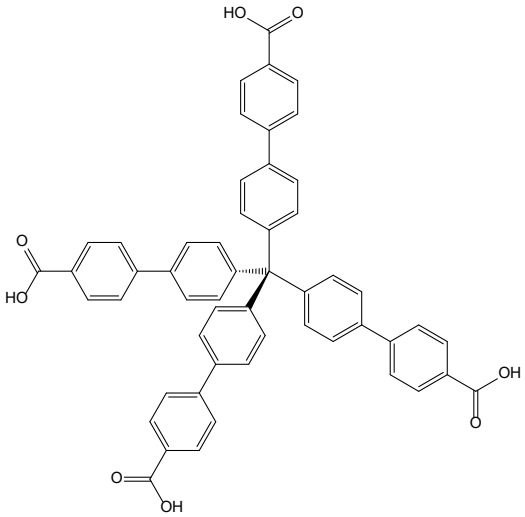

Figure 1.12: Chemical structure of the methane-tetrakis(*p*-biphenylcarboxylate) (MTBC) linker.

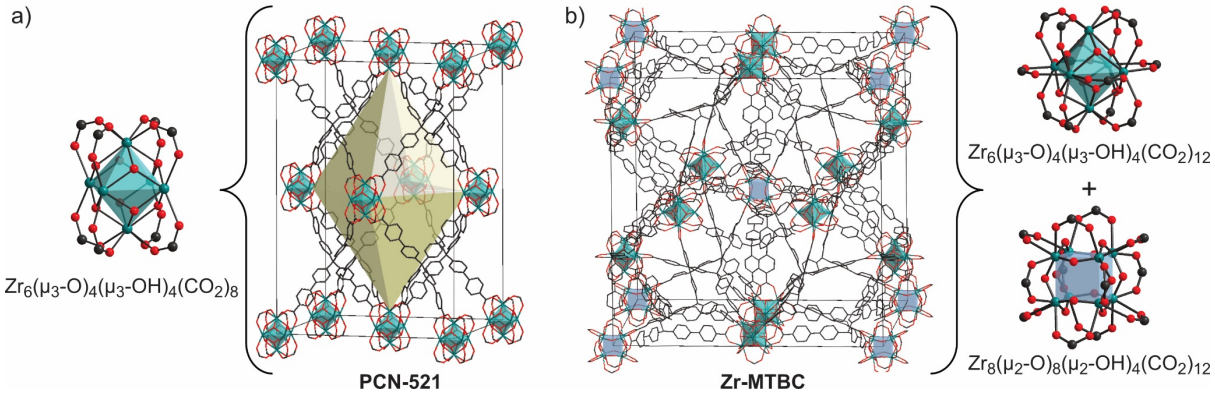

Figure 1.13: a) Structure of PCN-521 with **flu** topology built from $Zr_6(\mu_3\text{-}O)_4(\mu_3\text{-}OH)_4(CO_2)_8$ SBUs with 8-fold coordination by methane-tetrakis(*p*-biphenylcarboxylate) (MTBC) linkers and octahedral pores (yellow). b) Structure of cubic Zr-MTBC built from the same MTBC linker and $Zr_6(\mu_3\text{-}O)_4(\mu_3\text{-}OH)_4(CO_2)_{12}$ as well as with $Zr_8(\mu_2\text{-}O)_8(\mu_3\text{-}OH)_4(CO_2)_{12}$ SBUs, both with 12-fold linker coordination.

1.3 Defects in MOFs

So far, only ideal MOF structures have been described. These systems, however, can possess a range of deviations from their ideal structures referred to as defects. Generally, defects are defined as *"sites that locally break the regular periodic arrangement of atoms or ions of the crystalline parent framework because of missing or dislocated atoms or ions"*.[98] Defects can occur along different dimensions in crystalline materials: (i) zero-dimensional defects, so called point defects that occur on isolated sites, (ii) one-dimensional defects, or line defects, which break crystal patterns along a line, (iii) two-dimensional defects, which are typically found as grain boundaries or surfaces, and (iv) three-dimensional defects or volume defects that change crystal lattices over a finite volume.[99]

Defects are an efficient tool to tune the physical and chemical properties of solid-state materials. For example, conductivity of Si dramatically increases upon doping with phosphorus (P) or boron (B), which introduce negative charge carriers or positive holes into the structure, respectively, allowing for the movement of electrical charge through the material.[100]

Thermodynamically, point defects are always present in solid state material above 0 K.[101] The creation of point defects increases the disorder, and hence the configurational entropy of the system. However, point defects also increase the internal energy of the system resulting in a positive enthalpy of defect formation.[101] As a result, the concentration of defects reaches an equilibrium when the free enthalpy of the system is minimized, which depends on the type of defect, the temperature, and other variables.[101-102] Defects with high formation enthalpy are thus more likely to form at higher temperatures. In the case of self-assembled structures such as MOFs, however, the enthalpy between two different structure arrangements is often small.[103-104] Consequently, these systems lean towards high equilibrium concentrations of defects.

Point defects are the most important defects in crystalline MOFs and are characterized through the absence or additional presence of single atoms or molecules inside the crystal lattice (vacancies and interstitial defects, respectively; Figure 1.14).[105] They not only change the density or porosity of a material, but also give rise to local fields such as strain or chemical potential, which may interact with one another.[106] As a result, point defects can strongly affect a material's properties and, therefore, are strategically introduced into frameworks to tune their properties.[106-107]

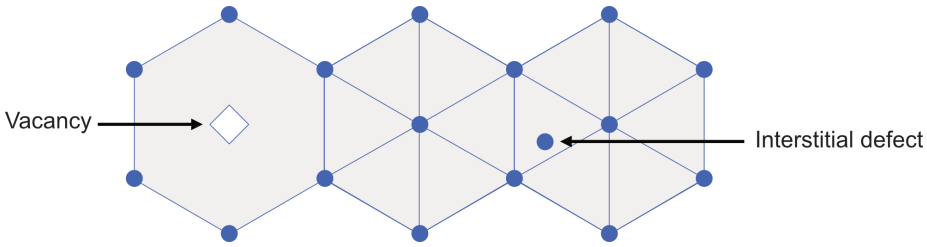

Figure 1.14: Schematic representation of two common point defects, vacancies and interstitial defects, in a 2D hexagonal lattice.

1.3.1 Point defects in Zr-based MOFs

The high stability of $Zr_6O_4(OH)_4$ clusters, combined with the ability to cap free coordination sites, allows for large quantities of point defects in Zr-based MOFs.[107] These are either incorporated into the framework during synthesis of the MOF, or after MOF assembly *via* post-synthetic treatments.[108] Fast crystallization or the addition of modulators (see Section 1.5.3), for example, often increases the amount of defects incorporated into the framework.[109-112] Mechanical or acid/base treatment are, on the other hand, commonly used to introduced defects post-synthetically.[108]

In Zr-based MOFs, point defects can affect both organic and inorganic building blocks.[106,113-115] The absence of organic linkers is referred to as missing-linker defects or linker vacancies and generates free coordination sites on Zr-clusters. Depending on the reaction environment, terminal ligands such as monocarboxylates or hydroxy water pairs compensate the charge imbalances on the clusters (Figure 1.15).[107,110]

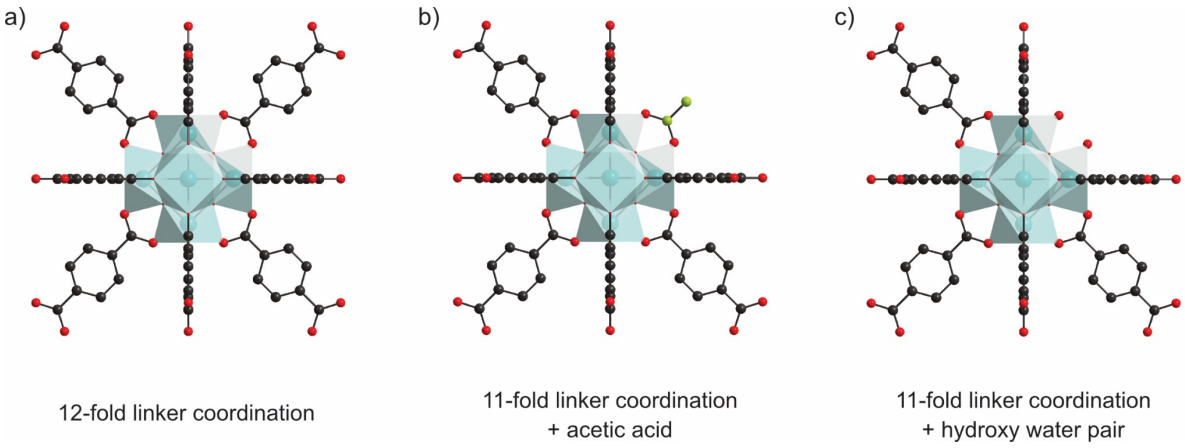

Figure 1.15: Representation of linker vacancies in UiO-66 showing a) a $Zr_6O_4(OH)_4$ cluster with 12-fold linker coordination, and b-c) $Zr_6O_4(OH)_4$ clusters with 11-fold linker coordination where acetic acid (green) and a hydroxy water pair compensate the linker charges, respectively.

In contrast, missing-cluster defects often occur together with larger amounts of linker vacancies in the framework. When a set of linkers is missing that would all coordinate one Zr cluster, the Zr cluster at its center is missing as well. As a result, the framework contains new, larger cavities that notably enhance diffusion of products within porous structures.[106,110,112] In UiO-66, for example, combined linker and cluster vacancies create octahedral cages of 18 Å, in addition to the regular pores of 7 Å and 9 Å in UiO-66.[107]

1.3.2 From random vacancies to new ordered defect MOF phases

In MOFs, defects can be ordered, disordered, or somewhere in between (correlated disorder).[106,116] Defects are ordered when linker or cluster vacancies occur repeatedly in a specific fashion throughout the entire framework (Figure 1.16). The defects then show long-range order and form a new crystallographic phase with additional superstructure reflections in the X-ray diffraction (XRD) pattern, compared to the parent phase. Systematic cluster defects in hexagonal, porphyrinic PCN-223 with **shp** topology, for example, yields the ordered missing-cluster phase PCN-222 with **csq** topology.[85,94] The same applies to defective **reo** UiO-66, where one quarter of the Zr clusters is missing compared to the defect-free **fcu** UiO-66 phase.[107] On the contrary, local or randomly arranged vacancies yield frameworks without long-range periodicity (Figure 1.16). Here, the vacancies do not follow a pattern in the framework and, therefore, do not generate superlattice peaks in powder X-ray diffraction (PXRD) patterns. Interestingly, the order of defects can affect the mechanical stability of the MOF: **reo**-UiO-66 with ordered cluster defects has a higher mechanical stability than highly defective UiO-66 with randomly arranged vacancies.[117-118]

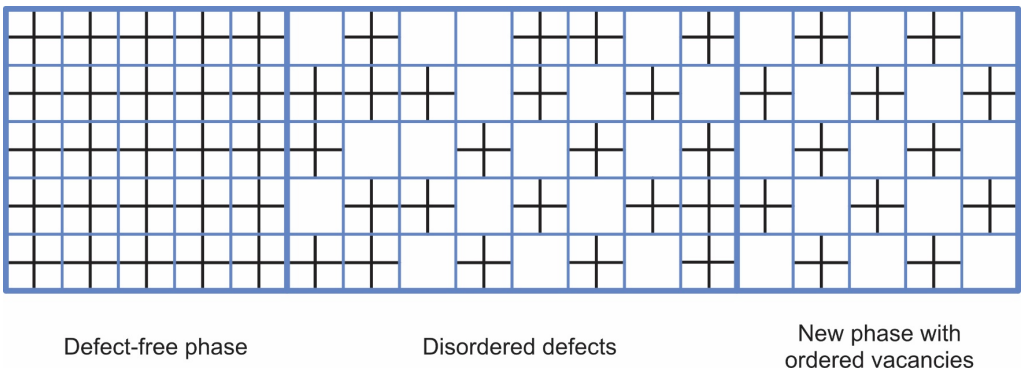

Figure 1.16: Schematic illustration of a defect-free phase (left), disordered defects (middle), and ordered vacancies forming a new phase (right).

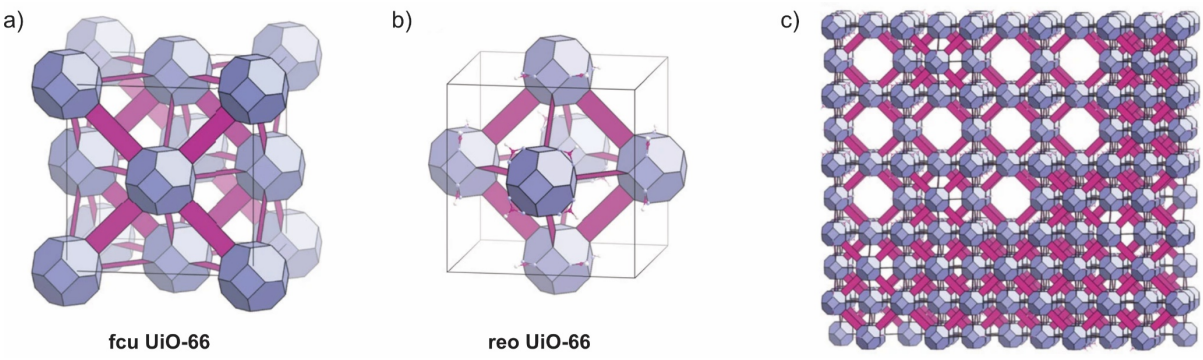

Figure 1.17: Adapted figure with polyhedral representations of a) UiO-66 with **fcu** topology, b) UiO-66 with **reo** topology and c) nanodomains of defect-rich regions within a matrix of defect-free **fcu** framework.[106] Adapted by permission from Springer Nature License: Springer Nature, Nature Communications, Correlated defect nanoregions in a metal–organic framework, Matthew J. Cliffe *et al*, Copyright (2014).

In 2014, Cliffe *et al*. observed that in UiO-66 with supposedly random cluster defects, vacancies may actually be correlated,[106] and their study on cluster vacancies represented a milestone in the field of defective MOFs. They observed that during synthesis of UiO-66, one cluster defect promotes cluster defects in neighbouring sites yielding domains of ordered vacancies. In fact, defective UiO-66 contains nanodomains of missing-cluster phase **reo**-UiO-66 in four possible orientations relative to the bulk framework, which correspond to the four Zr-cluster positions in the unit cell (Figure 1.17).[106] Subsequent studies have shown that both linker and cluster defects likely affect neighbouring entities during the self-assembly of MOF structures, thereby creating regions of correlated vacancies that can no longer be considered random.[112,119] The correlation between these vacancies causes diffuse scattering in XRD patterns that manifest as weak, broad superstructure peaks.[106]

Overall, topological disorder can occur on different length scales throughout MOF structures. When defects or vacancies occur randomly or in small correlated domains, the product is often referred to as a defect variant of the pristine framework. Linker or cluster vacancies with long-range order in turn often yield a new MOF phase with a different topology.

1.4 Synthesis of MOFs

1.4.1 MOF self-assembly

Self-assembly describes the process in which a disordered system of components forms an organized structure without external direction and is widely adopted both in nature and in the lab.[120] The assembly of complex structures often occurs in multiple steps. Consider a protein: first, amino acids condense into peptide chains to form a primary structure. The chains then fold into α-helices

or β-sheets (the secondary structure), *via* non-covalent interactions. Further interactions between secondary structures drive the formation of tertiary structures, which in turn can form higher-ordered quaternary structures.[121] The assembly of proteins typically occur at biological temperatures and pH, and can be manipulated by local environments within the organism.[122] Synthetically, scientists can promote self-assembly in many of the same ways for a variety of applications such as in drug delivery, where a liposome is self-assembled around a therapeutic, or in the development of new structures, as is the case for MOFs.[121,123-126]

The formation of MOFs relies on coordinative self-assembly between metal (clusters) and organic molecules. The crystallization of MOF particles classically involves three steps: (i) an induction period, where the solution is supersaturated, (ii) nucleation which initiates the formation of MOF crystals, and (iii) growth from MOF nuclei into larger, periodic structures.[126-129] Interestingly, the formation of MOF particles often substantially differ from one MOF to another.[126] Nucleation of HKUST-1, for example, follows the "classical" pathway in which monomers spontaneously form stable crystalline HKUST-1 nuclei.[130-131] In contrast, MOF-5 nucleates "non-classically" *via* formation of metastable intermediates that further depend on reaction conditions.[132-134] Similar to step (ii), there are also several pathways through which growth step (iii) can occur during MOF synthesis. In general, growth of MOF particles in solution involves diffusion and subsequent incorporation of the building units into the crystal surface.[135] However, MOF growth can also occur *via* sequential precipitation following the Ostwald's Rule of Stages, whereby kinetic phase growth is prominent at the beginning before transforming into a thermodynamically stable product.[63,136] On top of that, MOFs have also been demonstrated to form *via* aggregation-mediated crystal growth, where pre-formed crystalline building blocks such as transient nanoparticles, or 1D chains, aggregate to larger (2D or 3D) MOF crystals.[126,135,137]

The various paths of MOF nucleation and growth renders MOF crystallization very complex. While new topologies are easily predicted, the actual synthesis of MOFs often requires extensive optimization of reaction conditions to achieve the desired MOF phase.[27] Synthetic conditions such as solvent, temperature, and metal-to-ligand ratio all greatly affect the nucleation and the growth of MOF crystals.[138] Thus, identifying the set of conditions that allow the formation of a specific MOF topology is difficult, and oftentimes mixtures of phases are obtained.[62] Due to this complex relationship, series of MOFs with varying metal cations/nodes or linkers rarely form under the same reaction conditions and discovery of new MOFs often requires laborious optimization of synthetic protocols.[27]

The broad research interest in MOFs has led to a variety of synthetic methodologies among different research groups around the world. Indeed, MOF synthesis has evolved from different fields, ranging from mild coordination chemistry to harsh zeolite chemistry.[27] Early MOF chemistry mainly relied on low-temperature routes—MOF-5, for example, can form at room temperature.[25,139] Nowadays, MOF synthesis often requires heating of the reaction mixture to increase crystallinity and reaction rate, especially when reactants are kinetically more inert.[27] To this end, solvothermal MOF syntheses, i.e. in closed vessels below or above (solvothermal in the strict sense) the boiling point of the solvent, have become the most common method for the synthesis of crystalline MOFs.[140-142] Over the years, several approaches have been implemented to introduce energy during MOF synthesis to promote greater reactivity. Besides electrical heating, microwave-assisted (MW) and ultrasonic heating have become well-established in MOF synthesis.[140] Other methods include sonochemical, electrochemical, ionothermal, and mechanochemical synthesis, where the last is solvent free and therefore more environmentally friendly.[143-146]

Given the utility of MOFs, considerable attention has been devoted to the development of strategies allowing for controlled particle size down to the nanoscale. Interestingly, the choice of heating methods can greatly affect the growth of MOF particles. For example, MW-assisted synthesis of MOF-5 promotes faster nucleation of MOF-particles, which not only reduces the synthesis time significantly compared to conventional heating (15 min *vs*. 12 h), but can also reduce the particle size by a factor of 20 (20–25 μm *vs*. 500 μm).[147-149] This is of particular interest for applications where particle morphology is relevant, such as optics, electronics, and catalysis.[150] On the other hand, additives such as organic polymers, surfactants, or vesicles, may regulate the nucleation, growth, and morphology of MOF particles during synthesis.[150-152] For example, the addition of the capping agent *p*-perfluoethylbenzoic acid during the synthesis of MOF-5, affords colloidal MOF-5 particles 100 nm in size and is one of the first instances of modulated MOF synthesis.[153] These examples are promising for accurate control over the structure and morphology during synthesis.

1.4.2 Modulated MOF self-assembly

Solvothermal MOF synthesis often yields micro-sized intergrown MOF aggregates which limits their range of application.[154] To overcome this, coordination chemists introduced the concept of modulated synthesis allowing for more controlled particle size and morphology during MOF synthesis.[154] The approach involves the addition of a monodentate ligand, the modulator, which has only one functional group able to coordinate to the metal node. The modulator and linker are added

either simultaneously to compete for coordination on the metal cation or cluster, or in a two-step process, where the modulator is first added to coordinate to the active sites on the metal/cluster followed by the linker, which displaces the modulator and forms the MOF. The "coordination equilibria" between modulator and linker slows down the reaction, thereby regulating nucleation and particle growth (Figure 1.18).[151] As a result, modulated synthesis typically yields individual nano- or microcrystals instead of intergrown particles.[154]

Figure 1.18: Reaction equilibrium during modulated MOF synthesis where the modulator and the linker compete for the coordination on the metal node (M).

The amount of modulator directly affects the particle size of the synthesized MOF. When the modulator concentration increases, the "coordination equilibrium" shift towards a slower nucleation process since more modulator molecules compete in the reaction. As a result, fewer nuclei are formed and a smaller number of crystals grow, resulting in larger particles with greater polydispersity (Figure 1.19).[155] On the other hand, a lower modulator concentration shifts the equilibrium in the opposite direction, leading to an increase in MOF nuclei formation and hence smaller MOF crystals (in the nanoscale regime) with a more homogeneous size distribution.[155] Similar trends exist when the acidity of the modulator is changed. When the p*K*a is decreased, interactions between the modulator and growing crystals increase, which leads to smaller MOF particles, and *vice versa*.[156] Schaate *et al.* first implemented this approach on Zr-based MOFs in 2011.[116,154] In this work, a MOF with the linker H_2TPDC-NH_2 (TPDC = terphenyl-4,4''-dicarboxylic acid) was synthesized under the addition of benzoic acid as the modulator. The modulator competes with the linker for coordination of the $Zr_6(\mu_3\text{-}O)_4(\mu_3\text{-}OH)_4$ cluster allowing for more controlled growth of crystalline, micro-sized MOF particles. The modulated synthesis yielded crystallites 100 µm in size which were suitable for the first single crystal structure analysis of a Zr-based MOF.

In addition to controlling MOF particle sizes, the modulator can also act as templating agent and direct the particle growth along certain directions.[151,155] In 2008, Cho *et al.* reported that during synthesis of an In-BDC-based framework, the modulator pyridine reversibly coordinates to indium centers along hexagonal facets thereby blocking particle growth in that direction. By increasing the equivalents of pyridine added to the reaction, the growth speed along hexagonal facets was reduced,

ultimately changing the morphology of the particles—0, 2, or 25 equivalent pyridine yields hexagonal rods, lump, and discs, respectively (Figure 1.20).[157]

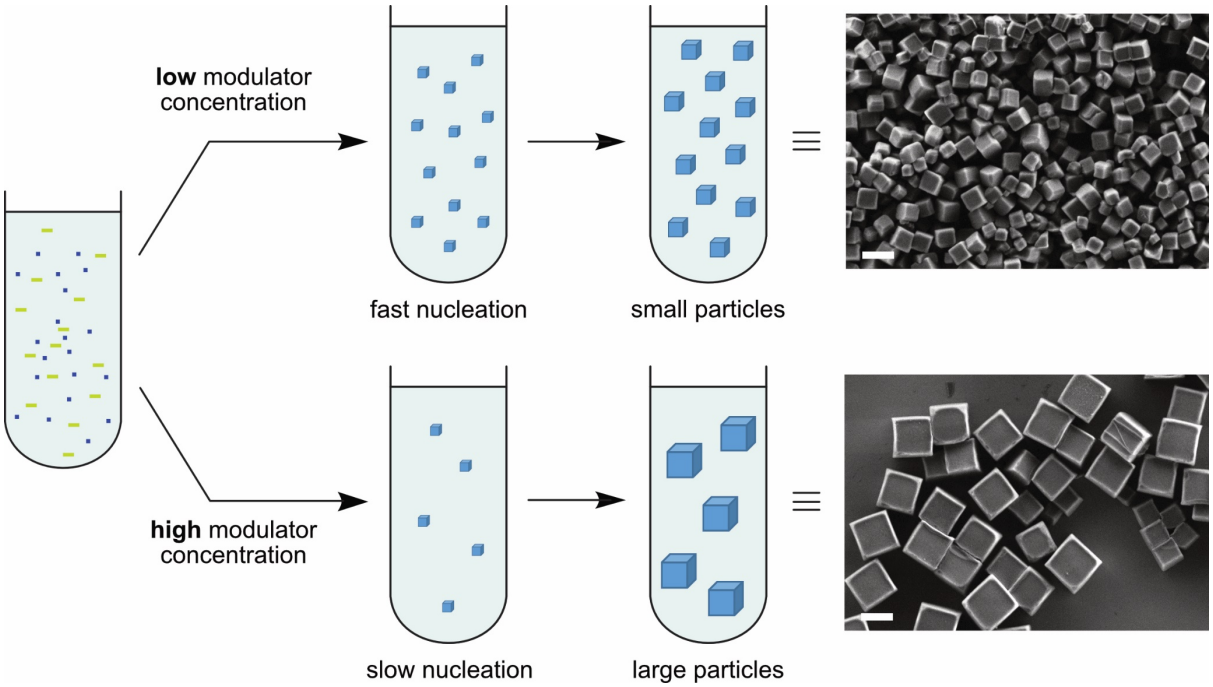

Figure 1.19: Representation of particle nucleation and growth depending on the modulator concentration in the reaction. With increasing modulator concentration, nucleation of MOF particles slows down yielding larger MOF particles. The differences in particle size can, for example, be seen in scanning electron microscopy images of porphyrinic PCN-224 particles (scale bar = 1 µm).

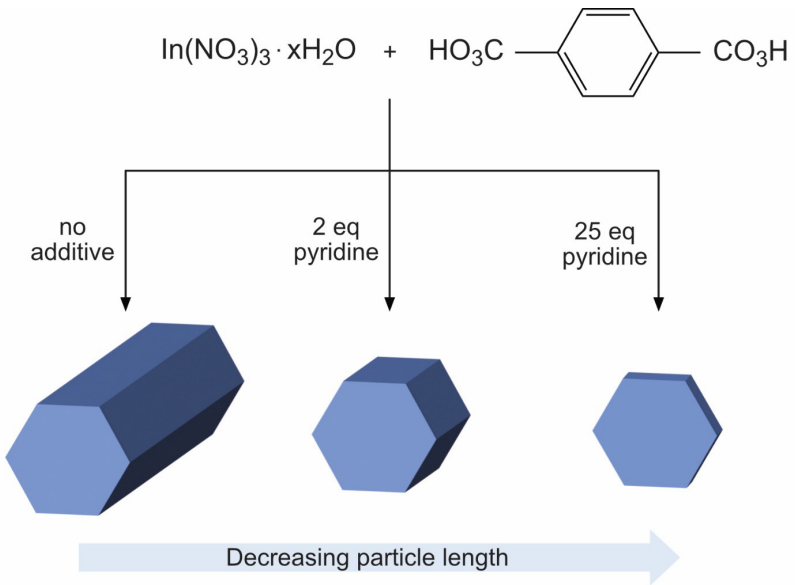

Figure 1.20: Comparison of the particle morphology formed during synthesis of the In-BDC-based framework from $In(NO_3)_3 \cdot xH_2O$ and 1,4-benzodicarboxylate (BDC) under addition of pyridine. The length of the hexagonal particles decreases with increasing amount of pyridine added to the reaction.[157]

It is worth mentioning that MOF properties such as gas adsorption may vary with changing crystallite shape and size.[150] These changes are often unintentional and should be taken into account when adjusting the modulator to tune particle size and shape. In addition, changing the modulator or its concentration may also change the MOF phases that are formed; this is something that is especially prominent in Zr-based MOF chemistry due to the varying coordination number of hexanuclear Zr-clusters.[68,138]

1.4.3 Phase engineering of Zr-based MOFs

Zr-based MOFs are of the primary focus of this thesis and the remainder of the chapter will therefore focus on phase engineering of this class of frameworks by means of modulator choice, reaction temperature and duration, and water content in the reaction. Direct synthesis from a Zr salt and organic linker often results in quick precipitation of polycrystalline powders due to the high charge density of Zr(IV) and mostly irreversible Zr–O bond formation.[64,154,158] To this end, synthesis of crystalline Zr-based MOFs often requires the addition of a modulator. Importantly, modifying the linker-to-modulator ratio or the nature of the modulator does not only impact the particle size and morphology of the product.[85,91,159] In fact, the modulator partially guides the MOF phase that is formed by organizing discrete clusters and controlling the kinetics of the self-assembly.[116] Combination of the porphyrinic TCPP linker and $Zr_6(\mu_3\text{-}O)_4(\mu_3\text{-}OH)_4$ cluster, for example, allows for at least six possible MOF phases (see Section 1.2.1). Here, the employed modulator mostly guides which MOF phase is formed during synthesis. Studies on MOF-525, MOF-545, and PCN-223 formation revealed that as the p*K*a of the modulator decreases, there is an increasing preference to form 8-fold coordinated MOF-545 over 12-fold coordinated MOF-525 and PCN-223.[159] This suggests that stronger cluster–modulator bonds slow down the exchange rate between modulator and linker during particle growth, thereby shifting the product towards phases with reduced linker coordination on the cluster.[159] This relation also holds for UiO-66, where the amount of linker vacancies correlates with the modulator used in the reaction.[110] During the synthesis of UiO-66, the modulators compete with the linkers for coordination to the cluster thereby generating vacancies in the framework. With decreasing p*K*a and increasing modulator concentration, the ligand-to-modulator ratio decreases in the final product, yielding up to four vacant linker sites on $Zr_6(\mu_3\text{-}O)_4(\mu_3\text{-}OH)_4$.[110] Increasing the acidity and concentration of the modulator also systematically enhances the number of missing $Zr_6(\mu_3\text{-}O)_4(\mu_3\text{-}OH)_4$ cluster defects in UiO-66.[110] These defects directly correlate with linker vacancies: when 12 neighboring clusters possess vacant linker sites pointing towards the same cavity, clusters that would ordinarily be in that cavity are missing as well.[110-111]

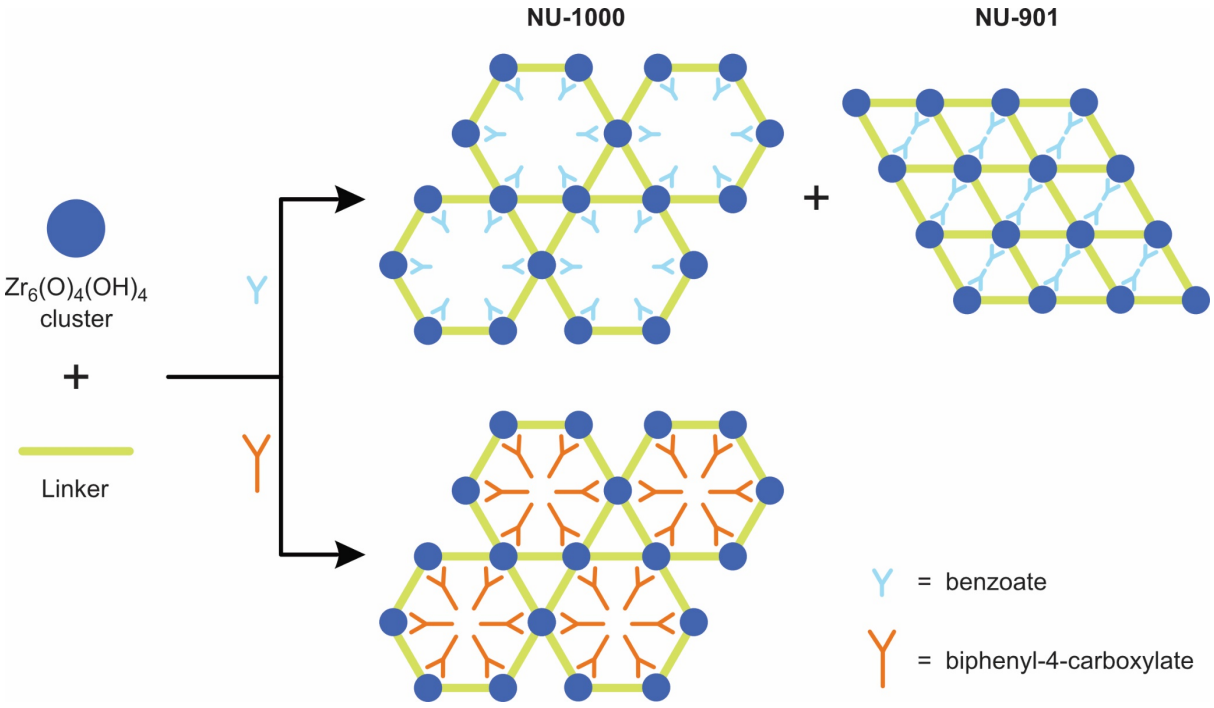

Figure 1.21: Schematic illustration of how the modulator size guides the MOF phase formed during reaction of $Zr_6O_4(OH)_4$ cluster and tetrakis(4-carboxyphenyl)pyrene linkers. When benzoic acid (blue) is used as the modulator both NU-1000 and NU-901 are formed. In contrast, the use of biphenyl-4-carboxylic acid (orange) as the modulator prevents the formation of NU-901 due to steric interactions, yielding NU-1000 only.

Another design element is the modulator length and/or size. The MOF polymorphs NU-1000[160] and NU-901[161] (NU = Northwestern University) are both built from tetrakis(4-carboxyphenyl)pyrene linkers and 8-fold coordinated $Zr_6(\mu_3\text{-}O)_4(\mu_3\text{-}OH)_4$ clusters; however, NU-901 exhibits a higher cluster density and smaller pores (11 Å) compared to NU-1000 (hexagonal pores of 31 Å and smaller pores of 10 Å).[161-162] Using biphenyl-carboxylic acid instead of benzoic acid as the modulator directs synthesis towards NU-1000: the larger modulator causes stronger steric interactions between neighbouring Zr clusters, thus inhibiting the growth of the denser NU-901 phase and promoting formation of NU-1000 with larger pores (Figure 1.21).[163] The bulky modulator can be removed *via* HCl-activation, yielding a highly porous product with hydroxy ions that balance the charges instead.[85,160,164] This also results in open metal sites, which are useful for both catalysis and post-synthetic ligand introduction to further tune the MOFs properties.[69-70]

Aside from the modulator, other factors such as temperature or reaction time strongly affect the phase selectivity of Zr-based MOFs during the synthesis. [159] During the synthesis of TCPP-based MOFs, for example, hexagonal PCN-222 was reported to preferentially form over cubic MOF-525 with increasing reaction times.[159] Gong *et al*. further showed that the reaction of pre-formed Zr_6 clusters with TCPP linker using formic acid as a modulator yields cubic MOF-525 and PCN-224 phases at 60 °C, whereas a mixture of PCN-222, PCN-223, and NU-902 was formed at 145 °C.[63]

At the same time, adjusting the temperature is also an efficient tool to tune linker vacancies in the MOF. Specifically, synthesis of UiO-66 at higher temperatures remarkably increases the amount of incorporated linkers into the MOF compared to room-temperature synthesis.[165]

Water is also an important factor in the synthesis of Zr-based MOFs.[166] Water provides the oxide and hydroxide groups required for the backbone of the hexanuclear cluster.[96] As a consequence, a greater water content during MOF synthesis also accelerates hydrolysis, hence nucleation and crystallization, and can thus affect the particle size and shape.[167] Additionally, water can tune the phase of the formed MOFs and change crystallinity of the product. Butova *et al*. found that the reaction of $ZrCl_4$ and BDC linker at 220 °C yielded UiO-66 in the presence of water, but the polymorph MIL-140A in its absence. The influence of water content was further demonstrated by Chen *et al.,* who showed that UiO-66 with **hcp** phase was only obtained with an acetic acid-to-water ratio of 1:1, whereas higher and lower acid-to-water ratios yielded other phases.[168-169]

The multitude of factors that influence Zr-based MOF growth gives chemists the ability to precisely tune reaction conditions towards a desired MOF phase with specific particle size. At the same time, however, the number of variables introduces many sources of errors that reduce reproducibility of synthetic protocols between groups. To this end, optimizing conditions towards phase pure Zr-based MOFs often remains laborious and time consuming, but is obligatory to study phase-dependent properties and promote the wide application potential of MOFs.

1.5 Phase and defect characterization of MOFs

The synthesis of MOFs often yields multiple phases built from the same metal node and linker. In addition, the frameworks often contain disorder and defects, which can both affect a material's properties. Identifying the composition of the product and whether disorder and vacancies are present is therefore essential when analysing structure–property relationships and designing new materials with improved functionality.

PXRD is a common analysis method in MOF chemistry to identify the product formed during self-assembly. Different MOF topologies show distinct X-ray diffraction patterns. When vacancies occur in an ordered manner throughout the crystal lattice, these cause additional superstructure reflections in the diffraction pattern of the material, due to the change in symmetry. Ordered linker and cluster vacancies over a long range can therefore be easily identified using PXRD analysis. In contrast, disordered vacancies are often overlooked as the resulting diffuse scattering is less easy to interpret. For example, correlated vacancies in small domains occur over short ranges, which generate weak broad peaks in the diffraction pattern and require high-quality data collection.

To better probe these features, MOFs are often analysed by single crystal XRD (SCXRD). A downside to this, however, is that the growth of MOF single crystals usually necessitates alterations of the reaction conditions to favor larger crystals. These can affect the MOF phase formed, as well as the amount and ordering of defects in the crystal lattice. In addition, MOF single crystals are often small (<50 μm) and the organic linkers are weak X-ray scatterers. High-quality SCXRD measurements obtained through a synchrotron are therefore necessary to probe diffuse scattering in MOF crystals. Importantly, SCXRD diffraction probes the long-range structural average and does not consider any short-range deviation from the average structure.

To examine the local ordering in MOFs, characterization techniques probing the short-range structure are therefore needed in addition to the methods discussed above. High-resolution transmission electron microscopy (HR-TEM) is frequently used for imaging non-periodic local structures of crystalline materials.[170] However, MOFs are very sensitive to electron beam irradiation and are prone to damage during imaging. TEM imaging of MOFs therefore requires cryogenic temperatures combined with low electron doses and extremely sensitive cameras to obtain meaningful data.[171]

Pair-distribution function (PDF) analysis can also be used to probe the local range in MOFs.[172-173] PDF experiments use the total scattering of a material (Bragg diffraction and diffuse scattering) and hence contain information about the atomic ordering in both the short and long range. Put simply, the X-ray PDF is a histogram of bond lengths that provide information about the bond distances weighted by the X-ray scattering power.[174] The technique therefore gives a local view of the structure, as opposed to XRD, which only probes the long-range structural average. In Zr-based MOFs, PDF analysis is a powerful technique to determine inter- and intracluster Zr–Zr distances, which helps to identify structural details about disorder and defects in the framework.[172-173]

Apart from crystallographic methods, nuclear magnetic resonance (NMR) spectroscopy can provide important insights into the local structure of building blocks in a MOF. ^{13}C solid-state NMR analysis, for example, can describe the coordination modes of carboxylate linkers on Zr clusters.[175] On the other hand, solution NMR can be used to identify defects in a MOF. Linker vacancies, for example, leave free coordination sites on the metal nodes, which usually are occupied by modulators to balance the charges. NMR analysis after MOF digestion allows for determining the amount of linkers replaced by modulators which provides information on the linker connectivity to the nodes.[112]

Sorption analysis and thermogravimetric analysis (TGA) are two other techniques frequently used to characterize MOFs. Generally, introducing vacancies into MOFs increases the porosity of the

framework, which in turn increases the pore volume and the BET surface area.[112] Physisorption isotherms, which measures the uptake of an adsorbent, such as nitrogen or argon, over a wide range of pressures, helps to determine whether a frameworks contains vacancies.[176] The isotherm shape gives information on the size and shape of the pores, which are expected to vary in defective structures compare to the pristine MOF.[177] TGA is used to determine the linker-to-metal ratio in MOFs and provides information about the overall composition and reveals the presence of additional components such as modulators.[108]

1.6 Goals and scope of this thesis

Since their discovery in 2008, Zr-based MOFs have become one of the most prevalent frameworks studied for applications including gas sensing, gas adsorption, catalysis, and drug delivery.[36] However, to optimize the functionality of these frameworks towards targeted applications, it is important to understand the structure–property relationships, and therefore, the structure of the material across several length scales. This thesis aims to shed light on unexplored disorders and vacancies that occur in Zr-based MOFs and to examine the link between synthetic conditions and the final structure.

In Chapter 2, the structures of cubic porphyrinic PCN-221[75], MOF-525[92], and PCN-224[91] will be subject to investigation. Intriguingly, the three structures have been reported with varying cluster compositions and linker occupancies in literature, but often show the same PXRDs patterns.[77] Particular focus will be placed on PCN-221, originally published with cubic Zr_8O_6 clusters that feature remarkably short Zr–Zr distances.[75] Through a comprehensive synthetic and structural study examining both the local- and long-range structure, the nature of the cluster should be elucidated in order to solve the long-standing questions pertaining to the existence of Zr_8O_6 clusters in PCN-221. Building off of these findings, Chapter 3 aims to explores the link between synthetic conditions and phase selectivity during the synthesis of porphyrinic Zr-based MOFs. Oftentimes, synthetic protocols are not reproducible, which hinders scientific advances. Here, the formation pathway of the MOF should be examined at each step of the synthesis to get a better understanding of the nucleation and growth of porphyrinic MOF particles. Special emphasis should be given to the influence of both the employed Zr source and the water content in the reaction on the obtained MOF product.

Chapter 4 will examine Zr-based MOFs formed from MTBC linkers.[76,97] Careful structural analysis should unveil the real cluster composition of Zr-MTBC, which was originally published with $Zr_8(O)_8(OH)_4$ clusters which are called into question.[76] In addition, this chapter aims to explore

disorder, vacancies, and linker–cluster coordination types that occur in MTBC-based MOFs. Importantly, the study will be expanded to the Hf-based analogues to prove that the structural flexibility is not limited to MTBC–Zr compounds.

Lastly, Chapter 5 will offer insights into ongoing investigations that should be pursued in the future and summarize all findings of this thesis.

CHAPTER 2

DISORDER AND VACANCIES IN PORPHYRINIC Zr-BASED MOFs

As outlined in Chapter 1, MOFs built from Zr-oxo clusters gained significant attention for their high stability and flexible coordination geometry. The variety of cluster species and the linker arrangements imbues attractive functionality compared to other frameworks, but also results in complicated structures that are difficult to synthesize and characterize. While octahedral $Zr_6O_4(OH)_4$ clusters are the most common and well understood, the existence of cubic Zr_8O_6 clusters, such as those reported in PCN-221, remains controversial. This chapter resolves the long-standing Zr_8O_6 cluster conundrum and demonstrates that PCN-221 actually consists of statistically disordered $Zr_6O_4(OH)_4$ clusters oriented in four directions, accompanied by 50 % linker vacancies. These findings lead to a new structure model—*disordered PCN-224*—which allows for an improved understanding of cubic porphyrinic Zr-based MOFs.

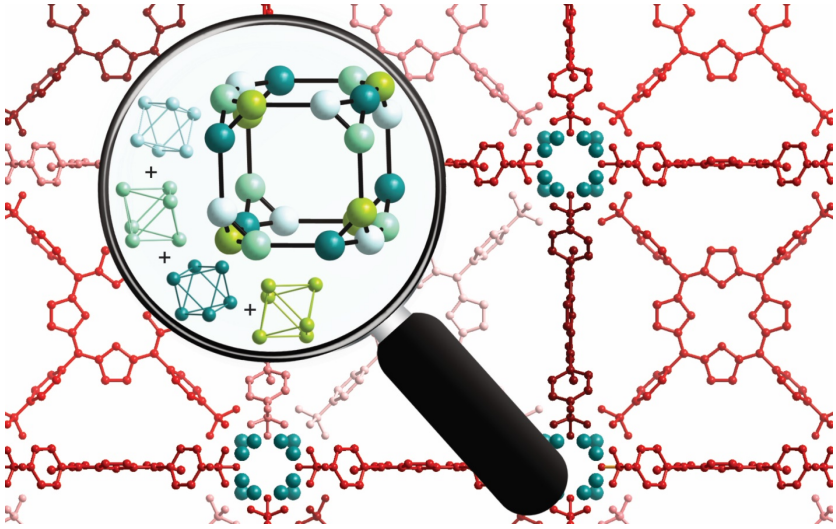

Cover image of Chapter 2: Illustration of orientational $Zr_6O_4(OH)_4$ cluster disorder and randomly distributed linker vacancies in PCN-221/dPCN-224.

Understanding Disorder and Linker Deficiency in Porphyrinic Zirconium-based Metal–Organic Frameworks by Resolving the Zr_8O_6 Cluster Conundrum in PCN-221

Charlotte Koschnick*, Robert Stäglich*, Tanja Scholz*, Maxwell W. Terban*, Alberto von Mankowski, Gökcen Savasci, Florian Binder, Alexander Schökel, Martin Etter, Jürgen Nuss, Renée Siegel, Luzia S. Germann, Christian Ochsenfeld, Robert E. Dinnebier, Jürgen Senker, Bettina V. Lotsch

* the authors contributed equally

Published in

Nature Communications **2021**, *12*, 3099.
DOI: 10.1038/s41467-021-23348-w
https://www.nature.com/articles/s41467-021-23348-w
Adapted with permission from Nature Springer

2.1 Abstract

Porphyrin-based metal-organic frameworks (MOFs), exemplified by MOF-525, PCN-221, and PCN-224, are promising systems for catalysis, optoelectronics, and solar energy conversion. However, subtle differences between synthetic protocols for these three MOFs give rise to vast discrepancies in purported product outcomes and description of framework topologies. Here, based on a comprehensive synthetic and structural analysis spanning local and long-range length scales, we show that PCN-221 consists of $Zr_6O_4(OH)_4$ clusters in four distinct orientations within the unit cell, rather than Zr_8O_6 clusters as originally published, and linker vacancies at levels of around 50 %, which may form in a locally correlated manner. We propose disordered PCN-224 (*d*PCN-224) as a unified model to understand PCN-221, MOF-525, and PCN-224 by varying the degree of orientational cluster disorder, linker conformation and vacancies, and cluster—linker binding. Our work thus introduces a new perspective on network topology and disorder in Zr-based MOFs and pinpoints the structural variables that direct their functional properties.

2.2 Introduction

Metal-organic frameworks (MOFs) have rapidly emerged as promising materials for diverse applications, such as gas storage and separation, catalysis, sensing, and biomedical applications.[158] The judicious choice and combination of organic linker and inorganic metal (cluster) allows for the precise tuning of pore shapes, sizes, and functionality towards specific applications.[178-180] Recently, MOFs based on Zr-oxo-cluster secondary building units (SBUs) linked by aromatic carboxylic acid linkers have garnered significant attention, as the high valence state of Zr^{4+} and the inertness of the Zr–O bond tolerate pronounced Zr^{4+}–O bond polarization and give rise to superior stability.[36,68,158] Furthermore, a wide variety of isolated Zr-oxo-clusters, including Zr_3, Zr_4, Zr_5, Zr_6, Zr_8, Zr_{10}, and Zr_{18}, have been reported, providing the basis for a rich diversity of new Zr-based MOFs with different network topologies and properties.[36,68] The prototypical $Zr_6O_4(OH)_4$ cluster is encountered most commonly and has been identified to form highly stable SBUs.[36] Well-studied MOFs built from this cluster include those with terephthalic acid (UiO-66[52]) and pyrene-based (NU-1000[160]) linkers, among others.[52,161,181-182] Combination of Zr SBUs with the chromophore tetrakis(4-carboxyphenyl)porphyrin (TCPP) gives rise to a series of porphyrinic MOFs with interesting (opto)electronic properties, which are exploited in energy conversion schemes or catalysis.[183-186] So far, six MOFs built from $Zr_6O_4(OH)_4$ clusters with different coordination of the TCPP linker have been reported: PCN-223[94] and MOF-525[92] (both 12-connected), MOF-545/PCN-222[85,92], PCN-225[86], and NU-902[93] (all 8-connected), and PCN-224[91] (6-connected).

In 2013, PCN-221, a MOF similar to MOF-525, was reported featuring Zr_8O_6 clusters instead of $Zr_6O_4(OH)_4$ clusters (Figure 2.1).[75] Curiously, the Zr–Zr distance in PCN-221 is only 2.69 Å, much shorter than in all inorganic Zr compounds compiled from the Inorganic Crystal Structure Database (ICSD) and Zr-cluster-based frameworks from the Cambridge Crystallographic Data Centre (CCDC) (Appx. A, Figure A.14). Both MOF-525 and PCN-221 are described with a cubic structure of similar unit cell size and with 12 coordination sites on the SBU. In MOF-525, the reported structure exhibits a completely planar TCPP linker, whereas in PCN-221 the phenyl rings are rotated out-of-plane by 90°.[75,92]

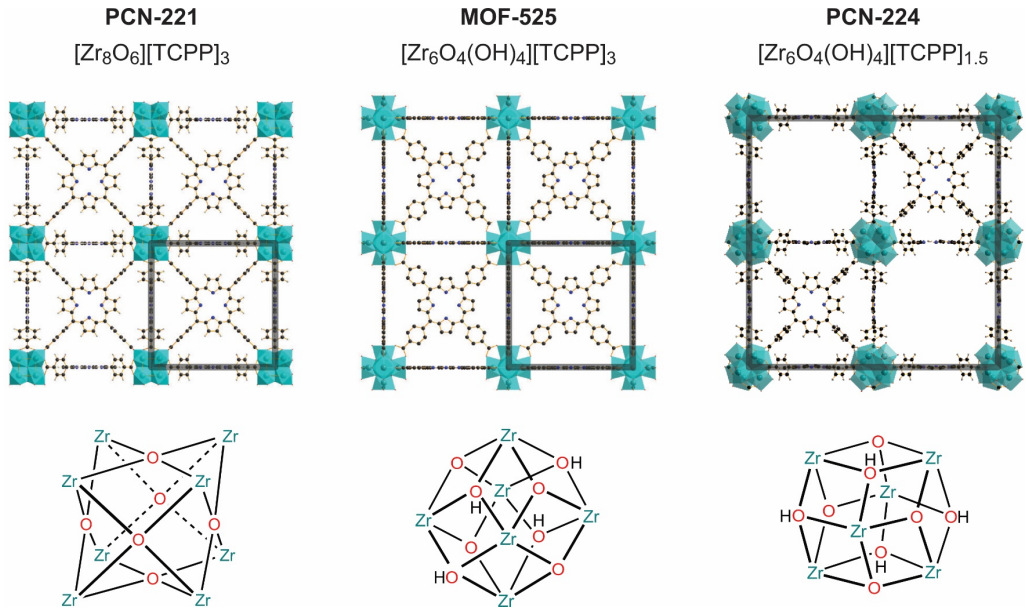

Figure 2.1: Published crystal structures of the cubic porphyrinic MOFs. PCN-221, MOF-525, and PCN-224 built of tetrakis(4-carboxyphenyl)porphyrin (TCPP) linkers and Zr-cluster (teal) with unit cells highlighted, viewed along the *c-axis*, and their corresponding Zr_8O_6, straight $Zr_6O_4(OH)_4$, and tilted $Zr_6O_4(OH)_4$ cluster, respectively.[75,91-92]

A difficulty in studying porphyrin-based MOF structures is the synthesis of phase-pure products, due to similar reaction conditions for all seven structures.[63] High-throughput syntheses of MOF-525 have shown the impact of modulator concentration, temperature, and reaction time on the crystallinity and phase purity, demonstrating the complexity in obtaining optimum reaction conditions.[159,187] Although not explicitly stated in the literature, it is discussed in the MOF community that syntheses of porphyrin-based Zr-based MOFs are notoriously difficult to reproduce, leading to the co-existence of different MOF-525 and PCN-221 protocols.[75,92,159,187-189] In fact, many studies report the same product for different experimental data,[91,190-204] suggesting that the synthetic protocols and the resulting structures are still not well understood. This is exacerbated by poor quality and insufficient powder X-ray diffraction (PXRD) data making structure assignment ambiguous. As a consequence, many publications do not reveal differences in the PXRD patterns between MOF-525, PCN-221, and the ordered defect structure PCN-224.[89,91,159,187-206] However, linker vacancies in MOFs have been found to impact the material's properties due to larger pores (adsorption applications) or open metal sites (e.g. Lewis acid catalyzed reactions), highlighting the importance of being able to reliably distinguish between these MOFs.[36,207]

$Zr_6O_4(OH)_4$ cluster-based MOFs have been found to be remarkably tolerant towards high linker deficiencies, especially in UiO-66 and its analogues.[113-115,208-209] The tolerance is a result of large linker coordination numbers and the ability to compensate defects with either modulator molecules,

hydroxy groups, or hydroxy water-pairs.[68,210-211] The amount of linker vacancies can be tuned synthetically, and the inclusion of defects has been shown to proceed in a correlated manner.[106,111,113] These defect sites can be utilized to introduce functional groups by means of solvent-assisted ligand incorporation to tune the MOF's properties.[69,212] Only recently, the notion that linker vacancies are prevalent also in the TCPP-based MOF-525 has gained attention, with vacancies reported up to 50 %.[187,207]

Here, we performed a comprehensive synthetic study on PCN-221 and undertook detailed investigations of the resulting structures using total scattering pair distribution function (PDF) analysis, powder and single crystal X-ray diffraction (PXRD/SCXRD), solid-state nuclear magnetic resonance (ssNMR) spectroscopy, and quantum-chemical calculations. We have determined that PCN-221 forms with orientationally disordered $Zr_6O_4(OH)_4$ clusters, rather than Zr_8O_6 cubes, correlated with vacant linker sites. The combined evidence suggests that the structure is a disordered variant of PCN-224, for which we recommend a new name, *d*PCN-224. This study thus highlights the large untapped potential for incorporating correlated orientational disorder of sub-components as a powerful design principle for developing synthetic protocols.

2.3 Results and discussion

2.3.1 Synthesis and diffraction behavior

Experimental protocols for PCN-221, MOF-525, and PCN-224 are substantially inconsistent throughout the literature. To get reliable access to these systems, we prepared a number of MOF products using different synthetic routes including the following Zr-sources: i) zirconium(IV) chloride (MOF_$ZrCl_4$) as originally reported[75], ii) zirconyl chloride octahydrate (MOF_$ZrOCl_2$ and MOF_$ZrOCl_2$_(II), and iii) pre-synthesized $Zr_6O_4(OH)_4Bz_{12}$ clusters (MOF_Zr_6). In particular, syntheses based on $ZrOCl_2$ (ii) showed good reproducibility (details on all syntheses see Appx. A, Section A.1.3). In addition, PCN-224 with TCPP linker vacancies appearing in an ordered 3D checkerboard fashion (Figure 2.1) was synthesized as reference.

The PXRD patterns of the products MOF_$ZrCl_4$, MOF_$ZrOCl_2$, and MOF_Zr_6 are all very similar and do not show features that would suggest significantly different structures (Figure 2.2). We compared these to calculated PXRD patterns based on the published crystal structures of PCN-221, which is reported with a Zr_8O_6 cluster and twisted phenyl linker conformation, and MOF-525, reported with a $Zr_6O_4(OH)_4$ cluster and planar linker conformation (for structural details see Figure 2.1). At low scattering angles the simulated patterns of the published structure of PCN-221 and MOF-525 are strikingly similar, due to the identical space group $Pm\bar{3}m$ and similar lattice

parameters (19.51 Å and 19.39 Å, respectively).[75,92] This makes structure assignment difficult in the absence of good quality data extending to higher angles. Nevertheless, all sample patterns show better agreement with the simulated structure of PCN-221, including the MOF_Zr_6 sample synthesized from pre-formed $Zr_6O_4(OH)_4Bz_{12}$ clusters. This is surprising, since PCN-221 is published with Zr_8O_6 clusters. A rearrangement of the pre-synthesized $Zr_6O_4(OH)_4$ cluster is not expected during the synthesis and crystallization of MOF_Zr_6, raising the question of whether $Zr_6O_4(OH)_4$ or Zr_8O_6 clusters are actually present. For comparison, we measured PXRD data of experimental PCN-224, with ordered TCPP linker vacancies, showing superstructure reflections at 3.2 and 5.5° 2θ (Figure 2.2).

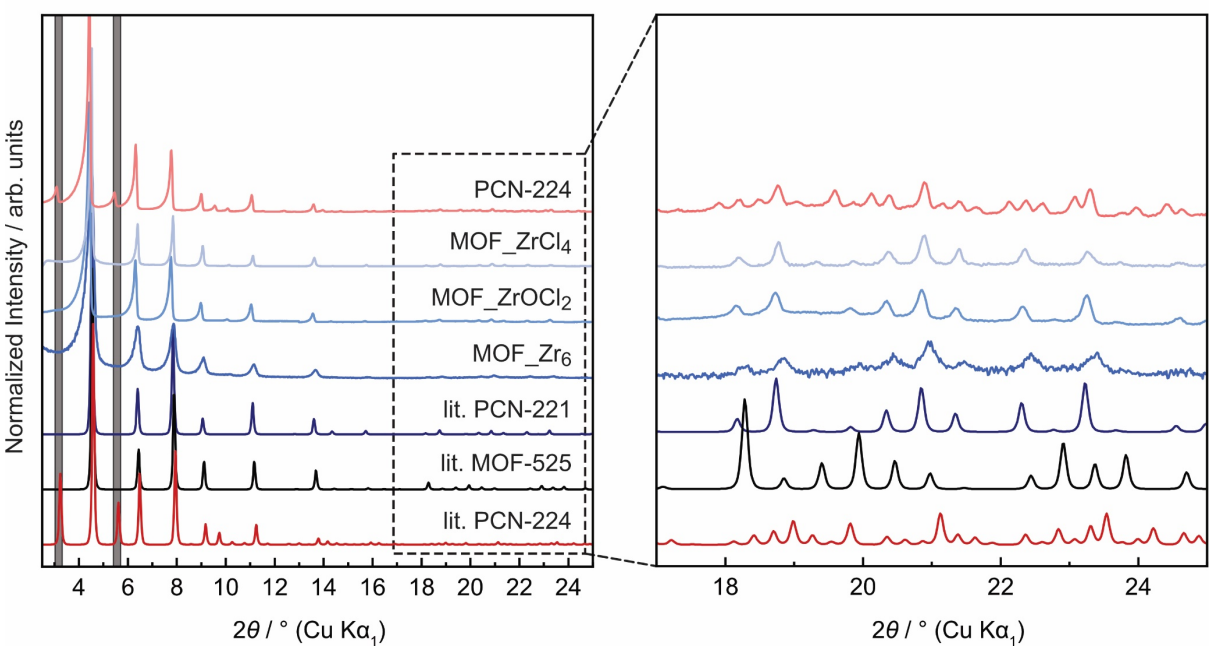

Figure 2.2: Powder X-ray diffraction (PXRD) patterns for samples and models. Comparison of measured PXRD patterns (Cu Kα_1) of MOF_$ZrCl_4$, MOF_$ZrOCl_2$, MOF_Zr_6, and experimental PCN-224 and simulated PXRD patterns (lit.) of PCN-221, MOF-525, and PCN-224.[75,91-92] The grey bars highlight the superstructure reflections of PCN-224 at 3.2 and 5.5° 2θ.

2.3.2 Cluster structure

Due to the ambiguity in cluster constitution based on comparison of measured and calculated PXRD data, we proceeded to use total scattering pair distribution function (PDF) analysis to investigate the short-range order of the Zr-oxo cluster. For all samples, the PDF data show peaks at the same atom-pair distances, which corroborates similar local Zr environments within the clusters of different samples (Figure 2.3a). The experimentally determined Zr–O distances of 2.28 Å and Zr–Zr distances of 3.54 Å are found to match with those expected for a $Zr_6O_4(OH)_4$ cluster, rather than 2.12 Å and 2.69 Å, respectively, for the Zr_8O_6 cluster (Figure 2.3b).[75] The

reported structure for MOF-525 gives slightly contracted distances, Zr–O (2.06 Å) and Zr–Zr (3.32 Å) compared to the experimental data, while the structure of PCN-224, with Zr–O (2.15 Å) and Zr–Zr (3.50 Å), gives the best overall agreement to the local structure. These findings are in agreement with quantum-chemical calculations on the structure of a Zr_8O_6 cluster, for which no energetically favorable geometry could be successfully determined. In contrast, an optimized $Zr_6O_4(OH)_4$ cluster shows very good agreement with the Zr–Zr distances from the PDF refinement (Appx. A, Figure A.19–A.21 and A.33).

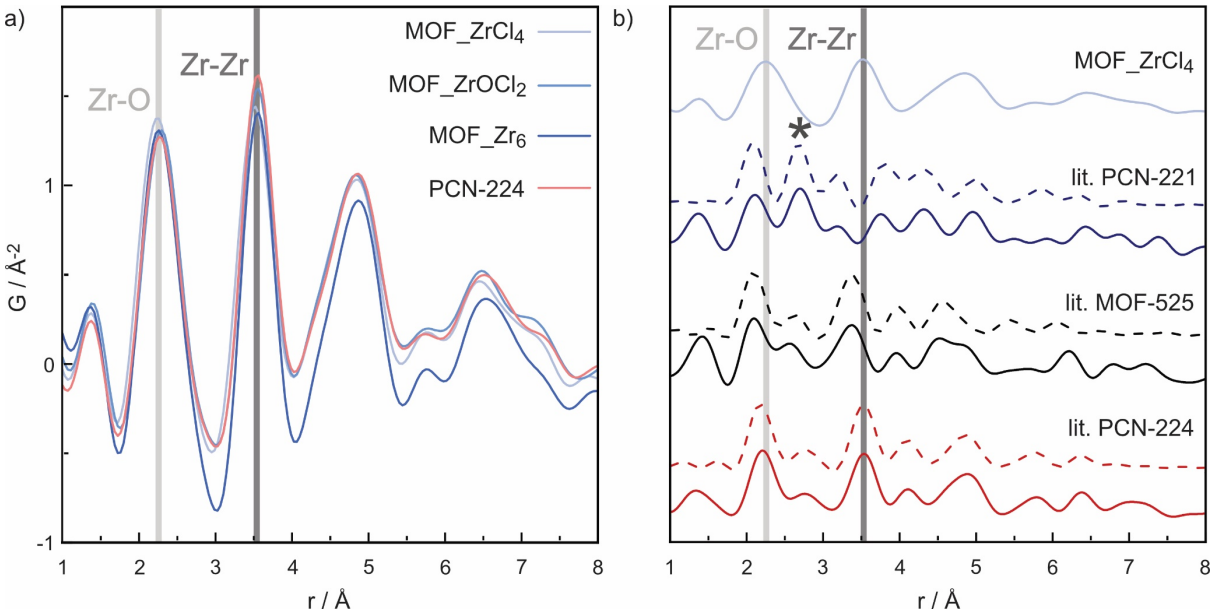

Figure 2.3: Local structures of MOF samples and models. a) Experimental pair distribution functions (PDFs) of MOF_$ZrCl_4$, MOF_$ZrOCl_2$, MOF_Zr_6, and experimental PCN-224; b) experimental PDF of MOF_$ZrCl_4$ compared to the simulated PDFs (lit.) of the published MOF structures (solid line) and SBUs only (dashed line) of PCN-224, MOF-525, and PCN-221.[75,91-92] The star highlights the Zr–Zr distance of 2.69 Å in PCN-221.

2.3.3 Structure model from X-ray data

All three synthetic routes (MOF_$ZrCl_4$, MOF_$ZrOCl_2$, and MOF_Zr_6) thus yielded a MOF whose structure agrees well in the long-range (PXRD) with the published structure for PCN-221 with a Zr_8O_6 cluster, but locally contradicts the presence of Zr_8O_6 clusters. To elucidate this discrepancy, we studied the structure of the MOF by SCXRD. Several reaction parameters had to be adjusted to grow single crystals of the same MOF with suitable sizes for SCXRD (Appx. A, Figure A.22). Indexing revealed a primitive cubic unit cell with a = 19.315(2) Å, and the initial structure solution gave a Zr_8O_6 cluster similar to the structure of PCN-221.[75] However, residual electron density arranged in a triangular shape remained around each Zr atom, manifesting itself as extremely flat,

disk-shaped thermal ellipsoids of the Zr in the Zr_8O_6 cluster (Figure 2.4a), as previously reported.[75] The corners of the Zr_8 cube point toward all eight triangles of the cuboctahedral cage formed by the carbon atoms of the coordinating linker molecules (Figure 2.4). In fact, it is possible to describe such a distribution of electron density by superimposing four different Zr_6 cluster orientations as seen in the 2 × 2 × 2 supercell of PCN-224, so that the corners of any Zr_6 octahedron point to six of the eight cuboctahedron's triangles. The four orientations are related by 90° rotations around the crystallographic axes (Figure 2.4a). Overlapping these four Zr_6 clusters adds up to a truncated cube (corner-to-corner distance = 2.70 Å) with a strong resemblance to the Zr_8O_6 cluster structure published for PCN-221 (Zr–Zr = 2.69 Å). Using this disoriented model, the *R*-value was improved by 12 %, compared to the structure model built of Zr_8O_6 cubes. For more details on the SC refinement and crystallographic data please refer to Appx. A, Section A.2.5. Our analysis is further consistent with the PDF data that suggest the local environment to be more similar to PCN-224. We found additional evidence for our structural model in the Fourier map of the (111) crystallographic plane through the truncated corners of the cube that show a 3-fold symmetry in the electron density map with maxima on the superimposed Zr sites (Figure 2.4b).

The tilted Zr_6O_8 cluster orientations offer 12 simultaneous carboxylate positions coordinating such that six of them bridge two adjacent Zr atoms (*bridging ligands*) and the other six chelate single Zr atoms (*chelating ligands*). This building unit shows similarities to the hexagonal TCPP-based PCN-223[94] featuring both bridging and chelating ligands, rather than only bridging as in MOF-525 and PCN-224.

The SCXRD model was solved with a 90° dihedral angle between the porphyrin and the phenyl ring, rather than 0° as reported for MOF-525. The refinement of this angle is prohibited by the symmetry restrictions of the cubic space group $Pm\bar{3}m$. These values are closer to the published structure of PCN-224, in which the phenyl rings of the porphyrin linker are twisted out-of-plane by approximately 78°.[91] The potential energy surface obtained from quantum-chemical calculations of TCPP in the gas phase shows a steep maximum at 0° and a very shallow minimum in the range of 60–90° (Appx. A, Figure A.36, Table A.15). This confirms the preference for a twisted dihedral angle of the phenyl rings.

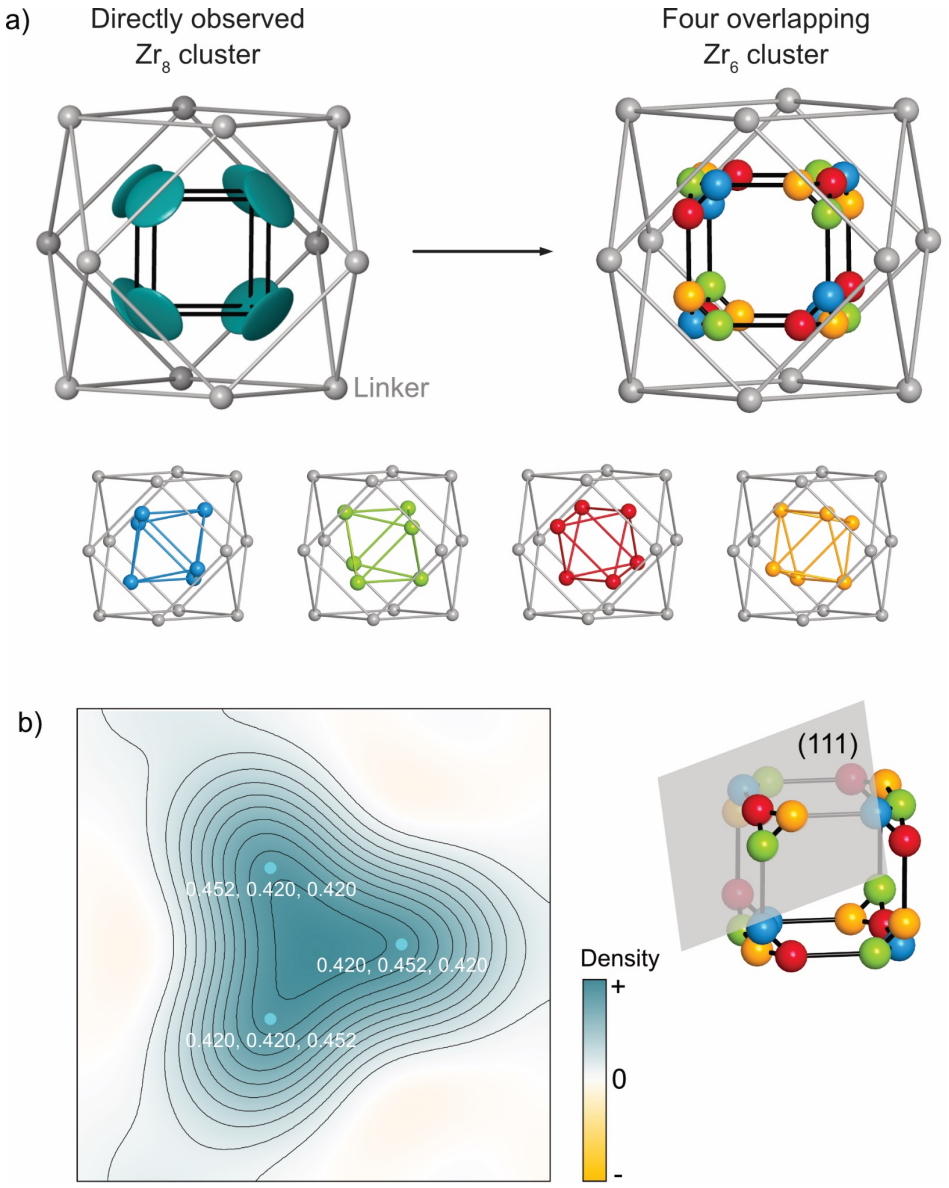

Figure 2.4: Cluster orientations from single crystal X-ray diffraction (SCXRD). a) Zr_8 cluster (teal) determined from SCXRD data, with a flat disk-shaped ellipsoid of the Zr atom (left) and a truncated cube created by the overlap of four different orientations of $Zr_6O_4(OH)_4$ clusters (blue, green, red, and orange), each occupied by 25 % (right); b) Fourier map of the (111) plane through the truncated corners of the cube showing the electron density map of three Zr atoms (positions indicated in white).

The occupancy of the linker was further investigated by SCXRD, PDF, Rietveld, and chemical analysis (Appx. A, Section A.2.3) as well as ssNMR spectroscopy. SCXRD analysis revealed that the porphyrin moiety of the linker is not fully occupied, but rather approximately 50 %; therefore, only 6 out of the 12 sites on the Zr_6O_8 cluster are coordinated by TCPP, similar to PCN-224. Compared to the porphyrin moiety, the phenyl rings refined to a higher occupancy of approximately 75 %. This suggests that besides six TCPP linkers, leftover pore content may occupy the TCPP-vacant sites.

PDF analysis provided further insights into the linker vacancies and cluster orientations (Figure 2.5). The intermediate-range atomic density distribution from 5–40 Å suggests a high degree of similarity to experimental PCN-224 with respect to the preferred coordination of linkers around the Zr-oxo clusters, and the relative concentration of linker present, confirmed by comparison to published models (Figure 2.5b). The PDFs of all samples thus also indicate 50–60 % porphyrin occupancy. Furthermore, slightly increased broadening of features at long distances suggests a more disordered long-range structure compared to the PCN-224 sample (Appx. A, Figure A.17). This could be attributed to more randomly distributed vacancies, in contrast to ordered vacancies in PCN-224.

For Rietveld refinements (Appx. A, Figure A.6), accounting for orientationally averaged clusters, nonplanar porphyrin linkers, and random linker vacancies led to substantially improved agreement with the PXRD data. Additional electron density coordinating cluster-surface sites was required to obtain a good fit. This could be primarily accounted for by remaining water content, though contribution from other remaining coordinative species is possible. Multiphase refinements performed found no preference for any ordered domains of MOF-525-like structure.

The models discussed still could not explain weak, diffuse features consistently observed at the superstructure reflection positions of PCN-224 (Figure 2.5c and Appx. A, Figure A.9), which were also observed by SCXRD (Appx. A, Figure A.24). We built a $2 \times 2 \times 2$ supercell and refined separate occupancy factors for each individual linker and cluster orientations for each cluster site, allowing for different local vacancy-orientation environments. This gave a good fit over the entire angular range and reproduced the weak features; however, it is not sufficient to identify a distinct local structure patterning of orientations and vacancies, as other supercell models can also produce similar diffuse features. Altogether, the findings suggest that these structures form more as a frustrated network than as a simple crystal, though the average structure can be described by orientationally disordered $Zr_6O_4(OH)_4$ clusters and linker vacancies distributed more randomly than in PCN-224. As such, we propose disordered PCN-224 (*d*PCN-224) as a more systematic description of PCN-221.

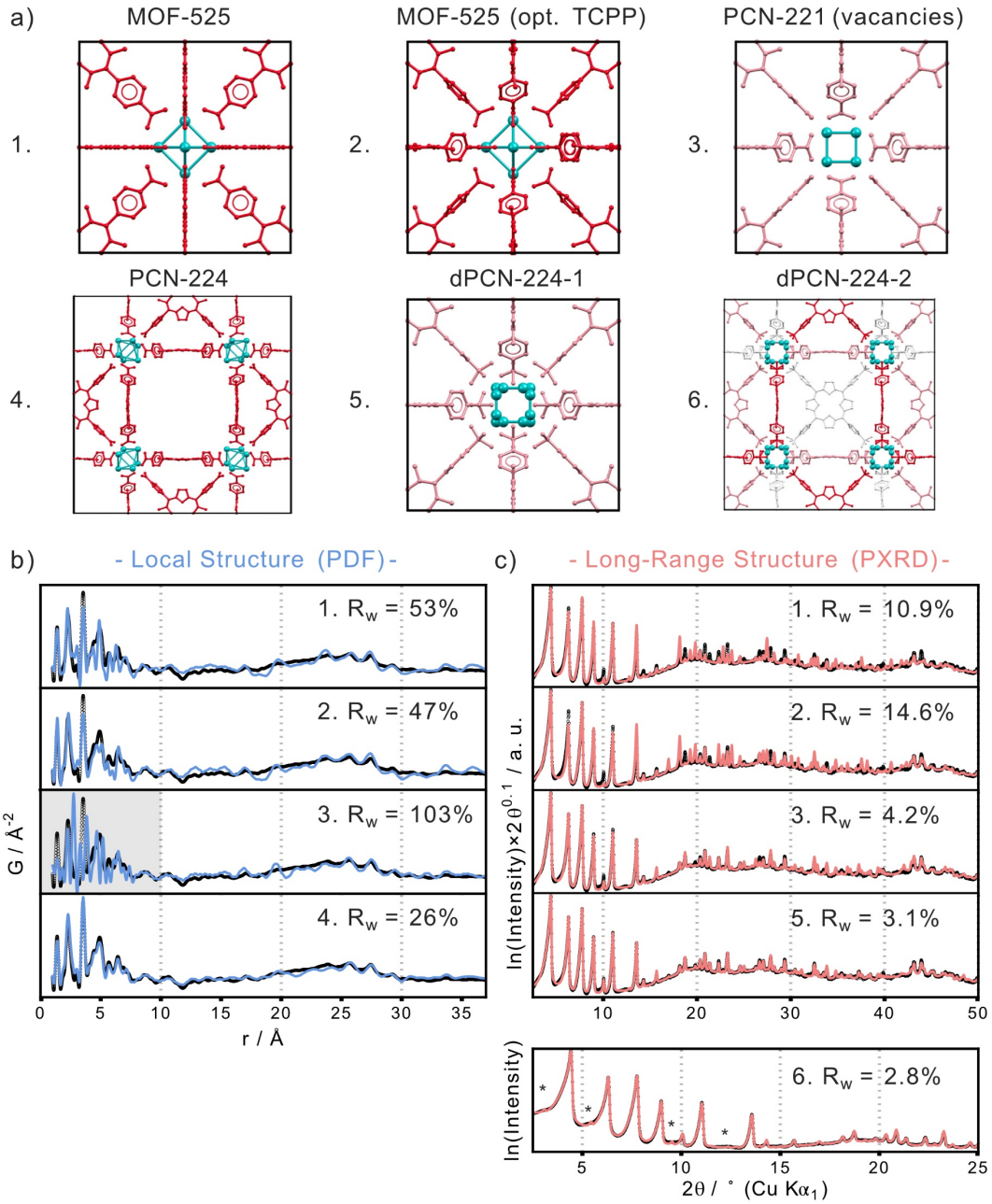

Figure 2.5: Structure models with corresponding pair distribution function (PDF) and Rietveld refinements. a) MOF structures shown with Zr (teal) and tetrakis(4-carboxyphenyl)porphyrin (TCPP) linkers with 100 % (red), 50 % (pink), and 0 % (grey) occupancy: (1) MOF-525 with planar TCPP linkers and no vacancies, (2) MOF-525 structure with twisted phenyl rings in the TCPP linker and no linker vacancies, (3) PCN-221 (Zr_8 clusters) with equally distributed linker vacancies, (4) PCN-224 structure with ordered TCPP vacancies, (5) *d*PCN-224-1 built of Zr_6 clusters with four different orientations and equally distributed linker vacancies, and (6) *d*PCN-224-2 with relative cluster orientations and linker occupation refined separately for each individual linker and cluster site, allowing for different possible local environments (the linker colors of (6) are an artistic representation and not specific to occupancies of the refined model). b) PDF fits compared to experimental *d*PCN-224 (blue, PDF of MOF_$ZrOCl_2$ measured using synchrotron radiation), showing poor agreement between the local environments in structures 1–3 and good agreement with the local structure of PCN-224 (structure 4). c) Improvement of the Rietveld refinements of experimental *d*PCN-224 (pink, also sample MOF_$ZrOCl_2$) for models shown. The extra intensities generated by the 2 x 2 x 2 supercell model of *d*PCN-224 are highlighted (*). *Rw* is the residual value (see Appx. A, Section A.2.4).

2.3.4 Chemical environments

To obtain insights into the local coordination environment of the Zr-oxo cluster in PCN-221 (*d*PCN-224), a comprehensive set of solid-state NMR measurements was carried out. High-resolution ^{1}H, ^{13}C, and ^{15}N magic angle spinning (MAS) NMR spectra of *d*PCN-224 and PCN-224 (Figure 2.6a–b and Appx. A, Figure A.25–A.27) are very similar, further supporting the proposed structural relation between both compounds on local length scales. The NMR spectra show well-resolved resonances for all characteristic chemical groups of the TCPP linkers, the modulator molecules (acetate (Ac) and benzoate (Bz)), and the Zr clusters. In particular, the presence of sharp and well-defined resonances for the μ3-OH groups at around 3.3 ppm in the ^{1}H MAS NMR spectra (Figure 2.6a and Appx. A, Figure A.25) underlines the presence of $Zr_6O_4(OH)_4$ units.[213] The ratio between the intensities of the μ3-OH (≈ 3.3 ppm) and the NH (≈ –3.2 ppm) resonances allowed us to derive a TCPP linker occupancy of 53(4) % for *d*PCN-224 and 40(4) % for PCN-224 of the $Zr_6O_4(OH)_4$ cluster.

The aromatic regions (7–9 ppm) of the ^{1}H NMR spectra show significantly more intensity than expected for TCPP linkers alone. Combined with the small amount of modulator molecules, as determined from the ^{1}H and ^{13}C cross polarized magic angle spinning (CPMAS) spectra (Figure 2.6a Appx. A, Figure A.25 and A.26), we conclude that the remaining six (*d*PCN-224) to seven (PCN-224) coordinatively unsaturated sites at the $Zr_6O_4(OH)_4$ clusters are mainly saturated by hydroxy water pairs (for details see Appx. A, Section A2.6). A similar situation was recently reported for the same cluster type in NU-1000.[210,214] The strong downfield shift for the protons within such pairs translates into comparably short O–O distances between 2.6 and 2.7 Å (Figure 2.6), characteristic for strong hydrogen bonds.[214-215] The additional spectral intensity between 6 and 4 ppm was attributed to mobile water in the neighborhood of the Zr clusters. Both the hydroxy water pairs at the coordinatively unsaturated sites of the clusters, as well as the mobile water may account for the additional electron density close to the cluster surface sites, required for the Rietveld refinement of the PXRD data.

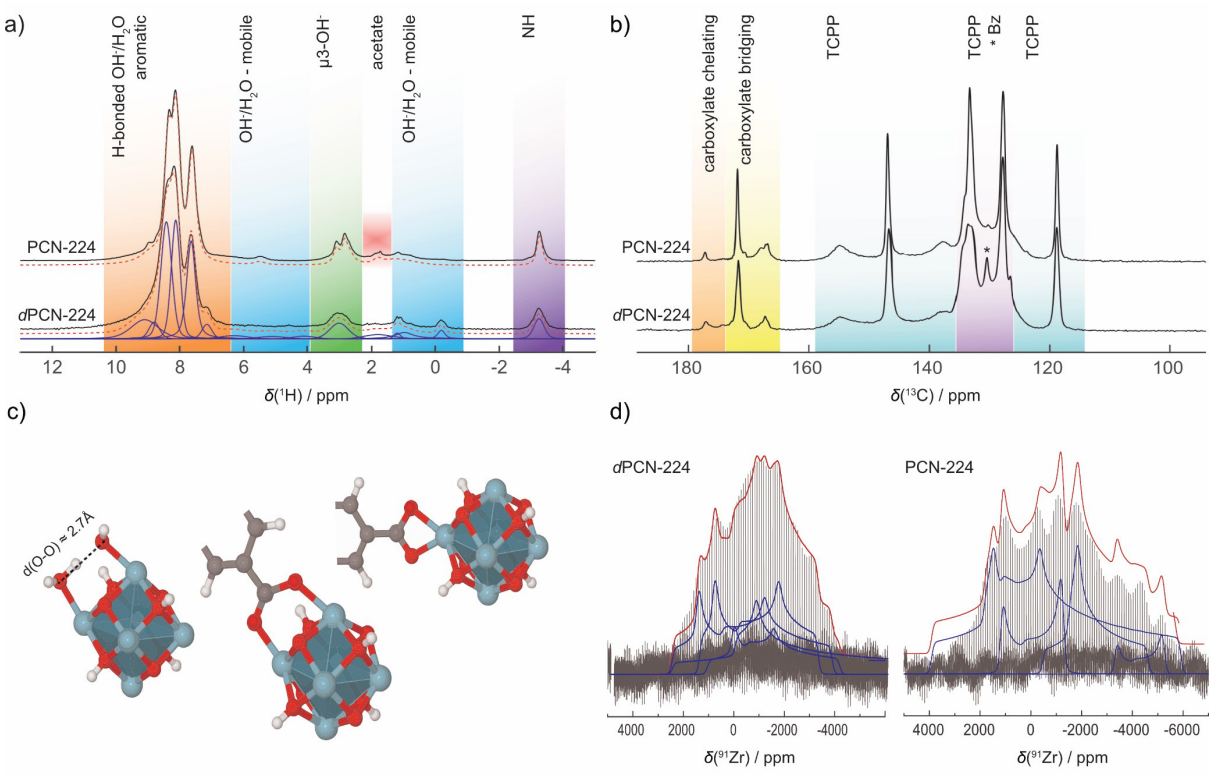

Figure 2.6: Solid state nuclear magnetic resonance (ssNMR) spectroscopic analysis of *d*PCN-224 (MOF_ZrOCl$_2$) and PCN-224. a) ^{1}H high-resolution magic angle spinning (MAS) NMR spectra recorded at a field of 23.48 T ($\nu_0(^{1}H)$ = 1 GHz). Characteristic resonances for the aromatic and NH protons of the tetrakis(4-carboxyphenyl)porphyrin (TCPP) linker, the μ3-OH groups of the $Zr_6O_4(OH)_4$ cluster[213], hydroxy groups, and water molecules[210-211] are highlighted by color-coded regions. b) ^{13}C cross polarization magic angle spinning (CPMAS) spectra with assignment of the aromatic carbons of the TCPP linkers and benzoic acid (Bz), and chemically inequivalent carboxylic acid groups, characteristic of chelating and bridging binding motifs for the carboxylic acid groups to the cluster. c) Main coordination motifs for the $Zr_6O_4(OH)_4$ clusters, from left to right: hydroxy water pairs and bridging and chelating carboxylate groups, which were found in decreasing proportions along this sequence. d) ^{91}Zr quadrupolar Carr-Purcell-Meiboom-Gill variable offset cumulative spectroscopy (qCPMG VOCS)[216-219] consisting of at least four different quadrupolar lineshapes (blue), typical for quadrupolar coupling constants between 20 and 25 MHz. Together with the non-axial symmetry of the quadrupolar coupling tensors, an environment with a low symmetry and complex coordination of the Zr atoms is revealed within the cluster. Individual lineshapes and spectral fits are illustrated in blue and red, respectively.

The carboxylic region of the ^{13}C MAS NMR spectra for *d*PCN-224 and PCN-224 contains several signals between 167.3 and 177.2 ppm centered around a main peak at ≈ 171.9 ppm (Figure 2.6b). Such a broad spread reflects different binding modes between the $Zr_6O_4(OH)_4$ clusters and the carboxylate units of the TCPP linkers and residual modulator molecules, in combination with a configurational variance from cluster to cluster. Based on DFT calculations (Appx. A, Figure A.30 and ref.[175]) we assigned the central resonance and its high-field region (165–173 ppm) to carboxylates in a bridging motif and the low-field region (173–176 ppm) to a chelating motif. As

such, the primary coordination motif consists in bridging TCPP linkers for both *d*PCN-224 and PCN-224, in accordance with the published structure model of PCN-224[91] and reported calculations showing that bridging carboxylate groups are favorable over chelating ones.[175] A small part of carboxylate groups is found in a chelating motif reflecting the local disorder of the clusters in both *d*PCN-224 and PCN-224.

The distribution of different binding modes is also reflected in the lineshapes of the ^{91}Zr wideline NMR spectra (Figure 2.6d). They consist of at least four different quadrupolar shapes with non-axial symmetric coupling tensors and coupling constants (C_Q) between 10 and 25 MHz. This proves a markedly more diverse coordination for the individual Zr atoms compared to a free $Zr_6O_4(OH)_4Bz_{12}$ cluster with 12-fold benzoate coordination[220] (Appx. A, Figure A.31). Compared to the free cluster, the broader variance for *d*PCN-224 and PCN-224 reflects the disorder induced by attached hydroxy water pairs, residual modulator molecules, and the strain on the Zr clusters imposed by the framework.

2.3.5 Linker vacancies

We revisit the implications of linker vacancies at approximately 50 % occupation as consistently derived from SCXRD, Rietveld, PDF, and ssNMR. Recently, highly defective MOF-525 structures with up to 50 % linker vacancies were reported, further supporting the observation of high vacancy concentrations in our proposed structure of PCN-221 (*d*PCN-224).[187] The favorable coordination of bridging ligands[175,207], as implied by ssNMR, suggests that TCPP vacancies should preferentially occur where chelating coordination would otherwise be required, similar to the reported PCN-224 structure. The presence of diffuse superstructure features in both XRPD and SCXRD further suggest that small domains of vacancy ordering may occur. Both *d*PCN-224 and MOF-525 are built from Zr_6 clusters, however, MOF-525 only has one cluster orientation, where the primary axes of the octahedron are aligned with the unit cell axes. This straight orientation imposes a more energetically demanding conformation of the TCPP molecules with either fully planar TCPP molecules, or with the carboxylate groups oriented unfavorably perpendicular to the twisted phenyl groups (Appx. A, Figure A.35 and A.36). Unlike the MOF-525 models, the six bridging TCPP linkers in *d*PCN-224 both have twisted phenyl rings and coplanar carboxylate groups, which represents an energetically more favorable situation. We thus conjecture that the formation of MOF-525 with only straight cluster orientations may be hindered by a combination of kinetic limitations and configurational entropy considerations. If TCPP initially attaches to one of the six discussed bridging sites between differently tilted clusters, the 12-fold bridging-only coordination

of MOF-525 can no longer form. The bridging sites with respect to the tilted cluster are shown in Appx. A, Figure A.37. This may well explain why we consistently obtained *d*PCN-224 as the dominant structure. While we cannot exclude the possibility of site-isolated MOF-525-like cluster orientations in *d*PCN-224, possibly in regions of higher coordination, we found no evidence for the formation of ordered domains of the reported MOF-525 structure.

2.4 Conclusion

In conclusion, we have resolved the long-standing question regarding the formation of a Zr_8O_6 secondary building unit within the MOF PCN-221. Based on a combination of local- and long-range sensitive structural techniques, we have revealed that the superposition of four statically disordered $Zr_6O_4(OH)_4$ clusters appears on average as a truncated cube, which can easily be misinterpreted as a Zr_8O_6 cluster. The orientations of the clusters, linker vacancies up to 50 %, and the conformation of the TCPP linker are all reminiscent of PCN-224; however, PCN-224 is distinct in that it forms an ordered 3D checkerboard arrangement of linker vacancies and ordered relative cluster orientations. We therefore recommend to describe the structure of PCN-221 as a disordered variant of PCN-224: *d*PCN-224. The remaining coordination sites at the $Zr_6O_4(OH)_4$ clusters are completed by hydroxy-water pairs and modulator molecules. The origin of the linker vacancies was traced back to two different coordination environments in PCN-221 (*d*PCN-224)—bridging and chelating. While the former is energetically more favorable according to quantum chemical calculations, the relatively flat energy landscape for the different coordination modes and linker conformations, and the high configurational entropy associated with the 12 coordination sites of the $Zr_6O_4(OH)_4$ clusters rationalizes the defect-prone nature of these MOFs. This work thus sheds light on the interplay between network topology, defects, and disorder in Zr-based MOFs, and opens up a unique design space by invoking additional degrees of freedom such as correlated cluster orientation, cluster disorder, and cluster–linker binding modes. In the context of these parameters, it may be useful to look for similar phenomena in other MOF systems displaying ordered defect variants and investigate the corresponding differences in properties. Once controlled, these design criteria could unleash a huge untapped potential for directing the functional properties of MOFs.

2.5 Acknowledgements

The authors gratefully acknowledge the help of Viola Duppel (MPI for Solid State Research) for the SEM images and Dr. Tobias Stuerzer (Bruker AXS GmbH, Karlsruhe, Germany) for carrying out SCXRD measurements. The authors further thank Lina Beisswenger and Jessica Wulfes for

experiments and Sebastian Bette for helpful discussion. Financial support was granted by the Max Planck Society, the University of Munich (LMU), the Center for NanoScience (CeNS), the Deutsche Forschungsgemeinschaft (DFG) through the priority program “Coornets” SPP 1928 (proj. nos. SE 1417/8-1 and LO 1801/4-1), the Cluster of Excellence “Nanosystems Initiative Munich” (NIM), and “*e*-conversion”. M.W.T. gratefully acknowledges support from BASF. C.O. acknowledges further support as Max-Planck-Fellow at the MPI-FKF Stuttgart. We acknowledge DESY (Hamburg, Germany), a member of the Helmholtz Association HGF, for the provision of experimental facilities. Parts of this research were carried out at beamline P02.1.

2.6 Authors contributions

C.K., R.St., A.M., J.S., and B.V.L. conceived the project and C.K. coordinated it. C.K., A.M., and F.B. designed and carried out sample synthesis and analysis. R.St., R.Si., and J.S. measured and analyzed solid-state NMR. T.S. performed SCXRD analysis. M.W.T. performed PXRD and PDF measurements and analysis. T.S. and M.W.T. performed structural modeling and refinements. G.S. and R.S performed quantum chemical calculations. A. S. and M.E. measured synchrotron X-ray data. J.N. helped with SCXRD measurement. L.G., C.O., and R.D. contributed useful discussion on measurements and modeling. C.K., R.St., T.S., M.W.T., G.S., A.M., J.S., and B.V.L contributed to overall interpretation, and C.K., R.St., T.S., M.W.T, J.S., and B.V.L. wrote the manuscript.

CHAPTER 3

SYNTHESIS OF PORPHYRINIC Zr-BASED MOFs

In Chapter 2, a new structure model, namely *disordered PCN-224* (dPCN-224), was introduced to describe cubic porphyrinic MOFs with varying degrees of orientational cluster disorder, linker vacancies, and cluster–linker coordination type. A major obstacle in studying porphyrinic Zr-based MOFs, however, remains the lack of reproducibility of reported syntheses. This leads to the co-existence of a variety of different synthetic procedures, coupled with insufficient characterization and questionable structure models, signaling that these MOF products are still not well understood. Here, the formation of dPCN-224 was studied step-by-step in order to understand the critical steps of nucleation and growth of dPCN-224 particles. In addition, this chapter highlights the importance of water in directing the composition of the formed framework and reveals that controlling the amount of water in the reaction is crucial for the synthesis of phase-pure porphyrinic Zr-based MOFs.

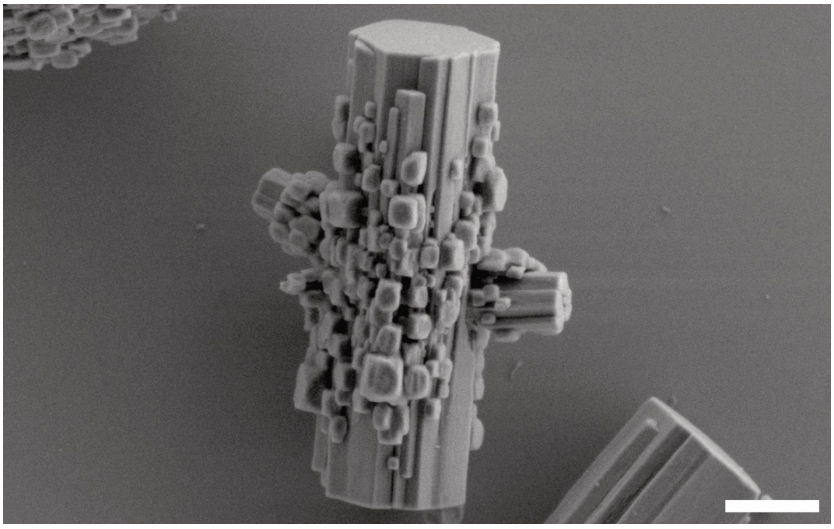

Cover image of Chapter 3: Scanning electron microscopy image showing dPCN-224 particle nucleation on a metal–organic intermediate. Scale bar = 1 μm.

Influence of Water Content on Phase Formation of Zr-Porphyrin-based MOFs

Charlotte Koschnick, Maxwell W. Terban, Stefano Canossa, Martin Etter, Robert E. Dinnebier, Bettina V. Lotsch

Parts of this chapter are published in

Advanced Materials **2023**, 2210613.
DOI: 10.1002/adma.202210613
https://doi.org/10.1002/adma.202210613
Text and figures adapted with permission from Wiley

3.1 Abstract

Controlled synthesis of phase-pure metal–organic frameworks (MOFs) is essential to establishing their application in technological platforms such as catalysis or gas sorption. However, synthetic protocols often lack reproducibility, and as a result, mixtures of different MOF products from the same node and linker can form. In this work, the formation of the Zr-porphyrin MOF dPCN-224 is investigated under variable conditions. Powder X-ray diffraction and pair distribution function analysis in combination with scanning electron microscopy revealed that dPCN-224 forms *via* a metal-organic intermediate that consists of $Zr_6O_4(OH)_4$ clusters linked by tetrakis(4-carboxy-phenyl)porphyrin molecules. This work further shows that water is essential to the formation of both the $Zr_6O_4(OH)_4$ clusters and final dPCN-224 framework, dictates the formation kinetics of the MOF products, and ultimately directs the composition of the products obtained through varying reaction times.

3.2 Introduction

The formation of metal–organic frameworks (MOFs) relies on coordinative self-assembly of inorganic nodes and organic linkers into periodic coordination networks.[127,221] The variety of both inorganic and organic building units allows for a wide array of MOF topologies that may cater to the specific materials requirements in catalysis, drug delivery, or gas separation.[20-23] Often, the same node and linker can arrange in different ways yielding different framework topologies or even distinct MOF phases with different compositions.[96,222] As a consequence, typical MOF synthesis can yield mixtures of two or more phases, sometimes even in the same reaction mixture.[222] In addition to mixed products, mixtures of phases can also occur in the same crystallite.[222] Such

phenomenon are particularly prevalent in Zr-based MOFs. Pyrene-based NU-1000, for example, can contain structural motifs of the polymorph NU-901 in the middle of the crystallite.[223] Even though both frameworks consist of 8-connected clusters, NU-901 has a more densely packed structure with lower pore volume compared to NU-1000.[223] On the other hand, UiO-66 was shown to often contain domains of the ordered missing cluster phase **reo** UiO-66, in which one quarter of the Zr-oxo clusters are missing.[106] This is important, since the differences in pore sizes or network topologies effect the properties.[96] The situation is further complicated by the fact that many synthetic protocols additionally require the formation of the inorganic nodes from precursor species prior to MOF formation. Zr-based MOFs built form $Zr_6O_4(OH)_4$ clusters, for example, need to form the hexanuclear Zr-oxo nodes from the $ZrCl_4$ or $ZrOCl_2 \cdot 8H_2O$ precursors prior to the MOF assembly.[224-226]

In general, a wide variety of parameters affect the nucleation and growth of MOF particles, including temperature, pressure, pH, solvent, precursors, or choice of modulators to compete with the linker and allow for more controlled MOF growth.[116,132,154,159,227] During the synthesis of NU-1000, for example, using biphenyl-carboxylic acid instead of benzoic acid as the modulator prevents the formation of the denser NU-901 phase, allowing for synthesis of phase pure NU-1000 crystallites.[163] Importantly, water also plays a crucial role during the formation of Zr-based MOFs.[154] In fact, the formation of $Zr_6O_4(OH)_4$ clusters requires hydrolysis of the $ZrCl_4$ or $ZrOCl_2 \cdot 8H_2O$ precursors.[96,154,228-230] The amount of water added during synthesis of Zr-based MOFs can therefore influence both the phase of the formed MOFs and the crystallization rate.[154,167,230] When synthesizing UiO-66, for example, a higher water content in the reaction increases the formation rate of the $Zr_6O_4(OH)_4$ clusters, which in turn enhances the rate of crystallization of UiO-66.[167] On the contrary, when no water is present, $Zr_6O_4(OH)_4$ clusters do not form and instead, reaction at 220 °C yields the polymorph MIL-140A which consists of Zr_2O_2 chains.[96]

The many factors that influence the growth of MOF particles allow a great deal of control and tuning of the reaction conditions towards the formation of a desired MOF phase. At the same time, however, the multitude of factors and their complex interplay inherently leads to a high level of irreproducibility in the synthesis of phase-pure MOFs, especially when the crystallization pathway of a MOF is unknown. This is especially apparent in porphyrinic Zr-based MOF formation, where the phase formed depends on the modulator used, its concentration, the reaction temperature and time, and other less controllable, factors.[63,159,187] Synthesis of these MOFs thus often involves laborious screening of reaction conditions between research groups, leading to the existence of multiple synthetic protocols for the same phase, but also formation of different phases when

following the same protocol. Needless to say, this greatly impedes scientific progress in MOF chemistry.[63,92,231-237]

Understanding the critical instances during MOF formation can help to better control the growth of phase-pure products. Despite vast research efforts, the nucleation and growth processes of MOFs remain a black box for most frameworks. One reason is that the crystallization path not only depends on the composition of the reaction mixture, but also on sometimes subtle reaction conditions.[126,132-134] Two common models exist to describe the formation of MOFs: classical and non-classical. In the classical pathway, the monomers (i.e. linker and metal nodes) first spontaneously form crystalline nuclei, which then grow into well-faceted MOF crystals *via* the sequential layer-by layer deposition of building units onto the nuclei.[135] An example of this is HKUST-1, which was shown to follow homogeneous nucleation and particle growth from solution.[130,238] The non-classical pathway comprises multiple steps during which clusters of metal ions and linkers aggregate to form intermediates, which then transform into crystalline MOFs.[131] ZIF-8, for example, nucleates from solution *via* three distinct steps. Initially, the solution separates into solute-rich and solute-poor regions. Subsequently, the solute-rich phases condense into dense amorphous metal-organic aggregates, which in turn crystallize to MOF nanoparticles in the third step.[131] Synthesis of MOF-5 in turn was shown to form crystalline $Zn_5(OH)_8(NO_3)_2 \cdot 2H_2O$–1,4-BDC (BDC = 1,4-benzene-dicarboxylate) nanoplatelets at first. These aggregate into layered inorganic-organic composites followed by nucleation of MOF-5 inside the composite.[134] Given the variability and complexity of MOF formation, it is thus necessary to study particle growth and synthetic protocols individually for each subset of MOFs, if not each MOF individually, in order to not only understand, but also control the formation of phase-pure MOFs.

This work aims to shed light on the formation pathway of a representative of one of the most prominent classes of MOFs that are currently studied: Zr-porphyrin-based dPCN224. The structure model for this MOF, which was originally published as PCN-221 and MOF-525, was recently updated to account for the disordered Zr_6 cluster in this cubic porphyrin-MOF, which can be considered the cluster- and linker vacancy-disordered variant of PCN-224.[77] As laid out in Chapter 2, the synthesis of phase-pure dPCN-224 is challenging and often yields multiphase mixtures of porphyrinic MOFs instead.[63,159] Besides dPCN-224, six more MOF structures were reported from the same building blocks with coordination numbers of the Zr-oxo clusters varying from 6 to 12: PCN-224 (6-connected), PCN-222/MOF-545, PCN-225, and NU-902 (all 8-connected), and PCN-223 and MOF-525 (both 12-connected).[85-86,91-94] The different frameworks can have different lattices (*e.g.* dPCN-224 and PCN-222 are cubic and hexagonal, respectively) as well as variable ordering of linker vacancies (dPCN-224 has disordered linker vacancies compared

to PCN-224, see above), both of which affect the resulting properties.[36,72,77,85,208,239] Here, we study the formation of dPCN-224 and its dependence on the reaction conditions and reveal that dPCN-224 does not follow the classical nucleation pathway but forms *via* an intermediate instead. The study is arranged as follows: First, we discuss the effects of the Zr source and water content on the MOF product, then we turn to the step-by-step formation pathway of dPCN-224 using different Zr sources, and finally, we conclude by commenting on the important role of water during synthesis of the MOF.

3.3 Results and discussion

3.3.1 Role of the zirconium(IV) chloride source and water content on product formation

To begin, we explored the role of the Zr precursor on the phase formation of cubic Zr-porphyrin-based MOFs. Two different $ZrCl_4$ sources were used: $ZrCl_4$ stored in a glovebox ($ZrCl_4$_GB), and $ZrCl_4$ stored in a closed jar under ambient conditions for several months prior to synthesis ($ZrCl_4$_lab) (see Appx. B, Figure B.1–B.3 for more information on precursors). A solvothermal reaction was performed according to a procedure published for PCN-224 by reacting $ZrCl_4$ and tetrakis(4-carboxyphenyl)porphyrin (TCPP) linker under addition of benzoic acid which serves as the modulator.[91] $ZrCl_4$_GB and $ZrCl_4$_lab yielded different products after a 24 h reaction. Neither formed PCN-224 that features ordered linker vacancies and superstructure reflections around 3.2 and 5.5° 2θ as shown by powder X-ray diffraction (PXRD) analysis (Figure 3.1a-b). Instead, $ZrCl_4$_lab yielded the disordered PCN-224 variant dPCN-224, whereas $ZrCl_4$_GB gave an unknown phase. Notably, the few sharp reflections observed for the unknown phase are similar to the (h00) (where $h = 2n$) reflections in the PXRD pattern of dPCN-224 (Figure 3.1b).[77] Scanning electron microscopy (SEM) imaging shows cubic particles as expected for $ZrCl_4$_lab, but highly anisotropic, rod-shaped particles from $ZrCl_4$_GB (Figure 3.1c-d).

Nitrogen sorption measurements were used to determine the porosity and surface area of the product materials (Figure 3.1 e-f). $ZrCl_4$_lab showed a Type I isotherm with micropores of 2.0 nm and a Brunauer-Emmett-Teller (BET) surface area of 2288 $m^2\ g^{-1}$. In contrast, the rod-shaped particles obtained from $ZrCl_4$_GB showed a Type II isotherm typical for non-porous or macroporous structures.[5]

From this information, it was determined that $ZrCl_4$_lab promoted the formation of dPCN-224 while $ZrCl_4$_GB did not, revealing that the different $ZrCl_4$ sources can greatly affect the product formation. In fact, PXRD analysis reveals clear differences in the starting materials: while $ZrCl_4$_GB contained a mixture of the monoclinic[240] and orthorhombic[241] $ZrCl_4$ phases, the phase

composition of $ZrCl_4$_lab—which had aged in the lab over several months—could not determined from PXRD data (Appx. B, Figure B.3).

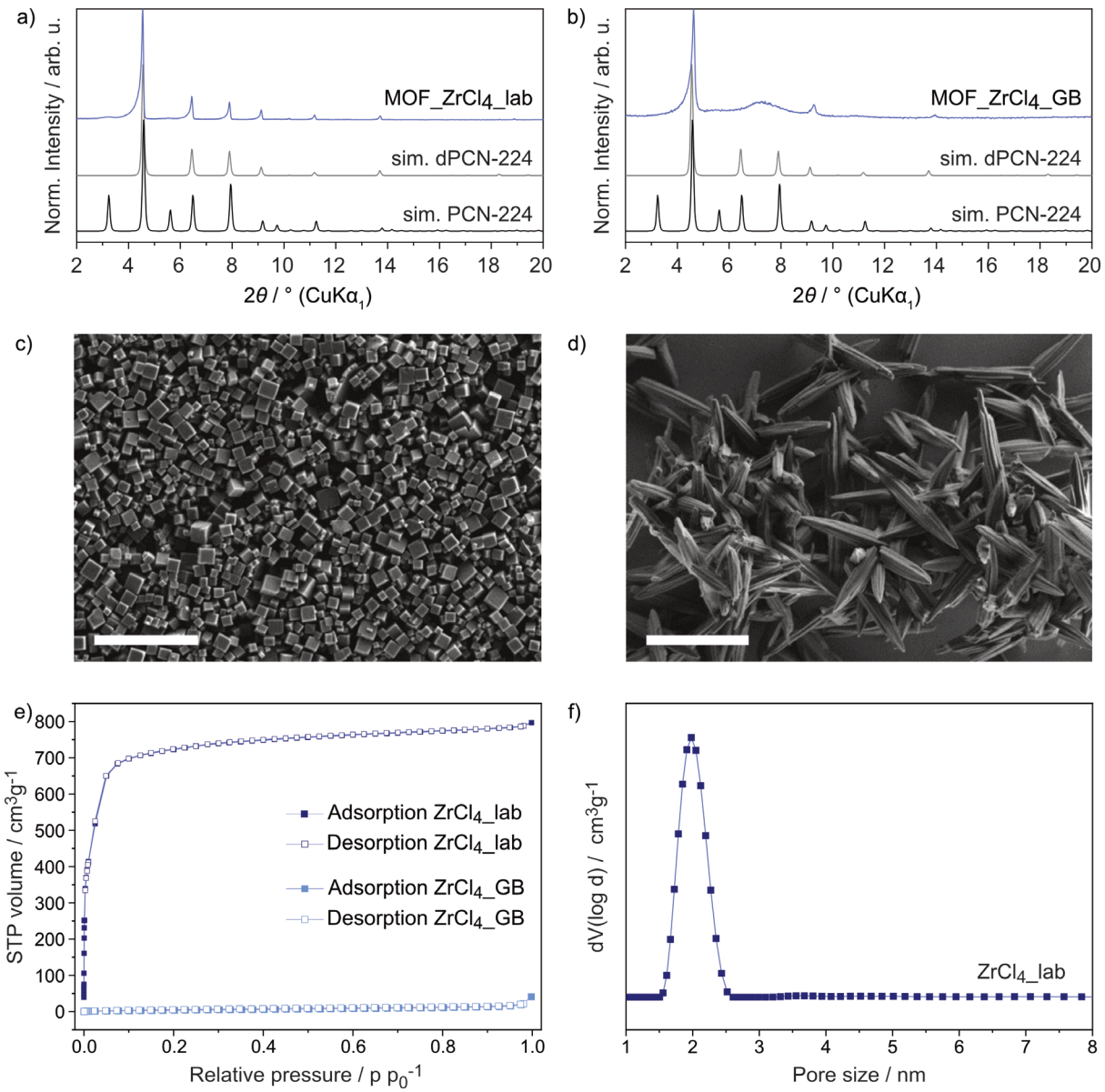

Figure 3.1: PXRD patterns of products obtained from a) $ZrCl_4$_lab and b) $ZrCl_4$_GB after 24 h reaction time compared to the simulated (sim.) patterns of dPCN-224[77] and PCN-224[91]. SEM images of products obtained from c) $ZrCl_4$_lab and d) $ZrCl_4$_GB; scale bar = 5 µm. e) Nitrogen sorption isotherm (77 K) of products obtained from $ZrCl_4$_lab and $ZrCl_4$_GB after 24 h reaction time. f) Pore size distribution of products obtained from $ZrCl_4$_lab.

The different products obtained from $ZrCl_4$_GB and $ZrCl_4$_lab suggest that the aging environment of the Zr source significantly affects its role as a precursor to framework formation. To test this further, we left $ZrCl_4$_GB to age under ambient conditions for one and three days prior to use in the reaction ($ZrCl_4$_1d and $ZrCl_4$_3d, respectively). PXRD analysis showed that the use of both $ZrCl_4$_1d and $ZrCl_4$_3d yielded crystalline MOFs when compared to $ZrCl_4$_GB. Synthesis from

ZrCl4_1d yielded a product mixture of the porphyrin-based MOFs PCN-222 and NU-902, while $ZrCl_4$_3d yielded phase pure dPCN-224 (Figure 3.2a and Appx. B, Figure B.4). With respect to morphology, the use of $ZrCl_4$_1d resulted in rod-shaped particles characteristic of PCN-222 and NU-902, while $ZrCl_4$_3d produced cubic particles typical of PCN-224 and resembling the product obtained from $ZrCl_4$_lab (Figure 3.2b-c).[72,77] The observed behavior may be explained by the fact that when exposed to air, hygroscopic $ZrCl_4$ absorbs water and hydrolyses (Appx. B, Figure B.3), suggesting that the amount of water in the reaction influences product formation.

To better quantify the role of water in phase formation, the reaction was also performed with $ZrCl_4$_GB, after addition of 20 µL or 50 µL water yielding $ZrCl_4$_20µL and $ZrCl_4$_50µL, respectively. When 20 µL of water was added to the reaction, a mixture of PCN-222/NU-902 was formed after 24 h similar to the synthesis from $ZrCl_4$_1d (Figure 3.2a). In contrast, addition of 50 µL water yielded dPCN-224. Compared to the synthesis from $ZrCl_4$_GB, the addition of water therefore promoted the formation of crystalline frameworks. SEM images show that sample $ZrCl_4$_20µL formed thin rods that aggregated onto the surface of hexagonal rods (Figure 3.2d) sample $ZrCl_4$_50µL yielded intergrown, cubic particles (Figure 3.2e). Overall, these findings suggest that the quantity of absorbed water guides the framework formation and is essential for the growth of dPCN-224.

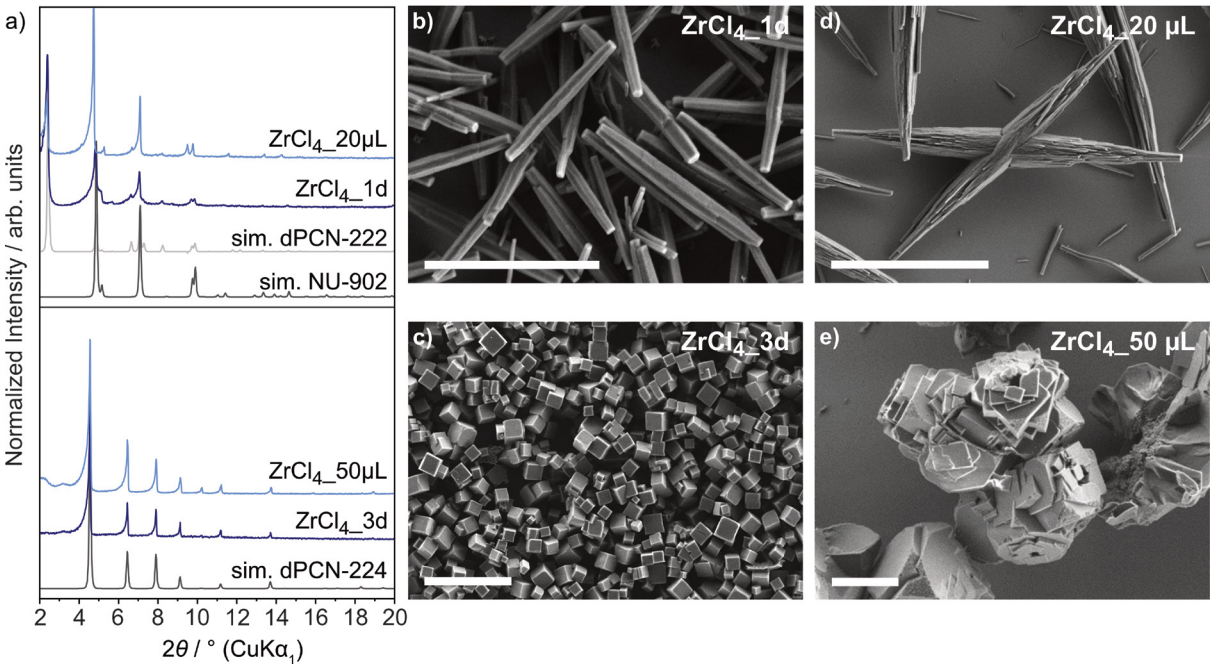

Figure 3.2: a) PXRD patterns of the products obtained from $ZrCl_4$_GB that was left to age for 1 d ($ZrCl_4$_1d) and 3 d ($ZrCl_4$_3d) prior to reaction, and from $ZrCl_4$_GB under addition of 20 µL ($ZrCl_4$_20µL) and 50 µL ($ZrCl_4$_50µL) water compared to the simulated patterns of dPCN-224, PCN-222, and NU-902. SEM images of the products obtained from b) $ZrCl_4$_1d, c) $ZrCl_4$_3d, d) $ZrCl_4$_GB with 20 µL water, and e) $ZrCl_4$_GB with 50 µL water. Scale bar = 5 µm.

3.3.2 Time dependent study from different zirconium(IV) chloride sources

To further elucidate the crystallization process of dPCN-224, time-dependent experiments were carried out during the synthesis from both $ZrCl_4$_GB and $ZrCl_4$_lab (see Appx. B, Section B.1.3 for further details). PXRD analysis and SEM imaging of the products revealed that multiple phases were formed during the reactions (Figure 3.3 and Figure 3.4).

Synthesis from $ZrCl_4$_GB yielded two different phases, depending on the reaction time (Figure 3.3). Synthesis times of less than 1 h led to string-like particles with a width of *ca.* 30–50 nm consisting of an unknown first phase (Phase I). The PXRD pattern could not be assigned to any known Zr-TCPP-based framework. When the reaction time was extended to 24 h, we observed the formation of a second unknown phase (Phase II) with reflections at 4.64, 9.28, and 13.93° 2θ. Increase of the reaction time up to 20 d led to an apparent aggregation of the anisotropic particles (SEM), but did not substantially change the phase structure (PXRD), suggesting that dPCN-224 cannot form from $ZrCl_4$_GB.

When $ZrCl_4$_lab was used, the same two unknown phases were observed after 2 min and 1 h, respectively (Figure 3.4), suggesting a similar initial reaction pathway. However, unlike $ZrCl_4$_GB, further transformation was observed with increasing reaction time. Reaction for 2 h yielded a mixture of hexagonal PCN-222 and cubic dPCN-224. Increasing the reaction time to 6 h and 18 h decreased PCN-222 in favor of dPCN-224. After 24 h, phase pure dPCN-224 was obtained.

Accordingly, SEM imaging showed changes of the MOF particle morphologies over time. Similar to $ZrCl_4$_GB, string-like particles were obtained after 2 min and 1 h, respectively. Remarkably, few cubic particles grew on the surface of the rods after 1 h. As the reaction time increased, thicker hexagonal rods were observed, which are characteristic of PCN-222.[72] From 2–18 h, a large number of truncated cubes in the range of 300–600 nm, and later up to 5 μm, grew from the surface and appeared to *consume* the rods (Figure 3.4 and Appx. B, Figure B.9). After 24 h, no rods were left, and the remaining dPCN-224 crystallites adopted a cubic morphology with sizes between 400–700 nm.

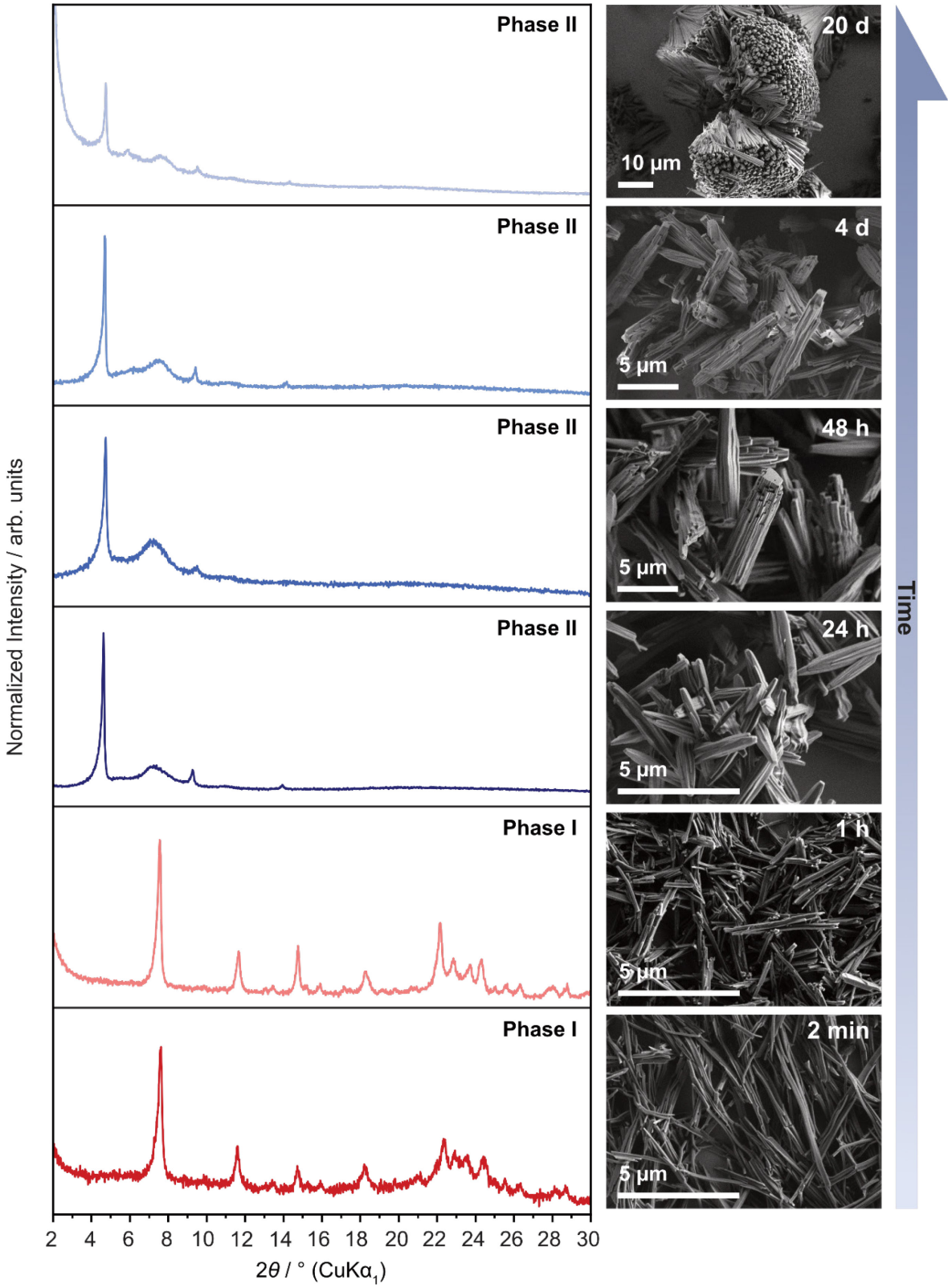

Figure 3.3: PXRD patterns (left) and SEM images (right) from the products obtained during synthesis from $ZrCl_4$_GB after 2 min, 1 h, 24 h, 48 h, 4 d, and 20 d reaction time. After 2 min and 1 h Phase I (organic intermediate) was formed whereas reaction for 24 h, 48 h, 4 d, and 20 d yielded Phase II (metal–organic intermediate).

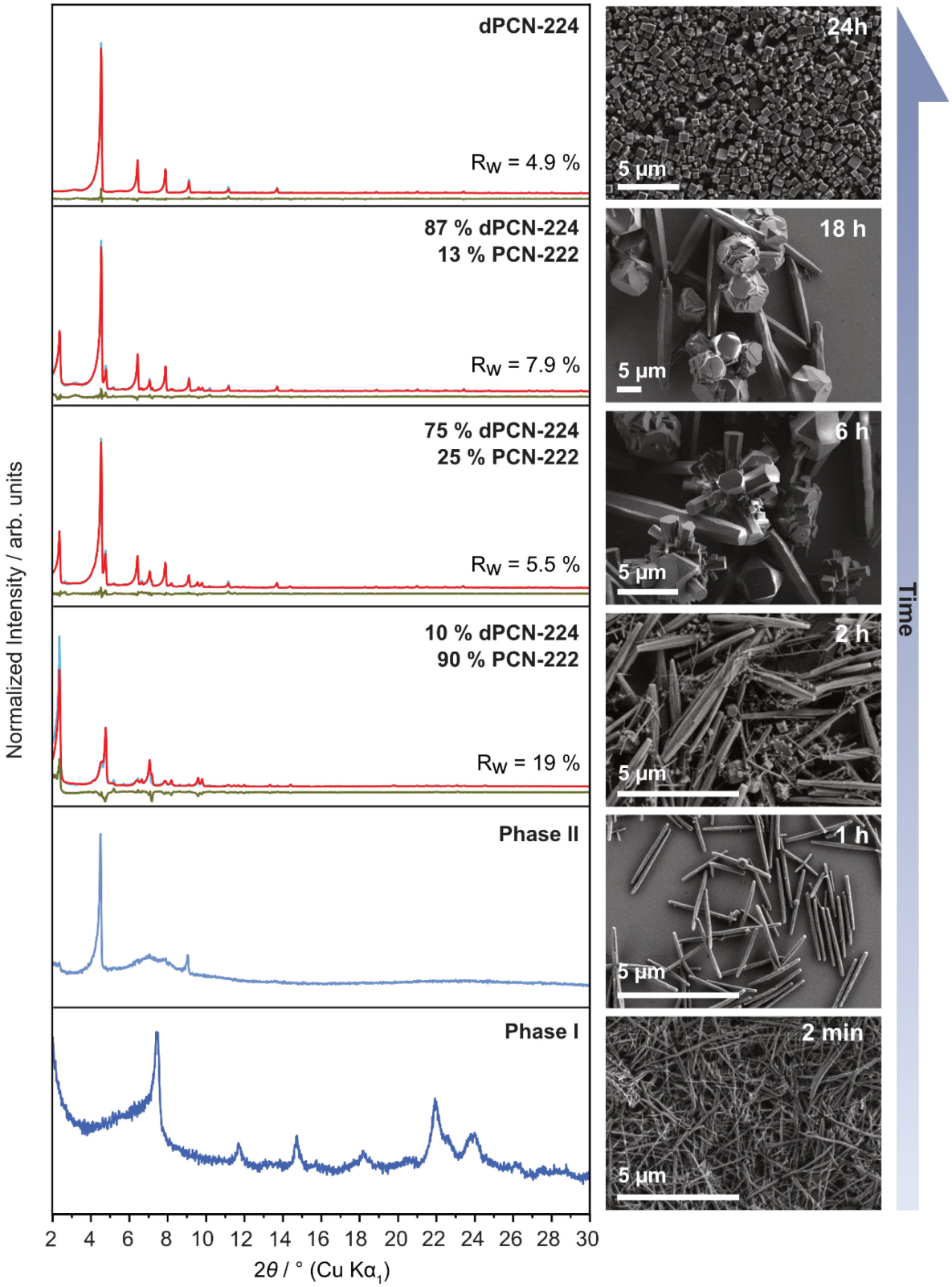

Figure 3.4: PXRD patterns from the products obtained during synthesis from $ZrCl_4$_lab after 2 min and 1 h reaction time and Rietveld refinements and residual value *Rw* of PCN-222[85] and dPCN-224[77] against observed patterns from the products obtained during synthesis from $ZrCl_4$_lab after 2 h, 6 h, 18 h, and 24 h reaction time (left). After 2 min Phase I (organic intermediate) was formed whereas reaction for 1 h yielded Phase II (metal–organic intermediate). The SEM images show a transformation of the particles' morphology with increasing reaction time (right).

3.3.3 Identifying the unknown phases formed during synthesis from zirconium(IV) chloride

During the reactions of both $ZrCl_4$_lab and $ZrCl_4$_GB, the unknown Phase I consisted of particles with a string-like morphology. Elemental analysis revealed that this phase is purely organic (Appx. B, Table B.3) and energy dispersive X-Ray analysis showed the presence of chloride in the sample (Appx. B, Figure B.14). NMR spectroscopy was used to probe the organic phase. The product only consisted of TCPP and did not contain the benzoic acid modulator (Appx. B, Figure B.15). The intense green color (Appx. B, Figure B.19) of the product indicated that the TCPP species was protonated.[242] Neutral TCPP (H_2TCPP) can be successively protonated to form the monocationic (H_3TCPP^+) and dicationic (H_4TCPP^{2+}) forms, thereby changing the color from purple to green.[242-243] The combined evidence suggests that for both sources, the initial product consists of molecular H_4TCPP^{2+} crystals, where the positive charges are balanced by chloride anions. The crystal structure of this TCPP phase will be subject of future studies.

After the formation of the H_4TCPP^{2+}-based intermediate, a second unknown intermediate (Phase II) formed from both Zr sources. This phase was isolated after 1 h during synthesis from $ZrCl_4$_lab, and after 24 h to 20 d during synthesis from $ZrCl_4$_GB. NMR analysis after digestion confirmed the presence of both TCPP and benzoic acid (Appx. B, Figure B.16–B.18), and elemental analysis revealed that this phase contained Zr (Appx. B, Table B.3). In other words, a metal–organic compound formed at this stage of the reaction. PXRD analysis showed reflections at similar angles to the 200, 400, and 600 reflections in dPCN-224, indicating a periodic ordering similar to dPCN-224 along at least one dimension. Electron diffraction also showed one-dimensional (1D) order with a periodicity of *ca.* 19.65 Å, in agreement with the PXRD data and the intercluster spacing of dPCN-224 (Appx. B, Figure B.20).

To understand the local structure, the samples formed from $ZrCl_4$_GB after 24 h and 20 d ($ZrCl_4$_GB_24h and $ZrCl_4$_GB_20d) and the samples formed from $ZrCl_4$_lab after 1 h and 24 h ($ZrCl_4$_lab_1h and $ZrCl_4$_lab_24h) were investigated with pair distribution function (PDF) analysis (Table 3.1 and Figure 3.5). Interestingly, the local structure from 0–10 Å differs significantly between the samples obtained from $ZrCl_4$_GB and $ZrCl_4$_lab. The PDFs of $ZrCl_4$_lab_1h and $ZrCl_4$_lab_24h, which consist of the metal–organic intermediate compound and dPCN-224, respectively, are very similar. Both PDFs feature peaks at 2.24, 3.53, and 4.92 Å. These correspond to Zr–O, adjacent Zr–Zr, and diagonal Zr–Zr pair distances in a Zr_6O_8 cluster.[77] The inorganic nodes in the $ZrCl_4$_lab_1h sample therefore consist of Zr_6O_8 clusters revealing that the hexanuclear Zr clusters in dPCN-224 form during the early stages of the reaction.

Table 3.1: Comparison of samples characterized *via* pair distribution function analysis indicating the Zr source, reaction time, and Zr node that best describes the local structure.

Sample	Zr source	Reaction time	Zr nodes
$ZrCl_4$_lab_1h	$ZrCl_4$_lab	1 h	Zr_6O_8
$ZrCl_4$_lab_24h	$ZrCl_4$_lab	24 h	Zr_6O_8
$ZrCl_4$_GB_24h	$ZrCl_4$_GB	24 h	$[Zr_2O_2]_2$-like
$ZrCl_4$_GB_20d	$ZrCl_4$_GB	20 d	Best described by Zr_2O_2 dimers, Zr-oxo chains, or Zr_4O_7 tetramers

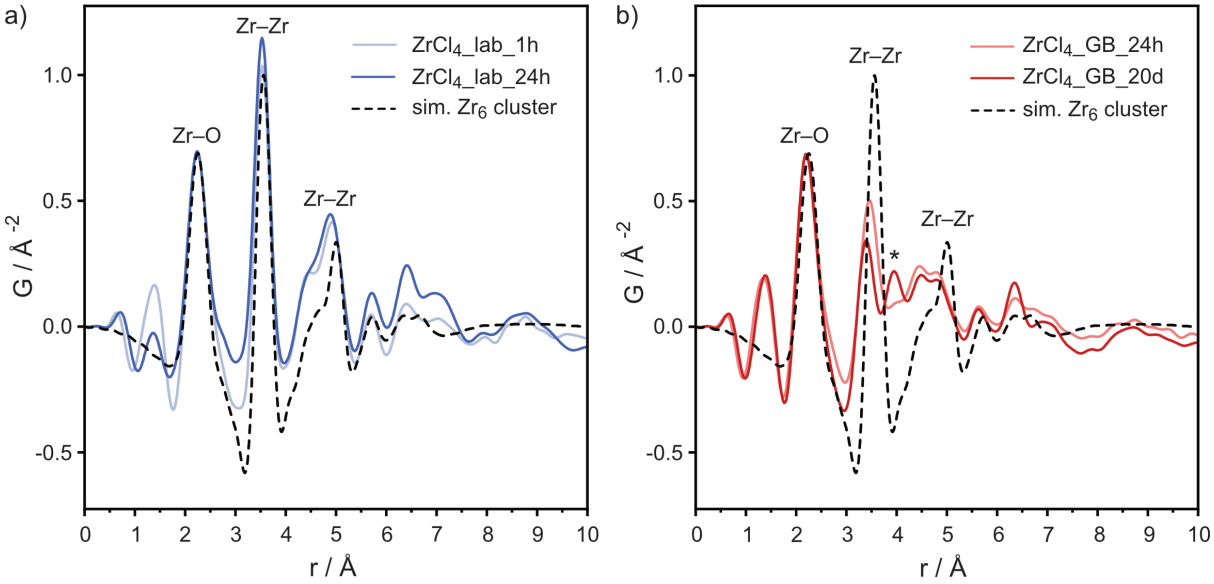

Figure 3.5: a) Experimental PDFs of $ZrCl_4$_lab_1h and $ZrCl_4$_lab_24h after 1 h and 24 h reaction, respectively, compared to the simulated (sim.) PDFs of a Zr_6O_8 cluster. b) Experimental PDFs of $ZrCl_4$_GB_24h and $ZrCl_4$_GB_20d after 24 h and 20 d reaction, respectively, compared to the simulated PDFs of a Zr_6O_8 cluster. Compared to $ZrCl_4$_GB_24h, the PDF of $ZrCl_4$_GB_20d features a peak at 3.95 Å (*) which likely corresponds to next-nearest neighbor Zr–Zr distances between two Zr_2O_2 units.

In contrast, the PDFs of $ZrCl_4$_GB_24h and of $ZrCl_4$_GB_20d do not match the simulated PDF of a Zr_6O_8 cluster. The relative intensities of the 1st Zr-O pair at 2.38 Å and Zr–Zr pair at 3.47 Å are mismatched, and the 2nd Zr–Zr peak is not visible. The PDF of $ZrCl_4$_GB_20d further shows a peak at 3.95 Å, which cannot be assigned to any atomic distance in the octahedral Zr_6O_8 cluster. These features suggest that Zr_6O_8 clusters are not formed during synthesis with $ZrCl_4$_GB, even after 20 d.

The differences in cluster formation as a function of water content are expected. Several studies highlight the key role of water content in metal-oxide cluster formation. Ragon *et al.* showed that in the absence of water, reaction of $ZrCl_4$ and 1,4-benzenedicarboxylate (BDC) in DMF formed an

amorphous product instead of UiO-66.[167] They argued that water is needed to form the secondary building unit (SBU) $Zr_6(\mu_3\text{-}O)_4(\mu_3\text{-}OH)_4(CO_2)_{12}$, and hence UiO-66.[167] Another study by Butova *et al.* showed that in the absence of water, the MOF polymorph MIL-140A built of Zr_2O_2 chains forms instead of UiO-66.[96] Leubner *et al.* further reported that MIL-140A forms from dense, layered $Zr_2O_2(OAc)_2(BDC)$ (OAc = acetate) intermediates that further transform into porous MIL-140.[244] This last example may suggest an analogous pathway for the dPCN-224 formation reported here where an intermediate formed before nucleation of dPCN-224 particles.

Inspired by this, we compared the experimental PDFs of $ZrCl_4$_GB_24h and $ZrCl_4$_GB_20d—which did not form $Zr_6O_4(OH)_4$ clusters—to simulated PDFs of a variety of Zr-oxo species including $[Zr_2O_2]_x$ chains of different lengths (x = 2, 3, or, 6), derived from a $Zr_2O_2(OAc)_2(BDC)$ precursor (Appx. B, Section B.2.10).[244] Interestingly, the $[Zr_2O_2]_x$ chain models include the peak at 3.95 Å, which corresponds to next-nearest neighbor Zr–Zr distances between two Zr_2O_2 units (Figure 3.6a-b).

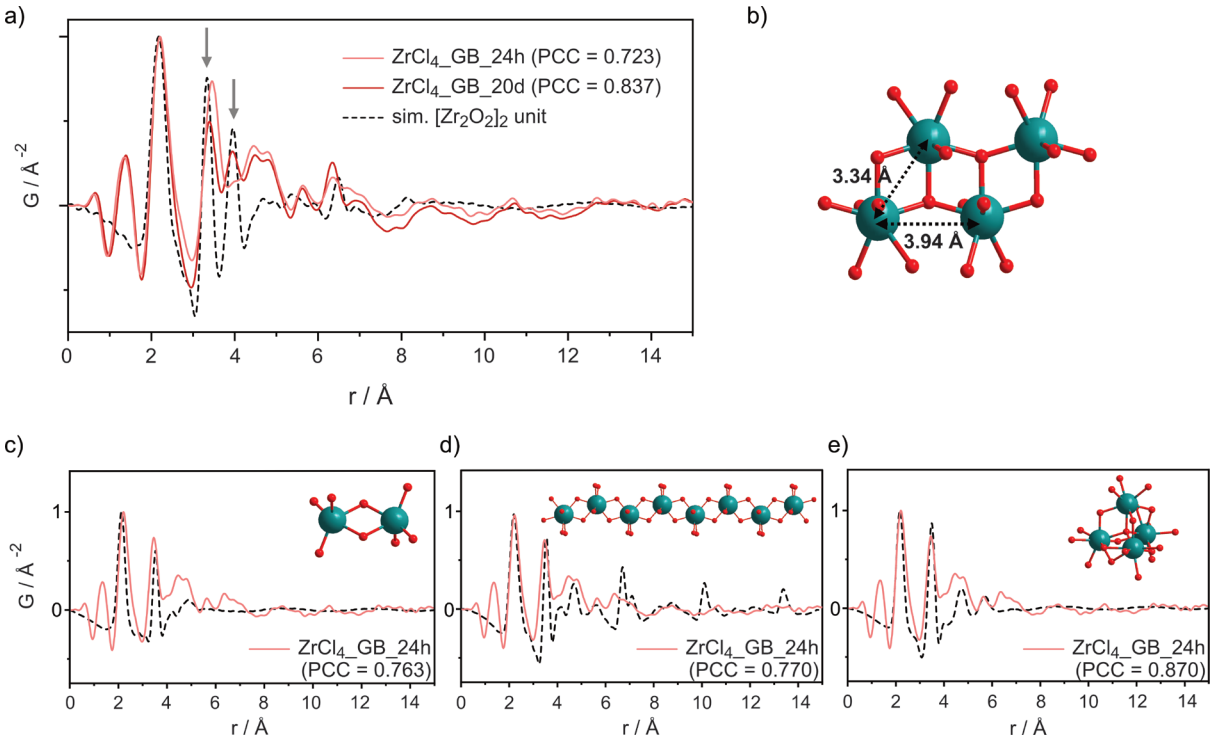

Figure 3.6: a) Experimental PDFs of $ZrCl_4$_GB_24h and $ZrCl_4$_GB_20d compared to the simulated (sim.) PDF of a $[Zr_2O_2]_2$ unit. b) $[Zr_2O_2]_2$ unit with nearest and next-nearest Zr–Zr distances of 3.34 and 3.94 Å, respectively. c–e) Experimental PDFs of $ZrCl_4$_GB_24h compared to sim. PDFs of a Zr_2O_2 dimer, a $[ZrO_2]_3$ chain, and a Zr_4O_7 tetramer, respectively, which are shown in insets. The PCC value corresponds to Pearson correlation coefficient. All PDF curves have been renormalized for visual comparison such that the height of the Zr-O peak equals 1.

When comparing the PDF of $ZrCl_4$_GB_20d to the theoretical PDFs of $[Zr_2O_2]_2$ building units and Zr_6O_8 clusters, the Pearson correlation coefficient (PCC), which measures the linear correlation between experimental and theoretical PDFs, increased from 0.587 to 0.837 (see Appx. B, Figure B.25). Thus, the inorganic nodes in $ZrCl_4$_GB_20d show similarity to short segments of $[Zr_2O_2]_x$ chains.

The experimental PDF of $ZrCl_4$_GB_24h agrees less well with the simulated PDF of the $[Zr_2O_2]_2$ model (PCC = 0.723) (Figure 3.6a). In fact, when comparing the PDF of $ZrCl_4$_GB_24h to the PDF of $ZrCl_4$_GB_20d, the next-nearest neighbor Zr–Zr distance increases from 3.38 Å to 3.45 Å and the intensity of the peak at 3.95 Å decreases, which may indicate either a different arrangement of Zr atoms in the inorganic nodes or a different distribution of cluster types. For instance, the PDF of $ZrCl_4$_GB_24h showed the best agreements for Zr_2O_2 dimers, Zr-oxo chains, or Zr_4O_7 tetramers (Figure 3.6c–e).

As discussed above, synthesis from both $ZrCl_4$_lab and $ZrCl_4$_GB yielded metal–organic compounds (Phase II) with a periodicity of 19 Å, which suggests alternating Zr nodes and TCPP linkers. PDF analysis provided further information on the ordering of products (Figure 3.7). The intermediate-range atomic density distributions from 10–50 Å revealed periodic oscillations for all four samples. The PDF of $ZrCl_4$_lab_24h showed broad features at long distances due to the periodic arrangement of tilted $Zr_6O_4(OH)_4$ clusters in dPCN-224 and some sharp peaks (e.g., 24–30 Å) due to preferred intercluster Zr–Zr pair distances. As suggested by the few Bragg reflections in reciprocal space, $ZrCl_4$_lab_1h also showed broad, high-*r* features, albeit at relatively lower intensity compared to those of $ZrCl_4$_lab_24h. It also showed sharp peaks at the intercluster distances (15–30 Å), suggesting that metal-organic oligomers with intermediate-range order between the nearest and next-nearest neighboring $Zr_6O_4(OH)_4$ clusters formed after 1 h.

The products obtained from $ZrCl_4$_GB at 24 h and 20 d also both showed broad, high-*r* peaks, but without sharp peaks at the intercluster distances, indicating a different, and possibly more disordered arrangement of Zr nodes along the ordered directions.

The 50–100 Å range gave further insights into the mid-range order (Figure 3.7). In the PDFs of $ZrCl_4$_lab_1h and $ZrCl_4$_GB_24, the oscillations above 50 Å were weak, indicating a lower distance of coherent ordering, whereas the dPCN-224 sample ($ZrCl_4$_lab_24h) retained oscillation and sharp peaks due to a higher degree of long-range order. $ZrCl_4$_GB_20d featured stronger oscillation in the high-*r* atomic density distribution relative to the product obtained after a 24 h reaction. Increasing the reaction time therefore yielded a product with longer-range order.

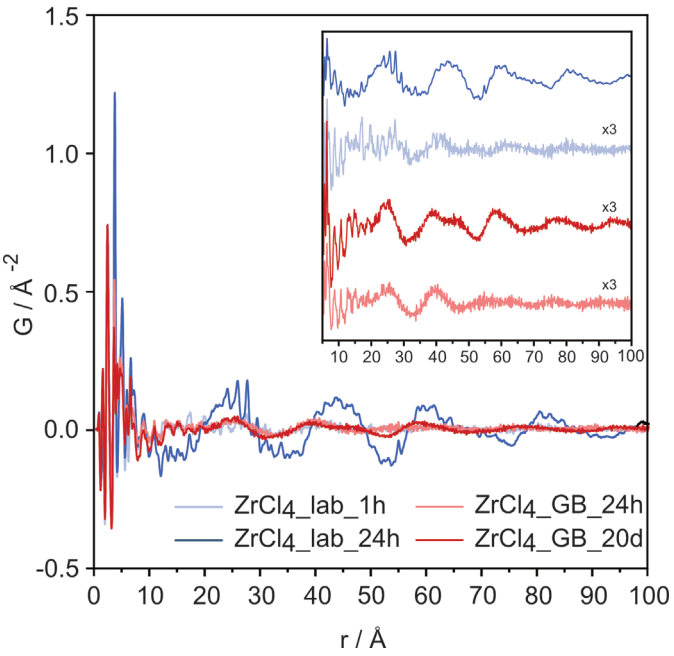

Figure 3.7: Experimental PDFs of $ZrCl_4$_lab_1h, $ZrCl_4$_lab_24h, $ZrCl_4$_GB_24h and $ZrCl_4$_GB_20d PDF in the long range. Inset shows enlarged views (scaled x3) of the oscillation in the long range.

To summarize, the use of $ZrCl_4$_lab led to fast formation of Zr_6O_8 clusters, whereas reaction from $ZrCl_4$_GB produced different clusters, even at extended reaction times. The Zr-oxo nodes formed after 24 h reaction with ZrCl4_GB could not be unambiguously identified, but showed highest similarity to PDFs simulated for Zr_2O_2 dimers, ZrO chains, or Zr_4O_7 tetramers, whereas the product formed after 20 d may contain $[Zr_2O_2]_2$-like units. All compounds featured periodic arrangement of altering Zr nodes and TCPP molecules in the intermediate range, and the ordering increased with increasing reaction times.

3.3.4 Control experiment using zirconyl chloride as a zirconium source

To further test the effects of precursor type and water content, we used $ZrOCl_2 \cdot 8H_2O$ as the Zr source, which is also widely used for the synthesis of porphyrin-based Zr-based MOFs, and conducted the same time-dependent study. The same one-step procedure was performed as before in which $ZrOCl_2 \cdot 8H_2O$, TCPP, and benzoic acid were reacted in DMF at 120 °C for 15 min, 30 min, 60 min, 90 min, 4 h, and 24 h (see Appx. B, Section B.1.3 for further details).

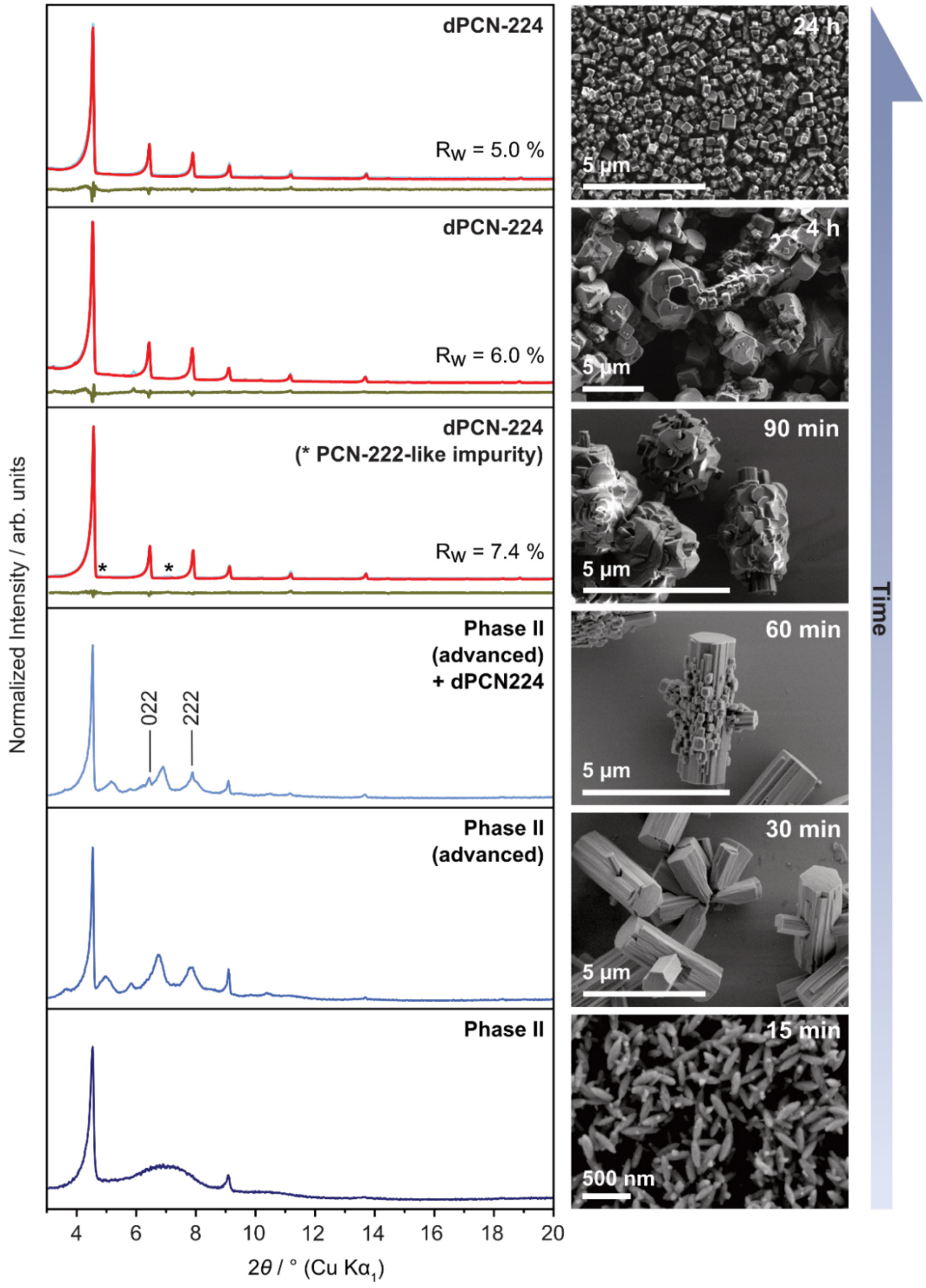

Figure 3.8: PXRD patterns from the products obtained during synthesis from $ZrOCl_2 \cdot 8H_2O$ after 15 min, 30 min, and 60 min reaction time. Rietveld refinements and residual value *Rw* of dPCN-224 are shown against observed patterns from the products obtained during synthesis from $ZrOCl_2 \cdot 8H_2O$ after 90 min, 4 h, and 24 h reaction time (left). After 60 min, dPCN-224 started to form as indicated by the peaks at 6.4 and 7.9° 2θ, which correspond to the 022 and 222 indices of the dPCN-224 phase. After 90 min, the product mostly consists of dPCN-224 but contains small impurities of a PCN-222-like product, highlighted with an asterisk (*), that could not be modelled (Appx B, Figure B.7). The SEM images show a transformation of the particles' morphology with increasing reaction time (right). Further SEM images are shown in Appx. B, Figure B.9.

The PXRD patterns revealed a similar formation pathway of dPCN-224 as for $ZrCl_4$_lab. The patterns collected after 15 min to 24 h of reaction time showed a transformation from the one-dimensionally (1D) ordered, metal–organic intermediate to crystalline dPCN-224 (Figure 3.8). After 30 min, new broad peaks appeared between 3.50 and 10.60° 2θ, suggesting an onset of three-dimensional (3D) ordering of the metal–organic intermediate. The PXRD pattern of the product isolated after 1 h showed that dPCN-224 started to form from the intermediate. Longer reaction times yielded dPCN-224 as product. Interestingly, only minor PCN-222 or NU-902 impurities were formed when using $ZrOCl_2 \cdot 8H_2O$ (Figure 3.8 and Appx. B, Figure B.7), unlike the synthesis from $ZrCl_4$.

The morphology of the particles was verified by SEM (Figure 3.8). Rice-shaped particles of *ca.* 250 nm were formed after 15 min, which transformed into 3–5 µm long rods after 30 min. After 1 h, cubic nanoparticles formed on the surface of the rods. As the reaction progressed, the small cubes grew into 3–4 µm wide intergrown particles and the rods disappeared (Appx. B, Figure B.9). After 24 h, only cubic nanoparticles (200–500 nm) were observed.

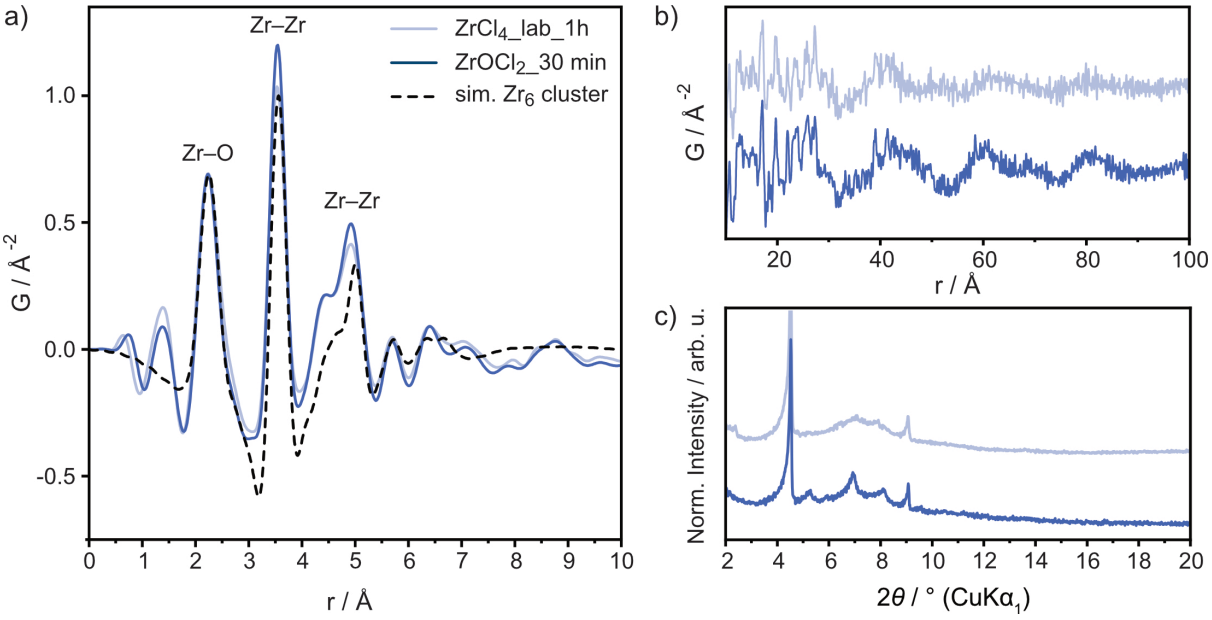

Figure 3.9: a) Experimental PDFs of products obtained from $ZrOCl_2 \cdot 8H_2O$ after 30 min reaction ($ZrOCl_2$_30min), compared to the PDF of $ZrCl_4$_lab_1h and to the simulated PDF (sim.) of a Zr_6O_8 cluster. b) Experimental PDFs of $ZrOCl_2$_30min and $ZrCl_4$_lab_1h showing oscillation in the long range. c) Comparison of the PXRD patterns of $ZrOCl_2$_30min and $ZrCl_4$_lab_1h.

PDF analysis revealed that the intermediate formed after 30 min during synthesis with $ZrOCl_2 \cdot 8H_2O$ resembles the intermediate formed from $ZrCl_4$_lab after 1 h (Figure 3.9a). Again, the product features the characteristic peaks at 2.24, 3.53 and 4.92 Å, which correspond to the Zr–O,

adjacent Zr–Zr, and diagonal Zr–Zr distances of a Zr_6O_8 cluster. Similar to $ZrCl_4$_lab_1h, the product shows periodic oscillation between 20–100 Å, indicating a periodic arrangement of alternating Zr_6O_8 cluster and TCPP linkers. Compared to $ZrCl_4$_lab_1h, the peaks around 25 and 45 Å are sharper and the oscillation remains strong above 50 Å, which indicates a more ordered structure (Figure 3.9b). This is in agreement with the PXRD analysis, which showed additional peaks and more ordering in the intermediate formed from $ZrOCl_2$·8H2O (Figure 3.9c).

3.3.5 Proposed mechanism of dPCN-224 growth

From this study, it is clear that the Zr source influences the product formation. While synthesis from neat $ZrCl_4$_GB did not form Zr_6O_8 clusters or dPCN-224, synthesis from $ZrCl_4$_lab that had aged under ambient conditions for several months yielded crystalline dPCN-224. Use of $ZrOCl_2 \cdot 8H_2O$ as the Zr source, which is also widely used for the synthesis of porphyrin-based Zr-based MOFs, also yielded dPCN-224 (Figure 3.10). In both cases, however, dPCN-224 does not follow the classical nucleation path. Instead, disordered intermediates are first formed, consisting of 1D-ordered motifs of alternating linker and node, which are present as highly anisotropic, aggregated rods. Then, nucleation of cubic MOF structures takes place on the surface of the intermediate particles and eventually *consumes* them, resulting in the final dPCN-224 product.

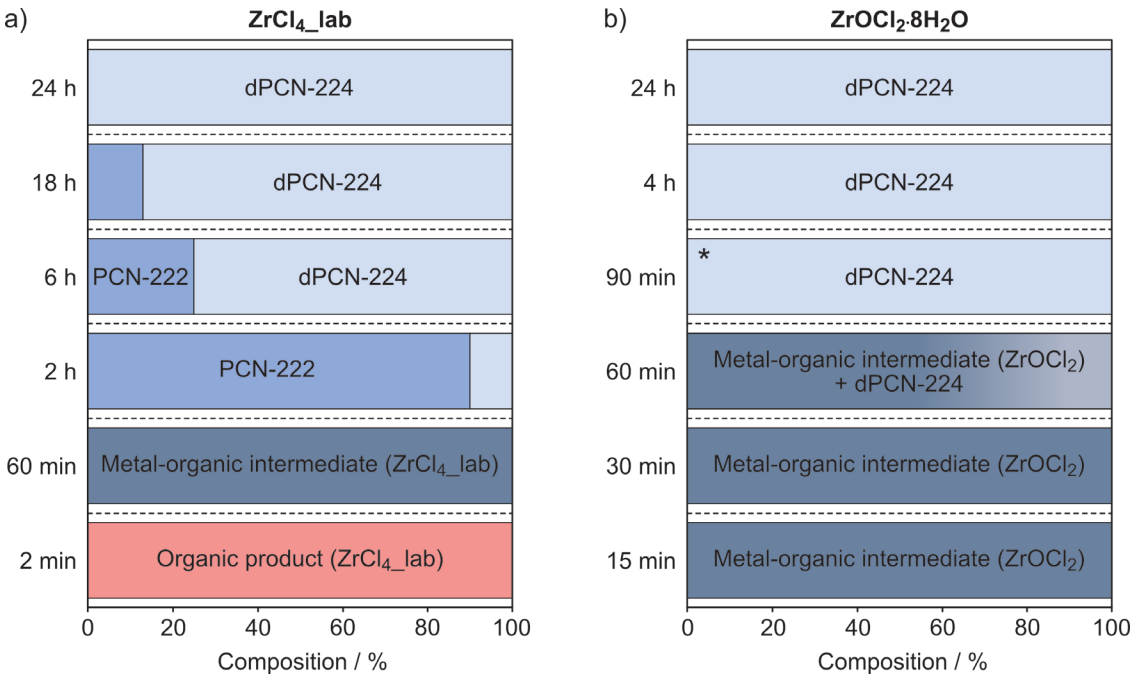

Figure 3.10: Phase compositions of products isolated after different reaction times during synthesis of dPCN-224 from a) $ZrCl_4$_lab and b) $ZrOCl_2 \cdot 8H_2O$. *Synthesis from $ZrOCl_2 \cdot 8H_2O$ after 90 min reaction contained PCN-222/NU-902-like impurities.

The observed steps in the synthesis of dPCN-224 from $ZrCl_4$_lab and $ZrOCl_2 \cdot 8H_2O$ allow us to propose the following nucleation and growth mechanism for the formation of dPCN-224 under the tested reaction conditions. Initially, a purely organic TCPP-based product forms (step 1). Following this, metal–organic intermediates consisting of Zr_6O_8 cluster and TCPP molecules form (step 2), which grow into microrods (step 3). The crystallites show 1D periodicity with a repeating unit of 19 Å, suggesting that motifs with an altering arrangement of Zr_6O_8 clusters and TCPP molecules are ordered within the rods (Appx. B, Figure B.26). As shown from PDF analysis, the rods feature ordering in the intermediate range between the nearest and next-nearest neighboring Zr_6O_8 clusters. To speculate, the rod-shaped intermediates consist of a large number of small Zr_6O_8–TCPP chain-like domains, which are bridged by TCPP molecules. Once the metal-organic rod intermediate is formed, dPCN-224 starts nucleating on the surface of the rods, suggesting that the metal-organic intermediate possibly acts as template and source of Zr-oxo clusters and TCPP linkers (step 4). With increasing reaction times, the dPCN-224 cubes increase in size whilst the intermediate dissolves (step 5). Once the intermediates have been completely dissolved, the dPCN-224 crystallites progress to a more monodisperse distribution of smaller dPCN-224 single crystals (step 6). Step 6 shares similarities to digestive ripening (or reversed Ostwald ripening) *via* surface etching of capping agents where smaller particles form at the expense of larger particles, and further investigation of this process will be the focus of future work.[245-247]

It is worth highlighting that PCN-222 forms as intermediates during synthesis of dPCN-224. This is in contrast to other studies on the synthesis of porphyrinic Zr MOFs in which hexagonal PCN-222 was the thermodynamic product compared to cubic porphyrinic MOFs.[63,159,187] Judging from the SEM images during synthesis from $ZrCl_4$, it appears that PCN-222 forms from the same metal–organic intermediate, suggesting a similar formation path for these two MOF phases under the tested conditions. Compared to synthesis from $ZrCl_4$, only minor impurities of a PCN-222-like intermediate are observed when $ZrOCl_2 \cdot 8H_2O$ acts as the Zr source. This could be explained by higher amounts of water in the reaction from the coordinated water in $ZrOCl_2 \cdot 8H_2O$ through which the PCN-222 intermediate vanishes and dPCN-224 forms more quickly.

3.3.6 Influence of water on the dPCN-224 formation

The addition of water to the synthesis of Zr-based MOFs is known to accelerate the formation of the framework. For example, during synthesis of UiO-66, water increases the formation rate of the $Zr_6O_4(OH)_4$ cluster which in turn allows for faster synthesis of the framework.[167] A similar trend

was observed for the formation of dPCN-224 when increasing the amount of water in the reaction (Figure 3.11).

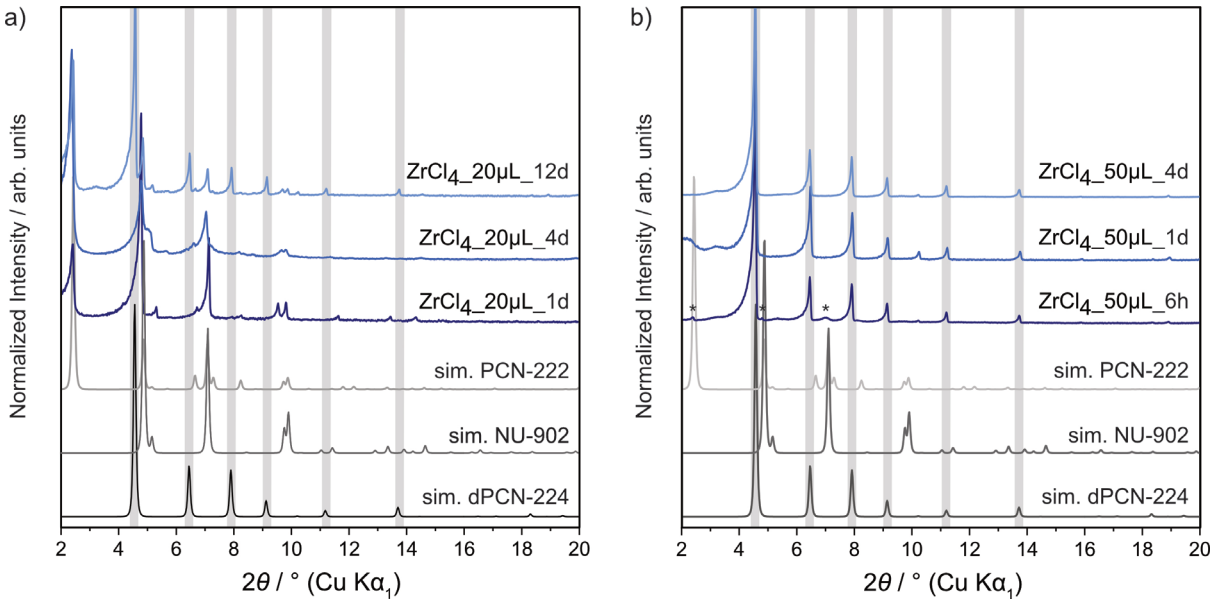

Figure 3.11: PXRD patterns of the products obtained from $ZrCl_4$_GB under addition of a) 20 µL water after 1d, 4d, and 12d reaction time and b) 50 µL water after 6 h, 1 d and 4 d reaction time. Peaks corresponding to dPCN-224 are highlighted with grey bars and the asterisks (*) indicates residual PCN-222- or NU-902-like impurities.[77,85]

PXRD analysis revealed that reaction from $ZrCl_4$_GB with 20 µL water yielded mixtures of PCN-222 and NU-902 between 24 h and 4 d. After 12 d, however, a mixture of cubic dPCN-224 and hexagonal PCN-222 was obtained showing that at longer reaction times dPCN-224 eventually forms. In contrast, synthesis with 50 µL water in the reaction proceeded at a faster rate. After 6 h, the product mostly consisted of dPCN-224 with minor PCN-222/NU-902 like impurities and after 24 h and 4 d reaction time, phase pure dPCN-224 was obtained. The increase of water in the reaction therefore considerably accelerated the growth of dPCN-224 and reduces the amount of the PCN-222-like intermediate formed during the reaction.

These findings exemplify the importance of water in the synthesis of dPCN-224. $ZrCl_4$ is hygroscopic and readily absorbs water. The aging time of $ZrCl_4$ in ambient conditions thus greatly affected the product formation in a 24 h reaction. In our study, neat $ZrCl_4$ that was left to stand for one day ($ZrCl_4$_1d) yielded a mixture of PCN-222 and NU-902 as the products, whereas when left to age for three days (ZrCl4_3d), it yielded phase-pure dPCN-224. However, the daily temperature and relative humidity fluctuations impact the hydrolysis rate of $ZrCl_4$. For instance, in some cases $ZrCl_4$_3d yielded mixtures of dPCN-224 and hexagonal PCN-222 instead of dPCN-24 after 24 h, suggesting that the formation of dPCN-224 was slower, presumably due to less water in the reaction

(Appx. B, Figure B.8a). Another point to consider is that DMF is also hygroscopic and will also have varying quantities of water contamination. Reaction from $ZrCl_4$_GB in DMF from a freshly opened bottle and from the same bottle after keeping it in the laboratory for a month yielded different products which further exemplifies the importance of controlling the water content during synthesis (Appx. B, Figure B.8b). As a matter of fact, the formation of $Zr_6O_4(OH)_4$ clusters, and hence, of dPCN-224 requires hydrolysis of the Zr precursor. Hence, the hygroscopic nature of both $ZrCl_4$ and DMF affects the growth of dPCN-224 and is a primary source for reproducibility issues across reactions and laboratories. The choice of reactants and solvent, but also the relative humidity and temperature all determine the amount of water in the reaction and therefore need to be monitored with caution when synthesizing porphyrinic Zr-based MOFs. While many of these factors are difficult to control, the use of $ZrOCl_2 \cdot 8H_2O$—which already contains coordinated water and is therefore less sensitive to atmospheric moisture—as opposed to $ZrCl_4$ can reduce reproducibility issues often encountered during synthesis of porphyrinic Zr-based MOFs.[167,248]

3.4 Conclusion

The study on dPCN-224 formation from both $ZrCl_4$ and $ZrOCl_2 \cdot 8H_2O$ shows that its formation follows a complex pathway *via* at least one intermediate, composed of Zr_6O_8 clusters and TCPP molecules that form anisotropic particles with apparently 1D-ordered chain-like motifs. The intermediate then grows into larger rods, on the surface of which dPCN-224 starts nucleating. As the reaction progresses, dPCN-224 particles then grow into single crystals, whilst the intermediate dissolves. Interestingly, hexagonal PCN-222 particles were intermittently obtained as a side product, indicating that the formation of PCN-222 may occur *via* the same metal–organic intermediate. Further investigation of this process will be the focus of future work.

In addition, we demonstrate that the Zr source can substantially change the reaction pathway during dPCN-224 formation. Reaction from neat $ZrCl_4$ did not form $Zr_6O_4(OH)_4$ clusters; hence no dPCN-224 was formed. In fact, water is necessary for the formation of $Zr_6O_4(OH)_4$ clusters and should be considered a reactant during synthesis of dPCN-224. Consequently, the aging time of $ZrCl_4$, and by extension the amount of water present, influences the composition of the obtained product where $Zr_6O_4(OH)_4$ clusters, and ultimately dPCN-224, form faster with increasing water content in the reaction. Whilst hydrolysis of the Zr precursor is key to the formation of a crystalline product, analysis and discussion of the water content during synthesis remains sparse in literature despite its impact on the type of cluster formed, the reaction pathway, and resultant framework. The lack of understanding in this regard is expected to greatly contributes to reproducibility issues

in literature. In light of this, the work in this chapter emphasizes the importance of monitoring the presence of water in both the reactants and environment during MOF crystallization and serves as a general guide to optimize synthetic protocols towards phase-pure porphyrinic MOFs, and more generally, Zr-based MOFs.

3.5 Acknowledgements

The authors gratefully acknowledge the help of Viola Duppel (MPI for Solid State Research) for the SEM images and Stefano Canossa for electron diffraction analysis. The authors further thank Marie-Luise Schreiber for elemental analysis, Stefan Clewing for helping with experiments, Lars Grunenberg for NMR analysis, Fabian Heck for sorption analysis, and Hanna Boström for help with TGA analysis and helpful discussion. Financial support was granted by the Max Planck Society, the University of Munich (LMU), the Center for NanoScience (CeNS), the Deutsche Forschungsgemeinschaft (DFG) through the priority program "Coornets" SPP 1928 (proj. nos. SE 1417/8-1 and LO 1801/4-1), the Cluster of Excellence "*e*-conversion". M.W.T. gratefully acknowledges support from BASF. We acknowledge DESY (Hamburg, Germany), a member of the Helmholtz Association HGF, for the provision of experimental facilities. Parts of this research were carried out at beamline P02.1.

3.6 Authors contributions

C.K. and B.V.L. conceived the project. C.K. designed and carried out sample synthesis and analysis. M.W.T. performed PXRD, PDF measurements and analysis, and structural modeling and refinements. M.E. and R.D. contributed useful discussion on measurements and modeling. C.K. and M.W.T contributed to overall interpretation and C.K. wrote the manuscript.

CHAPTER 4

STRUCTURAL VERSATILITY IN Zr-MTBC-BASED MOFs

As discussed in the previous chapters, the versatile coordination geometry of Zr-oxo clusters in Zr-based MOFs often allows for multiple topologies built from the same inorganic and organic building units. Reticular design of Zr-based MOFs and the prediction of framework topologies can therefore be challenging, particularly when taking into account their high tolerance towards vacancies and structural disorder. This chapter explores structural disorder observed in Zr-based MOFs built from methane-tetrakis(*p*-biphenylcarboxylate) (MTBC) linkers. Compared to rigid TCPP linkers, the tetrahedral geometry of MTBC is less rigid which increases the number of achievable Zr-based MOF topologies. Two new, highly disordered structure models are presented which feature 12-fold cluster coordination despite the poor compatibility of the building blocks for such connectivity. This chapter introduces a new perspective on disorder and structural flexibility in MOFs to help understand the formation of geometrically "forbidden" frameworks. In addition, the Hf-based analogues of both structures were investigated revealing that the disorder observed in MTBC-based MOFs is not specific to the chemical composition of the cluster.

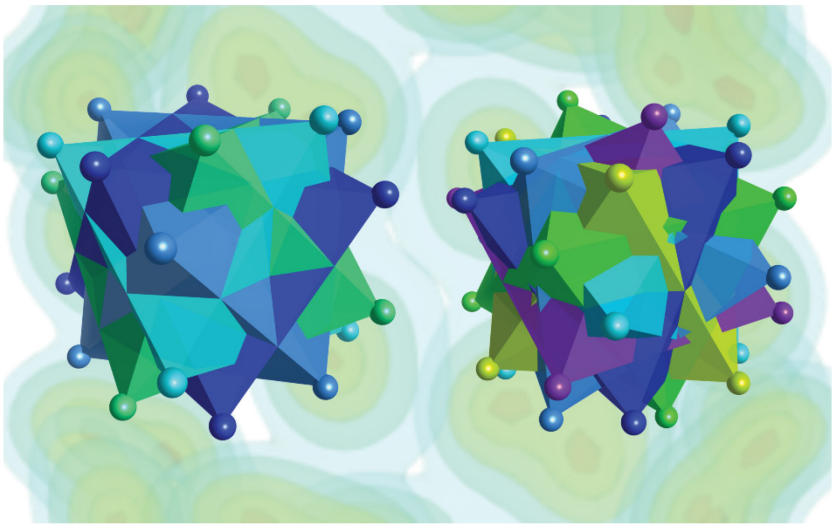

Cover image of Chapter 4: $Zr_6O_4(OH)_4$ cluster disorder in c-(4,12)MTBC-Zr_6 in four or six orientations, depending on the employed reaction conditions.

Unlocking new Topologies in Zr-based Metal–Organic Frameworks *via* Building Block Disorder

Charlotte Koschnick, Maxwell W. Terban, Ruggero Frison, Martin Etter, Felix A. Böhm, Davide M. Proserpio, Simon Krause, Robert E. Dinnebier, Stefano Canossa, Bettina V. Lotsch

Parts of this chapter are published in

Journal of the American Chemical Society **2023**, *145*, 10051–10060.
DOI: 10.1021/jacs.2c13731
https://doi.org/10.1021/jacs.2c13731
Text and figures adapted with permission from ACS

4.1 Abstract

The outstanding diversity of Zr-based frameworks is inherently linked to the variable coordination geometry of Zr-oxo clusters and the conformational flexibility of the linker, both of which allow for different framework topologies based on the same linker-cluster-combination. In addition, intrinsic structural disorder provides a largely unexplored handle to further expand the accessibility of novel metal–organic frameworks (MOFs) structures that can be formed. In this work we report the concomitant synthesis of three topologically different MOFs based on the same $M_6O_4(OH)_4$ clusters (M = Zr or Hf) and methane-tetrakis(*p*-biphenyl-carboxylate) (MTBC) linkers. Two novel structural models are presented based on single crystal diffraction analysis, namely cubic c-(4,12)MTBC-Zr_6/Hf_6 and trigonal t-(4,12)MTBC-Zr_6/Hf_6, which comprise 12-coordinated clusters and 4-coordinated tetrahedral linkers. Notably, the cubic phase features a new architecture based on orientational cluster disorder, which is essential for its formation and has been analysed by a combination of average structure refinements and diffuse scattering analysis from both powder and single crystal X-ray diffraction data. Similarly, the trigonal phase also features structure disorder, although involving both linkers and secondary building units (SBUs). In both phases, remarkable geometrical distortion of the MTBC linkers illustrates how linker flexibility is also essential for their formation and expands the range of achievable topologies in Zr-based MOFs and its analogues.

4.2 Introduction

With more than 2,000 publications today, Zr-based metal–organic frameworks (MOFs) are among the most intensely investigated classes of MOFs for a variety of applications including gas storage and separation, catalysis, and drug delivery.[36,65] When combined with carboxylate-terminated organic linkers, the strong Zr–O bonds impart high chemical and thermal stability to these MOFs.[36,52,158] Hexanuclear $Zr_6O_4(OH)_4$ clusters are by far the most commonly observed in Zr-based MOFs and can accommodate up to 12 linker-connected carboxylate groups, thus reaching charge neutrality.[36,66-67] $Zr_6O_4(OH)_4$ coordination sites not occupied by linker carboxylate groups often host reactive and displaceable OH/H_2O pairs, which are key for post-synthetic modifications to introduce functional groups onto the cluster.[69-70,73] Given their versatile coordination capacity, combined with the possibility of capping some of these sites with hydroxy anions or monocarboxylates, Zr clusters can lead to a wide range of MOF topologies depending on the geometric properties of the selected linkers and synthesis conditions.[36,62-64] Combination of $Zr_6O_4(OH)_4$ clusters with tetrakis(4-carboxyphenyl)porphyrin (TCPP) linkers, for example, leads to five different MOF networks: **she** in PCN-224[91], averaged **ftw** in disordered PCN-224 (dPCN-224)[77], **scu** in NU-902[72], **csq** in PCN-222/MOF-545[85,92], **sqc** in PCN-225[86], and **shp** in PCN-223[94]. In contrast, formation of **ith** and **flu** type networks require tetrahedral linkers such as methanetetrabenzoic acid (MTB) yielding MOF-812 and MOF-841, respectively.[181] The elongated methane-tetrakis(*p*-biphenylcarboxylate) (MTBC) linker yields the isoreticular MOF PCN-251 with the same **flu** network as MOF-841, but with larger cavities.[97]

The topological diversity of Zr-based MOFs is generally limited to combinations of linkers and clusters whose geometries are compatible with the formation of three-dimensional (3D) periodic architectures. In this regard, linker flexibility can be key to expanding the number of topologies by compromising with moderate geometrical frustrations of the MOF; that is, when the ideal geometry of the building blocks does not allow the formation of extended structures. In addition to linker flexibility, orientational disorder of the building blocks can also afford topologies otherwise incompatible due to geometrical frustration by making the geometry of the disordered species less relevant for the framework connectivity. This can occur when during the formation of a framework, some of its inorganic nodes accept linker coordination with a geometry that is not compatible with a unique orientation of the metal cluster, thus resulting in multiple cluster orientations bearing analogous—when not equivalent—energies.[77,94,249-250] It is worthwhile keeping in mind that the structural complexity of such disordered MOFs can complicate the interpretation of crystallographic data and even result in non-intuitive structural features. For example, it was recently shown that cubic Zr_8O_6 clusters appearing via structure refinements from single crystal

X-ray diffraction (SCXRD) of PCN-221 actually resulted from the superimposition of disordered $Zr_6O_4(OH)_4$ clusters.[77]

Analogous octanuclear clusters were also reported in Zr-MTBC[76], a MOF based on 4-connected MTBC linkers and a combination of 12-connected cubic $Zr_8(OH)_4$ and octahedral $Zr_6O_4(OH)_4$ clusters. Here, we show that observation of these cubic clusters is, similar to dPCN-224, a marker for orientational disorder, which allows the formation of this particular framework topology. We thus present a new model to describe the structure, herein abbreviated c-(4,12)MTBC-Zr_6, based on disordered $Zr_6O_4(OH)_4$ clusters, which shares fundamentally the same unit cell metrics and framework topology as Zr-MTBC. We further describe the complex variety of other structures obtained by the combination of octahedral clusters of the type $M_6O_4(OH)_4$ (M = Zr, Hf) and MTBC linkers, which includes an unreported structure with trigonal symmetry, t-(4,12)MTBC-M_6, featuring a complex disordered structure. By these means, we highlight a new approach to investigate, resolve, and structurally define disorder as a new design tool for Zr-and Hf-based MOFs towards unexpected structural motifs. This poorly explored phenomenon and the overlooked degrees of freedom is likely present in many other reported structures. In addition, our results present disorder as an aspect of structural frustration which may lead to novel properties in these frameworks.

4.3 Results and discussion

4.3.1 Crystal structure and cluster disorder in c-(4,12)MTBC-Zr_6

Solvothermal synthesis of c-(4,12)MTBC-Zr_6 was achieved by reacting $ZrCl_4$ and MTBC in diethylformamide (DEF) with benzoic acid (modulator) following a reported procedure (see Appx. C, Section C.1.3 for further details).[76] Under these conditions, cuboctahedral crystals with sizes in the range of 2–5 μm were obtained (Appx. C, Figure C.1). The experimental powder X-ray diffraction (PXRD) pattern of the product agrees well with the simulated pattern of the published Zr-MTBC structure, which was reported with both cubic Zr_8O_6 and octahedral $Zr_6O_4(OH)_4$ clusters (Figure 4.1a).[76] To probe the presence of Zr_8 clusters we analysed the Zr-MTBC crystals with pair distribution function (PDF) analysis, which suggests the presence of $Zr_6O_4(OH)_4$ clusters only (Figure 4.1b). This draws parallels to porphyrinic PCN-221 previously published with Zr_8O_6 clusters, which according to our recent study is better described by the new structure model *d*PCN-224 with disordered $Zr_6O_4(OH)_4$ clusters.[77]

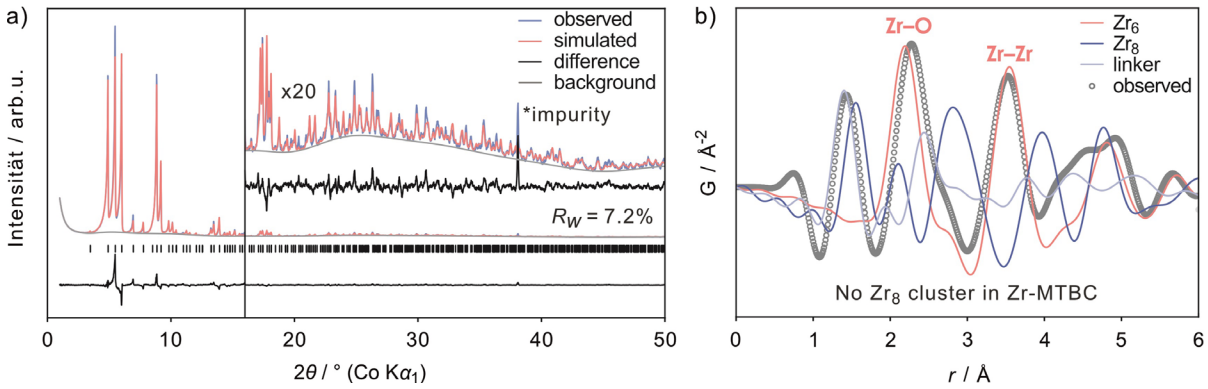

Figure 4.1: a) Rietveld refinement of the experimental c-(4,12)MTBC-Zr_6 PXRD pattern (Co $K\alpha_1$) using the structure model of the published Zr-MTBC structure.[76] b) Experimental PDF of c-(4,12)MTBC-Zr_6 compared to the simulated PDFs of Zr_6 and Zr_8 clusters, and the MTBC linker from the published Zr-MTBC structure.[76]

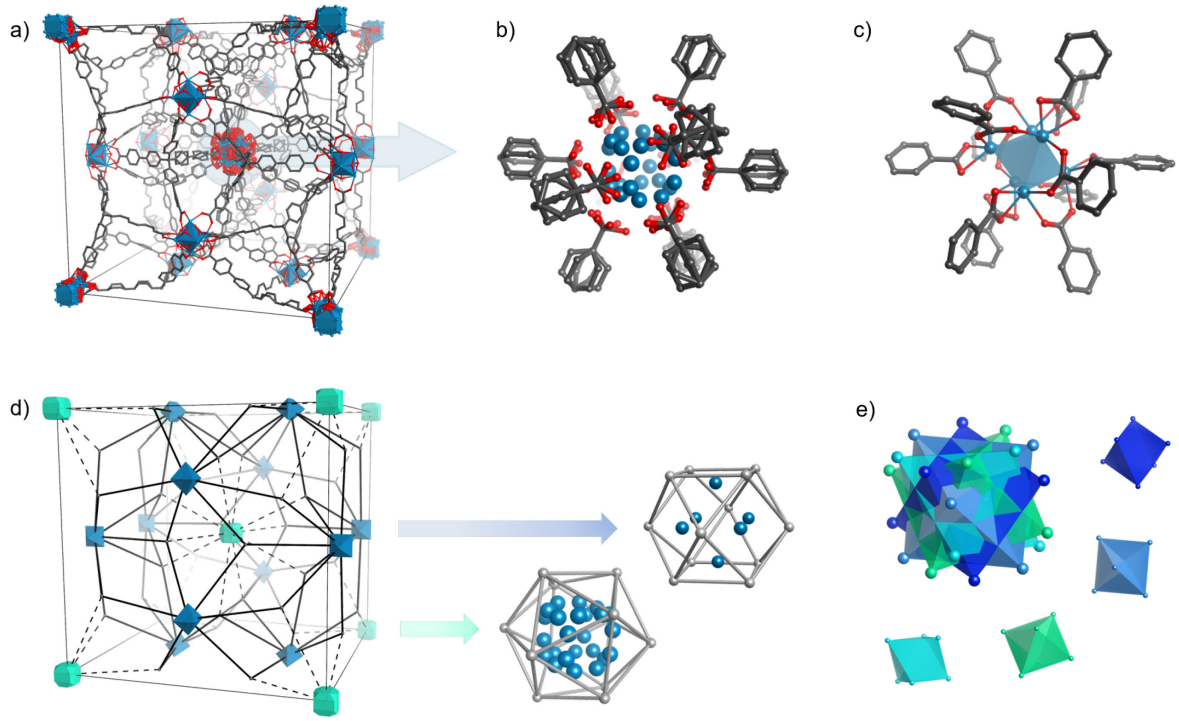

Figure 4.2: Crystal structure of cubic c-(4,12)MTBC-Zr_6. a) The complete unit cell, b) visualization of the disordered cluster sites, and c) coordination environment of one selected cluster (of the four possible) based on the orientational disorder. d) Topological representation highlighting the differences in cluster binding geometry where blue cluster sites have a tetracapped square prismatic coordination environment resulting in a single cluster orientation and teal cluster sites have an icosahedral coordination environment resulting in orientational cluster disorder. e) The disordered cluster sites comprise four $Zr_6O_4(OH)_4$ clusters tilted in four directions.

We next optimized the synthesis for increasing the crystal size. By conducting the reaction without stirring, to favor heterogeneous over homogeneous nucleation (as supersaturation decreases in proximity of nucleation sites when diffusion layers are not eliminated by mixing), we obtained single crystals of up to 200 µm in size with the same cuboctahedral morphology (Appx. C, Figure C.3). Structure refinements using the SCXRD data revealed a cubic framework where two distinct cluster sites are present, both accepting 12 carboxylate groups of 12 linkers exhibiting a moderate distortion from their ideal tetrahedral geometry (100–123°). As far as the secondary building units (SBUs) are concerned, c-(4,12)MTBC-Zr_6 hosts two types of $Zr_6O_4(OH)_4$ 12-connected clusters: one perfectly ordered and one disordered in four alternative positions (Figure 4.2). Sites which accommodate a single, ordered, cluster orientation possess a slightly distorted tetracapped square prismatic coordination environment (similar to the $Zr_6O_4(OH)_4$ environment found in UiO-66). The geometrical distortion for the other site is, however, severe enough to cause multiple degenerate orientations of the cluster (Figure 4.2e). Here, metal-nodes are approached by 12 linker carboxylate groups with a distorted icosahedral geometry, which significantly deviates from the ideal coordination environment of the cluster. Thus, $Zr_6(O)_4(OH)_4$ clusters adopt one of four possible orientations, resulting in a framework with well-defined linker positions, but disordered, 12-fold coordinated $Zr_6O_4(OH)_4$ clusters.

The disorder in c-(4,12)MTBC-Zr_6 leaves characteristic diffuse scattering visible in reciprocal space reconstructions of the SCXRD data. As shown in Figure 4.3, Bragg reflections reach relatively low resolution, while broad cloud-like features become more prominent with increasing distance from the origin. The rather weak diffraction of this MOF was significantly improved by changing the synthetic conditions. By decreasing the concentration of $ZrCl_4$ and MTBC linker in the reaction mixture and increasing the reaction time, the same MOF structure was obtained but with cubic, instead of cuboctahedral, crystal morphology (Appx. C, Figure C.3). Even though the crystal size remained similar (≈200 µm), the cubic-shaped c-(4,12)MTBC-Zr_6 features a significantly higher diffraction limit. At the same time, the orientational disorder of the cluster differs distinctively, as additional electron density maxima can be observed from different electron density maps. These were successfully modelled as additional metal positions consistent with an overall superimposition of six Zr_6 octahedra instead of four, showing that by changing the synthetic conditions not only did the crystallinity can be improved, but the cluster disorder could also be influenced. To the best of our knowledge this is the first time such enhancement of structural disorder has been observed through simple manipulation of the synthetic procedure, thereby establishing a new method to rationally generate structural complexity.

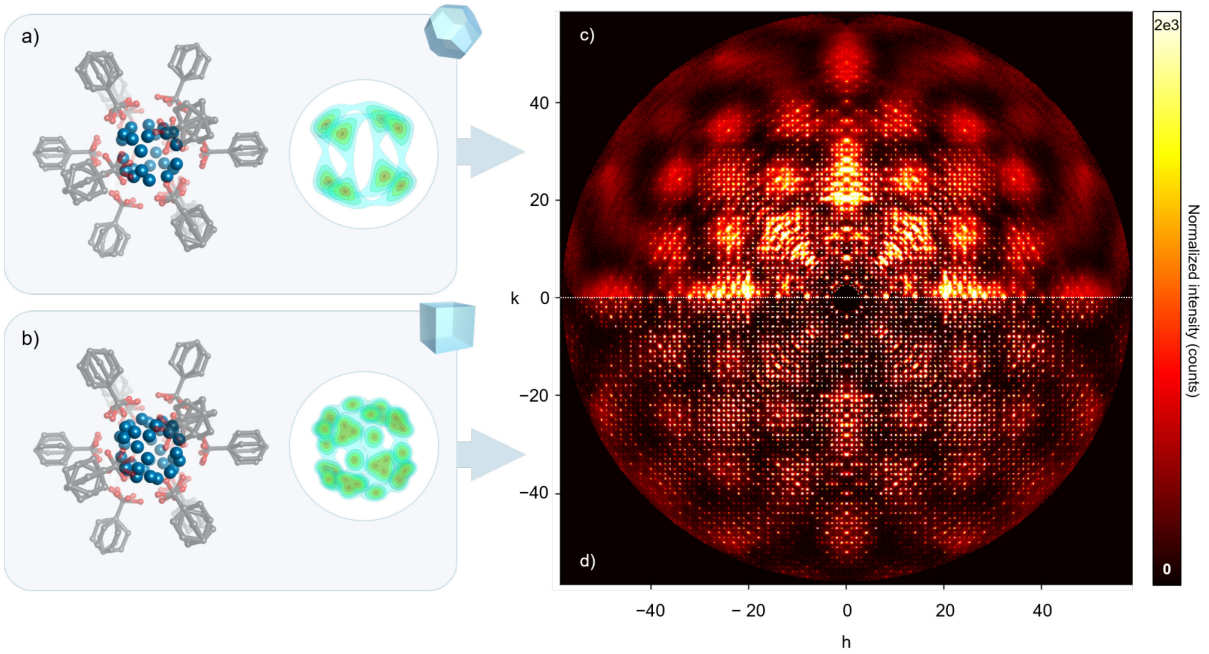

Figure 4.3: The two obtained forms of c-(4,12)MTBC-Zr_6 as a) cuboctahedra and b) cube, are displayed by highlighting the differences in electron density maps and crystallographic model of their disordered cluster sites. These coincide with marked differences in crystallinity as can be seen from c) and d), the reciprocal space reconstruction of the respective *hk*0 planes.

4.3.2 Multiphase behavior of Zr-MTBC: t-(4,12)MTBC-Zr6

The optimized synthesis of c-(4,12)MTBC-Zr_6 single crystals did not yield a phase-pure product (Appx. C, Figure C.8 and Table C.2), but instead resulted in phase mixtures where two additional compounds were found as elongated octahedral crystals and hexagonal platelets. The first was identified by SCXRD as the tetragonal MOF PCN-521,[97] while the latter revealed another yet unreported MTBC-Zr_6 framework with the same (4,12)MTBC-Zr_6 connectivity, but with a trigonal symmetry (space group *P*-3*c*1): t-(4,12)MTBC-Zr_6.

The trigonal structure features a complex combination of mutually exclusive topologies originating from correlated disorder of the building blocks (Figure 4.4). In particular, while some clusters are not disordered and fully occupied (grey in Figure 4.4), one third of the clusters lie in two alternative positions: either above or below the crystallographic sites (0, 0, ¼) and (0, 0, ¾) and shifted from them by 1.027(3) Å. Accordingly, three sets of highly distorted linkers (tetrahedral angle: 89–125°) can be identified depending on whether they are ordered or disordered and linked to the upshifted or downshifted Zr_6 clusters (violet and turquoise, respectively, in Figure 4.4). We dismissed the possibility of wrong symmetry assignment by repeating the data reduction and structure solution using the P1 space group, which showed the same kind of framework disorder. Given the continuous alternation of clusters and linkers along the unique axis *c*, and the general absence of

vacancy defects suggested by our refinements, it can be reasonably assumed that a single column of building blocks along *c* comprise only upshifted or downshifted building blocks, thus making the structure disorder along *c* highly correlated—ideally affording periodicity.

On the other hand, the framework structure is compatible with different columns of building blocks being shifted differently with respect to one another, thereby creating aperiodicity in the *ab* plane of the crystals. This agrees with diffuse scattering features present in reciprocal space reconstructions, which evidence extra reflections and diffuse streaks within the *hk*0 plane, while only sharp intensities are present along the orthogonal direction. Nonetheless, the latter appears to be inconsistent with a well-defined value of *c*-axis, and suggest the presence of an incommensurate structure modulation whose analysis is beyond the scope of this study. Interestingly, the linkers belonging to the framework's upshifted variant bind the ordered clusters with a typical bridging coordination, where each oxygen binds to a different Zr centre. Conversely, the other fraction of disordered linkers—downshifted variant— bind these clusters with a monodentate coordination (Figure 4.4b). While a smaller occupancy could be expected for these last linkers due to their weaker bonding to the clusters, it was not possible to refine their occupancies separately since both parts are crystallographically equivalent. On the other hand, if their occurrence is indeed less energetically favorable, one would expect the formation of frameworks where only the upshifted configuration is present, resulting in an ordered structure. The fact that instead the system selects a disordered structure with monodentate linker coordination suggest that the fully ordered variant might not be a stable product due to geometrical frustration, and that, as in the case of c-(4,12)MTBC-Zr_6, structure disorder might be essential to allow for the formation of this MOF.

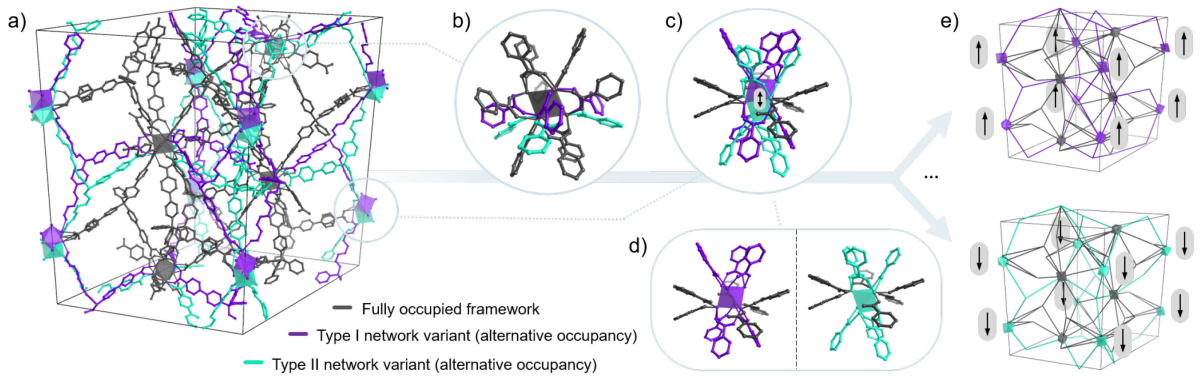

Figure 4.4: Characteristics of the defective t-(4,12)MTBC-Zr_6 structure. a) Complete unit cell where fully occupied clusters and linkers are marked in grey, while alternative framework fractions are shown in violet and turquoise. Coordination environment of b) the ordered and c) the disordered cluster and d) separated environment of the upshifted and downshifted clusters variants. e) Topological representation of two combinations of disordered building blocks (all upshifted or all downshifted) that can be found in the extended framework.

Aiming to obtain a pure t-(4,12)MTBC-Zr_6 product, we tested several conditions including variation of the reaction time, temperature, concentration of reactants, solvent, and water content during synthesis from $ZrCl_4$ (see Appx. C, Section C.1.3 and C.2.4 for further details). Changes in temperature and concentrations of reactants marginally affect the overall phase composition as analyzed by PXRD and mostly yield the previously described c-(4,12)MTBC-Zr_6. Increasing the reaction time shifts the yield more in favor of tetragonal PCN-521 and trigonal t-(4,12)MTBC-Zr_6, and a smaller percentage of the cubic phase is obtained. When employing dimethylacetamide as solvent instead of DEF to disfavor solvent decomposition, cubic c-(4,12)MTBC-Zr_6 was not formed. Here, 24 h reaction times yielded a mixture of the trigonal and tetragonal phase, whereas reaction for 3 d considerably shifted the yield in favor of the tetragonal MOF, suggesting that the trigonal phase might transform into the tetragonal phase under these conditions. Additional details on the synthesis screening and phase compositions can be found in Appx. C, Section C.1.3 and C.2.4. Overall, achieving synthesis of phase pure t-(4,12)MTBC-Zr_6 has not yet been possible. This draws parallels to MTB-based MOF-812, where one third of linker–cluster linkages consist of monodentate η^1-coordination, and that was only obtained as a byproduct along with tetragonal MOF-841.[181]

4.3.3 Extension to Hf-MTBC-based frameworks

The multiphase behavior in Zr-MTBC chemistry is not specific to their chemical composition. Indeed, the Hf-based isostructural compounds of the three discussed Zr-MTBC phases could be obtained by simply changing the metal precursor in the synthesis, thereby yielding cubic c-(4,12)MTBC-Hf_6, trigonal t-(4,12)MTBC-Hf_6, and tetragonal PCN-523 (Appx. C, Figure C.5 and C.6). Similar to c-(4,12)MTBC-Zr_6, PDF analysis of c-(4,12)MTBC-Hf_6 revealed the presence of octahedral $Hf_6O_4(OH)_4$ clusters only, which suggests that reported cubic Hf_8 clusters also result from an incorrect modelling of what in fact is the superimposition of orientational disordered $Hf_6O_4(OH)_4$ clusters (Figure 4.5a). In fact, the electron density map of the Hf cluster sites obtained from SCXRD analysis resembles the electron density map of the Zr cluster sites in cuboctahedral c-(4,12)MTBC-Zr_6 crystals (Figure 4.5b-c). Crystals of c-(4,12)MTBC-Hf_6 obtained as cuboctahedra are thus isostructural to their Zr-based analogues both in their ordered building blocks and in the 4-fold orientational disorder affecting the metal clusters.

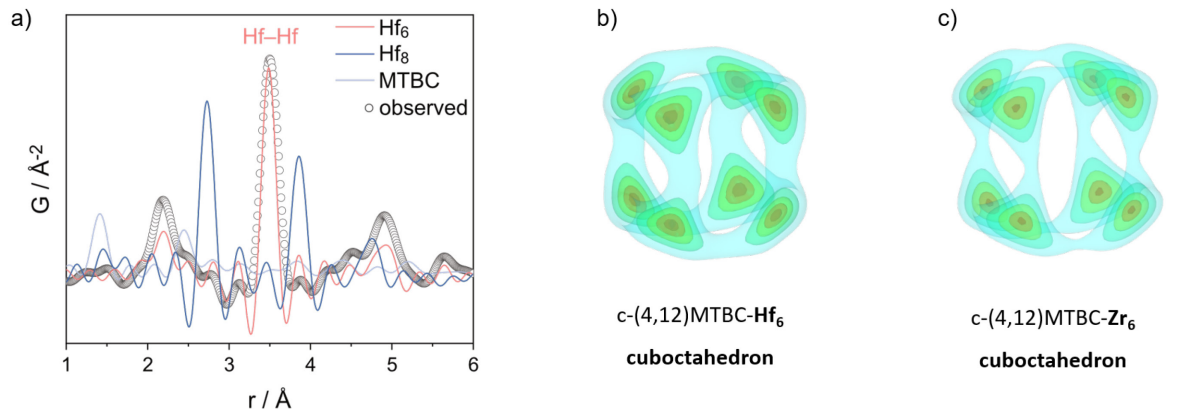

Figure 4.5: a) Experimental PDF of c-(4,12)MTBC-Hf_6 compared to the simulated PDFs of Hf_6 and Hf_8 clusters, and the MTBC linker from the published Hf-MTBC structure.[76] Electron density maps of the disordered cluster sites obtained from single crystal X-ray diffraction analysis of b) c-(4,12)MTBC-Zr_6 and c) c-(4,12)MTBC-Hf_6.

The multiphase behavior encountered in both Zr- and Hf-MTBC likely results from relatively small changes in energy for the molecular and coordination geometries of the building blocks, rather than specifically from their chemical composition. By expanding this concept, analogous structures could be formed not only by adopting metal–oxo clusters with comparable coordination chemistry, but also linkers with different lengths but similar binding capability and geometries, i.e., following an isoreticular approach.[38] Although this might be true in some cases, the importance of the linker's flexibility should not be underestimated as it might be decisive for whether a given linker-metal combination results in the formation of a crystalline framework as well as its tolerance to locally distorted bonding geometries and/or vacancies.[251] The structure of t-(4,12)MTBC-Zr_6 exemplifies this concept. Here, the geometry of the large MTBC linker strongly deviates from an ideal tetrahedron, as the mean angle between the central sp^3 carbon (linker node) and the terminal sp^2 carbons ranges approximately from 88° to 123°. Such rather extreme deviations from the ideal 109.5°, necessary for the framework's architecture, result from a combination of distorted bonding geometry of the sp^3 carbon and bending of the aromatic arms of the linker. This flexibility naturally increases when using larger linkers in synthesizing isoreticular frameworks, thus suggesting that expanding the linkers' size while maintaining their geometry could lead to the occurrence of more diverse phase mixtures, and possibly unknown polymorphic behaviours. This observation also might provide a basis for the formation with linkers which intrinsically feature geometries similar to the distorted structures in these MOFs.

4.4 Conclusion

The family of Zr-based MOFs presents extremely diverse structural possibilities, particularly with respect to synthesizing different frameworks sharing the same molecular building blocks. In this regard, the work herein presents the multiphase behavior of Zr- and Hf-MTBC, where identical synthesis conditions yield a phase mixture comprising up to three different phases, including the two unprecedented structures c-(4,12)MTBC-Zr_6/Hf_6 and t-(4,12)MTBC-Zr_6/Hf_6. Interestingly, in these new frameworks distinct types of disorder are present, which complicate the rationalisation of the MOF synthesis and its optimization towards phase purity. While such disordered states will affect the properties of the material, they can be critical in allowing the formation of such highly connected crystalline structures in the first place. For instance, in the case of c-(4,12)MTBC-Zr_6/Hf_6, specific cluster sites are approached by linker moieties with a geometry that is incompatible with a unique cluster orientation. On the other hand, a periodic configuration of the t-(4,12)MTBC-Zr_6/Hf_6 structure could be in principle hypothesized, but despite the remarkable distortion of the linkers in this framework, no periodic network could be formed. This suggests that the combination of linker flexibility with disorder is key for the formation of a crystalline framework in cases of excessive geometrical frustration.

These considerations lead to three main conclusions. First, the available information is currently insufficient to identify routes to rationally synthesize phase pure Zr- or Hf-MTBC MOFs. Thus, a broader exploration of synthetic variables such as solvent, methodologies, additives, etc. is needed. Secondly, the new structures we reported highlight how building block disorder can be of crucial benefit in MOF chemistry as a solution to the problem of geometrical frustration and a useful source of new, high-connected framework topologies. In the case of t-(4,12)MTBC-Zr/Hf_6 this leads not only to one topology but to virtually infinite variations thereof, depending on how alternative kinds of framework connectivity are distributed in space, which could be in principle controlled upon varying synthetic conditions. Lastly, detailed structural information on framework disorder is still relatively rare. The most current understanding relies on powder diffraction and spectroscopy data, which is often complex to interpret and less sensitive to distinct directions within the material structure. While the importance of acquiring reliable insights into polycrystalline samples is paramount, a more detailed 3D picture of the real structure of MOFs can be extracted from single crystal diffuse scattering data. This practice is currently rare but highly needed, particularly in the context of reticular chemistry and defect engineering. It will allow for better understanding of MOF formation when disorder is not induced to create variants of an ordered MOF, but is intrinsic to the structure and essential for its formation. Further development and establishment of single crystal diffraction techniques for both average and local structure analysis, combined with more extended

synthetic screenings, will be key to effectively chart the vast chemistry and structural landscape of Zr- and Hf-MTBC frameworks as well as many other analogous systems.

4.5 Acknowledgements

The authors gratefully acknowledge the help of Viola Duppel for the SEM images and Lars Grunenberg for help with organic synthesis. The authors further thank Stefan Clewing for experiments and Jürgen Nuss and Tanja Scholz for helpful discussion. Financial support was granted by the Max Planck Society, the University of Munich (LMU), the Center for NanoScience (CeNS), the Cluster of Excellence "*e*-conversion". M.W.T. gratefully acknowledges support from BASF. The authors further acknowledge BESSYII (beamline 14.2, Berlin, Germany), a member of the Helmholtz Zentrum Berlin, and DESY (beamline 14.2, Hamburg, Germany), a member of the Helmholtz Association HGF, for the provision of experimental facilities.

4.6 Authors contributions

C.K., S.C., and B.V.L. conceived the project. C.K. and F.B. designed and carried out sample synthesis and analysis. S.C., S.K., and C.K measured synchrotron SCXRD data. M.W.T. performed PXRD and PDF measurements and analysis. M.W.T. performed structural modeling and refinements. R.F., M.E., D.M.P., and R.D. contributed useful discussion on measurements and modeling. C.K., S.C., M.W.T., and B.V.L contributed to overall interpretation, and C.K. and S.C. wrote the manuscript.

CHAPTER 5

FUTURE DIRECTIONS AND SUMMARY

5.1 Future directions

This section contains novel directions in which to take this body of research along with preliminary data and offers a basis for future studies on particle formation, structure disorder, thin film fabrication, post-synthetic modifications, and characterization of Zr-based MOFs.

5.1.1 Disorder in other porphyrinic MOFs

Chapter 2 proposed a new structure model, dPCN-224, to describe cubic porphyrinic Zr-based MOFs with varying degrees of cluster disorder, linker vacancies, and cluster–linker binding modes. Compared to PCN-224 with ordered linker vacancies arranged in a 3D checkerboard fashion, dPCN-224 features disordered linker vacancies without superstructure reflections in the PXRD pattern which are easily overlooked.[77,91] The structural analysis lays the foundation for further research on disorder and defects in porphyrinic Zr-based MOFs. PCN-223, PCN-222, and NU-902, for example, all have similar structures, but different cluster orientations, cluster connectivities, and linker occupancies (see section 1.2.1).[85,93-94] PCN-223 contains $Zr_6(O)_4(OH)_4$ clusters with 12-fold linker coordination consisting of both the energetically more favorable chelating and energetically less favorable bridging binding motifs. PCN-222 and NU-902 in turn consist of an 8-fold connected $Zr_6(O)_4(OH)_4$ cluster and feature ordered linker vacancies where chelating coordination of the TCPP linker would otherwise be required. In addition, the Zr clusters in PCN-222 are arranged in three orientations, which draws parallels to the PCN-224 structure model with tilted clusters. Future studies should investigate whether a disordered PCN-222 variant with disordered cluster tilting and randomly distributed linker vacancies can form, similar to dPCN-224. Such a disordered variant would not feature superstructure reflections in the PXRD pattern and could be easily misinterpreted as PCN-223. On the other hand, a PCN-223-like product could also form from a 3-fold NU-902 twin structure, as observed for isoreticular NU-904.[252] Such a twin structure would consist of NU-902 domains with three orientations along the *c*-axis, that when averaged would give rise to the **shp** structure of PCN-223 (Figure 5.1).

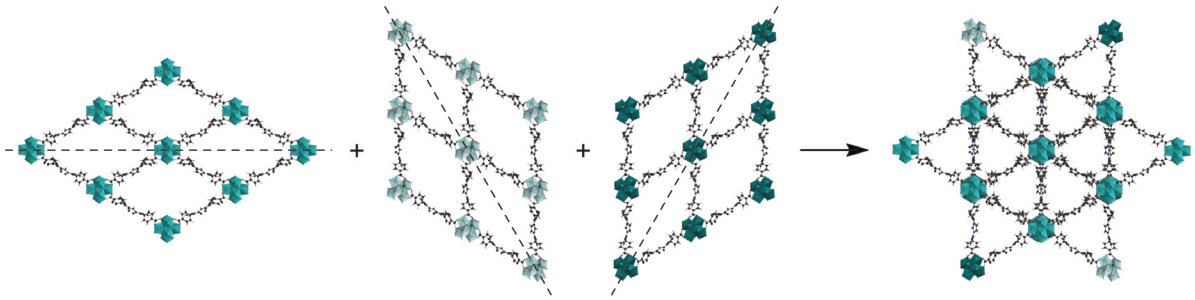

Figure 5.1: Possible 3-fold NU-902 twin structures consisting of NU-902 oriented in three orientations with 60° twisting between each other. The three NU-902 twins are stacked along the *c*-axis giving rise to a PCN-223-like product.

5.1.2 Particle growth of MOFs

Chapter 3 explored the particle growth of dPCN-224. The step-by-step study during reaction of $ZrOCl_2 \cdot 8H_2O$ or $ZrCl_4$ with TCPP and benzoic acid in DMF revealed that dPCN-224 forms *via* an intermediate when heated in an oven at 120 °C. In addition, PCN-222 formed as a side product during the growth of dPCN-224, suggesting that PCN-222 may form from the same metal–organic intermediate under certain reaction conditions. Interestingly, this route is seemingly not the only available formation mechanism for Zr-porphyrin MOFs. Preliminary findings from the growth of PCN-224 during the reaction of $ZrOCl_2 \cdot 8H_2O$, TCPP, and acetic acid in DMF as described in Chapter 2, for example, revealed that PCN-224 nucleated directly from solution under these conditions. Similarly, no intermediate could be isolated during microwave synthesis of dPCN-224 (PCN-224 synthesis protocol from Chapter 2), which suggests that the heating method and stirring strongly affect the formation pathway of the framework (see Appx. D, Section D.2.1). To expand the understanding of the formation of Zr-TCPP-based MOFs, future research should therefore focus on the particle formation and growth under varying reaction conditions, include other phases from the porphyrinic MOF family, and perform *in-situ* formation studies.

In Chapter 4, a highly disordered MTBC-based structure, namely trigonal t-(4,12)MTBC-Zr_6, was formed as a side product, that could not be obtained phase pure when varying the reaction conditions (reaction time, temperature, concentration of reactants, and water content). Remarkably, t-(4,12)MTBC-Zr_6 seemed to transform into tetragonal PCN-521 during synthesis in dimethylacetamide when increasing the reaction time. Future studies should investigate whether the disordered t-(4,12)MTBC-Zr_6 structure forms as an intermediate during growth of tetragonal PCN-521. As shown in Chapter 4, this could be established by a detailed formation study of PCN-521 using SCXRD, PXRD, and PDF analysis.

5.1.3 Probing defects and disorder between MOF products from different synthetic protocols

Chapter 4 revealed that changes to the reaction conditions affected the morphology of the cubic c-(4,12)MTBC-Zr_6 particles (cuboctahedral *vs.* cubic) and simultaneously, the cluster disorder in the formed framework. Interestingly, the synthetic study on cubic porphyrinic MOFs in Chapter 2 also showed that the morphology of dPCN-224 particles varied from cuboctahedral to cubic between different reaction protocols. Future studies should therefore investigate whether the reaction conditions during dPCN-224 synthesis cause structural changes in the MOF, in addition to varying formation pathways and particle morphologies.

High-quality SCXRD data can probe diffuse scattering, and with this disorder and defects in MOF structures. However, the growth of MOF single crystals usually requires variations of the reaction conditions which often affect the MOF structure. Examining structural disorder and defects of MOF particles obtained from reactions that do not yield single crystals therefore requires further characterization techniques including PDF analysis, cryo-TEM imaging, and ssNMR spectroscopy. In addition to this, the photoluminescence (PL) lifetime may be an efficient technique to probe porphyrinic MOFs. For instance, the PL lifetime is an intrinsic characteristic of luminescent species such as porphyrin-based materials and previous reports have shown that the lifetime of the porphyrin linker, TCPP, depends on the local chemical environment and rotation of the molecule in the MOF structure.[95,253]

An interesting discovery was made when probing the PL lifetime of PCN-224 and dPCN-224 samples synthesized in Chapter 2 and Chapter 3 (see Appx. D, Section D.1.3 for more details on samples). The measured PL lifetimes of the dPCN-224 samples in DMF changed depending on the Zr sources used ($ZrOCl_2 \cdot 8H_2O$ *vs.* $ZrCl_4$) and the reaction conditions (one-step synthesis in an oven *vs.* two-step synthesis in a microwave) indicating structural variations between the samples (Figure 5.2). However, the measured dPCN-224 lifetimes could all be fit to two-component exponential curves with the same lifetimes τ_1 = 3.35 ns and τ_2 = 4.78 ns, with different weighting (α_1 and α_2) between samples (Table 5.1 and Appx. D, Figure D.5–Figure D.9). In addition, the lifetimes of the PCN-224 sample with ordered vacancies are identical to the disordered variants, suggesting that the two lifetimes' components are characteristic for all cubic porphyrinic Zr-based MOFs. These findings are in agreement with previous reports in which the lifetimes correlate with the MOF structure.[95] The changes of the lifetime weighting, however, indicate variances between the different MOF samples and warrant further investigation in combination with other characterization techniques that probe the local MOF structure. Once understood, measuring the PL decay could be a fast and powerful method to characterize and compare porphyrinic MOF samples synthesized under different conditions, but also between different laboratories.

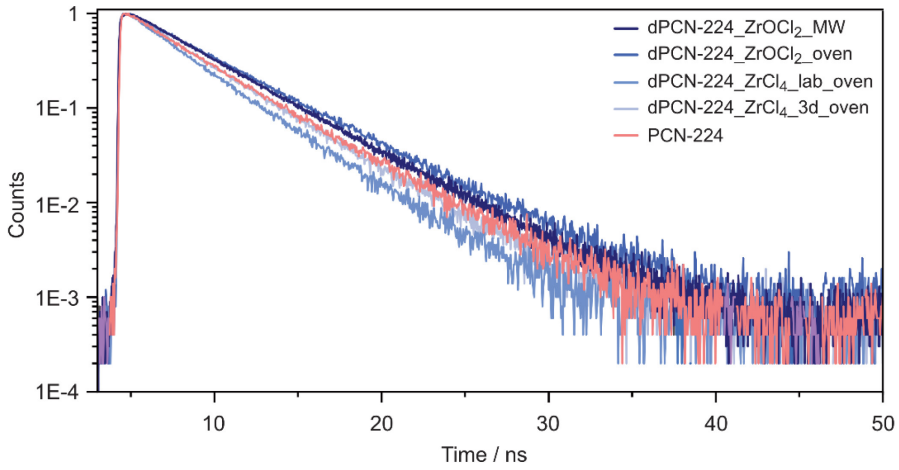

Figure 5.2: Measured photoluminescence lifetime in DMF for dPCN-224-$ZrOCl_2$_MW synthesized from $ZrOCl_2 \cdot 8H_2O$ in two steps in a microwave, dPCN-224-$ZrOCl_2$_oven synthesized from $ZrOCl_2 \cdot 8H_2O$ in one step in an oven, dPCN-224-$ZrCl_4$_lab_oven and dPCN-224-$ZrCl_4$_3d_oven synthesized from $ZrCl_4$_lab and $ZrCl_4$_3d, respectively, in one step in an oven, and ordered PCN-224 (λ_{ex} = 715 nm; see Table 5.1 for time constants).

Table 5.1: Photoluminescence lifetimes and relative weighting for dPCN-224-$ZrOCl_2$_MW, dPCN-224-$ZrOCl_2$_oven, dPCN-224-$ZrCl_4$_lab_oven, dPCN-224-$ZrCl_4$_3d_oven and PCN-224 (see Appx. D, Figure D.5–Figure D.9 for lifetime fittings).

Sample	τ_1 [ns]	α_1	τ_2 [ns]	α_2
dPCN-224_$ZrOCl_2$_MW	3.35	0.25	4.78	0.75
dPCN-224_$ZrOCl_2$_oven	3.35	0.02	4.78	0.98
dPCN-224_$ZrCl_4$_lab_oven	3.35	0.84	4.78	0.16
dPCN-224_$ZrCl_4$_3d_oven	3.35	0.54	4.78	0.46
PCN-224	3.35	0.43	4.78	0.57

5.1.4 Thin film fabrication and post-synthetic modifications toward (photo)electrocatalytic applications

In recent years, MOFs have emerged as promising materials for photo- and electrocatalytic applications as well as optoelectronic devices.[254] For these applications, the fabrication of thin films is essential. Numerous techniques have been established for the fabrication of MOF thin films, including electrochemical deposition, chemical vapor deposition, *in-situ* crystallization on a substrate, and direct growth of surface-anchored MOFs (SURMOFs) by sequential immersion of a substrate into metal precursor and organic linker solution.[255-257] In addition, spin-coating is an experimentally easy and fast method to deposit pre-formed nano-sized MOF particles onto substrates.[258] Here, a MOF suspension is applied onto a substrate that rotates under high speed which causes solvent evaporation and yields an evenly casted film of MOF particles.[258-259]

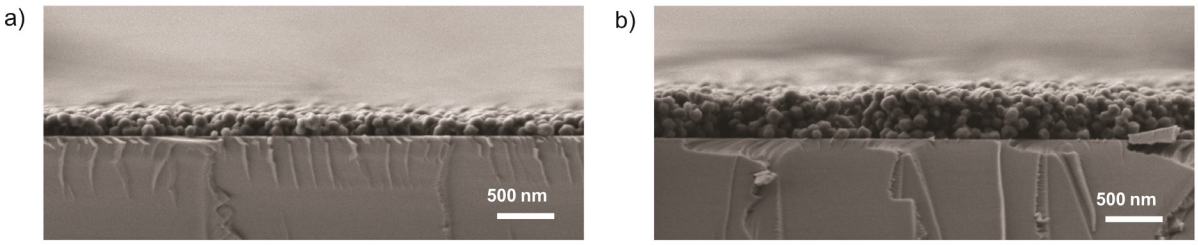

Figure 5.3: SEM image of dPCN-224 thin film cross-sections after spin-coating a) one layer and b) three layers.

To test the porphyrinic MOF particles for their (photo)electrocatalytic activity, thin films of porphyrinic dPCN-224 nanoparticles were fabricated by multilayer spin-coating yielding homogenous thin films with tunable thicknesses between 100 and 500 nm (Figure 5.3 and Appx. D, Section D.1.2).

Unfortunately, the thin films fabricated from pure dPCN-224 were electrically insulating as indicated by impedance measurements (Appx. D, Figure D.10) and readily decomposed in basic media since hydroxide anions form stronger bonds with Zr(IV) than the carboxylates from the linker and will replace the latter.[36,52] To tune the properties of the thin films, the MOF particles were therefore modified post-synthetically before film fabrication (see Appx. D, Section D.1.3 and D.2.3). For instance, porphyrinic dPCN-224 can be modified on several levels including (i) metalation of the porphyrin core, (ii) solvent-assisted linker incorporation (SALI) to introduce new linkers onto the Zr-oxo clusters, and (iii) introducing a guest species into the porous framework.[69,188,260-262]

Of the many modification routes investigated, two are particularly noteworthy and significantly altered the properties of the dPCN-224: dPCN-224 modified with iodine in the pores (I_2@dPCN-224), and dPCN-224 modified with 6,6-phenyl C_{61} butyric acid through SALI (PCBA@dPCN-224) on the Zr-oxo cluster (Figure 5.4). Both modifications remained crystalline upon functionalization and did not feature any changes in the PXRD pattern (Appx. D, Figure D.11).

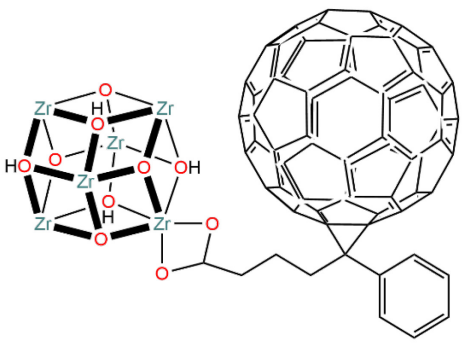

Figure 5.4: Schematic illustration of 6,6-phenyl C_{61} butyric acid linker grafted to the $Zr_6(O)_4(OH)_4$ cluster.

In the case of modification with iodine, cyclic voltammetry (CV) experiments showed a 10-fold increase in the current range for I_2@dPCN-224 compared to the pristine MOF (Figure 5.5a-b). This can be interpreted as a rise in electrochemical activity upon incorporation of iodine as previously shown for other MOFs.[262-263] Iodine doping could therefore be an effective method to increase the conductivity of dPCN-224, and porphyritic MOFs in general, which should further be investigated *via* impedance spectroscopy.

In contrast, modification with PCBA increased the stability of the MOF in basic medium. Whereas pristine dPCN-224 readily decomposed in 0.01 M NaOH (pH = 11), PCBA@dPCN-224 did not dissolve in the basic medium, likely owing to the hydrophobic nature of the fullerene derivative grafted on the Zr-oxo cluster (Figure 5.5c-d). Fullerenes are also known to increase the conductivity of MOFs and impedance measurements of PCBA@dPCN-224 thin films should be performed next.[264-265]

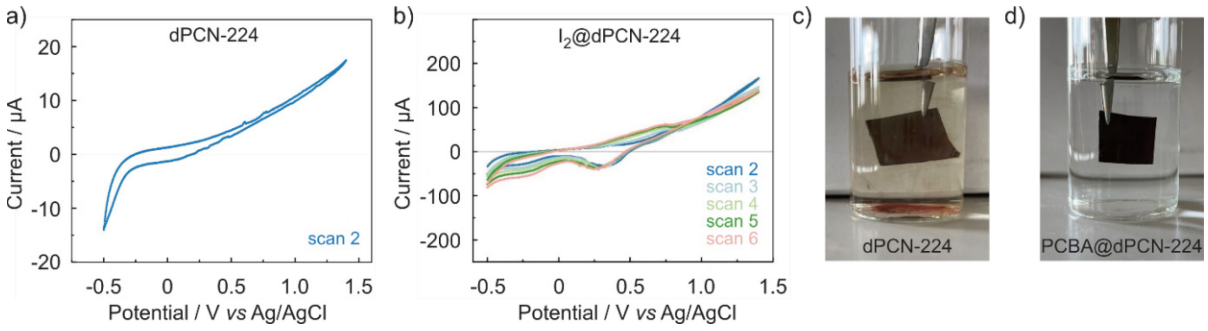

Figure 5.5: CV of a) pristine dPCN-224 and b) dPCN-224 modified with iodine (I_2@dPCN-224) measured in the range -0.5 to 1.4 V at a scan rate of 100 mV s^{-1}. The CV of I_2@dPCN-224 shows a prominent reduction event around 0.4 V which correspond to the reduction of I_3^- to I^-.[266-267] The first scan of each CV experiments was used to stabilize the system and is not included. c) Image of a dPCN-224 film which readily decomposes in 0.01 M NaOH and d) image of modified PCBA@dPCN-224 film which remains stable in 0.01 M NaOH.

Overall, homogeneous thin films could be successfully fabricated *via* spin-coating of dPCN-224 nanoparticles, and by modifying the MOF pre-film fabrication the properties of the thin films could be tuned. Future work should expand post-synthetic iodine incorporation to other porphyrinic MOFs, and SALI on the Zr-oxo cluster to other hydrophobic linkers. In addition, multiple modifications on the same material such as combined iodine-doping and SALI of hydrophobic linkers might be a key to develop both stable and conductive porphyrin-based MOF films. Once this is achieved, it should be investigated whether cluster and linker vacancies and their ordering affect the proton and electron conductivity of the material towards improved (photo)electrocatalytical activity.

5.2 Summary

In the last three decades, MOFs have become one of the foremost classes of porous materials in materials science. The versatile combination of inorganic ions or nodes, and organic linkers has allowed for the development of porous materials that exhibit long-range order and high surface areas with tunable chemical composition. By carefully choosing the molecular building blocks, new MOF topologies can be synthesized, and their properties selected to meet a certain application. However, it is often difficult to obtain phase-pure products and the frameworks often contain poorly understood forms of disorders and defects, which can impact the performance of the material. Amongst the different known MOFs, Zr-based MOFs are one of the most complex owing to the variable coordination environment of the Zr nodes and their high tolerance towards defects. Hence, optimizing Zr-based MOFs towards improved functionality can be challenging and requires careful understanding and control of the resultant structures. This thesis explored the structural complexity arising in Zr-based MOFs built from tetrakis(4-carboxyphenyl) porphyrin (TCPP) and methane-tetrakis(*p*-biphenylcarboxylate) (MTBC) linkers and investigated the impact of synthesis conditions on phase selectivity and MOF particle growth.

In Chapter 2, a detailed synthetic study on cubic porphyrinic MOFs was undertaken and the resultant structures were investigated by both short- and long-range characterization techniques. Using PDF analysis, PXRD, SCXRD, ssNMR, and quantum-chemical calculations, we were able to answer the long-standing conundrum on the existence of cubic Zr_8O_6 clusters in PCN-221. It was found that the MOF consists of statistically disordered octahedral $Zr_6O_4(OH)_4$ clusters, which add up to a truncated cube when superimposed. The study further revealed randomly distributed linker vacancies of up to 50 % which likely originate from energetic differences between two different linker coordination environments on the $Zr_6O_4(OH)_4$ cluster, namely chelating and bridging linker coordination. The orientation of the clusters, the conformation of the linkers, and the large amount of linker vacancies (up to 50 %) were all reminiscent of the PCN-224 structure, but the order of linker vacancies differed. Hence, the new structure model, *disordered PCN-224* (dPCN-224), was established, which invokes additional degrees of freedom in cubic porphyrinic MOFs including cluster disorders, linker vacancies, and cluster–linker binding modes. The new structure model will aid the understanding of Zr-based MOFs and their complex coordination environment. This will improve the performance for applications where disorder and defects play an important role, including (photo)catalysis, gas separation, and drug delivery.

Chapter 3 extended the work presented in Chapter 2 and contains an in-depth investigation into the synthesis and formation pathways of dPCN-224 in order to examine the link between synthetic conditions and phase selectivity. A step-by-step analysis during dPCN-224 formation revealed that

an intermediate composed of $Zr_6O_4(OH)_4$ clusters and TCPP was formed during the early stages of the reaction. Nucleation of dPCN-224 occurred on the surface of this intermediate. PDF analysis showed that the $Zr_6O_4(OH)_4$ clusters formed early in the reaction but featured greater disorder between neighbouring clusters in the intermediate when compared to crystalline dPCN-224. Importantly, the Zr source used during the reaction strongly affected the product. For instance, synthesis from neat $ZrCl_4$ did not form $Zr_6O_4(OH)_4$ clusters; thus, no dPCN-224 was formed. Instead, a metal–organic composite consisting of Zr-oxo species and TCPP was formed. In contrast, synthesis from neat $ZrCl_4$ with the addition of water led to the formation of crystalline MOFs. Interestingly, the amount of water in the reaction affected the growth of dPCN-224, and ultimately the composition of the final product. Both the choice of Zr source and the water content in the reaction are therefore important parameters to consider when synthesizing dPCN-224 in a controlled and reproducible manner. Understanding these correlations will help inform new synthetic protocols for porphyrinic Zr-based MOFs, and more generally Zr-based MOFs.

In Chapter 4, the structural flexibility in Zr-based MOFs built from MTBC linker was explored. As predicted from reticular chemistry, the combination of tetragonal MTBC linkers and $Zr_6O_4(OH)_4$ nodes can lead to the formation of tetragonal PCN-521 with 8-fold connected Zr-oxo clusters. This work demonstrated that the same building units can additionally be combined to form two other MOF structures with (4,12) type coordination, namely cubic c-(4,12)MTBC-Zr_6 and trigonal t-(4,12)MTBC-Zr_6. In both structures, the 12-fold cluster coordination is enabled by high structural flexibility. In cubic c-(4,12)MTBC-Zr_6 one fourth of the cluster sites feature icosahedral symmetry owing to the ligand field. Here, the site symmetry of the MOF is higher than the point symmetry of the $Zr_6(O)_4(OH)_4$ cluster. The clusters therefore adopt one of multiple orientations resulting in a framework with well-defined linker orientations, but disordered $Zr_6(O)_4(OH)_4$ clusters. Importantly, structural disorder was found to differ (4- *vs.* 6-fold) by purely adjusting the synthesis procedures. Trigonal t-(4,12)MTBC-Zr_6 in turn features complex monodentate linker-coordination and a multivariate topology. Here, the large, flexible MTBC linker adopts a geometry that strongly deviates from a tetrahedron in order to form the crystalline framework. Interestingly, this trigonal MOF phase was only obtained as a side product together with the cubic or tetragonal phase which further illustrates the complex entanglement of phases formed during the synthesis of Zr-based MOFs. Overall, this study introduces a new perspective on structural disorder to understand the formation of geometrically “forbidden” MOFs and demonstrates that reticular chemistry is best practiced by combining reticular design with exploratory synthesis.

REFERENCES

1. B.-L. Su, C. Sanchez, X.-Y. Yang, *Hierarchically Structured Porous Materials: From Nanoscience to Catalysis, Separation, Optics, Energy, and Life Science*, Wiley-VCH Verlag, Weinheim, **2011**.
2. R. Xu, W. Pang, J. Yu, Q. Huo, J. Chen, *Chemistry of Zeolites and Related Porous Materials: Synthesis and Structure*, Wiley & Sons, Singapore, **2007**.
3. A. F. Miguel, *Lungs as a Natural Porous Media: Architecture, Airflow Characteristics and Transport of Suspended Particles*, Springer, Berlin, Heidelberg, **2012**.
4. E. C. Dillon, J. H. Wilton, J. C. Barlow, W. A. Watson, *Annals of Emergency Medicine* **1989**, *18*, 547-552.
5. K. S. W. Sing, *Pure and Applied Chemistry* **1985**, *57*, 603-619.
6. M. W. Ackley, S. U. Rege, H. Saxena, *Microporous and Mesoporous Materials* **2003**, *61*, 25-42.
7. T. D. Bennett, F.-X. Coudert, S. L. James, A. I. Cooper, *Nature Materials* **2021**, *20*, 1179-1187.
8. M. E. Davis, *Nature* **2002**, *417*, 813-821.
9. H. Furukawa, K. E. Cordova, M. O'Keeffe, O. M. Yaghi, *Science* **2013**, *341*, 1230444.
10. M. Sai Bhargava Reddy, D. Ponnamma, K. K. Sadasivuni, B. Kumar, A. M. Abdullah, *RSC Advances* **2021**, *11*, 12658-12681.
11. Y. H. Budnikova, *Dalton Transactions* **2020**, *49*, 12483-12502.
12. Y. Yu, P. Liu, M. Dou, J. Niu, Z. Zhang, F. Wang, *Catalysis Science & Technology* **2021**, *11*, 2997-3001.
13. P. Van Der Voort, K. Leus, E. De Canck, *Introduction to Porous Materials*, 1st Edition, Wiley & Sons, **2019**.
14. O. M. Yaghi, G. Li, H. Li, *Nature* **1995**, *378*, 703-706.
15. H. Li, M. Eddaoudi, M. O'Keeffe, O. M. Yaghi, *Nature* **1999**, *402*, 276-279.
16. T. D. Connelly, R. M. Hartshorn, A. T. Hutton, *Nomenclature of Inorganic Chemistry IUPAC Recommendations 2005*, The Royal Society of Chemistry, Cambridge, **2005**.
17. S. R. Batten, N. R. Champness, X.-M. Chen, J. Garcia-Martinez, S. Kitagawa, L. Öhrström, M. O'Keeffe, M. P. Suh, J. Reedijk, *Pure and Applied Chemistry* **2013**, *85*, 1715-1724.
18. Z. Chen, P. Li, R. Anderson, X. Wang, X. Zhang, L. Robison, L. R. Redfern, S. Moribe, T. Islamoglu, D. A. Gómez-Gualdrón, T. Yildirim, J. F. Stoddart, O. K. Farha, *Science* **2020**, *368*, 297-303.
19. I. M. Hönicke, I. Senkovska, V. Bon, I. A. Baburin, N. Bönisch, S. Raschke, J. D. Evans, S. Kaskel, *Angewandte Chemie International Edition* **2018**, *57*, 13780-13783.
20. J. L. C. Rowsell, A. R. Millward, K. S. Park, O. M. Yaghi, *Journal of the American Chemical Society* **2004**, *126*, 5666-5667.
21. U. Mueller, M. Schubert, F. Teich, H. Puetter, K. Schierle-Arndt, J. Pastré, *Journal of Materials Chemistry* **2006**, *16*, 626-636.
22. J. Lee, O. K. Farha, J. Roberts, K. A. Scheidt, S. T. Nguyen, J. T. Hupp, *Chemical Society Reviews* **2009**, *38*, 1450-1459.
23. Y. Sun, L. Zheng, Y. Yang, X. Qian, T. Fu, X. Li, Z. Yang, H. Yan, C. Cui, W. Tan, *Nano-Micro Letters* **2020**, *12*, 103.
24. S. Kitagawa, R. Kitaura, S.-I. Noro, *Angewandte Chemie International Edition* **2004**, *43*, 2334-2375.
25. B. F. Hoskins, R. Robson, *Journal of the American Chemical Society* **1990**, *112*, 1546-1554.
26. B. F. Hoskins, R. Robson, *Journal of the American Chemical Society* **1989**, *111*, 5962-5964.
27. N. Stock, S. Biswas, *Chemical Reviews* **2012**, *112*, 933-969.

28. S. S.-Y. Chui, S. M.-F. Lo, J. P. H. Charmant, A. G. Orpen, I. D. Williams, *Science* **1999**, *283*, 1148-1150.
29. K. Świrk, G. Delahay, A. Zaki, K. Adil, A. Cadiau, *ChemCatChem* **2021**, *13*, 4029-4037.
30. K. K. Gangu, S. Maddila, S. B. Jonnalagadda, *RSC Advances* **2022**, *12*, 14282-14298.
31. J. Getzschmann, I. Senkovska, D. Wallacher, M. Tovar, D. Fairen-Jimenez, T. Düren, J. M. van Baten, R. Krishna, S. Kaskel, *Microporous and Mesoporous Materials* **2010**, *136*, 50-58.
32. https://www.ccdc.cam.ac.uk/support-and-resources/support/case/?caseid=9833bd2c-27f9-4ff7-8186-71a9b415f012
33. G. Cai, P. Yan, L. Zhang, H.-C. Zhou, H.-L. Jiang, *Chemical Reviews* **2021**, *121*, 12278-12326.
34. M. J. Kalmutzki, N. Hanikel, O. M. Yaghi, *Science Advances* **2018**, *4*, 9180.
35. M. Eddaoudi, D. B. Moler, H. Li, B. Chen, T. M. Reineke, M. O'Keeffe, O. M. Yaghi, *Accounts of Chemical Research* **2001**, *34*, 319-330.
36. Y. Bai, Y. Dou, L.-H. Xie, W. Rutledge, J.-R. Li, H.-C. Zhou, *Chemical Society Reviews* **2016**, *45*, 2327-2367.
37. O. M. Yaghi, M. O'Keeffe, N. W. Ockwig, H. K. Chae, M. Eddaoudi, J. Kim, *Nature* **2003**, *423*, 705-714.
38. M. Eddaoudi, J. Kim, N. Rosi, D. Vodak, J. Wachter, M. O'Keeffe, O. M. Yaghi, *Science* **2002**, *295*, 469-472.
39. C.-W. Lv, J. Li, Z. Hou, M.-k. Li, *Inorganic Chemistry Communications* **2013**, *36*, 1-3.
40. X. Bu, Z. Wei, C. Zhang, S. Ren, *Inorganic Chemistry Communications* **2014**, *48*, 158-160.
41. L. S. Xie, G. Skorupskii, M. Dincă, *Chemical Reviews* **2020**, *120*, 8536-8580.
42. A. von Mankowski, K. Szendrei-Temesi, C. Koschnick, B. V. Lotsch, *Nanoscale Horizons* **2018**, *3*, 383-390.
43. S. Roy, Z. Huang, A. Bhunia, A. Castner, A. K. Gupta, X. Zou, S. Ott, *Journal of the American Chemical Society* **2019**, *141*, 15942-15950.
44. F. Millange, C. Serre, G. Férey, *Chemical Communications* **2002**, 822-823.
45. C. Serre, F. Millange, C. Thouvenot, M. Noguès, G. Marsolier, D. Louër, G. Férey, *Journal of the American Chemical Society* **2002**, *124*, 13519-13526.
46. F. Millange, R. I. Walton, *Israel Journal of Chemistry* **2018**, *58*, 1019-1035.
47. G. Férey, C. Serre, *Chemical Society Reviews* **2009**, *38*, 1380-1399.
48. S. Mukherjee, B. Manna, A. V. Desai, Y. Yin, R. Krishna, R. Babarao, S. K. Ghosh, *Chemical Communications* **2016**, *52*, 8215-8218.
49. E. D. Bloch, W. L. Queen, R. Krishna, J. M. Zadrozny, C. M. Brown, J. R. Long, *Science* **2012**, *335*, 1606-1610.
50. A. D. Wiersum, J.-S. Chang, C. Serre, P. L. Llewellyn, *Langmuir* **2013**, *29*, 3301-3309.
51. P. D. C. Dietzel, R. E. Johnsen, H. Fjellvåg, S. Bordiga, E. Groppo, S. Chavan, R. Blom, *Chemical Communications* **2008**, 5125-5127.
52. J. H. Cavka, S. Jakobsen, U. Olsbye, N. Guillou, C. Lamberti, S. Bordiga, K. P. Lillerud, *Journal of the American Chemical Society* **2008**, *130*, 13850-13851.
53. M. Kim, S. M. Cohen, *CrystEngComm* **2012**, *14*, 4096-4104.
54. N. C. Burtch, H. Jasuja, K. S. Walton, *Chemical Reviews* **2014**, *114*, 10575-10612.
55. J. J. Low, A. I. Benin, P. Jakubczak, J. F. Abrahamian, S. A. Faheem, R. R. Willis, *Journal of the American Chemical Society* **2009**, *131*, 15834-15842.
56. R. G. Pearson, *Journal of the American Chemical Society* **1963**, *85*, 3533-3539.
57. X.-L. Lv, M. Tong, H. Huang, B. Wang, L. Gan, Q. Yang, C. Zhong, J.-R. Li, *Journal of Solid State Chemistry* **2015**, *223*, 104-108.
58. X. Zhu, B. Li, J. Yang, Y. Li, W. Zhao, J. Shi, J. Gu, *ACS Applied Materials & Interfaces* **2015**, *7*, 223-231.
59. X. Zhu, J. Gu, Y. Wang, B. Li, Y. Li, W. Zhao, J. Shi, *Chemical Communications* **2014**, *50*, 8779-8782.

60. N. N. Greenwood, A. Earnshaw, *Chemie der Elemente, Vol. 93*, VCH Verlagsgesellschaft, Weinheim, **1988**.
61. D. B. N. Lee, M. Roberts, C. G. Bluchel, R. A. Odell, *ASAIO Journal* **2010**, *56, 550-556*.
62. B. Karadeniz, D. Žilić, I. Huskić, L. S. Germann, A. M. Fidelli, S. Muratović, I. Lončarić, M. Etter, R. E. Dinnebier, D. Barišić, N. Cindro, T. Islamoglu, O. K. Farha, T. Friščić, K. Užarević, *Journal of the American Chemical Society* **2019**, *141*, 19214-19220.
63. X. Gong, H. Noh, N. C. Gianneschi, O. K. Farha, *Journal of the American Chemical Society* **2019**, *141*, 6146-6151.
64. V. Bon, I. Senkovska, I. A. Baburin, S. Kaskel, *Crystal Growth & Design* **2013**, *13*, 1231-1237.
65. Searched for the term MOF and the key words metal, organic, and framework at scifinder.cas.org on 2022-10-03.
66. Y. Zhang, X. Zhang, J. Lyu, K.-i. Otake, X. Wang, L. R. Redfern, C. D. Malliakas, Z. Li, T. Islamoglu, B. Wang, O. K. Farha, *Journal of the American Chemical Society* **2018**, *140*, 11179-11183.
67. S. Yuan, W. Lu, Y.-P. Chen, Q. Zhang, T.-F. Liu, D. Feng, X. Wang, J. Qin, H.-C. Zhou, *Journal of the American Chemical Society* **2015**, *137*, 3177-3180.
68. S. Yuan, J.-S. Qin, C. T. Lollar, H.-C. Zhou, *ACS Central Science* **2018**, *4*, 440-450.
69. P. Deria, W. Bury, I. Hod, C.-W. Kung, O. Karagiaridi, J. T. Hupp, O. K. Farha, *Inorganic Chemistry* **2015**, *54*, 2185-2192.
70. P. Deria, W. Bury, J. T. Hupp, O. K. Farha, *Chemical Communications* **2014**, *50*, 1965-1968.
71. D. A. Gomez-Gualdron, O. V. Gutov, V. Krungleviciute, B. Borah, J. E. Mondloch, J. T. Hupp, T. Yildirim, O. K. Farha, R. Q. Snurr, *Chemistry of Materials* **2014**, *26*, 5632-5639.
72. P. Deria, D. A. Gómez-Gualdrón, I. Hod, R. Q. Snurr, J. T. Hupp, O. K. Farha, *Journal of the American Chemical Society* **2016**, *138*, 14449-14457.
73. A. A. Bezrukov, K. W. Törnroos, E. Le Roux, P. D. C. Dietzel, *Chemical Communications* **2018**, *54*, 2735-2738.
74. S. Leubner, H. Zhao, N. Van Velthoven, M. Henrion, H. Reinsch, D. E. De Vos, U. Kolb, N. Stock, *Angewandte Chemie International Edition* **2019**, *58*, 10995-11000.
75. D. Feng, H.-L. Jiang, Y.-P. Chen, Z.-Y. Gu, Z. Wei, H.-C. Zhou, *Inorganic Chemistry* **2013**, *52*, 12661-12667.
76. P. Ji, K. Manna, Z. Lin, A. Urban, F. X. Greene, G. Lan, W. Lin, *Journal of the American Chemical Society* **2016**, *138*, 12234-12242.
77. C. Koschnick, R. Stäglich, T. Scholz, M. W. Terban, A. von Mankowski, G. Savasci, F. Binder, A. Schökel, M. Etter, J. Nuss, R. Siegel, L. S. Germann, C. Ochsenfeld, R. E. Dinnebier, J. Senker, B. V. Lotsch, *Nature Communications* **2021**, *12*, 3099.
78. R. Giovannetti, *The Use of Spectrophotometry UV-Vis for the Study of Porphyrins* in *Macro To Nano Spectroscopy* (Ed.: J. Uddin), IntechOpen, London, **2012**.
79. H. Lu, X. P. Zhang, *Chemical Society Reviews* **2011**, *40*, 1899-1909.
80. G. C. Ferreira, *Heme Synthesis* in *Encyclopedia of Biological Chemistry*, 2nd Edition. (Eds.: W. J. Lennarz, M. D. Lane), Academic Press, Waltham, **2013**, 539-542.
81. G. S. Ananthnag, V. S. Shetti, *Dalton Transactions* **2017**, *46*, 14062-14082.
82. K.-H. Pfoertner, T. Oppenländer, *Photochemistry* in *Ullmann's Encyclopedia of Industrial Chemistry*, Wiley VCH, Weinheim, **2011**.
83. T. Mandal, S. Das, S. De Sarkar, *Advanced Synthesis & Catalysis* **2019**, *361*, 3200-3209.
84. M. L. Pegis, D. J. Martin, C. F. Wise, A. C. Brezny, S. I. Johnson, L. E. Johnson, N. Kumar, S. Raugei, J. M. Mayer, *Journal of the American Chemical Society* **2019**, *141*, 8315-8326.
85. D. Feng, Z.-Y. Gu, J.-R. Li, H.-L. Jiang, Z. Wei, H.-C. Zhou, *Angewandte Chemie International Edition* **2012**, *51*, 10307-10310.
86. H.-L. Jiang, D. Feng, K. Wang, Z.-Y. Gu, Z. Wei, Y.-P. Chen, H.-C. Zhou, *Journal of the American Chemical Society* **2013**, *135*, 13934-13938.
87. M. Zhao, S. Ou, C.-D. Wu, *Accounts of Chemical Research* **2014**, *47*, 1199-1207.
88. K. Sasan, Q. Lin, C. Mao, P. Feng, *Chemical Communications* **2014**, *50*, 10390-10393.

89. I. Hod, M. D. Sampson, P. Deria, C. P. Kubiak, O. K. Farha, J. T. Hupp, *ACS Catalysis* **2015**, *5*, 6302-6309.
90. K. Yu, D.-I. Won, W. I. Lee, W.-S. Ahn, *Korean Journal of Chemical Engineering* **2021**, *38*, 653-673.
91. D. Feng, W.-C. Chung, Z. Wei, Z.-Y. Gu, H.-L. Jiang, Y.-P. Chen, D. J. Darensbourg, H.-C. Zhou, *Journal of the American Chemical Society* **2013**, *135*, 17105-17110.
92. W. Morris, B. Volosskiy, S. Demir, F. Gándara, P. L. McGrier, H. Furukawa, D. Cascio, J. F. Stoddart, O. M. Yaghi, *Inorganic Chemistry* **2012**, *51*, 6443-6445.
93. P. Deria, D. A. Gómez-Gualdrón, I. Hod, R. Q. Snurr, J. T. Hupp, O. K. Farha, *Journal of the American Chemical Society* **2016**, *138*, 14449-14457.
94. D. Feng, Z.-Y. Gu, Y.-P. Chen, J. Park, Z. Wei, Y. Sun, M. Bosch, S. Yuan, H.-C. Zhou, *Journal of the American Chemical Society* **2014**, *136*, 17714-17717.
95. P. Deria, J. Yu, R. P. Balaraman, J. Mashni, S. N. White, *Chemical Communications* **2016**, *52*, 13031-13034.
96. V. V. Butova, A. P. Budnyk, K. M. Charykov, K. S. Vetlitsyna-Novikova, C. Lamberti, A. V. Soldatov, *Chemical Communications* **2019**, *55*, 901-904.
97. M. Zhang, Y.-P. Chen, M. Bosch, T. Gentle III, K. Wang, D. Feng, Z. U. Wang, H.-C. Zhou, *Angewandte Chemie International Edition* **2014**, *53*, 815-818.
98. Z. Fang, B. Bueken, D. E. De Vos, R. A. Fischer, *Angewandte Chemie International Edition* **2015**, *54*, 7234-7254.
99. R. J. D. Tilley, *Defects in Solids* in *Encyclopedia of Inorganic and Bioinorganic Chemistry* (Ed.: R. A. Scott), Wiley & Sons, **2018**, 1-23.
100. W. D. Callister, D. G. Rethwisch, *Materials science and engineering an introduction*, 10th Edition, Wiley & Sons, Hoboken, **2018**.
101. P. Kofstad, T. Norby, *Defects and Transport in Crystalline Solids*, University of Oslo, Oslo, **2004**.
102. J. Maier, *Festkörper — Fehler und Funktion*, Vieweg+Teubner Verlag, Wiesbaden, **2000**.
103. J. T. Hughes, A. Navrotsky, *Journal of the American Chemical Society* **2011**, *133*, 9184-9187.
104. J. C. Moreno Piraján, C. T. O'Mahony, R. A. Farrell, T. Goshal, J. D. Holmes, M. A. Morris, *The Thermodynamics of Defect Formation in Self-Assembled Systems*, IntechOpen, London, **2011**.
105. S. Dissegna, *Defect engineering of Zr-based MOFs,* Technische Universität München, Munich, **2018**.
106. M. J. Cliffe, W. Wan, X. Zou, P. A. Chater, A. K. Kleppe, M. G. Tucker, H. Wilhelm, N. P. Funnell, F.-X. Coudert, A. L. Goodwin, *Nature Communications* **2014**, *5*, 4176.
107. M. Taddei, *Coordination Chemistry Reviews* **2017**, *343*, 1-24.
108. S. Dissegna, K. Epp, W. R. Heinz, G. Kieslich, R. A. Fischer, *Advanced Materials* **2018**, *30*, 1704501.
109. U. Ravon, M. Savonnet, S. Aguado, M. E. Domine, E. Janneau, D. Farrusseng, *Microporous and Mesoporous Materials* **2010**, *129*, 319-329.
110. G. C. Shearer, S. Chavan, S. Bordiga, S. Svelle, U. Olsbye, K. P. Lillerud, *Chemistry of Materials* **2016**, *28*, 3749-3761.
111. G. C. Shearer, S. Chavan, J. Ethiraj, J. G. Vitillo, S. Svelle, U. Olsbye, C. Lamberti, S. Bordiga, K. P. Lillerud, *Chemistry of Materials* **2014**, *26*, 4068-4071.
112. Q. Pang, L. Yang, Q. Li, *Small Structures* **2022**, *3*, 2100203.
113. H. Wu, Y. S. Chua, V. Krungleviciute, M. Tyagi, P. Chen, T. Yildirim, W. Zhou, *Journal of the American Chemical Society* **2013**, *135*, 10525-10532.
114. C. A. Trickett, K. J. Gagnon, S. Lee, F. Gándara, H.-B. Bürgi, O. M. Yaghi, *Angewandte Chemie International Edition* **2015**, *54*, 11162-11167.
115. S. Øien, D. Wragg, H. Reinsch, S. Svelle, S. Bordiga, C. Lamberti, K. P. Lillerud, *Crystal Growth & Design* **2014**, *14*, 5370-5372.
116. R. S. Forgan, *Chemical Science* **2020**, *11*, 4546-4562.

117. S. Dissegna, P. Vervoorts, C. L. Hobday, T. Düren, D. Daisenberger, A. J. Smith, R. A. Fischer, G. Kieslich, *Journal of the American Chemical Society* **2018**, *140*, 11581-11584.
118. A. W. Thornton, R. Babarao, A. Jain, F. Trousselet, F. X. Coudert, *Dalton Transactions* **2016**, *45*, 4352-4359.
119. A. Simonov, A. L. Goodwin, *Nature Reviews Chemistry* **2020**, *4*, 657-673.
120. G. M. Whitesides, B. Grzybowski, *Science* **2002**, *295*, 2418-2421.
121. N. Ridgway, R. McLeod, *Biochemistry of Lipids, Lipoproteins and Membranes*, 5th Edition, Elsevier Science, **2008**.
122. H. S. Azevedo, R. M. da Silva, *Self-assembling Biomaterials: Molecular Design, Characterization and Application in Biology and Medicine*, Woodhead Publishing, **2018**.
123. A. Sharma, U. S. Sharma, *International Journal of Pharmaceutics* **1997**, *154*, 123-140.
124. S. M. Douglas, H. Dietz, T. Liedl, B. Högberg, F. Graf, W. M. Shih, *Nature* **2009**, *459*, 414-418.
125. A. Sharma, K. Vaghasiya, R. K. Verma, A. B. Yadav, *Chapter 3 - DNA nanostructures: chemistry, self-assembly, and applications* in *Emerging Applications of Nanoparticles and Architecture Nanostructures* (Eds.: A. Barhoum, A. S. H. Makhlouf), Elsevier, **2018**, 71-94.
126. B. Seoane, S. Castellanos, A. Dikhtiarenko, F. Kapteijn, J. Gascon, *Coordination Chemistry Reviews* **2016**, *307*, 147-187.
127. G. R. Desiraju, J. J. Vittal, A. Ramanan, *Crystal engineering: a textbook*, World Scientific, Singapore, **2011**.
128. Z. K. Nagy, M. Fujiwara, X. Y. Woo, R. D. Braatz, *Industrial & Engineering Chemistry Research* **2008**, *47*, 1245-1252.
129. S. Fan, X. Gu, X. Zhou, X. Duan, H. Li, *Energetic Materials Frontiers* **2021**, *2*, 62-68.
130. F. Millange, M. I. Medina, N. Guillou, G. Férey, K. M. Golden, R. I. Walton, *Angewandte Chemie International Edition* **2010**, *49*, 763-766.
131. X. Liu, S. W. Chee, S. Raj, M. Sawczyk, P. Král, U. Mirsaidov, *PNAS* **2021**, *118*, 2008880118.
132. C. McKinstry, E. J. Cussen, A. J. Fletcher, S. V. Patwardhan, J. Sefcik, *Crystal Growth & Design* **2013**, *13*, 5481-5486.
133. Y. Wu, M. I. Breeze, D. O'Hare, R. I. Walton, *Microporous and Mesoporous Materials* **2017**, *254*, 178-183.
134. C. Zheng, H. F. Greer, C.-Y. Chiang, W. Zhou, *CrystEngComm* **2014**, *16*, 1064-1070.
135. M. J. Van Vleet, T. Weng, X. Li, J. R. Schmidt, *Chemical Reviews* **2018**, *118*, 3681-3721.
136. R. A. Van Santen, *The Journal of Physical Chemistry* **1984**, *88*, 5768-5769.
137. A. Aerts, C. E. A. Kirschhock, J. A. Martens, *Chemical Society Reviews* **2010**, *39*, 4626-4642.
138. C. Ma, L. Zheng, G. Wang, J. Guo, L. Li, Q. He, Y. Chen, H. Zhang, *Aggregate* **2022**, *3*, 145.
139. D. J. Tranchemontagne, J. R. Hunt, O. M. Yaghi, *Tetrahedron* **2008**, *64*, 8553-8557.
140. G. Blanita, G. Borodi, M. D. Lazar, A.-R. Biris, L. Barbu-Tudoran, I. Coldea, D. Lupu, *RSC Advances* **2016**, *6*, 25967-25974.
141. G. Demazeau, *Journal of Materials Science* **2008**, *43*, 2104-2114.
142. M. Y. K. Byrappa, *Handbook of Hydrothermal Technology (Materials and Processing Technology)*, Noyes Publications, New York, **2002**.
143. E. R. Parnham, R. E. Morris, *Accounts of Chemical Research* **2007**, *40*, 1005-1013.
144. A. Pichon, A. Lazuen-Garay, S. L. James, *CrystEngComm* **2006**, *8*, 211-214.
145. L.-G. Qiu, Z.-Q. Li, Y. Wu, W. Wang, T. Xu, X. Jiang, *Chemical Communications* **2008**, 3642-3644.
146. U. P. Mueller, Hermann; Hesse, Michael; Wessel, Helge; Juergen Huff, Juergen; Guzmann, Marcus B. Aktiengesellschaft, **2011**, US7968739B2.
147. J.-S. Choi, W.-J. Son, J. Kim, W.-S. Ahn, *Microporous and Mesoporous Materials* **2008**, *116*, 727-731.
148. E. Haque, N. A. Khan, J. H. Park, S. H. Jhung, *Chemistry - A European Journal* **2010**, *16*, 1046-1052.
149. T. Ahnfeldt, J. Moellmer, V. Guillerm, R. Staudt, C. Serre, N. Stock, *Chemistry - A European Journal* **2011**, *17*, 6462-6468.

150. T. Uemura, Y. Hoshino, S. Kitagawa, K. Yoshida, S. Isoda, *Chemistry of Materials* **2006**, *18*, 992-995.
151. T. Tsuruoka, S. Furukawa, Y. Takashima, K. Yoshida, S. Isoda, S. Kitagawa, *Angewandte Chemie International Edition* **2009**, *48*, 4739-4743.
152. E. A. Flügel, A. Ranft, F. Haase, B. V. Lotsch, *Journal of Materials Chemistry* **2012**, *22*, 10119-10133.
153. S. Hermes, T. Witte, T. Hikov, D. Zacher, S. Bahnmüller, G. Langstein, K. Huber, R. A. Fischer, *Journal of the American Chemical Society* **2007**, *129*, 5324-5325.
154. A. Schaate, P. Roy, A. Godt, J. Lippke, F. Waltz, M. Wiebcke, P. Behrens, *Chemistry - A European Journal* **2011**, *17*, 6643-6651.
155. S. Diring, S. Furukawa, Y. Takashima, T. Tsuruoka, S. Kitagawa, *Chemistry of Materials* **2010**, *22*, 4531-4538.
156. D. Jiang, A. D. Burrows, K. J. Edler, *CrystEngComm* **2011**, *13*, 6916-6919.
157. W. Cho, H. J. Lee, M. Oh, *Journal of the American Chemical Society* **2008**, *130*, 16943-16946.
158. S. Yuan, L. Feng, K. Wang, J. Pang, M. Bosch, C. Lollar, Y. Sun, J. Qin, X. Yang, P. Zhang, Q. Wang, L. Zou, Y. Zhang, L. Zhang, Y. Fang, J. Li, H.-C. Zhou, *Advanced Materials* **2018**, *30*, 1704303.
159. M. L. Kelty, W. Morris, A. T. Gallagher, J. S. Anderson, K. A. Brown, C. A. Mirkin, T. D. Harris, *Chemical Communications* **2016**, *52*, 7854-7857.
160. J. E. Mondloch, W. Bury, D. Fairen-Jimenez, S. Kwon, E. J. DeMarco, M. H. Weston, A. A. Sarjeant, S. T. Nguyen, P. C. Stair, R. Q. Snurr, O. K. Farha, J. T. Hupp, *Journal of the American Chemical Society* **2013**, *135*, 10294-10297.
161. C.-W. Kung, T. C. Wang, J. E. Mondloch, D. Fairen-Jimenez, D. M. Gardner, W. Bury, J. M. Klingsporn, J. C. Barnes, R. Van Duyne, J. F. Stoddart, M. R. Wasielewski, O. K. Farha, J. T. Hupp, *Chemistry of Materials* **2013**, *25*, 5012-5017.
162. W.-G. Liu, D. G. Truhlar, *Chemistry of Materials* **2017**, *29*, 8073-8081.
163. T. E. Webber, W.-G. Liu, S. P. Desai, C. C. Lu, D. G. Truhlar, R. L. Penn, *ACS Applied Materials & Interfaces* **2017**, *9*, 39342-39346.
164. J. E. Mondloch, O. Karagiaridi, O. K. Farha, J. T. Hupp, *CrystEngComm* **2013**, *15*, 9258-9264.
165. M. R. DeStefano, T. Islamoglu, S. J. Garibay, J. T. Hupp, O. K. Farha, *Chemistry of Materials* **2017**, *29*, 1357-1361.
166. M. Taddei, J. A. van Bokhoven, M. Ranocchiari, *Inorganic Chemistry* **2020**, *59*, 7860-7868.
167. F. Ragon, P. Horcajada, H. Chevreau, Y. K. Hwang, U. H. Lee, S. R. Miller, T. Devic, J.-S. Chang, C. Serre, *Inorganic Chemistry* **2014**, *53*, 2491-2500.
168. X. Chen, Y. Lyu, Z. Wang, X. Qiao, B. C. Gates, D. Yang, *ACS Catalysis* **2020**, *10*, 2906-2914.
169. F. C. N. Firth, M. J. Cliffe, D. Vulpe, M. Aragones-Anglada, P. Z. Moghadam, D. Fairen-Jimenez, B. Slater, C. P. Grey, *Journal of Materials Chemistry A* **2019**, *7*, 7459-7469.
170. L. Liu, D. Zhang, Y. Zhu, Y. Han, *Communications Chemistry* **2020**, *3*, 99.
171. D. Zhang, Y. Zhu, L. Liu, X. Ying, C.-E. Hsiung, R. Sougrat, K. Li, Y. Han, *Science* **2018**, *359*, 675-679.
172. M. W. Terban, S. J. L. Billinge, *Chemical Reviews* **2022**, *122*, 1208-1272.
173. C. Castillo-Blas, J. M. Moreno, I. Romero-Muñiz, A. E. Platero-Prats, *Nanoscale* **2020**, *12*, 15577-15587.
174. C. A. Young, A. L. Goodwin, *Journal of Materials Chemistry* **2011**, *21*, 6464-6476.
175. P. Walther, M. Puchberger, F. R. Kogler, K. Schwarz, U. Schubert, *Physical Chemistry Chemical Physics* **2009**, *11*, 3640-3647.
176. K. S. W. Sing, D. H. Everett, R. A. W. Haul, L. Moscou, R. A. Pierotti, J. Rouquerol, T. Siemieniewska, *Reporting Physisorption Data for Gas/Solid Systems* in *Handbook of Heterogeneous Catalysis*, 1217-1230.
177. P. I. Ravikovitch, A. V. Neimark, *Langmuir* **2006**, *22*, 11171-11179.
178. W. Lu, Z. Wei, Z.-Y. Gu, T.-F. Liu, J. Park, J. Park, J. Tian, M. Zhang, Q. Zhang, T. Gentle Iii, M. Bosch, H.-C. Zhou, *Chemical Society Reviews* **2014**, *43*, 5561-5593.

179. Z. Wang, S. M. Cohen, *Chemical Society Reviews* **2009**, *38*, 1315-1329.
180. Z. Yin, S. Wan, J. Yang, M. Kurmoo, M.-H. Zeng, *Coordination Chemistry Reviews* **2019**, *378*, 500-512.
181. H. Furukawa, F. Gándara, Y.-B. Zhang, J. Jiang, W. L. Queen, M. R. Hudson, O. M. Yaghi, *Journal of the American Chemical Society* **2014**, *136*, 4369-4381.
182. V. Guillerm, F. Ragon, M. Dan-Hardi, T. Devic, M. Vishnuvarthan, B. Campo, A. Vimont, G. Clet, Q. Yang, G. Maurin, G. Férey, A. Vittadini, S. Gross, C. Serre, *Angewandte Chemie International Edition* **2012**, *51*, 9267-9271.
183. W.-Y. Gao, M. Chrzanowski, S. Ma, *Chemical Society Reviews* **2014**, *43*, 5841-5866.
184. C. Y. Lee, O. K. Farha, B. J. Hong, A. A. Sarjeant, S. T. Nguyen, J. T. Hupp, *Journal of the American Chemical Society* **2011**, *133*, 15858-15861.
185. Shaunak M. Shaikh, A. Chakraborty, J. Alatis, M. Cai, E. Danilov, A. J. Morris, *Faraday Discussions* **2019**, *216*, 174-190.
186. C. F. Pereira, M. M. Q. Simões, J. P. C. Tomé, F. A. Almeida Paz, in *Molecules, Vol. 21*, **2016**.
187. S. M. Shaikh, P. M. Usov, J. Zhu, M. Cai, J. Alatis, A. J. Morris, *Inorganic Chemistry* **2019**, *58*, 5145-5153.
188. C.-W. Kung, T.-H. Chang, L.-Y. Chou, J. T. Hupp, O. K. Farha, K.-C. Ho, *Chemical Communications* **2015**, *51*, 2414-2417.
189. S. W. Hong, J. W. Paik, D. Seo, J.-M. Oh, Y. K. Jeong, J. K. Park, *Inorganic Chemistry Frontiers* **2020**, *7*, 221-231.
190. D. Lin, X. Liu, R. Huang, W. Qi, R. Su, Z. He, *Chemical Communications* **2019**, *55*, 6775-6778.
191. K. Kim, S. Lee, E. Jin, L. Palanikumar, J. H. Lee, J. C. Kim, J. S. Nam, B. Jana, T.-H. Kwon, S. K. Kwak, W. Choe, J.-H. Ryu, *ACS Applied Materials & Interfaces* **2019**, *11*, 27512-27520.
192. N. Sharma, S. S. Dhankhar, C. M. Nagaraja, *Sustainable Energy & Fuels* **2019**, *3*, 2977-2982.
193. L. Wang, P. Jin, S. Duan, H. She, J. Huang, Q. Wang, *Science Bulletin* **2019**, *64*, 926-933.
194. D. Han, Y. Han, J. Li, X. Liu, K. W. K. Yeung, Y. Zheng, Z. Cui, X. Yang, Y. Liang, Z. Li, S. Zhu, X. Yuan, X. Feng, C. Yang, S. Wu, *Applied Catalysis B: Environmental* **2020**, *261*, 118248.
195. Q. Zhou, G. Li, K. Chen, H. Yang, M. Yang, Y. Zhang, Y. Wan, Y. Shen, Y. Zhang, *Analytical Chemistry* **2020**, *92*, 983-990.
196. M. Duguet, A. Lemarchand, Y. Benseghir, P. Mialane, M. Gomez-Mingot, C. Roch-Marchal, M. Haouas, M. Fontecave, C. Mellot-Draznieks, C. Sassoye, A. Dolbecq, *Chemical Communications* **2020**, *56*, 10143-10146.
197. J. Wang, Y. Fan, Y. Tan, X. Zhao, Y. Zhang, C. Cheng, M. Yang, *ACS Applied Materials & Interfaces* **2018**, *10*, 36615-36621.
198. J. Park, Q. Jiang, D. Feng, L. Mao, H.-C. Zhou, *Journal of the American Chemical Society* **2016**, *138*, 3518-3525.
199. K. Epp, A. L. Semrau, M. Cokoja, A. Fischer Roland, *ChemCatChem* **2018**, *10*, 3506-3512.
200. L. Zhang, S. Yuan, W. Fan, J. Pang, F. Li, B. Guo, P. Zhang, D. Sun, H.-C. Zhou, *ACS Applied Materials & Interfaces* **2019**, *11*, 22390-22397.
201. Y. Zhang, Q. Wang, G. Chen, P. Shi, *Inorganic Chemistry* **2019**, *58*, 6593-6596.
202. F. Zheng, F. Fu, Y. Cheng, C. Wang, Y. Zhao, Z. Gu, *Small* **2016**, *12*, 2253-2282.
203. W. Lin, J. Gong, L. Fang, K. Jiang, *Zeitschrift fur Anorganische und Allgemeine Chemie* **2019**, *645*, 1161-1164.
204. W.-L. Liu, M.-Z. Zou, T. Liu, J.-Y. Zeng, X. Li, W.-Y. Yu, C.-X. Li, J.-J. Ye, W. Song, J. Feng, X.-Z. Zhang, *Advanced Materials* **2019**, *31*, 1900499.
205. L.-Y. Wu, Y.-F. Mu, X.-X. Guo, W. Zhang, Z.-M. Zhang, M. Zhang, T.-B. Lu, *Angewandte Chemie International Edition* **2019**, *58*, 9491-9495.
206. W. Lin, Q. Hu, K. Jiang, Y. Yang, Y. Yang, Y. Cui, G. Qian, *Journal of Solid State Chemistry* **2016**, *237*, 307-312.
207. X. Gong, Y. Shu, Z. Jiang, L. Lu, X. Xu, C. Wang, H. Deng, *Angewandte Chemie International Edition* **2020**, *59*, 5326-5331.

208. L. Valenzano, B. Civalleri, S. Chavan, S. Bordiga, M. H. Nilsen, S. Jakobsen, K. P. Lillerud, C. Lamberti, *Chemistry of Materials* **2011**, *23*, 1700-1718.
209. S. M. J. Rogge, J. Wieme, L. Vanduyfhuys, S. Vandenbrande, G. Maurin, T. Verstraelen, M. Waroquier, V. Van Speybroeck, *Chemistry of Materials* **2016**, *28*, 5721-5732.
210. N. Planas, J. E. Mondloch, S. Tussupbayev, J. Borycz, L. Gagliardi, J. T. Hupp, O. K. Farha, C. J. Cramer, *The Journal of Physical Chemistry Letters* **2014**, *5*, 3716-3723.
211. T. Steiner, *Angewandte Chemie International Edition* **2002**, *41*, 48-76.
212. P. Deria, J. E. Mondloch, E. Tylianakis, P. Ghosh, W. Bury, R. Q. Snurr, J. T. Hupp, O. K. Farha, *Journal of the American Chemical Society* **2013**, *135*, 16801-16804.
213. M. C. Lawrence, C. Schneider, M. J. Katz, *Chemical Communications* **2016**, *52*, 4971-4974.
214. H. Grüninger, K. Armstrong, D. Greim, T. Boffa-Ballaran, D. J. Frost, J. Senker, *Journal of the American Chemical Society* **2017**, *139*, 10499-10505.
215. H. Eckert, J. P. Yesinowski, L. A. Silver, E. M. Stolper, *The Journal of Physical Chemistry* **1988**, *92*, 2055-2064.
216. D. Massiot, I. Farnan, N. Gautier, D. Trumeau, A. Trokiner, J. P. Coutures, *Solid State Nuclear Magnetic Resonance* **1995**, *4*, 241-248.
217. H. Y. Carr, E. M. Purcell, *Physical Review* **1954**, *94*, 630-638.
218. F. H. Larsen, H. J. Jakobsen, P. D. Ellis, N. C. Nielsen, *The Journal of Physical Chemistry A* **1997**, *101*, 8597-8606.
219. S. Meiboom, D. Gill, *Review of Scientific Instruments* **1958**, *29*, 688-691.
220. G. Kickelbick, U. Schubert, *Chemische Berichte* **1997**, *130*, 473-478.
221. G. Kickelbick, M. P. Feth, H. Bertagnolli, M. Puchberger, D. Holzinger, S. Gross, *Journal of the Chemical Society, Dalton Transactions* **2002**, 3892-3898.
222. K. McRoberts, W. Zhou, *CrystEngComm* **2021**, *23*, 7658-7662.
223. T. Islamoglu, K.-i. Otake, P. Li, C. T. Buru, A. W. Peters, I. Akpinar, S. J. Garibay, O. K. Farha, *CrystEngComm* **2018**, *20*, 5913-5918.
224. H. Noh, C.-W. Kung, T. Islamoglu, A. W. Peters, Y. Liao, P. Li, S. J. Garibay, X. Zhang, M. R. DeStefano, J. T. Hupp, O. K. Farha, *Chemistry of Materials* **2018**, *30*, 2193-2197.
225. T. E. Webber, S. P. Desai, R. L. Combs, S. Bingham, C. C. Lu, R. L. Penn, *Crystal Growth & Design* **2020**, *20*, 2965-2972.
226. P. Li, R. C. Klet, S.-Y. Moon, T. C. Wang, P. Deria, A. W. Peters, B. M. Klahr, H.-J. Park, S. S. Al-Juaid, J. T. Hupp, O. K. Farha, *Chemical Communications* **2015**, *51*, 10925-10928.
227. D. Salionov, O. O. Semivrazhskaya, N. P. M. Casati, M. Ranocchiari, S. Bjelić, R. Verel, J. A. van Bokhoven, V. L. Sushkevich, *Nature Communications* **2022**, *13*, 3762.
228. C. Ardila-Suárez, J. Rodríguez-Pereira, V. G. Baldovino-Medrano, G. E. Ramírez-Caballero, *CrystEngComm* **2019**, *21*, 1407-1415.
229. X. Sang, J. Zhang, J. Xiang, J. Cui, L. Zheng, J. Zhang, Z. Wu, Z. Li, G. Mo, Y. Xu, J. Song, C. Liu, X. Tan, T. Luo, B. Zhang, B. Han, *Nature Communications* **2017**, *8*, 175.
230. G. Zahn, P. Zerner, J. Lippke, F. L. Kempf, S. Lilienthal, C. A. Schröder, A. M. Schneider, P. Behrens, *CrystEngComm* **2014**, *16*, 9198-9207.
231. S. Carrasco, A. Sanz-Marco, B. Martín-Matute, *Organometallics* **2019**, *38*, 3429-3435.
232. J. Jin, *New Journal of Chemistry* **2020**, *44*, 15362-15368.
233. B. J. Deibert, J. Li, *Chemical Communications* **2014**, *50*, 9636-9639.
234. X. Xie, X. Zhang, M. Xie, L. Xiong, H. Sun, Y. Lu, Q. Mu, M. H. Rummeli, J. Xu, S. Li, J. Zhong, Z. Deng, B. Ma, T. Cheng, W. A. Goddard, Y. Peng, *Nature Communications* **2022**, *13*, 63.
235. X. Chen, Y. Zhuang, N. Rampal, R. Hewitt, G. Divitini, C. A. O'Keefe, X. Liu, D. J. Whitaker, J. W. Wills, R. Jugdaohsingh, J. J. Powell, H. Yu, C. P. Grey, O. A. Scherman, D. Fairen-Jimenez, *Journal of the American Chemical Society* **2021**, *143*, 13557-13572.
236. J. Yang, Z. Wang, Y. Li, Q. Zhuang, W. Zhao, J. Gu, *RSC Advances* **2016**, *6*, 69807-69814.
237. L. Shi, L. Yang, H. Zhang, K. Chang, G. Zhao, T. Kako, J. Ye, *Applied Catalysis B: Environmental* **2018**, *224*, 60-68.

238. D. Zacher, J. Liu, K. Huber, R. A. Fischer, *Chemical Communications* **2009**, 1031-1033.
239. K. Epp, A. L. Semrau, M. Cokoja, R. A. Fischer, *ChemCatChem* **2018**, *10*, 3506-3512.
240. B. Krebs, *Zeitschrift fur Anorganische und Allgemeine Chemie* **1970**, *378*, 263-272.
241. R. Borjas Nevarez, S. M. Balasekaran, E. Kim, P. Weck, F. Poineau, *Acta Crystallographica Section C* **2018**, *74*, 307-311.
242. Y. Zhang, M. X. Li, M. Y. Lü, R. H. Yang, F. Liu, K. A. Li, *The Journal of Physical Chemistry A* **2005**, *109*, 7442-7448.
243. A. B. Rudine, B. D. DelFatti, C. C. Wamser, *The Journal of Organic Chemistry* **2013**, *78*, 6040-6049.
244. S. Leubner, R. Siegel, J. Franke, M. T. Wharmby, C. Krebs, H. Reinsch, J. Senker, N. Stock, *Inorganic Chemistry* **2020**, *59*, 15250-15261.
245. T. F. Irzhak, V. I. Irzhak, *Doklady Physical Chemistry* **2019**, *486*, 77-79.
246. V. M. Burlakov, M. S. Bootharaju, T. M. D. Besong, O. M. Bakr, A. J. a. C. P. Goriely, *Reversing Ostwald Ripening*, arXiv, **2014**.
247. J. R. Shimpi, D. S. Sidhaye, B. L. V. Prasad, *Langmuir* **2017**, *33*, 9491-9507.
248. K. Nikoofar, Z. Khademi, *Research on Chemical Intermediates* **2016**, *42*, 3929-3977.
249. V. Quezada-Novoa, H. M. Titi, A. A. Sarjeant, A. J. Howarth, *Chemistry of Materials* **2021**, *33*, 4163-4169.
250. Z. Chen, Ł. J. Weseliński, K. Adil, Y. Belmabkhout, A. Shkurenko, H. Jiang, P. M. Bhatt, V. Guillerm, E. Dauzon, D.-X. Xue, M. O'Keeffe, M. Eddaoudi, *Journal of the American Chemical Society* **2017**, *139*, 3265-3274.
251. I. E. Collings, M. G. Tucker, D. A. Keen, A. L. Goodwin, *Zeitschrift für Kristallographie — Crystalline Materials* **2012**, *227*, 313-320.
252. J. Lyu, X. Zhang, K.-i. Otake, X. Wang, P. Li, Z. Li, Z. Chen, Y. Zhang, M. C. Wasson, Y. Yang, P. Bai, X. Guo, T. Islamoglu, O. K. Farha, *Chemical Science* **2019**, *10*, 1186-1192.
253. S. S. Rajasree, X. Li, P. Deria, *Communications Chemistry* **2021**, *4*, 47.
254. D. Fischer, A. von Mankowski, A. Ranft, S. K. Vasa, R. Linser, J. Mannhart, B. V. Lotsch, *Chemistry of Materials* **2017**, *29*, 5148-5155.
255. A. L. Semrau, Z. Zhou, S. Mukherjee, M. Tu, W. Li, R. A. Fischer, *Langmuir* **2021**, *37*, 6847-6863.
256. I. Stassen, M. Styles, G. Grenci, Hans V. Gorp, W. Vanderlinden, Steven D. Feyter, P. Falcaro, D. D. Vos, P. Vereecken, R. Ameloot, *Nature Materials* **2016**, *15*, 304-310.
257. O. Shekhah, J. Liu, R. A. Fischer, C. Wöll, *Chemical Society Reviews* **2011**, *40*, 1081-1106.
258. O. A. D. v. Mankowski, *Post-synthetic modification of MOF nanoparticles,* Ludwig Maximilian University of Munich, Munich, **2018**.
259. N. Sahu, B. Parija, S. Panigrahi, *Indian Journal of Physics* **2009**, *83*, 493-502.
260. D. Ray, S. Goswami, J. Duan, J. T. Hupp, C. J. Cramer, L. Gagliardi, *Chemistry of Materials* **2021**, *33*, 1182-1189.
261. Y.-C. Chen, W.-H. Chiang, D. Kurniawan, P.-C. Yeh, K.-i. Otake, C.-W. Kung, *ACS Applied Materials & Interfaces* **2019**, *11*, 35319-35326.
262. Y. Kobayashi, B. Jacobs, M. D. Allendorf, J. R. Long, *Chemistry of Materials* **2010**, *22*, 4120-4122.
263. Z. Hao, G. Yang, X. Song, M. Zhu, X. Meng, S. Zhao, S. Song, H. Zhang, *Journal of Materials Chemistry A* **2014**, *2*, 237-244.
264. S. Goswami, D. Ray, K.-i. Otake, C.-W. Kung, S. J. Garibay, T. Islamoglu, A. Atilgan, Y. Cui, C. J. Cramer, O. K. Farha, J. T. Hupp, *Chemical Science* **2018**, *9*, 4477-4482.
265. M. Dogru, M. Handloser, F. Auras, T. Kunz, D. Medina, A. Hartschuh, P. Knochel, T. Bein, *Angewandte Chemie International Edition* **2013**, *52*, 2920-2924.
266. W. Lee, A. Permatasari, B. W. Kwon, Y. Kwon, *Chemical Engineering Journal* **2019**, *358*, 1438-1445.
267. Z. Li, G. Weng, Q. Zou, G. Cong, Y.-C. Lu, *Nano Energy* **2016**, *30*, 283-292.

APPENDICES

LIST OF ABBREVIATIONS

°C	degree Celsius
1D	one-dimensional
3D	three-dimensional
Å	Ångström
BDC	1,4-benzenedicarboxylate
BET	Brunauer-Emmett-Teller
BTC	benzene-1,3,5-tricarboxylic acid
BzA	benzoic acid
CN	coordination number
CPMAS	cross polarization magic angle spinning
C_Q	coupling constants
DEF	*N,N*-Diethylformamide
DFT	density functional theory
DHTP	2,5-dihydroxyterephthalic acid
DMA	*N,N*-dimethylacetamide
DMF	*N,N*-Dimethylformamide
dPCN	disordered porous coordination network
HKUST	Hong Kong University of Science and Technology
HR-TEM	high-resolution transmission electron microscopy
HSAB	hard and soft acids and bases
IRMOF	isoreticular MOF
IUPAC	International Union of Pure and Applied Chemistry
K	Kelvin
MAS	magic angle spinning

MIL	Matériaux de l′Institut Lavoisier
MOF	metal–organic framework
MTB	methanetetrabenzoic acid
MTBC	4',4",4"',4""-methanetetrayltetrabiphenyl-4-carboxylic acid
MW	microwave
NMR	nuclear magnetic resonance
NU	Northwestern University
OAc	acetate
PCC	Pearson correlation coefficient
PCN	porous coordination network
PDF	pair distribution function
ppm	part per million
PXRD	powder X-ray diffraction
qCPMG VOCS	quadrupolar Carr-Purcell-Meiboom-Gill variable offset cumulative spectroscopy
R_W	residual value
SALI	solvent-assisted ligand incorporation
SC	single crystal
SBU	secondary building unit
SCXRD	single crystal X-ray diffraction
SEM	scanning electron microscopy
ssNMR	solid-state nuclear magnetic resonance
TCPP	tetrakis(4-carboxyphenyl) porphyrin
TGA	thermogravimetric analysis
TMS	tetramethylsilane
TPDC	terphenyl-4,4’’-dicarboxylic acid
UiO	University of Oslo
VOCS	variable offset cumulative spectra
wt%	weight percent
XRD	X-ray diffraction
ZIF	zeolitic imidazolate frameworks
λ	wavelength
δ	chemical shift

APPENDIX A: ADDITIONAL INFORMATION FOR CHAPTER 2

A.1 Experimental

A.1.1 Materials

Tetrakis(4-carboxyphenyl) porphyrin (TCPP) was purchased from Tokio Chemical Industry. Zirconylchloride octahydrate and benzoic acid were purchased from Sigma Aldrich. *N,N*-Diethylformamide (DEF) was purchased from Alfa Aesar. *N,N*-Dimethylformamide (DMF) and acetone were purchased from VWR. Acetic acid and hydrochloric acid were purchased from Carl Roth. All chemicals were used as received without further purification.

A.1.2 Instruments and methods

Ultrasonication was conducted via an ELMASONIC S 100 bath equipped with a high-performance 37 kHz sandwich transducer and state-of-the-art microprocessor. An *Initiator Classic* from BIOTAGE was used for microwave assisted synthesis. Centrifugation was performed with a benchtop centrifuge *Sigma-3-30K* from SIGMA. For SEM analysis MOF suspensions were spin-coated onto silicon wafers with a *WS-650S-NPP Lite* device from LAURELL TECHNOLOGY CORPORATION.

Microscope images were taken with a CMOS camera connected to a *DM2500* light microscope from LEICA.

Scanning electron microscopy was performed with a secondary electron (SE) detector with a Merlin SEM (Zeiss). Particle sizes were investigated with the software ImageJ.

Powder X-Ray diffraction was collected at room temperature on a Stoe Stadi-P diffractometer with Cu Kα_1 radiation (λ = 1.540596 Å), a Ge(111) Johann monochromator, and a DECTRIS Mythen 1K detector in Debye-Scherrer geometry. The samples were loaded into 1 mm inner diameter polyimide capillaries and measured over a range of 2θ = 1.000–90.505˚, with 0.405˚ step size and 27 s counting time per step. The PXRD pattern of the single crystal sample was loaded into a 0.3 mm inner diameter capillary and measured over a range of 2θ = 2.000–20.255˚, with

2.61˚ step size and 50 s counting time per step. The software package WinXPOW was used to analyze all data obtained by powder diffractometry and to simulate theoretical diffraction patterns.

Pawley and Rietveld refinements were performed using TOPAS v6 on diffraction data collected using Cu Kα_1 radiation. All refinements were performed using a 2θ offset correction, full axial model, and Lorentzian and Gaussian strain and crystallite size broadening convolutions to correct for instrumental and morphological peak-shape effects. The background was defined as a highly broadened Pawley phase. For Rietveld refinements of models giving a poor match to high-angle features, B_{iso} was fixed to 10.0 Å^2 for all atoms. For the *d*PCN-224-1 model, B_{iso} for linkers was fixed to 5.0 Å^2 and allowed to refine for cluster atoms. For the *d*PCN-224-2 model, both values were allowed to refine.

All models with only cluster and linkers, regardless of occupancies of any components, did not produce enough intensity to match the 100 diffraction peak. Use of the resulting Fourier map identified missing electron density on six locations around the clusters between the TCPP linkers. The missing intensities were successfully modeled using pseudo-atoms[1] (defined as Ag atoms in the crystal structure) with large atomic displacement parameters. Since all oxygen sites on the cluster were left at 100% occupancy, the additional electron density could be accounted for primarily by additionally coordinating layers of water, as seen in NMR of undried samples, though we expect that some contributions from other coordinating species is possible.

Single crystal X-Ray diffraction data were collected at 100 K with a D8-Venture X-ray diffractometer equipped with a Photon III detector (Bruker AXS, Karlsruhe, Germany), a microfocus X-ray source IμS 3.0 (Cu Kα radiation, Incoatec, Geesthach, Germany), and a Cryostream 800 cooling device (Oxford Cryosystems, Oxford, U.K.). The crystal was mounted with some high-viscous oil on a loop made of Kapton foil. The reflection intensities were integrated with the SAINT subprogram in the Bruker Suite software package.[2] A multi-scan absorption correction was applied using SADABS.[3] The structure was solved by direct methods and refined by full-matrix least-squares fitting with the SHEXTL software package.[4,5]

Pair distribution function analysis was carried out using P02.1, the Powder Diffraction and Total Scattering Beamline, at PETRA III of the Deutsches Elektronen-Synchrotron (DESY). The rapid acquisition PDF method (RAPDF)[6] was used with a large-area 2D PerkinElmer detector (2048×2048 pixels, 200×200 μm each) and sample-to-detector distance of 335.8767 mm. The incident energy of the x-rays was 59.850 keV (λ = 0.20716 Å). Samples were loaded into 1 mm inner diameter polyimide capillaries. An empty capillary was measured as background and subtracted, and a LaB6 standard was measured at room temperature for calibration of the setup.

Calibration, polarization correction, and azimuthal integration to 1D diffraction patterns were performed using the software Fit2D.[7,8]

Additional total scattering measurements were performed on the same samples in-lab using a Stoe Stadi-P diffractometer with Mo Kα_1 radiation (λ = 0.7093 Å), a Ge(111) Johann monochromator, and a DECTRIS Mythen 1K detector in Debye-Scherrer geometry. Measurements were carried out over a range of 2θ = 0–106.5˚, with 0.495˚ step size, 14 s counting time per step, summed over 19 repetitions. Data were directly corrected for the 2θ offset of the instrument.

Further correction and normalization of the 1D diffraction intensities were carried out to obtain the total scattering structure function, $F(Q)$, which was Fourier transformed to obtain the PDF, $G(r)$ using PDFgetX3 within xPDFsuite.[9,10] The maximum value used in the Fourier transform of the total scattering data was 15.55 Å^{-1} for the synchrotron data and 14.2 Å^{-1} for the Mo Kα_1 laboratory data.

Solid-state NMR studies of ^{1}H were performed on Bruker Avance III HD spectrometers at external magnetic fields of 14.1 T (ν_0 = 600.1 MHz) and 23.4 T (ν_0 = 1 GHz), respectively. Measurements were carried out in 1.3 mm HFXY MAS triple-resonance probes with commercial ZrO_2 rotors at a rotation frequency of 62.5 kHz. RF nutation frequency was set to 200 kHz / 150 kHz, with pulse lengths of 1.1 µs / 1.7 µs, 128 scans / 64 scans, a recycle delay of 10 seconds for ν_0 = 600.1 MHz and a recycle delay optimized on the sample for measurements at ν_0 = 1 GHz. 2D homonuclear ^{1}H correlation spectra (ν_0 = 600.1 MHz) were recorded using the double-quantum (DQ) recoupling sequence $R12_2^5$ composed of 180° pulses with a recoupling time of 128µs.[11,12]

^{91}Zr NMR spectra were recorded at a magnetic field of 14.1 T (ν_0 = 55.79 MHz) at lowered temperature of approximately 120 K in a static triple resonance HFXY wide bore probe. Acquisition of spectra was performed by qCPMG sequence with 160’000 scans per spectrum and 32 echoes acquired per scan.[13–15] Recycle delay was set to 0.25 s. For accumulation of the whole spectrum, successive measurements with offsets of 50 kHz each were recorded (variable offset cumulative spectra). ^{91}Zr NMR spectroscopic experiments did not reveal any significant Zr background.

^{13}C and ^{15}N CPMAS NMR spectra were recorded on a Bruker AvanceIII HD spectrometer with an external magnetic field of 9.4 T and Larmor frequency of $\nu(^{13}C)$ = 100.58 MHz and $\nu(^{15}N)$ = 60.83 MHz, respectively. Measurements were carried out in a 3.2 mm HFXY MAS triple-resonance wide bore probe with spinning speed of 12.5 kHz (^{13}C) and 10 kHz (^{15}N). For the measurements initial ^{1}H nutation frequencies were set to 100 kHz, with a pulse length of 2.6 µs for initial $\pi/2$ pulse. The contact times and nutation frequencies of the ^{13}C channel were set to 3 ms

and 62.5 kHz, while for ^{15}N CPMAS a contact time of 5 ms and approximately 60 kHz was utilized. For the ^{1}H channel the field strength was ramped linearly from 50 to 70 kHz.[16] Heteronuclear decoupling was performed with SPINAL-64 sequence[17] and a ^{1}H nutation frequency of 65 kHz with phase increments of 5 degrees and pulse lengths of 5.9 µs. A recycle delay of 2 s was used with 32'768 scans for ^{13}C CPMAS and 153'664 scans for ^{15}N CPMAS, respectively. All ^{1}H and ^{13}C spectra are referenced indirectly with respect to tetramethylsilane (TMS) using adamantine as secondary reference and ^{15}N spectra were referenced to ammonium nitrate.

DFT-D plane-wave calculations were carried out using the CASTEP 17.2 code.[18] The GGA with PBE functional was used.[19] A plane-wave basis set was utilized with an energy cutoff of 600 eV, and the electrons were represented by ultrasoft pseudopotentials. k points were distributed using a Monkhorst-Pack-grid[20] with spacing of 0.03 Å^{-1}. Tkatchenko-Scheffler semiempirical dispersion correction was employed.[21] NMR parameters were calculated using the GIPAW approach.[22]

Computational models were built from structures obtained by total scattering pair distribution function (PDF) analysis of *d*PCN-224. Structures for presented model compounds were optimized on PBE0-D3/def2-mSVP[23–26] level of theory. Subsequent frequency calculations were performed on the same level of theory to ensure all minima to be true minima on the potential energy hypersurface, where indicated. All calculations were carried out using Turbomole in version V7.3.[27]

A.1.3 Synthetic procedures

Synthesis $Zr_6O_4(OH)_4(Bz)_{12}$ cluster

The cluster was synthesized based on reported procedures with some changes.[28,29] 70 wt% $Zr(OPr)_4$ in 1-propanol (4.56 mL, 10.2 mmol) and benzoic acid (26.7 g, 0.218mmol) were added to 1-propanol (80 mL) in a round bottom flask (250 mL). The solution was sonicated for 20 min. The reaction mixture was heated in an oil bath (15 h, 110 °C) under reflux and stirring. The solvent was removed under vacuum at 40 °C. The precipitate was intensively washed with 1-propanol over a suction filter, dried at 40 °C, and identified as $Zr_6O_4(OH)_4(OBz)_{12}(PrOH)\cdot 4BzOH$ (short $Zr_6O_4(OH)_4Bz_{12}$) cluster via PXRD analysis.

Synthesis of MOF_$ZrCl_4$ (according to literature)

The synthesis was carried out according to a procedure published by Feng. et al.[30] with prolonged synthesis time for increased crystallinity. $ZrCl_4$ (7.0 mg, 0.03 mmol), TCPP (10.0 mg, 0.0127 mmol), and seven drops of acetic acid were ultrasonically dissolved in DEF (2.0 mL) in an 8 dram glass vial. The mixture was heated in an oven (24 h, 120 °C). The reaction product was recovered by centrifugation and left to dry at 60 °C overnight.

Half of the product (4.0 mg) was resuspended in DMF (2.0 mL) and activated with HCl (8M, 50 µL) in an oven (15 h, 100 °C). The product was collected by centrifugation and washed with DMF (three times, 16k rpm/20 min/16 °C) and acetone (twice, 16k rpm/8 min/16 °C). The mixture was soaked in acetone overnight and washed with acetone one more time. Centrifugation (16k rpm/5 min/16 °C) and drying for 3 h at room temperature yielded a purple powder as product.

Synthesis of MOF_$ZrOCl_2$

$ZrOCl_2 \cdot 8H_2O$ (98.8 mg, 0.307 mmol) and benzoic acid (1.30 g, 10.6 mmol) were solved in DMF (18 mL) in a 20 mL microwave vial by sonication for 2 min and heated in a microwave (1 h, 100 °C) under stirring. After cooling, TCPP (44.8 mg, 0.0567 mmol) was added and dissolved *via* sonication. The reaction mixture was heated in a microwave (1 h, 130 °C) under stirring, washed with DMF (three times, 16k rpm/15 min/16 °C) and resuspended in DMF (10 mL). The suspension was activated with HCl (8M, 0.20 mL) in an oven (15 h, 100 °C). The product was collected by centrifugation and washed with DMF (three times, 16k rpm/20 min/16 °C) and acetone (twice, 16k rpm/8 min/16 °C). The mixture was soaked in acetone overnight and washed with acetone one more time. Centrifugation (16k rpm/5 min/16 °C) and drying for 3 h at room temperature yielded a purple powder as product.

Synthesis of MOF_$ZrOCl_2$_(II)

For comparison, an additional PCN-221 (*d*PCN-224) sample was synthesized from $ZrOCl_2 \cdot 8H_2O$ derived from a PCN-224 protocol[32]. $ZrOCl_2 \cdot 8H_2O$ (120 mg, 0.372 mmol), TCPP (40.0 mg, 0.0506 mmol) and benzoic acid (1.30 g, 10.6 mmol) were dissolved in DMF (8.0 mL) in a 20 mL microwave vial *via* sonication. The solution was heated in an oven (24 h, 120 °C), washed with DMF (three times, 16k rpm/15 min/ 16 °C) and resuspended in DMF (10 mL). The reaction mixture was activated with HCl (8M, 0.50 mL) in an oven (15 h, 100 °C). The suspension was washed with DMF (twice, 16k rpm/20 min/16 °C) and acetone (twice, 16k rpm/8 min/ 16 °C). The mixture was soaked in acetone overnight and washed with acetone one more time. The product was obtained as purple powder.

Synthesis of MOF_Zr_6

$Zr_6O_4(OH)_4Bz_{12}$ cluster (138 mg, 0.372 mmol), TCPP (44.8 mg, 0.0567 mmol) and benzoic acid (1.20 g, 9.83 mmol) were dissolved in DMF (8.0 mL) in a 20 mL microwave vial *via* sonication. The solution was heated in an oven (24 h, 120 °C), washed with DMF (three times, 16k rpm/15 min/16 °C) and resuspended in DMF (10 mL). The reaction mixture was activated with HCl (8M, 1.0 mL) in an oven (15 h, 100 °C). The suspension was washed with DMF (twice, 16k rpm/20 min/16 °C) and acetone (twice, 16k rpm/8 min/16 °C). The mixture was soaked in acetone overnight and washed with acetone one more time. The product was obtained as purple powder.

Synthesis of experimental PCN-224

The synthesis was carried out based on a MOF-525 procedure published by Morris et al.[31] in which PCN-224 was yielded instead of MOF-525. $ZrOCl_2 \cdot 8H_2O$ (188 mg, 0.582 mmol) and TCPP (37.5 mg, 0.047 mmol) were dissolved in DMF (150 mL) in a 500 mL laboratory bottle *via* sonication. Acetic acid (37.0 mL, 647 mmol) was added and the mixture was sonicated again. The reaction mixture was heated in an oven (72 h, 65 °C), washed with DMF (twice, 16k rpm/15 min/16 °C) and resuspended in DMF (10 mL). The suspension was activated with HCl (8M, 0.50 mL) in an oven (15 h, 100°C). The product was collected by centrifugation and washed with DMF (twice, 16k rpm/20 min/16 °C) and acetone (twice, 16k rpm/8 min/16 °C). The mixture was soaked in acetone overnight and washed with acetone one more time. Centrifugation (16k rpm/5 min/16 °C) and drying for 3 h at room temperature yielded a purple powder as product.

Synthesis of Single Crystal

$ZrOCl_2 \cdot 8H_2O$ (30 mg, 0.093 mmol), TCPP (10.0 mg, 0.013 mmol) and benzoic acid (700 mg, 5.71 mmol) were dissolved in DMF (2.0 mL) in an 8 dram glass vial *via* sonication. The solution was heated in an oven (24 h, 120 °C), washed with DMF (three times, 16k rpm/15 min/16 °C) and resuspended in DMF (10 mL). The reaction mixture was activated with HCl (8M, 0.50 mL) in an oven (15 h, 100°C). The suspension was washed with DMF (twice, 16k rpm/20 min/16 °C) and acetone (twice, 16k rpm/8 min/16 °C). The mixture was soaked in acetone overnight washed with acetone one more time. Dark purple powder was obtained as product, composed of 10–20 µm big cubic crystals and needle-shaped crystals identified as PCN-222 impurities.

A.2 Results and discussion

A.2.1 SEM imaging

Scanning electron microscopy (SEM) images of all samples show distinctively different crystal shapes and sizes ranging from cuboctahedra/truncated cubes (MOF_$ZrCl_4$ and MOF_$ZrOCl_2$) to perfectly shaped cubes (MOF_$ZrOCl_2$_(II)), whereas no particular morphology can be identified for the crystallites of MOF_Zr_6 due to the very small size of the particles (Figure A.1). We attribute the apparent differences of the particles sizes and morphologies to the different modulators (acetic acid *vs.* benzoic acid) and relative concentrations in the synthesis, which regulate both the nucleation and growth of MOF particles and not to different crystal structures.[33–35] For comparison, PCN-224 was imaged as well, which consists of cubic particles (Figure A.2).

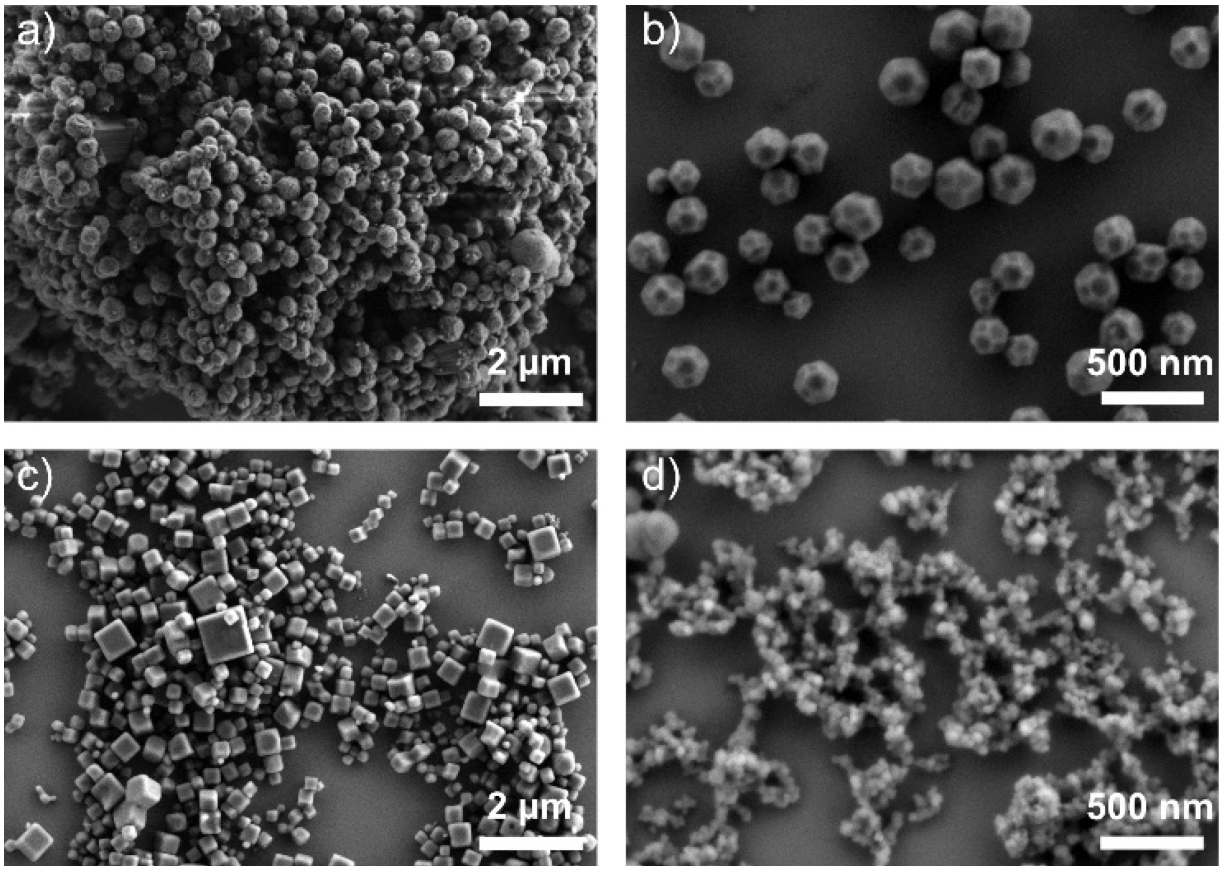

Figure A.1: Scanning electron microscopy (SEM). SEM images of a) MOF_$ZrCl_4$, b) MOF_$ZrOCl_2$, c) MOF_$ZrOCl_2$_(II), and d) MOF_Zr_6.

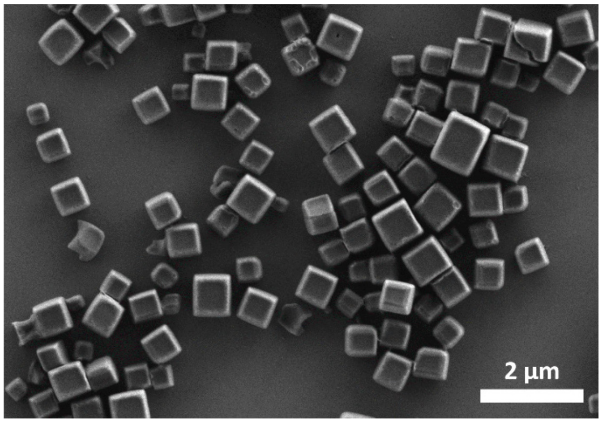

Figure A.2: Scanning electron microscopy image of experimental PCN-224.

A.2.2 Powder X-ray diffraction

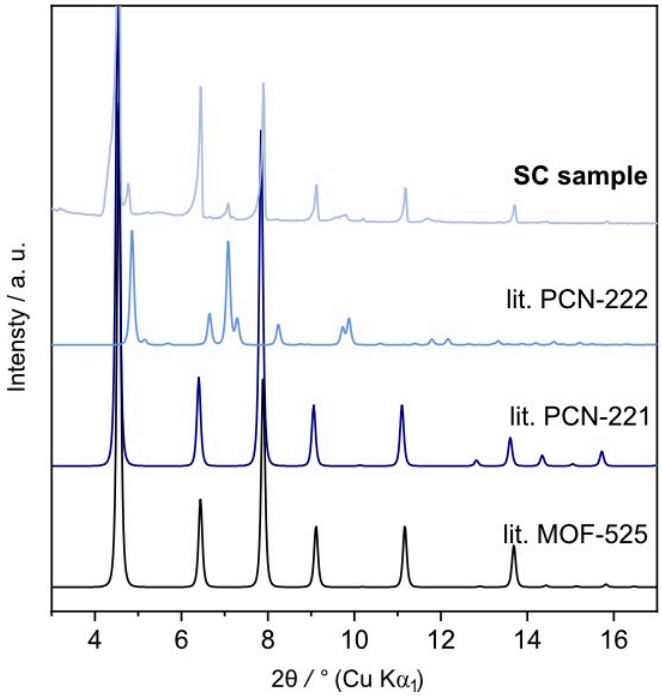

Figure A.3: Powder X-ray diffraction (PXRD) pattern of single crystal. PXRD pattern of the sample containing the measured single crystal compared to the simulated patterns (lit.) of MOF-525, PCN-221, and PCN-222.[30,31,36]

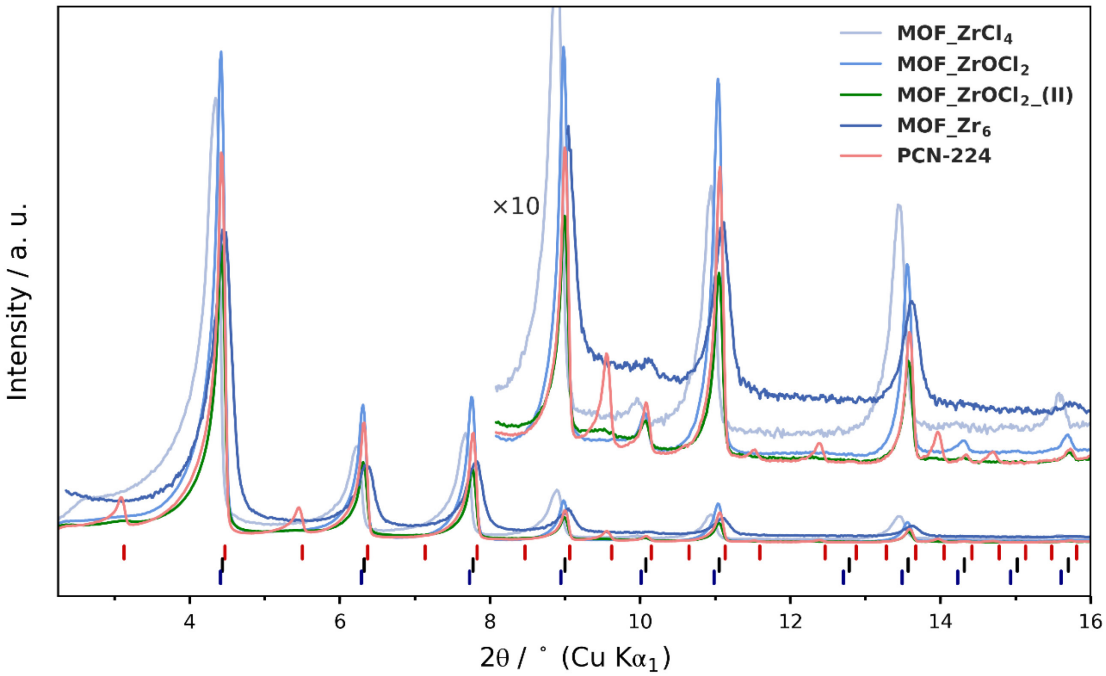

Figure A.4: Comparison of powder X-ray diffraction patterns for all samples. The patterns are also multiplied by a factor of ten beyond 8° 2θ to show a zoomed comparison of the patterns. The reflection positions for published structures are given below for reference: PCN-224 (red), MOF-525 (black), PCN-221 (purple).

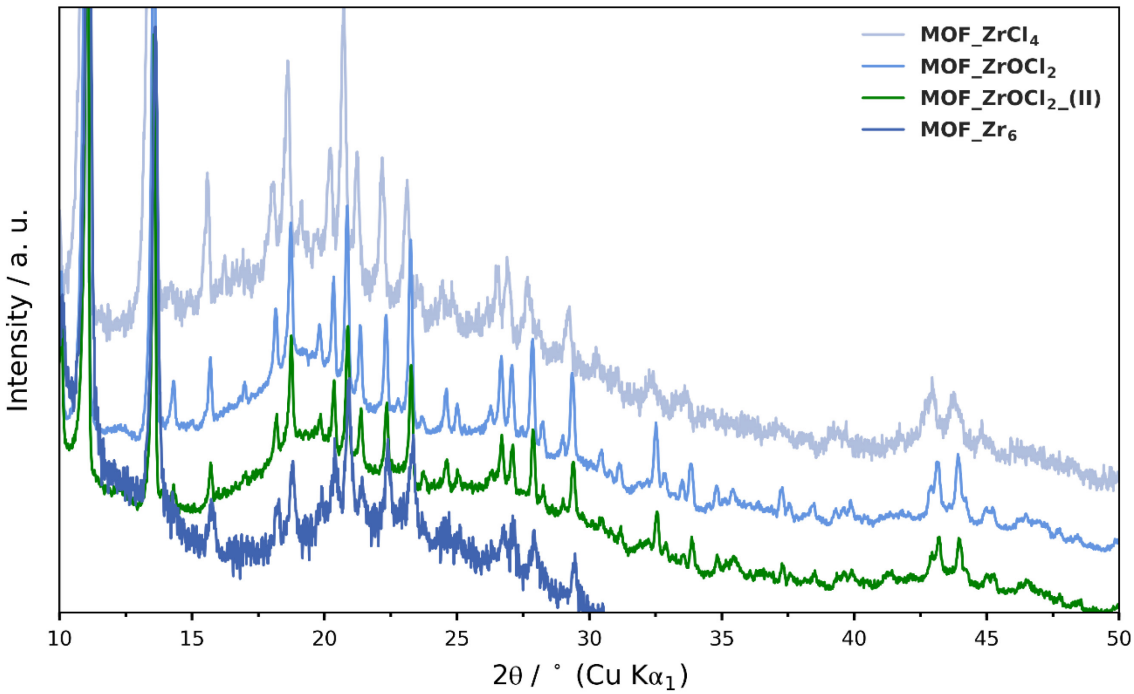

Figure A.5: Comparison of powder X-ray diffraction patterns at high ranges. Comparison for MOF_$ZrCl_4$, MOF_$ZrOCl_2$, MOF_$ZrOCl_2$_(II), and MOF_Zr_6 zoomed into a high 2θ range to show the similarity in the high-angle diffraction features. Peak positions and relative intensities match well, although there are some differences, for example a small peak in MOF_$ZrCl_4$ at approximately 19°. MOF_Zr_6 was only measured up to 30°.

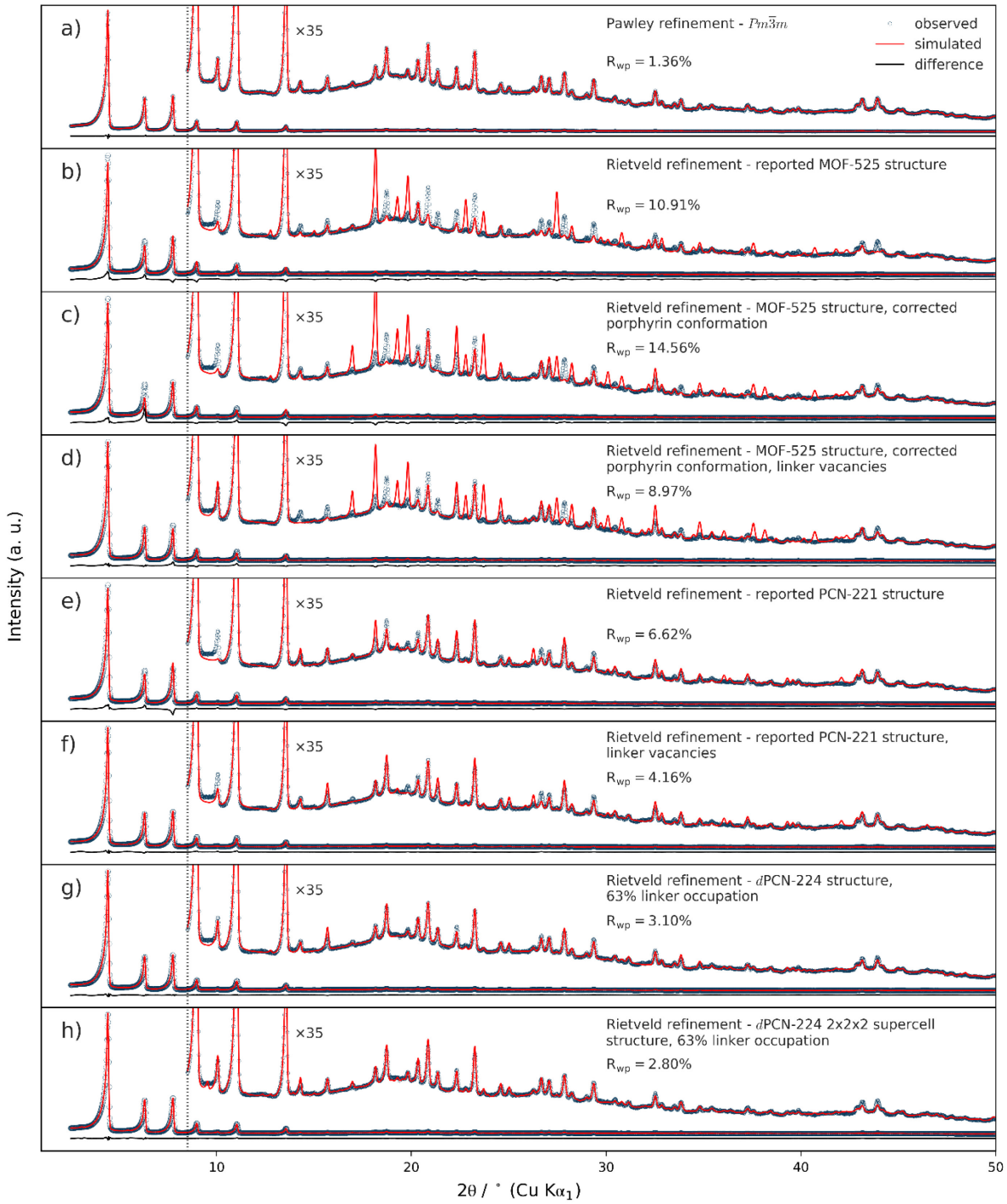

Figure A.6: Pawley and Rietveld refinements of sample MOF_ZrOCl$_2$. a) Resulting fit from Pawley refinement to the diffraction pattern of MOF_ZrOCl$_2$ using the published cell with $Pm\bar{3}m$ symmetry. Rietveld refinements to the same sample data are shown for b) published MOF-525 structure, c) MOF-525 with twisted linker conformation, d) MOF-525 with twisted linker conformation and linker vacancies, e) published PCN-221 structure with Zr_8 clusters, f) published PCN-221 structure with Zr_8 clusters and linker vacancies, g) dPCN-224-1 structure with 25% occupancy of each cluster orientation, twisted linker conformations, and linker vacancies, and h) 2x2x2 dPCN-224-2 supercell model, which allows refinement of separate occupancies for each individual linker and cluster orientation for each site. All models considered the occupancy of pseudo-atom densities at additional open sites on the cluster, which were accounted for primarily by additional water and possibly other leftover coordinating species. For this sample, both dPCN-224 models lead to linker occupation of 63%, i.e. ~7.5 linkers per cluster.

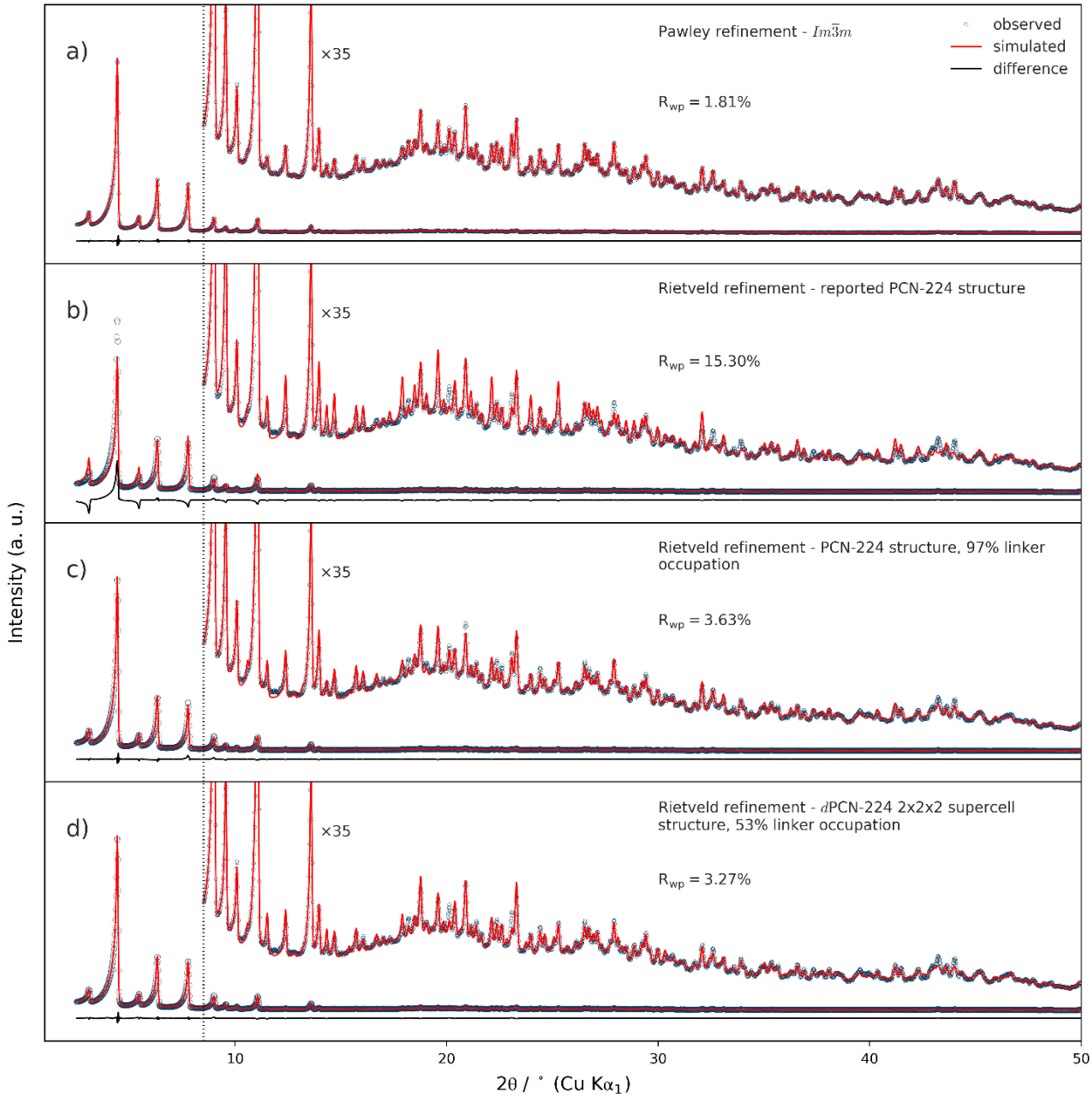

Figure A.7: Pawley and Rietveld refinements of sample PCN-224. a) Resulting fit from Pawley refinement to the diffraction pattern of PCN-224 using the published cell with Im–3m symmetry. Rietveld refinements to the same sample data are shown for b) published PCN-224 structure, c) PCN-224 with additional linker vacancies and modulator densities, and d) the dPCN-224-2 supercell model from Figure A.6(h). The PCN-224 model gave 97% linker occupation of 6 possible sites, i.e. ~5.8 linkers per cluster. In this case, the extra pseudo-atoms refined to the typical vacant tetrakis(4-carboxyphenyl) porphyrin (TCPP) sites of PCN-224. The supercell model gave slightly different occupations, i.e. ~6.4 linkers per cluster, with pseudo-atom sites on the 6 additional sites between TCPP positions.

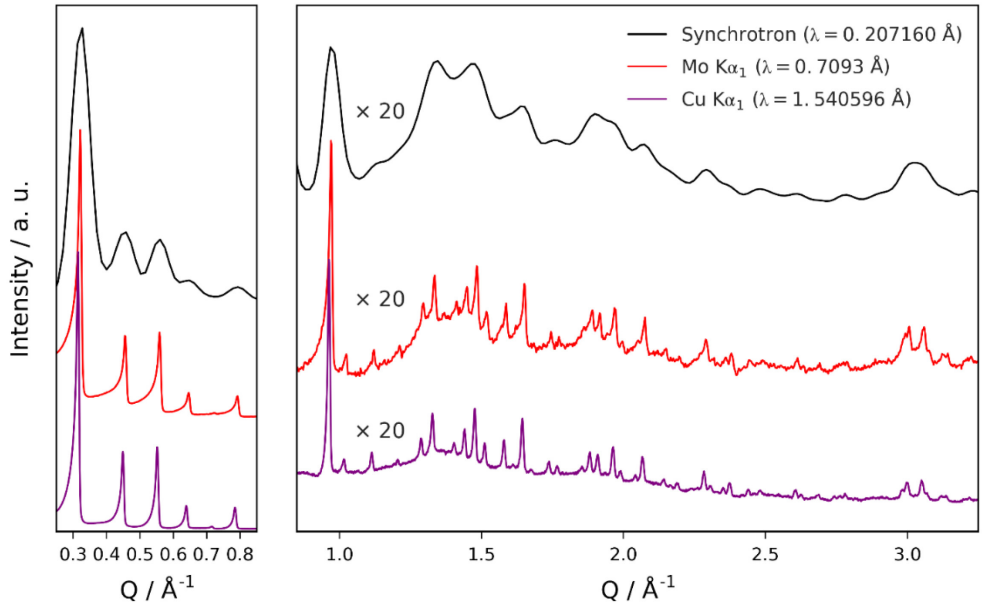

Figure A.8: Powder X-ray powder diffraction (PXRD) of sample MOF_ZrOCl$_2$_(II). PXRD intensities measured from the same MOF_ZrOCl$_2$_(II) sample (1 mm ID polyimide capillary) using synchrotron, Mo Kα_1, and Cu Kα_1 radiation. Broadening of the Bragg peaks occurs due to the increase in incident photon energies, and in the case of the synchrotron measurements, due also to decreased resolution of the detector.

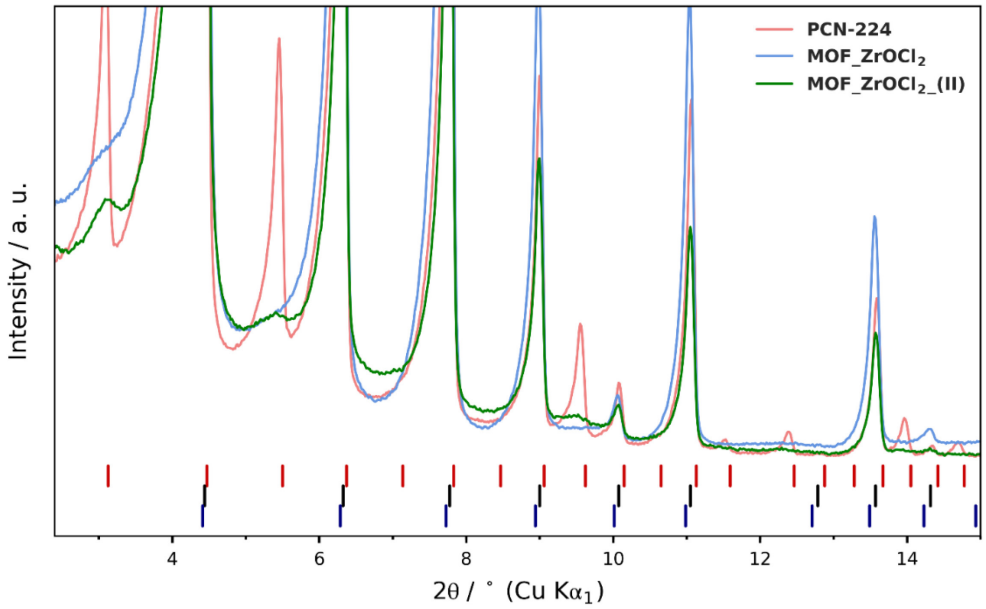

Figure A.9: Powder X-ray diffraction (PXRD) of all samples at low angles. Since the pair distribution function (PDF) refinements suggest occupational disorder of the linkers at the level of about 50–60% occupancy, we show again the PXRD patterns measured for the four samples, but zoomed closely into the low angle region. PCN-224 has two extra distinct peaks at approximately 3.1 and 5.4° 2θ, which help distinguish the Im–3m symmetry from Pm–3m. However, upon close inspection we can see that there is also very small peaks at these angles for the MOF_ZrOCl$_2$_(II) sample, and further, e.g. 9.6°. The MOF_ZrOCl$_2$ sample also shows additional diffuse intensities. This suggests that linker vacancies are random, rather than ordered in Im–3m symmetry as with PCN-224, therefore only producing diffraction effects with only limited spatial coherence.

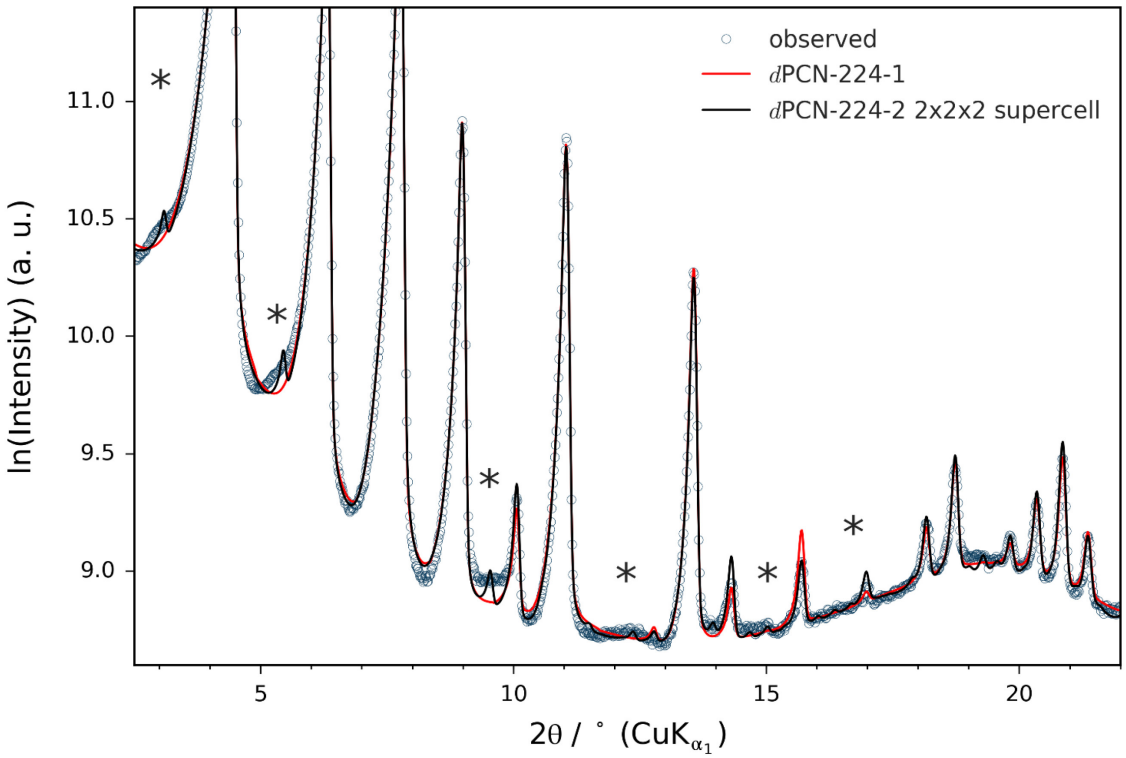

Figure A.10: Overlay of the Rietveld refinements of dPCN-224 models to the observed MOF_ZrOCl$_2$ pattern. The refinements here are from the single cell dPCN-224-1 model (red) and the 2x2x2 supercell dPCN-224-2 model (black). The fit for the supercell was performed using a P1 symmetry, and separate occupancy factors have been set for each individual porphyrin linker and each individual cluster orientation for all eight cluster sites. We see that the supercell, with lattice parameter similar to PCN 224, allows for the modeling of the additional weak intensities in the peaks at approx. 2.8, 5.1, 9.4, 12° 2θ and further, marked by black asterisks (*). In the experimental data, the peaks are broader indicating the limited spatial coherence of these features. Overall, the supercell is still only a limited expansion of the possibilities for types of linker vacancies/cluster orientation patterns which may occur locally. However, this supports the plausibility for this frustrated network picture of the structure to explain the observed data.

A.2.3 Chemical composition analysis

Chemical analysis was performed for MOF_ZrCl$_4$, MOF_ZrOCl$_2$, MOF_ZrOCl$_2$_(II), MOF_Zr$_6$, and experimental PCN-224. The theoretical and experimental weight percent of Zr, C, H, and N and the calculated Zr/C and Zr/N ratios are given in Table S1–S5. For comparison, the percentage of vacancies was calculated as function of the Zr/C or Zr/N ratio considering either modulator (benzoic acid (BzA) or acetic acid (AcA)) on the TCPP vacant sites or hydroxy groups with additional water in the pores. The polynomial fits of the Zr/C and Zr/N ratios with the amount of TCPP vacancies x, are shown in Figure A.11–A.13. We found high amounts of TCPP vacancies for all samples, including experimental PCN-224 which is reported with only 50% TCPP linkers.[37] However, solvent molecules such as water, DMF, and Acetone may remain in the pores of the MOFs, which may falsify the calculated percentage of defects.

Table A.1: Calculated chemical composition and amount of linker vacancies of $Zr_6O_4(OH)_4(TCPP)_{3-x}(BzA)_x$, where x represents the amount of tetrakis(4-carboxyphenyl) porphyrin vacancies replaced by benzoic acid.

x	3-x	Vacancies [%]	Zr [wt%]	C [wt%]	H [wt%]	N [wt%]	Zr/C	Zr/N
0.00	3.00	0.00	17.3	57.4	2.77	5.32	0.30	3.26
0.60	2.40	20.0	20.7	54.3	2.65	5.09	0.38	4.07
0.70	2.30	23.3	21.3	53.8	2.64	5.01	0.40	4.25
0.80	2.20	26.7	21.8	53.3	2.62	4.92	0.41	4.44
0.90	2.10	30.0	22.4	52.7	2.61	4.82	0.43	4.65
1.00	2.00	33.3	23.1	52.1	2.59	4.72	0.44	4.89
1.10	1.90	36.7	23.7	51.5	2.57	4.61	0.46	5.15
1.20	1.80	40.0	24.4	50.8	2.56	4.50	0.48	5.43
1.30	1.70	43.3	25.2	50.1	2.54	4.38	0.50	5.75
1.40	1.60	46.7	26.0	49.4	2.52	4.25	0.53	6.11
1.50	1.50	50.0	26.8	48.6	2.49	4.12	0.55	6.51

Table A.2: Calculated chemical composition and amount of linker vacancies of $Zr_6O_4(OH)_4(TCPP)_{3-x}(AcA)_x$, where x represents the amount of tetrakis(4-carboxyphenyl) porphyrin vacancies replaced by acetic acid.

x	3-x	Vacancies [%]	Zr [wt%]	C wt%]	H [wt%]	N [wt%]	Zr/C	Zr/N
0.00	3.00	0.00	17.7	56.6	2.77	5.42	0.31	3.26
0.60	2.40	20.0	21.0	53.7	2.64	5.17	0.39	4.07
0.70	2.30	23.3	21.6	53.1	2.63	5.09	0.41	4.25
0.80	2.20	26.7	22.3	52.4	2.61	5.02	0.43	4.44
0.90	2.10	30.0	23.0	51.7	2.59	4.93	0.44	4.66
1.00	2.00	33.3	23.7	50.9	2.57	4.85	0.46	4.88
1.10	1.90	36.7	24.4	50.1	2.55	4.75	0.49	5.15
1.20	1.80	40.0	25.3	49.2	2.53	4.66	0.51	5.42
1.30	1.70	43.3	26.1	48.3	2.51	4.55	0.54	5.75
1.40	1.60	46.7	27.1	47.3	2.48	4.44	0.57	6.10
1.50	1.50	50.0	28.1	46.2	2.46	4.31	0.61	6.52

Table A.3: Calculated chemical composition and amount of linker vacancies of $Zr_6O_4(OH)_4(TCPP)_{3-x}(OH)_x(H_2O)_{12}$, where x represents the amount of tetrakis(4-carboxyphenyl) porphyrin vacancies replaced by hydroxyl groups.

x	3-x	Vacancies [%]	Zr [wt%]	C wt%]	H [wt%]	N [wt%]	Zr/C	Zr/N
0.00	3.00	0.00	16.72	52.85	3.30	5.14	0.316	3.25
0.10	0.90	3.33	17.22	52.60	3.28	5.11	0.327	3.37
0.20	0.80	6.67	17.65	52.04	3.28	5.06	0.339	3.49
0.30	2.70	10.0	18.09	51.46	3.28	5.00	0.352	3.62
0.40	2.60	13.3	18.57	50.85	3.28	4.94	0.365	3.76
0.50	2.50	16.7	19.06	50.20	3.28	4.88	0.380	3.91
0.60	2.40	20.0	19.59	49.52	3.28	4.81	0.396	4.07
0.70	2.30	23.3	20.15	48.80	3.28	4.74	0.413	4.25
0.80	2.20	26.7	20.73	48.04	3.28	4.67	0.432	4.44
0.90	2.10	30.0	21.36	47.24	3.28	4.59	0.452	4.65
1.00	2.00	33.3	22.02	46.38	3.28	4.51	0.475	4.88
1.10	1.90	36.7	22.72	45.47	3.28	4.42	0.500	5.14
1.20	1.80	40.0	23.47	44.50	3.28	4.32	0.527	5.43
1.30	1.70	43.3	24.27	43.46	3.29	4.22	0.558	5.75
1.40	1.60	46.7	25.13	42.35	3.29	4.12	0.593	6.10
1.50	1.50	50.0	26.05	41.16	3.29	4.00	0.633	6.51

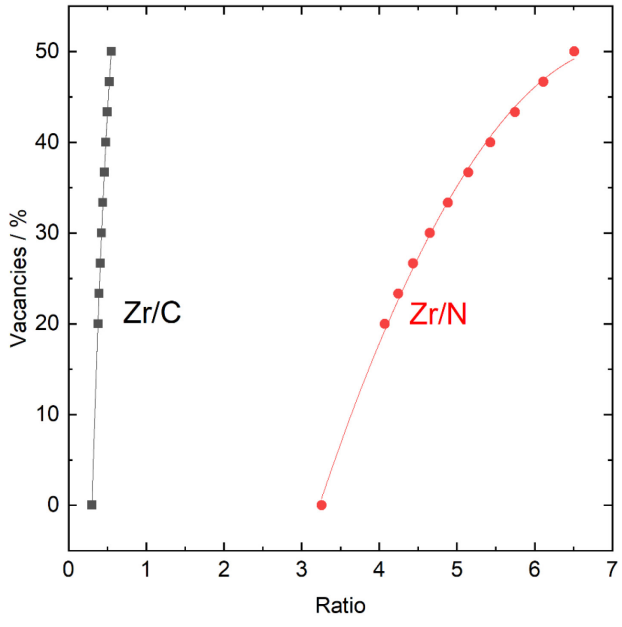

Figure A.11: Percentage of vacancies replaced by the modulator benzoic acid (BzA). Vacancies as a function of Zr/C ratio (black) and Zr/N ratio (red) in $Zr_6O_4(OH)_4(TCPP)_{3-x}(BzA)_x$ where x represents the amount of tetrakis(4-carboxyphenyl) porphyrin (TCPP) vacancies, replaced by modulator: $x = 0$ (0 % vacancies) and 0.6 (20% vacancies) $< x <$ 1.5 (50% vacancies). Polynomial fit for Zr/C (black): $y = -116.08 + 484.69x + (-333.07)x^2$ and for Zr/N (red): $y = -115.61 + 46.165x + (-3.2027)x^2$.

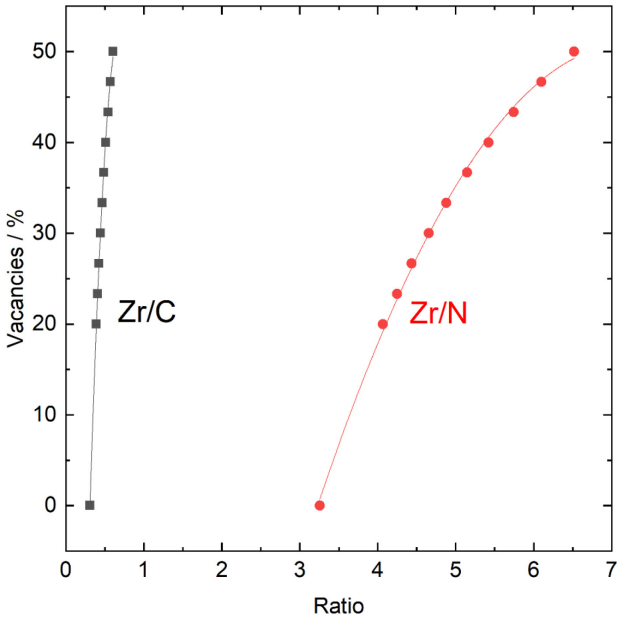

Figure A.12: Percentage of vacancies replaced by the modulator acetic acid (AcA). Vacancies as a function of Zr/C ratio (black) and Zr/N ratio (red) in $Zr_6O_4(OH)_4(TCPP)_{3-x}(AcA)_x$ where x represents the amount of tetrakis(4-carboxyphenyl) porphyrin (TCPP) vacancies, replaced by modulator: x = 0 (0% vacancies) and 0.6 (20% vacancies) < x < 1.5 (50% vacancies). Polynomial fit for Zr/C (black): y = -117.7+ 487.4x + (-349.5)x^2 and Zr/N (red): y = -116.2 + 46.39x + (-3.223)x^2.

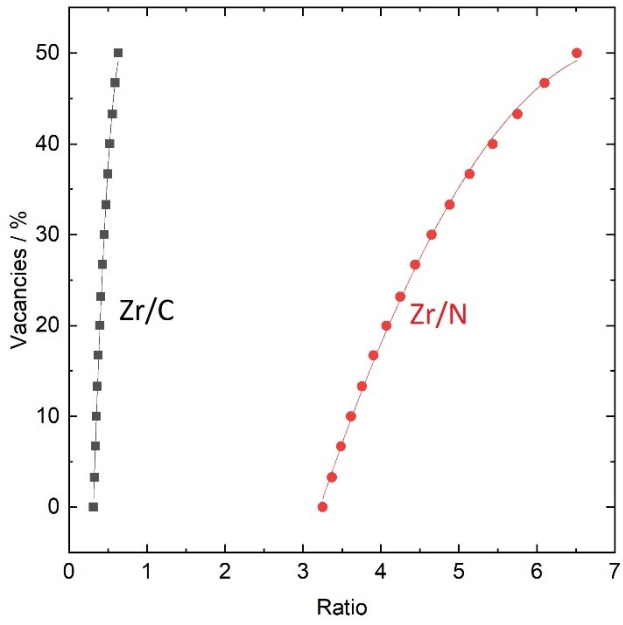

Figure A.13: Percentage of vacancies replaced by hydroxyl groups. Vacancies as a function of Zr/C ratio (black) and Zr/N ratio (red) in $Zr_6O_4(OH)_4(TCPP)_{3-x}(OH)_x(H_2O)_{12}$ where x represents the amount of tetrakis(4-carboxyphenyl) porphyrin (TCPP) vacancies, replaced by hydroxy groups: x = 0 (0% vacancies) < x < 1.5 (50% vacancies). Polynomial fit for Zr/C (black): y = -115.1+ 474.2x + (-339.1)x^2 and Zr/N (red): y = -114.9 + 45.99x + (-3.193)x^2.

Table A.4: Particle sizes determined from scanning electron microscopy images and chemical compositions of synthesized MOFs.

	Size [nm]	Zr [wt%]	C [wt%]	H [wt%]	N [wt%]	Zr/C	Zr/N
MOF_$ZrCl_4$	427(111)	19.82	48.25	3.84	4.63	0.411	4.28
MOF_$ZrOCl_2$	182(34)	21.1	46.27	3.49	4.01	0.456	5.26
MOF_$ZrOCl_2$_(II)	233(117)	22.3	42.50	3.45	3.92	0.525	5.69
MOF_Zr_6	39(11)	23.3	46.90	3.31	4.50	0.496	5.17
Exp. PCN-224	469(129)	23.47	41.22	3.49	3.67	0.569	6.40

Table A.5: Zr/C and Zr/N ratios obtained from chemical composition analysis of synthesized MOFs and calculated amount of linker vacancies with and without modulator on the vacant sites.

	Zr/C	Zr/N	Vacancies with mod. Zr/C [%]	Vacancies with mod. Zr/N [%]	Vacancies without mod. Zr/C [%]	Vacancies without mod. Zr/N [%]
MOF_$ZrCl_4$	0.411	4.28	23.6	23.3	22.5	23.4
MOF_$ZrOCl_2$	0.456	5.26	35.7	38.7	30.6	38.7
MOF_$ZrOCl_2$_(II)	0.525	5.69	46.6	43.4	40.4	43.4
MOF_Zr_6	0.496	5.17	42.4	37.5	36.7	37.5
Exp. PCN-224	0.569	6.40	46.5	48.7	44.9	48.7

A.2.4 Pair distribution function analysis

The Zr–Zr pair distance reported for the Zr_8O_6 cluster in the PCN-221, structure reported by Feng et al.[30], is r = 2.688 Å. This is significantly contracted when compared to the Zr–Zr distance expected, for instance, for the Zr_6 cluster. To get a sense for the likelihood of the Zr_8 Zr–Zr distance to exist, we performed a meta-analysis of the Zr–Zr nearest neighbor (NN) pair distances reported for both other metal–organic structures obtained from the Cambridge Crystallographic Data Centre (CCDC) and inorganic structures obtained from the Inorganic Crystal Structure Database (ICSD). CCDC structures were obtained from the WebCSD portal. A formula search was performed with the following criteria (Zr > 1, O > 1, C > 1, H > 1), netting at the time 472 structures. Further filtering of structures was determined by the following criteria. It was determined that all structures containing Zr–O bond distances below 1.8 contained spurious structural errors or disordered sites which do not make sense in a true local structural sense, and were not considered *(CCDC 1858054, CCDC 1006913, CCDC 1976030, CCDC 1588089, CCDC 1858052, CCDC 1838332, CCDC 1838334, CCDC 955328, CCDC 1580358, CCDC 1587886, CCDC 1908939, CCDC 1908940).* Structures which contained Zr–Zr distances below 3.0 were determined to contain disordered sites or Zr_8-type clusters, and were not included *(CCDC 1955286, CCDC 1850690, CCDC 1486878, CCDC 1471480, CCDC 1487038).* Structures with Zr–Zr distances above 4.0, which were not

connected by an oxygen, were not included, and some structures contained no atomic coordinates. Structures from the ICSD were filtered by structures that contain only Zr and O, and which were obtained at ambient pressure, and at 300 K or below. This resulted in 92 structures.

Bond distances for all structures were determined using the python code from xPDFsuite software program.[10] In the case of the CCDC structures, there are still some significant outliers, though we did not further check the remaining structures for quality markers, and other structures with mistakes or disordered sites may still be represented in the list. Either way, it is clear that the Zr–Zr distances for the Zr_8O_6 cluster is an extreme outlier, despite the representation of a wide variety of ZrO based molecular cluster stoichiometries. The case is the same for comparison to inorganic ZrO crystal structures, indicating that this Zr_8O_6 motif is highly unlikely based on known structuring behavior.

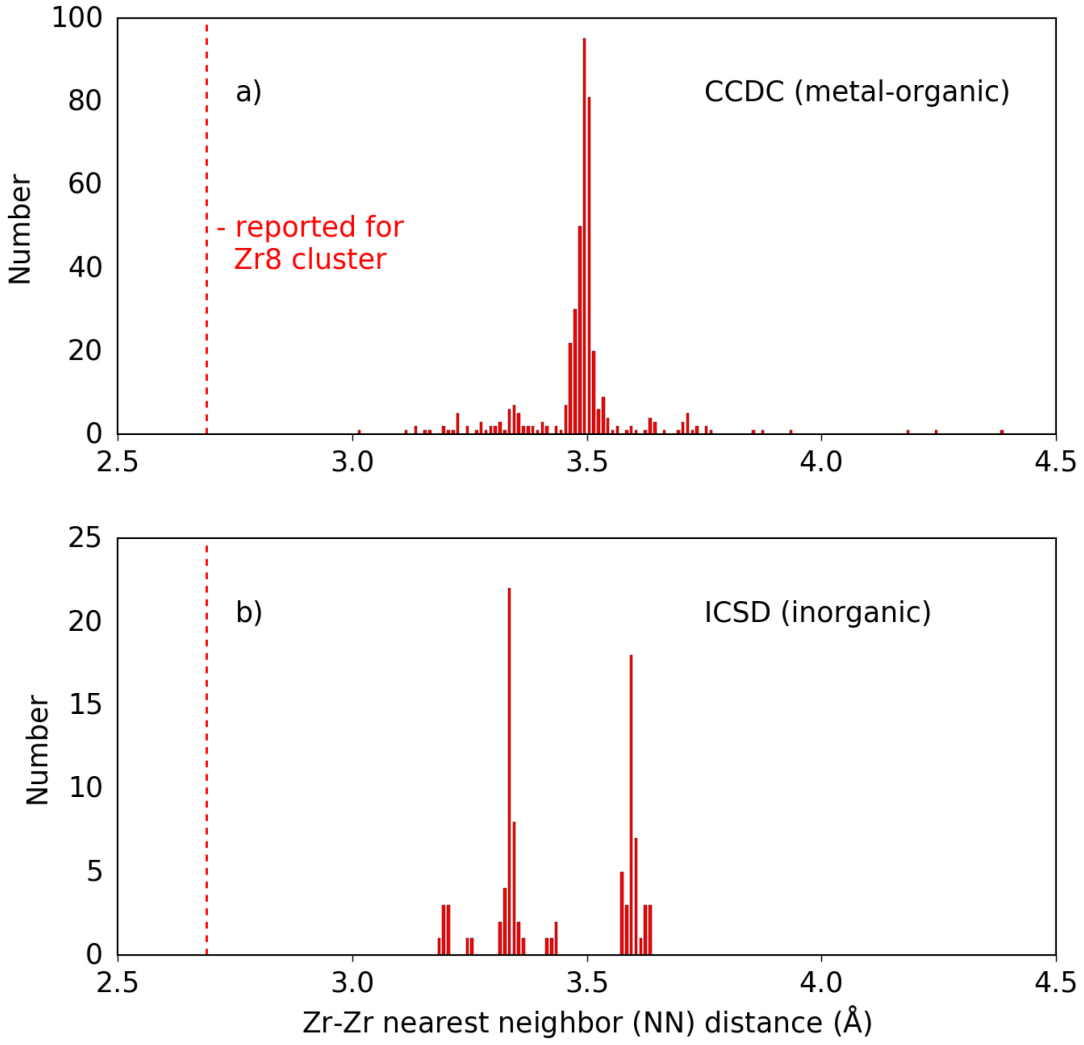

Figure A.14: Distribution of first nearest neighbor (NN) Zr–Zr pair distances. Distribution observed in structures obtained from a) CCDC and b) ICSD structure databases. A red dashed line is shown indicating the Zr–Zr pair distance reported for the Zr_8 cluster, which is an extreme outlier.

Analysis of the PDF provides a useful method for interpreting structure information from total scattering data. It provides a sensitive probe of the local structure in amorphous and nanostructured materials, because it does not require symmetry, and treats both Bragg and diffuse scattering equally.[38] A diffraction measurement over a wide range of momentum transfer and with good statistics is required to obtain suitable PDFs for structure analysis. To obtain the PDF, the measured coherent powder diffraction intensities are first normalized by the average form factor squared to obtain the total scattering structure function $S(Q)$, defined as

$$S(Q) = \frac{I(Q) - \langle f(Q)^2 \rangle + \langle f(Q) \rangle^2}{\langle f(Q) \rangle^2}.$$

The experimental PDF, denoted $G(r)$, is the truncated Fourier transform of the reduced, total scattering structure function, $F(Q) = Q[S(Q) - 1]$, as

$$G(r) = \frac{2}{\pi} \int_{Q_{min}}^{Q_{max}} F(Q) sin(Qr) dQ,$$

where $G(r)$ is the magnitude of the scattering momentum transfer. For elastic scattering,

$$Q = 4\pi sin\theta / \lambda,$$

where λ is the probe wavelength and 2θ is the scattering angle. In practice, values of Q_{min} and Q_{max} are determined by the experimental setup, and Q_{max} is often reduced below the experimental maximum to reduce the effects of low signal-to-noise in the high-Q region on the Fourier transformation. To aid in qualitative assessment of the long-distance structural correlations, a modification function can be applied to $F(Q)$ prior to Fourier transformation by,

$$G(r) = \frac{2}{\pi} \int_{Q_{min}}^{Q_{max}} M(Q) F(Q) sin(Qr) dQ$$

and,

$$M(Q) = \frac{sin(Qr_{ij})}{Qr_{ij}}.$$

$M(Q)$ is called a modification function, in this case a Lorch function[39,40], which damps the intensity of $F(Q)$ to 0 at Q_{max}. This reduces the effects of termination from high-Q signal and noise intensities in the reduced structure function, which suppresses non-structural high frequency oscillations in the PDF. In this study, a Lorch function was only used for processing PDFs from the Mo $K\alpha_1$ measurements, for qualitative analysis.

The PDF gives the scaled probability of finding two atoms in a material a distance r apart and is relative to the density of atom pairs in the material. For a macroscopic scatterer, $G(r)$ is calculated from a known structure model according to

$$G(r) = 4\pi r[\rho(r) - \rho_0],$$

$$\rho(r) = \frac{1}{4\pi r^2 N}\sum_i \sum_{j \neq i} \frac{f_i f_j}{\langle f \rangle^2} \delta(r - r_{ij}).$$

Here, ρ_0 is the average number density of the material and ρ(r) is the local atomic pair density, which is the mean weighted density of neighbor atoms at distance r from an atom at the origin. The sums in $\rho(r)$ run over all atoms in the sample, f_i is the scattering factor of atom i, $\langle f \rangle$ is the average scattering factor and r_{ij} is the distance between atoms i and j. In this study, these equations were used to fit the PDF generated from a structure model to the experimental PDFs in using the program PDFgui.[41] The delta functions were Gaussian-broadened to account for atom displacements and the finite Q_{range} of the experiment, and the equation was modified to account for signal damping and broadening due to experimental effects. PDF modeling was performed by adjusting the lattice parameter *a***,** atomic displacement parameters (ADPs) for Zr, O, and the linkers, correlated motion of neighboring atoms using *rcut* and *sratio* parameters to sharpen peaks within cluster or linker components, domain size (*spdiameter*), and a global scale factor. The refinements were run by minimizing R_w, calculated as

$$R_w = \sqrt{\frac{\sum_{i=1}^{n}[G_{obs}(r_i) - G_{calc}(r_i, P)]^2}{\sum_{i=1}^{n} G_{obs}(r_i)^2}},$$

which was used to quantify the goodness-of-fit for the model.

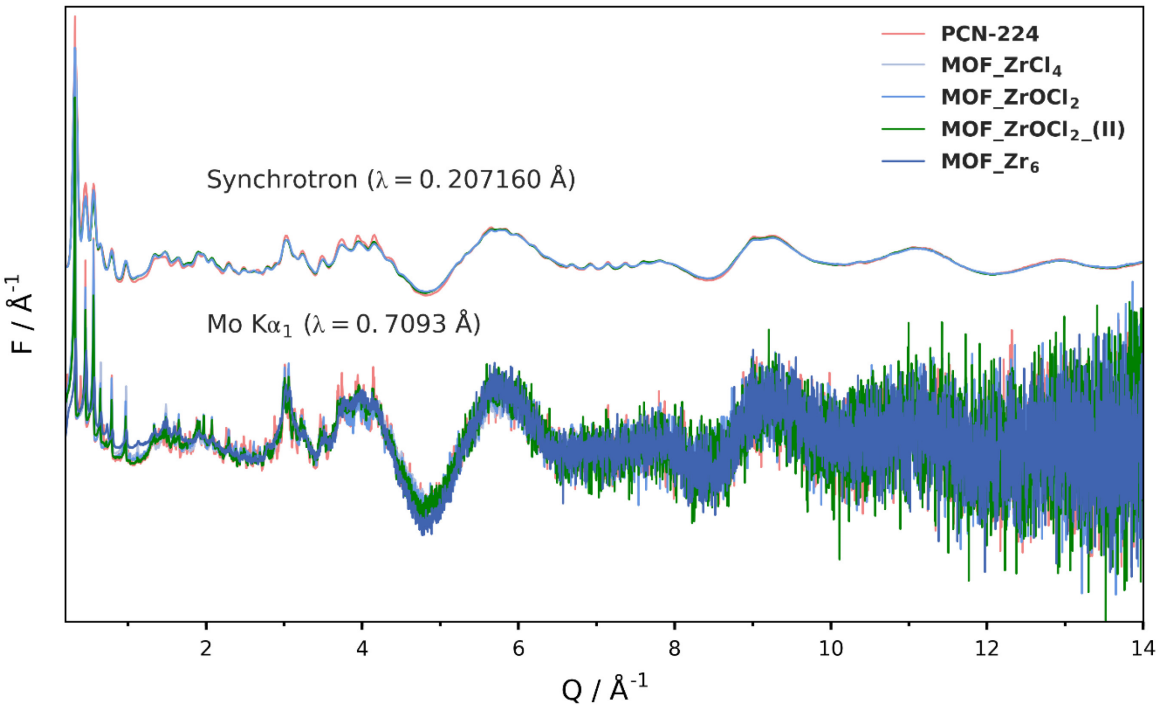

Figure A.15: Reduced X-ray total scattering $F(Q)$. Patterns are shown as obtained from both synchrotron and Mo $K\alpha_1$ measurements. The signal-to-noise is significantly improved in the synchrotron data.

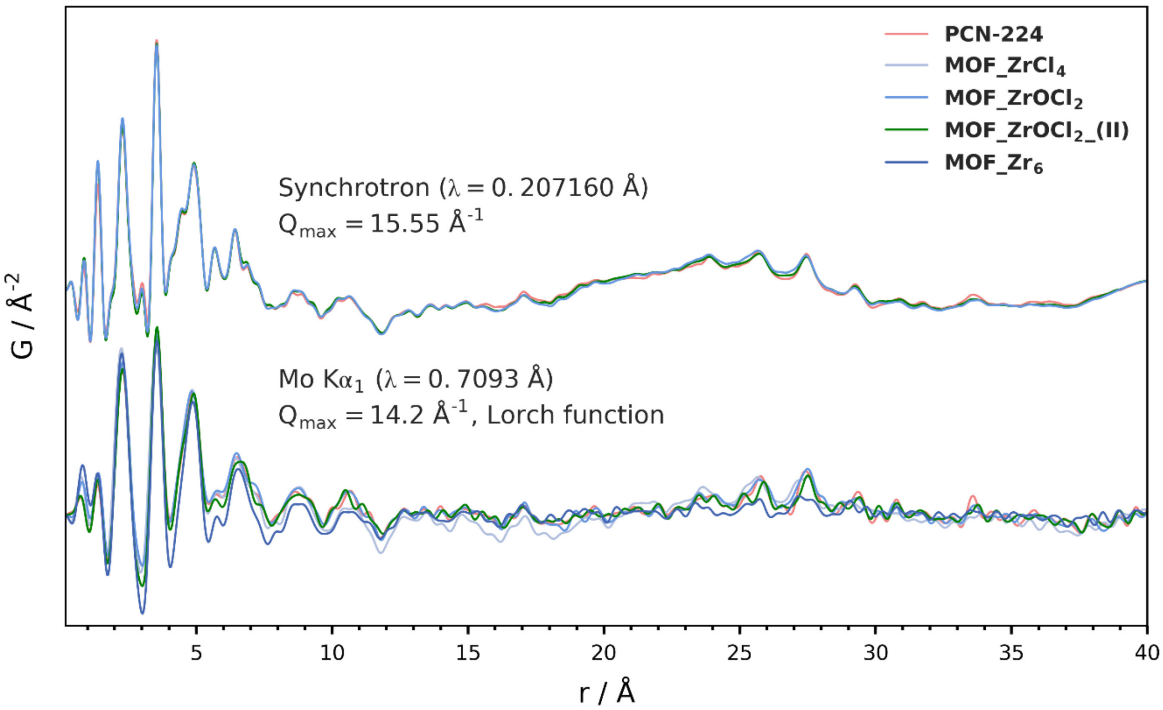

Figure A.16: Pair distribution functions $G(r)$ (PDFs) of all samples. PDFs shown as obtained from both synchrotron and Mo $K\alpha_1$ measurements. The Mo $K\alpha_1$ PDFs were obtained by Fourier transformation of the reduced structure function after multiplication with a Lorch function to reduce the effects of low signal-to-noise at high Q. There is good agreement between the PDFs obtained for all samples, indicating that the local and intermediate range ordering is very similar for all samples.

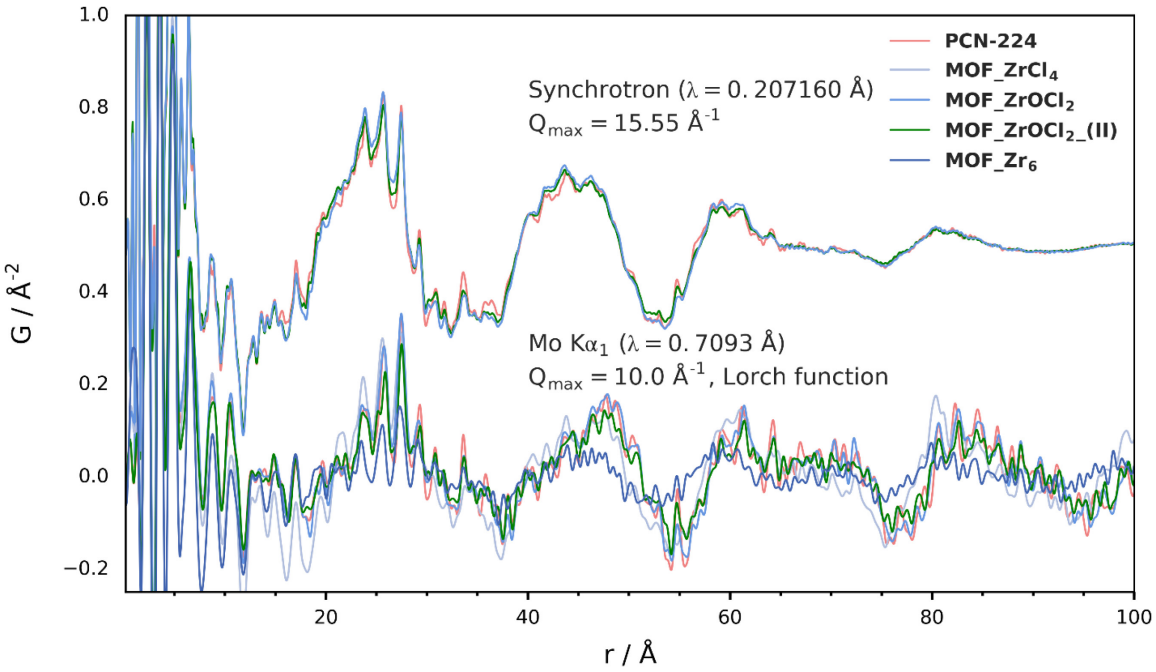

Figure A.17: Pair distribution functions $G(r)$ (PDFs) of all samples at long ranges. PDFs shown as obtained from both synchrotron and Mo $K\alpha_1$ measurements shown over a longer distance range. There is additionally good agreement between the PDFs obtained for all samples at high distances, indicating that despite differences in the diffraction patterns, the long range structuring is also highly similar.

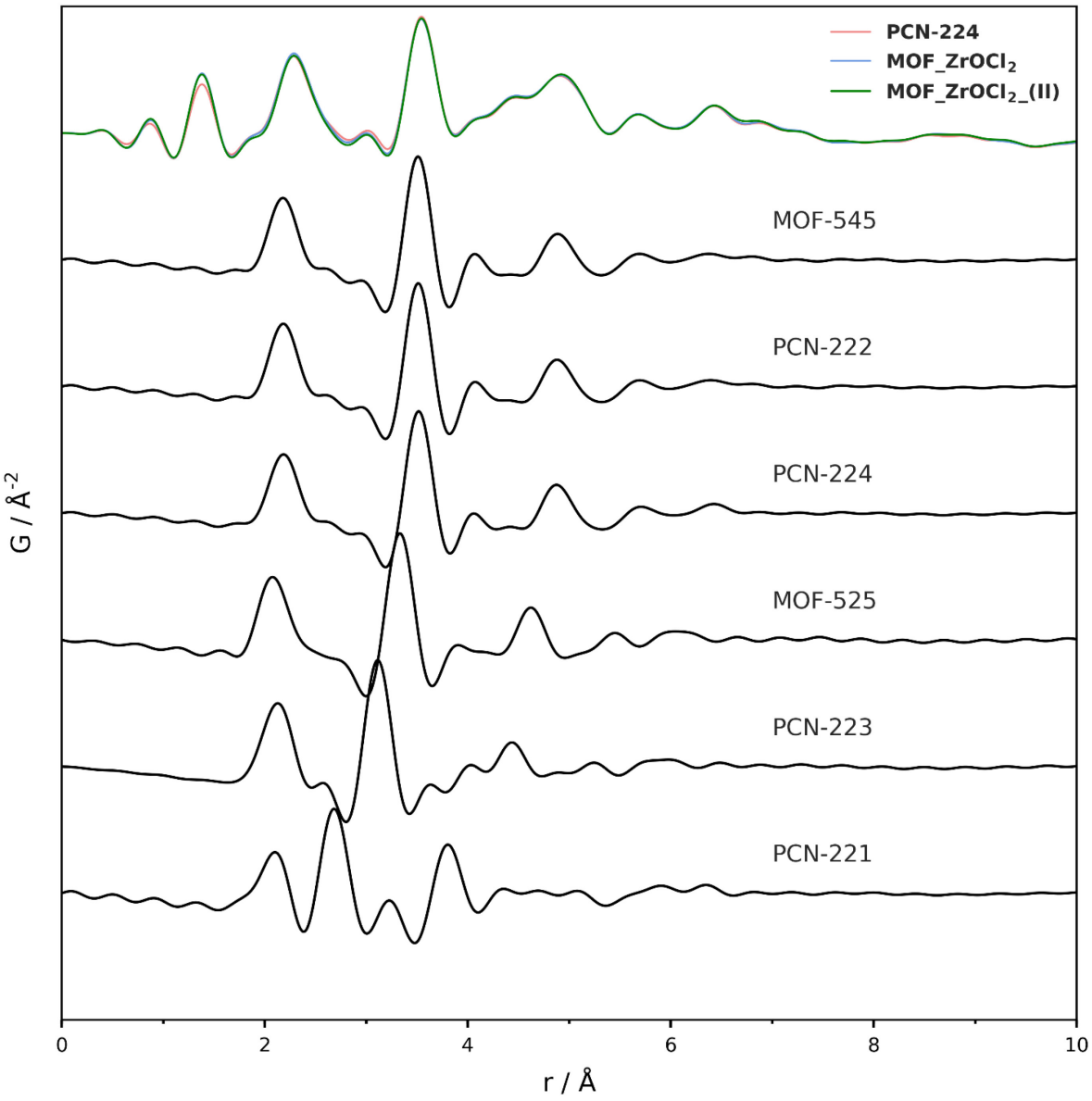

Figure A.18: Comparison of the pair distribution functions (PDFs) of samples PCN-224, MOF_$ZrOCl_2$, MOF_$ZrOCl_2$_(II) to PDFs simulated for the ZrO clusters from different crystal structures published for this MOF family. It is clear that the cluster structure is the same for all experimental structures, and matches well to the bond distances for the Zr_6 clusters published for MOF-545, PCN-222, and PCN-224. The bond distances for the Zr_6 cluster in MOF-525, and especially in PCN-223, are contracted compared to what we observe experimentally, but otherwise the signals match. A completely different bond distance distribution is observed for the Zr_8 clusters published for PCN-221, which contains Zr–Zr pair distances not observed experimentally.

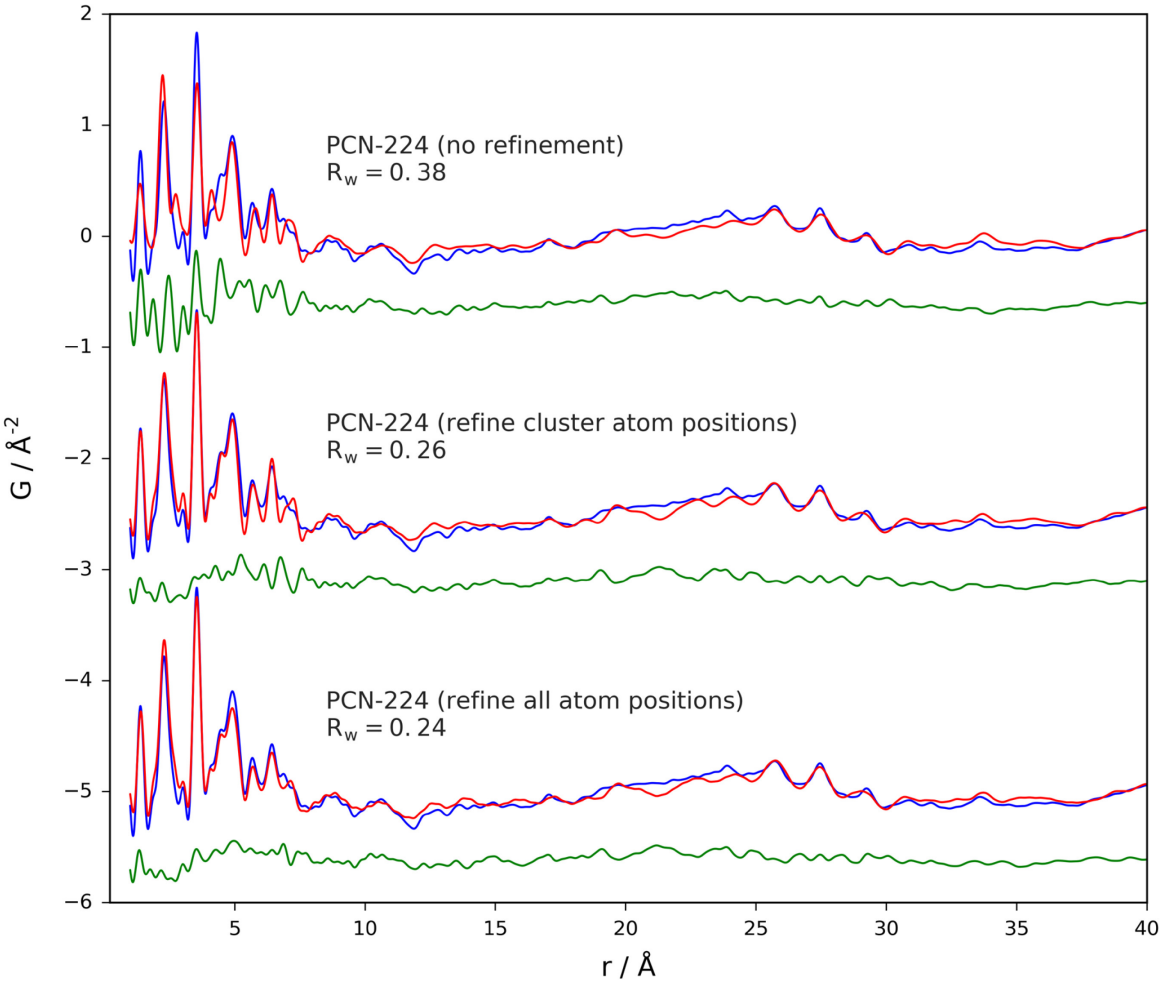

Figure A.19: Fits from structure refinement of the published PCN-224 structure to the observed synchrotron pair distribution function of sample PCN-224. Fitting was carried out first by refinement of only the lattice parameter, scale factor, and peak sharpening due to correlated motion. The fit was significantly improved just by refining the Zr and O atom positions within the cluster by symmetry. The best fit came by additionally refining the porphyrin atom positions by symmetry as well, which did not vary substantially from their original positions. The fit gives very good agreement at short distances, and fairly good agreement to the density distribution over longer distances. There are still some differences which may result from differences in the possible twisting of phenyl groups, slight differences in neighboring cluster structure or orientation, additional coordinating water and/or modulator content, or other factors such as pore content and other defects. Blue: experimental, red: simulation, green: difference.

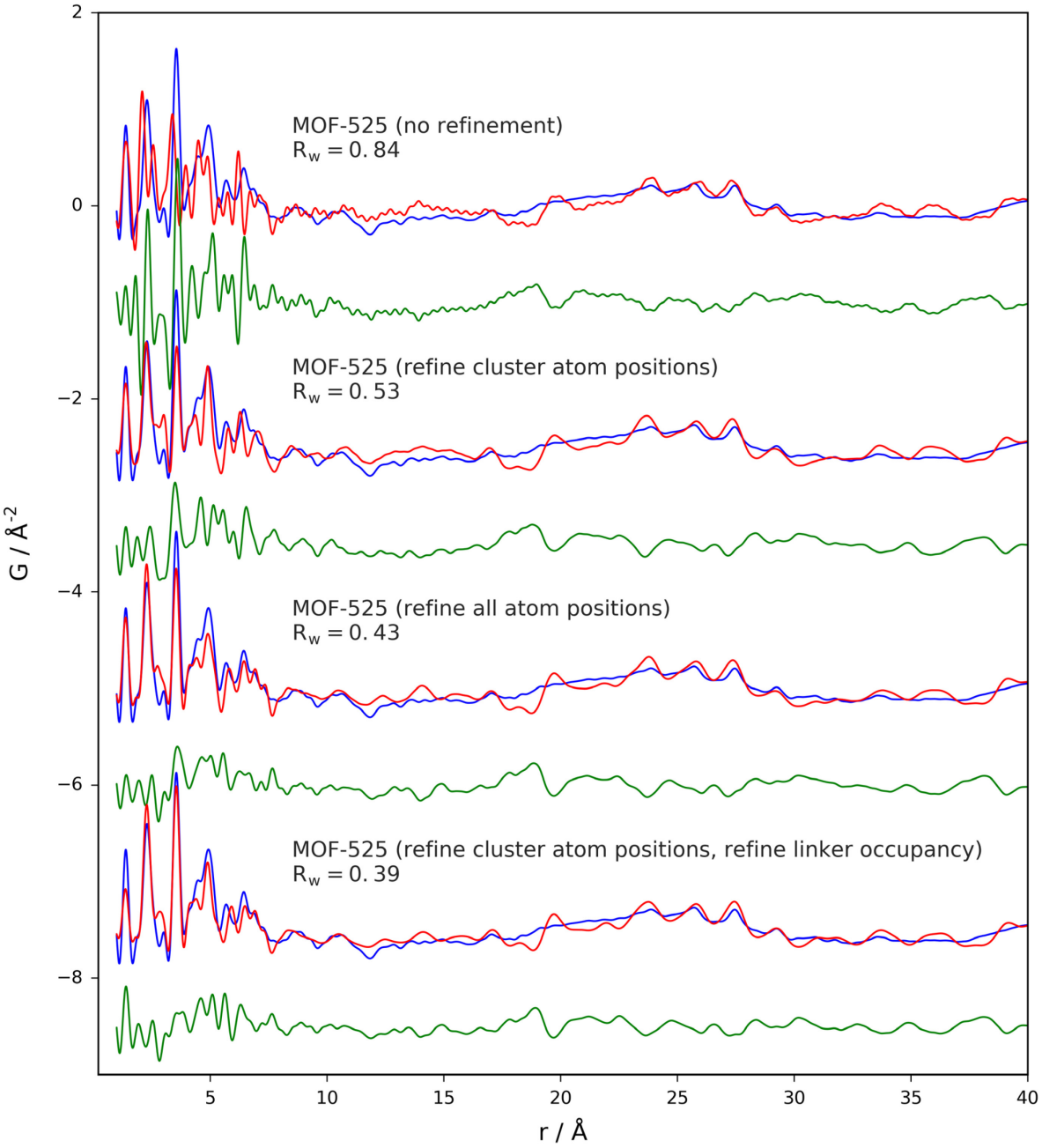

Figure A.20: Fits from structure refinement of the published MOF-525 structure to the observed synchrotron pair distribution function (PDF) of sample MOF_ZrOCl$_2$_(II). The first comparison is shown only with sharpened peaks at short distances, and no refinement of lattice parameter or atom positions. As with the Rietveld refinement, the fit is very poor indicating an incorrect structure model. The second fit allowed the lattice parameter and Zr and O positions to refine, and the third fit allowed the porphyrin atoms to refine as well. The fit agreement improved substantially in both cases, but is still very poor. As the density distribution appears to be off in the simulated PDF (e.g. for the long wavelength oscillation of the simulated PDF signal, the trough at approximately 12.5 Å is too shallow), we additionally allowed for there to be occupational vacancies of the linker. An occupation of approximately 68% improved the fit slightly. Blue: experimental, red: simulation, green: difference.

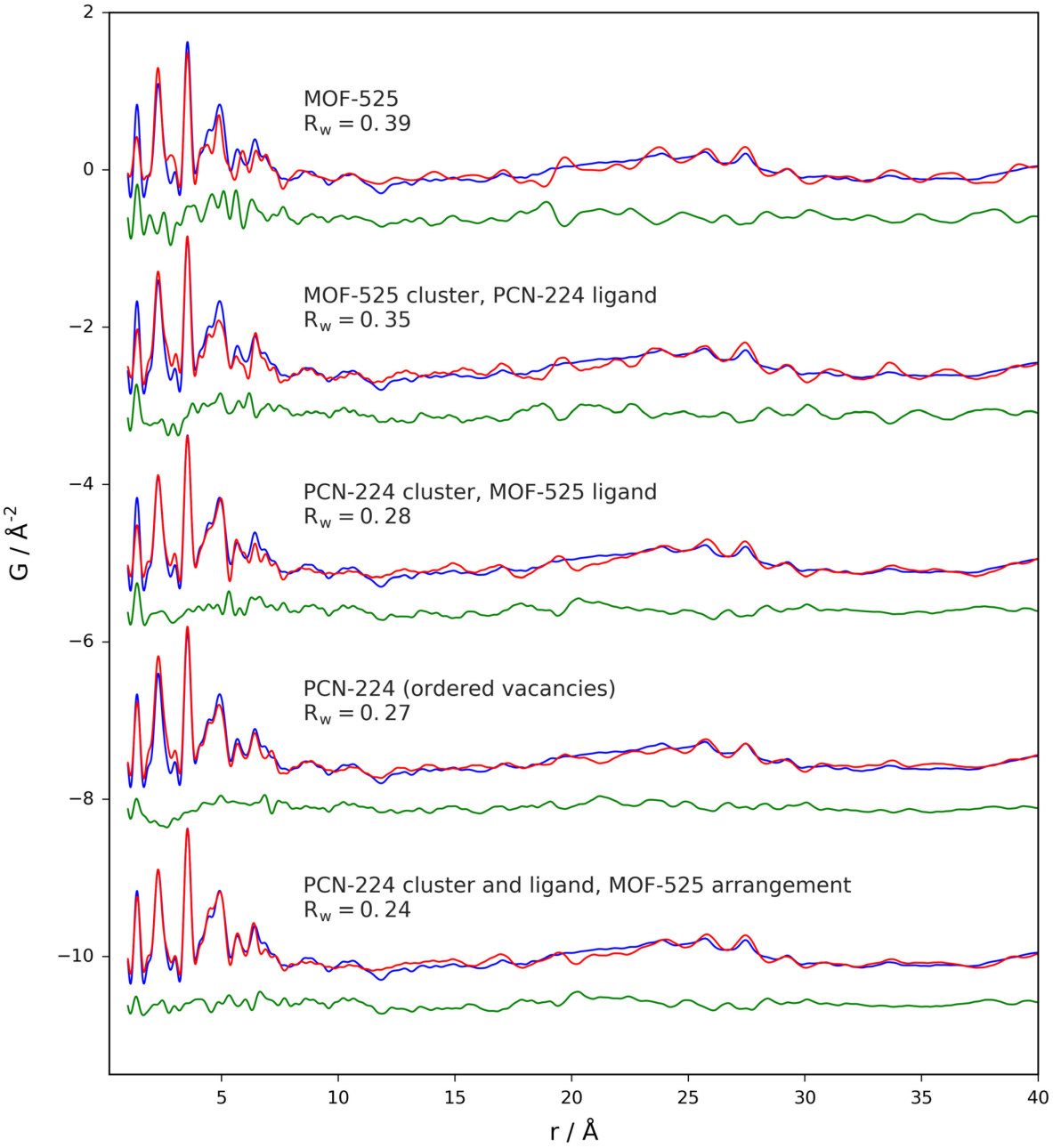

Figure A.21: Fits from structure refinement of further modified structures to the observed synchrotron pair distribution function (PDF) of sample MOF_$ZrOCl_2$_(II). The first fit is the last from the previous image, from the MOF-525 model with lattice parameter and atom sites refined along with linker vacancies. In the second fit, the linker was replaced by the conformation found in PCN-224. The third fit instead leaves the flat conformation and replaces the cluster with that found in PCN-224. The fourth fit uses the Im-3m structure published for PCN-224 with ordered vacancies. The last fit uses the MOF-525 structure but with PCN-224 linker and cluster orientation along with refined linker occupation (52%). As with the PDF fits of the experimental PCN-224 sample, some remaining misfit may be due to distributions of twists in the phenyl groups, slight differences in neighboring cluster structure or orientation, additional coordinating water and/or modulator content, or other factors such as pore content and other defects. Blue: experimental, red: simulation, green: difference.

A.2.5 Single crystal X-ray diffraction

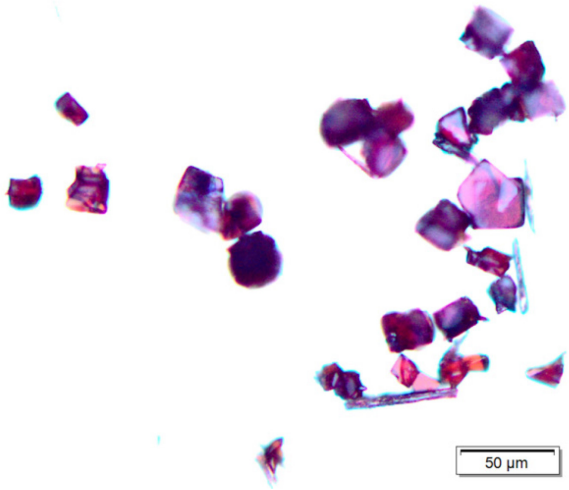

Figure A.22: Microscope image of dPCN-224 singles crystals. Powder X-ray diffraction pattern of the single crystals can be found in Figure A.3 showing no superstructure reflections as in PCN-224.

A purple block-shaped crystal of 0.025 x 0.015 x 0.015 mm^3 size was measured (Figure A.22). The diffraction data was indexed with a primitive, cubic unit cell with a = 19.315(2) Å and had an internal R-value of 34% due to small crystal size and a low scattering intensity of the MOF. The structure solution in several primitive, cubic space groups gave the linker molecule in good completeness and revealed repeatedly a Zr_8O_6 cube with a Zr–Zr distance of 2.55 Å. Accepting these solutions, residual electron density was mainly found around the Zr atom, arranged in the triangle. Based on this, we considered a superposition of Zr_6 octahedra and designed the structural model of four differently oriented Zr_6 clusters with in the cuboctahedron of linker molecules.

This structural model can be described in space group $Pm\bar{3}m$ (no. 221) by only one Zr position (Wyckoff position 24m) with an occupancy of 25% for the structure refinement (only one out of four orientations of the Zr_6 clusters can be present). The refinement optimized the Zr position so that the averaged corner-to-corner distance of the truncated cube arrived at 2.70 Å, which agrees perfectly with the originally published edge length of the Zr_8O_6 cluster of 2.69 Å.[30] The Zr–Zr distances are on average 3.49 Å (6×3.457(1) Å and 6×3.529(1) Å) and agree well with the bond length in ZrO_2 (3.45 Å). The disoriented model improved the R-value compared to the Zr_8 cube by 12%. Next, we added the O atoms of a typical Zr_6O_8 cluster to our model. O1 is localized in the corner of the truncated cube when there is no Zr present in that corner (occupancy = 25%). O2 is above the faces of the cube (in all the cases, occupancy = 100%). The O atoms of the carboxylate group could be found by residual electron density around the carboxylate carbon atom in two different orientations (O3 and O4, occupancy = 0.5×phenyl ring occupancy = 38%) that are necessary to bridge and chelate the Zr atoms of the Zr_6 clusters (Figure A.23). By adding the O

atoms to our model the *R*-value improved by 10%. Further, Hydrogen atoms, bonded to carbon atoms, were added to the structure model on calculated positions using a riding model. Isotropic displacement parameters were set to $1.2\times U_{eq}$ of the attached carbon atom We divided the linker in two group to refine its occupancy, namely the porphyrin ring (N, C1–C3, H2) and the phenyl ring (C4–C8, H6, H7, O3, O4). The occupancy of the porphyrin ring (refined to 50%) represents the actual linker molecule while the occupancy of the phenyl ring (refined to 75%) is the sum of linker and modulator molecule of the same structure (benzoate). We assume the latter occupancy deviates from 100% due to the enormous degree of freedom of the benzoate. We have refrained from refining C and N atoms with anisotropic ADP but we were able to refine them individually. The ADPs of the porphyrin ring atoms are smaller than the ADPs of the phenyl ring atoms. The largest ADPs are found for C6 and C7 pointing towards a porphyrin–phenyl dihedral angle deviating locally from 90°. In the end, low residual electron density is located only in the middle of the pores (0.770/–0.496 e $Å^{-3}$) and may be attributed to solvent and modulator molecules left in the porous material. We have refrained from manipulating our raw diffraction data to subtract this small value for a small *R*-value reduction. Furthermore, we have refrained from refining O, C, and N atoms with anisotropic displacement parameters. The refinement arrived at an R_1-value of 17% ($I > 2\sigma(I)$) or 26% (all data) which is high in general for a single crystal refinement but agreeable for a MOF due to small crystallite size, low intensity of the collected data, and the fast decay of the intensity to high diffraction angles.

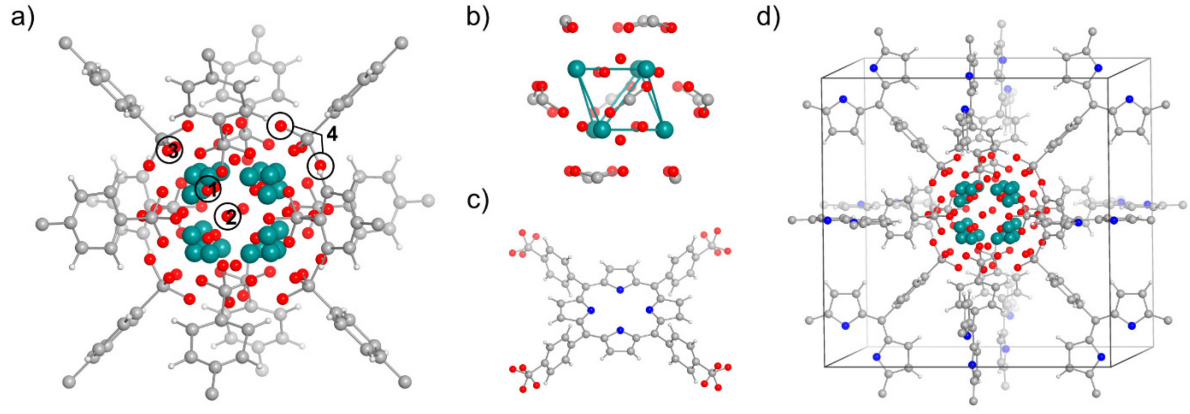

Figure A.23: Structure model obtained from single crystal X-ray diffraction (SCXRD). a) SCXRD refined oxygen positions 1–4 (red) in the disordered model. Please refer to text for explanation and note that O3 and O4 might result from coordination with benzoic acid as well. b) Oxygen environment for an individual Zr_6 cluster (teal) with bridging and chelating linker molecules, indicated by the carboxylate groups. c) Tetrakis(4-carboxyphenyl) porphyrin linker obtained from SCXRD. d) Unit cell of the disordered MOF.

The orientation of the Zr_6 cluster in the presented *d*PCN-224 model (corners pointing towards the triangles of the surrounding cuboctahedron of linker molecules) resembles the orientation of the ordered clusters in PCN-224.[37] For this reason we checked the diffraction data for superstructure reflections of a doubled unit cell as in PCN-224 and found indeed *extremely* weak reflections in the *hk*1/2*l* plane for $h = \pm 1/2$ and $l = -1/2$ (Figure A.24). These diffuse features imply different local vacancy–orientation environments in the *disordered* single crystal.

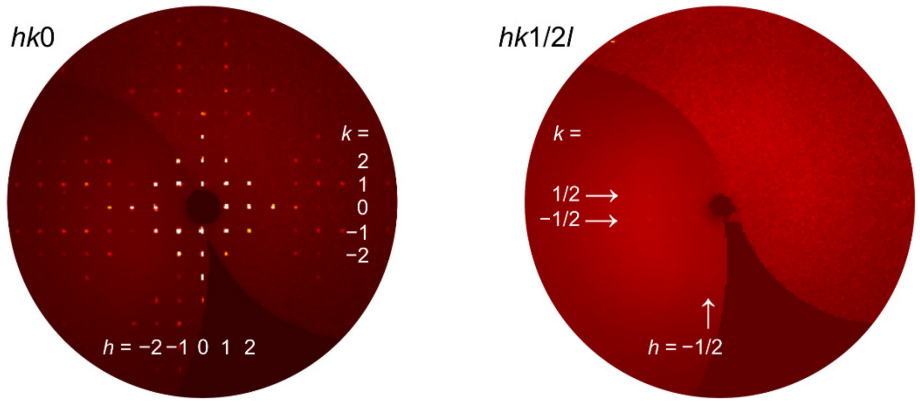

Figure A.24: Single crystal X-ray diffraction. Data presented for the hk0 and hk1/2l scattering planes.

MOF-525 differs from both *d*PCN-224 and PCN-224 such that the Zr_6 cluster point toward the squares built by the linker molecules. We tested for the MOF-525 cluster orientation[31] in our single crystal data and found only overlapping positions ($Zr_{MOF\text{-}525}$ on O2 and $O_{MOF\text{-}525}$ on O1). Kinetic limitations and configurational entropy are discussed in the publications.

A few words on the limitations of this single crystal structure compared to the local structure: The solution in space group $Pm\bar{3}m$ (no. 221) restricts the linker molecule to be flat with a 90° dihedral angle between the porphyrin and phenyl ring as well as 0° and 90° dihedral angles between the phenyl ring and carboxylate group. Instead, we conclude from ADP sizes that the linker are more flexible to adapt the local structure as in PCN-224 with porphyrin–phenyl and phenyl–carboxylate dihedral angles of 78° and 4°, respectively.[37] However, single crystal diffraction detects long-range order and displays average electron density. For details on the local structure, linker defects, and the coordination with benzoic acid refer to results of the local probes PDF, Rietveld, NMR, and DFT in this publication.

Table A.6: Crystallographic data of dPCN-224 as obtained from single crystal X-ray diffraction.

Formula	$Zr_6\ O_{26}\ N_6\ C_{91}\ H_{42}$
Crystal shape	block, 0.025 x 0.015 x 0.015 mm^3
Crystal color	purple transparent
Radiation	Cu $K\alpha$
Temperature T, K	100
Crystal symmetry	cubic
Space group	$Pm\bar{3}m$ (no. 221)
Lattice parameter a, Å	19.315(2)
Cell volume V, $Å^3$	7206(2)
Cell constant Z	1
Density $d_{calc.}$, g/cm^3	0.517
Absorption coefficient μ, mm^{-1}	1.931
Structure factor $F(000)$	1112
2θ range, °	$2.287 \leq 2\theta \leq 58.972$
Index range	$-21 \leq h \leq 17$
	$-21 \leq h \leq 18$
	$-21 \leq h \leq 18$
Reflections collected	28398
Independent reflections	1106 (R_{int} = 0.3368)
Completeness to theta = 58.972°	100.0%
Refinement method	Full-matrix least-squares on F^2
Data / restraints / parameters	1106 / 0 / 34
R_1/wR_2 ($I > 2\sigma(I)$)	0.178/0.408
R_1/wR_2 (all data)	0.262/0.436
GOF on F^2	2.23
$\Delta\rho_{max}/\Delta\rho_{min}$ (max/min), e $Å^{-3}$	0.770/–0.496

Table A.7: Atomic coordinates and equivalent isotropic displacement factors U_{eq} (Å^2) for dPCN-224 as obtained from single crystal X-ray diffraction at T = 100 K.

atom	site	*x*/*a*	*y*/*b*	*z*/*c*	U_{eq}	S.O.F.
Zr1	24*m*	0.5447(2)	0.5847(2)	0.5847(2)	0.110(4)[§]	0.25
O1	8*g*	0.5530(20)	0.5530(20)	0.5530(20)	0.070(30)	0.25
O2	6*f*	1/2	0.6166(19)	1/2	0.255(16)	1.00
O3	24*m*	0.5551(13)	0.6403(9)	0.6403(9)	0.114(9)	0.375(8)
O4	24*l*	1/2	0.6906(15)	0.6034(16)	0.154(12)	0.375(8)
N1	12*h*	1/2	1	0.8922(15)	0.095(11)	0.471(17)
C1	24*l*	1/2	0.9412(13)	0.8512(13)	0.094(10)	0.471(17)
C2	24*l*	1/2	0.9617(13)	0.7811(15)	0.108(11)	0.471(17)
C3	12*j*	1/2	0.8734(13)	0.8734(13)	0.085(12)	0.471(17)
C4	12*j*	1/2	0.8186(12)	0.8186(12)	0.140(12)	0.749(16)
C5	12*j*	1/2	0.7217(14)	0.7217(14)	0.165(14)	0.749(16)
C6	24*m*	0.5621(16)	0.7411(12)	0.7411(12)	0.221(14)	0.749(16)
C7	24*m*	0.5569(15)	0.7976(12)	0.7976(12)	0.213(14)	0.749(16)
C8	12*j*	1/2	0.6616(15)	0.6616(15)	0.166(15)	0.749(16)
H2[Δ]	24*l*	1/2	0.9323	0.7417	0.130	0.471(17)
H6[Δ]	24*m*	0.6041	0.7230	0.72367230	0.266	0.749(16)
H7[Δ]	24*m*	0.5981	0.8165	0.8165	0.256	0.749(16)

[§] Anisotropic displacement factor: 0.116(5) 0.103(5) 0.103(5) 0.059(4) –0.064(3) –0.064(3).
[Δ] Calculated.

A.2.6 Solid-state NMR spectroscopy

High-resolution ^{1}H, ^{13}C and ^{15}N magic angle spinning (MAS) NMR spectra of *d*PCN-224 and ordered PCN-224 (Figures 2.6, A.25-A.27) are intriguingly similar, supporting the proposed structural relation between both compounds on local length scales. The NMR spectra show well resolved resonances for all characteristic chemical groups of the TCPP linkers, the modulator molecules (acetate (Ac) and benzoate (Bz)) and the Zr clusters. In particular, the presence of sharp and well-defined resonances for the μ3-OH groups at around 3.3 ppm in the ^{1}H MAS NMR spectra (Figures 2.6a and A.25) underlines the presence of $Zr_6O_4(OH)_4$ clusters, which is in line with both the diffraction and PDF data. Additional signals between 0 and 6 ppm were observed which, however, do not show double quantum (DQ) correlations (Figure A.28). This behavior is characteristic for hydrogen atoms of mobile hydroxy groups or water molecules, not involved in hydrogen bonding. The ratio between the intensities of the resonances of the μ3-OH (≈ 3.3 ppm)

and the NH units (≈ -3.2 ppm) of the TCPP linkers provides a straightforward estimate for the linker to cluster proportion for both *d*PCN-224 and experimental PCN-224. While on average 1.6(1) TCPP molecules complement one Zr cluster for *d*PCN-224, the value is somewhat lower for ordered PCN-224 with 1.2(1). Compared to 12-fold coordination of the $Zr_6O_4(OH)_4$ clusters, this amounts to 53(4)% (*d*PCN-224) and 40(4)% (experimental PCN-224) linker occupancy and thus to an average TCPP coordination number of the cluster of roughly 6 and 5, respectively. The lower coordination density for $Zr_6O_4(OH)_4$ for *d*PCN-224 and PCN-224 explains the lowfield shift of about 1 ppm for the μ3-OH groups with respect to the one observed for UiO-67.[42]

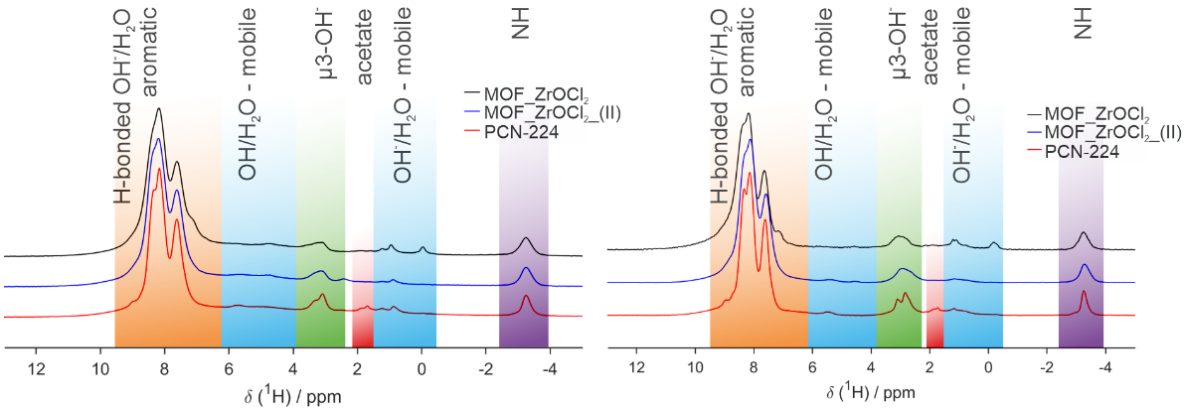

Figure A.25: High-resolution ^{1}H magic angle spinning (MAS) NMR. Spectra of MOF_ZrOCl$_2$ (black), MOF_ZrOCl$_2$_(II) (blue), and experimental PCN-224 (red). Left: ^{1}H spin echo spectra recorded at a Lamor frequency of 600 MHz. Right: ^{1}H single pulse spectra acquired at a Lamor frequency of 1 GHz. The difference for both data sets within region color-coded in blue is due to the faster spin-spin relaxation of mobile water molecules and hydroxy groups assigned to these regions. The results of deconvolution of the ^{1}H single pulse (SP) spectra (ν_0 = 1 GHz), with pseudo-Voigt (pVoigt) profiles is given in Tables A.8–A.10.

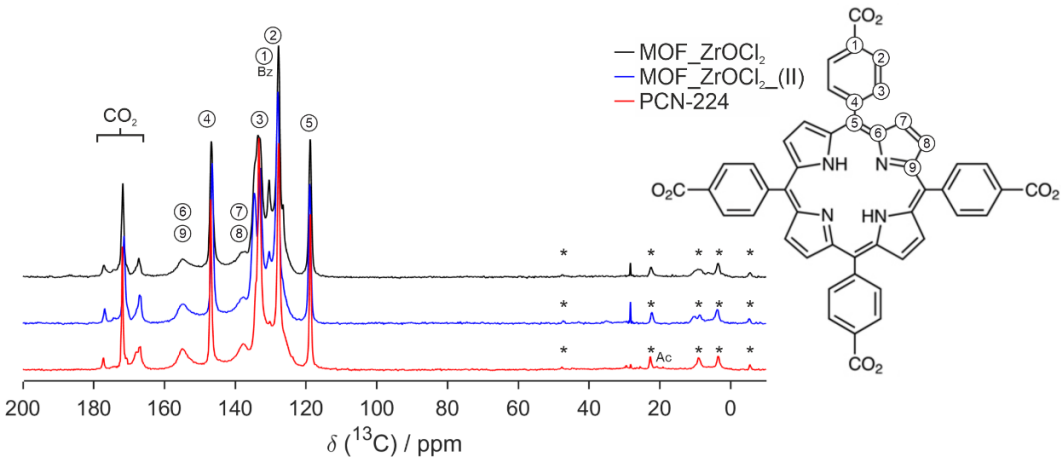

Figure A.26: ^{13}C cross polarization magic angle spinning (CPMAS) NMR. Spectra of MOF_ZrOCl$_2$ (black), MOF_ZrOCl$_2$_(II) (blue), and experimental PCN-224 (red). All resonances are assigned to the tetrakis(4-carboxyphenyl) porphyrin linkers, benzoate (Bz), and acetate (Ac). Spinning sidebands are marked by an asterisk.

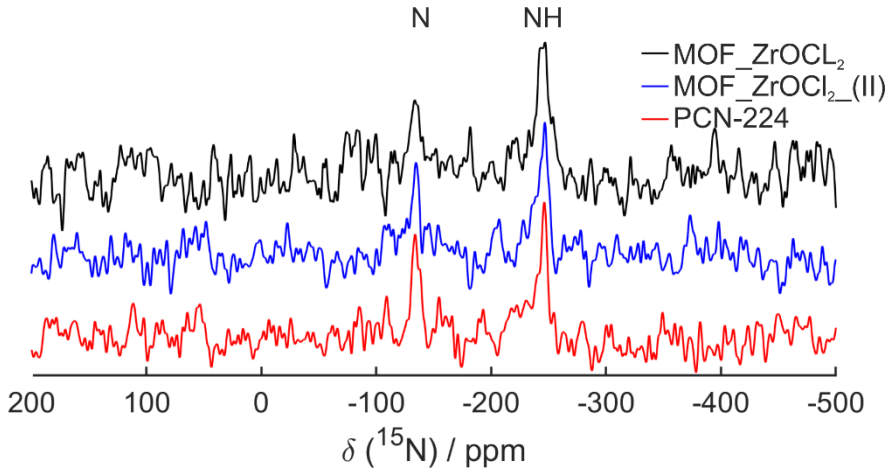

Figure A.27: ^{15}N cross polarization magic angle spinning (CPMAS) NMR. Spectra of MOF_ZrOCl$_2$ (black), MOF_ZrOCl$_2$_(II) (blue), and experimental PCN-224 (red), with the characteristic resonances for the tertiary (N) and secondary (NH) nitrogen atoms of the porphyrin rings of the tetrakis(4-carboxyphenyl) porphyrin linkers.

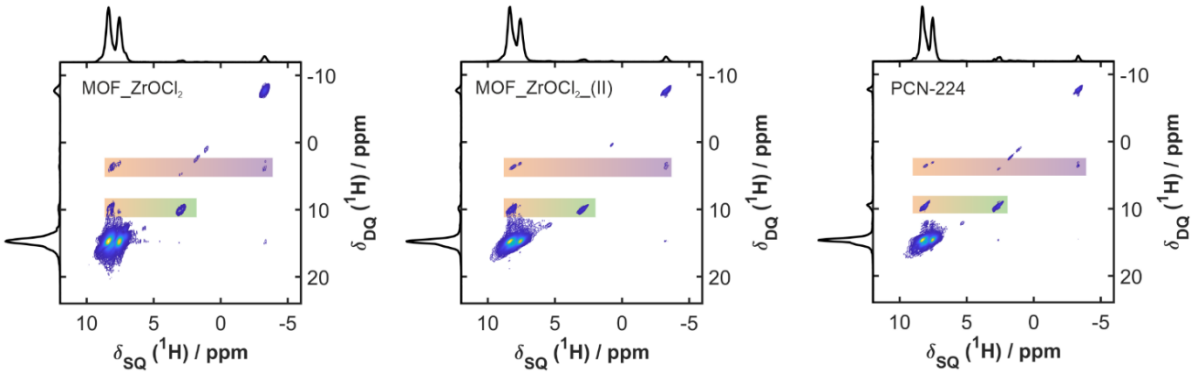

Figure A.28: 1H-1H double-quantum single-quantum (DQSQ) NMR. Spectra of the dPCN-224 variants MOF_ZrOCl$_2$ (left) and MOF_ZrOCl2_(II) (middle), and experimental PCN-224 (right). Cross correlations show proximities of aromatic protons to NH protons of the tetrakis(4-carboxyphenyl) porphyrin linkers (ν_{DQ} = 3.8 ppm, color-coded orange to purple), and aromatic protons to μ3-hydroxyl protons (ν_{DQ} = 9.7 ppm, color-coded orange to green).

Table A.8: Refinement parameters of the deconvolution of the $^{1}H(\nu_0 = 1\ GHz)$ SP spectrum of experimental PCN-224 with pVoigt profiles. G/L describes the ratio between Gaussian and Lorentzian part of the pVoigt profile, where the boundary values 1 and 0 represent pure Gaussian and Lorentzian functions, respectively. Color-codes are associated to assignments in Figure 2.6a and A.25.

δ_{iso} / ppm	*G/L*	*FWHM* / ppm	*Integral* / arb. units
–3.27	0.26	0.21	2.00
1.29	1.00	1.41	2.01
1.81	1.00	0.25	0.19
2.70	0.20	0.35	1.33
2.84	0.20	0.19	1.06
3.10	0.20	0.22	1.09
5.50	0.28	0.37	0.35
7.61	0.23	0.28	9.47
8.11	0.30	0.29	12.61
8.36	0.30	0.27	9.53
8.92	0.00	0.79	2.52

Table A.9: Refinement parameters of the $^{1}H(\nu_0 = 1\ GHz)$ SP spectrum of MOF_$ZrOCl_2$ fitted with pVoigt profiles. Color-codes are associated to assignments in Figure 2.6a and A.25.

δ_{iso} / ppm	*G/L*	*FWHM* / ppm	*Integral* / arb. units
–3.25	0.74	0.38	2.00
–0.19	0.58	0.26	0.59
0.97	0.00	0.65	1.35
1.20	1.00	0.23	0.29
1.80	1.00	1.00	0.96
1.94	0.25	0.01	0.01
3.01	0.90	0.69	2.59
4.10	0.80	0.80	0.54
5.11	0.80	1.00	0.60
6.30	0.80	1.00	0.79
7.14	0.80	0.36	1.32
7.64	0.50	0.33	9.25
8.13	0.80	0.33	9.81
8.42	0.80	0.40	11.88
9.10	0.70	1.00	5.04
8.80	0.80	0.38	1.62

Table A.10: Refinement parameters of the $^{1}H(\nu_0 = 1$ GHz) SP spectrum of MOF_$ZrOCl_2$_(II) fitted with pVoigt profiles. Color-codes are associated to assignments in Figure 2.6a and A.25.

δ_{iso} / ppm	*G/L*	*FWHM* / ppm	*Integral* / arb. units
–3.29	0.69	0.38	2.00
0.80	1.00	0.55	0.28
1.17	1.00	0.39	0.21
1.78	0.80	0.97	0.52
2.68	1.00	0.59	1.06
2.99	0.80	0.52	1.38
4.55	1.00	0.12	0.01
5.80	0.00	1.00	0.96
7.58	0.70	0.47	11.12
8.10	0.80	0.36	12.13
8.38	0.70	0.32	7.66
8.80	0.70	0.82	4.32

The intensity of the ^{1}H NMR resonances for the aromatic protons of the TCPP linkers (7–9 ppm) is coupled to the ones of the NH units (≈ –3.2 ppm). For one NH proton, 12 protons in the aromatic region are expected. However, for all *d*PCN-224 samples and the reference PCN-224, a ratio between 1:17 and 1:18 was determined, which requires either additional components with aromatic, or low-field shifted protons as for e. g. reported for hydroxy water pairs saturating the coordinatively unsaturated sites (CUS) of the $Zr_6O_4(OH)_4$ clusters in NU-1000.[43] As experimental PCN-224 was synthesized using acetic acid, only the second scenario is possible for this compound. The intensity of the methyl protons of residual acetate ions (Figures 2.6a and A.25; ≈ 1.9 ppm) is small and amounts to maximal 0.4(2) acetate ions and five to six hydroxyl water pairs attached to one $Zr_6O_4(OH)_4$ cluster on average. From the chemical shift within the aromatic region (7–9 ppm) of the latter, an O–O distance between 2.6 and 2.7 Å results (Figure 2.6c), characteristic for strong hydrogen bonds.[44–46] As the spectral line shapes for the ^{1}H and the ^{13}C MAS NMR spectra are very similar for *d*PCN-224 and PCN-224 (Figures 2.6a, 2.6b, A.25 and A.26) and only weak resonances characteristic solely of benzoate (130–140 ppm) were observed (about 0.5(2) Bz on average per cluster (Figure A.29)), we expect a similar situation to hold for *d*PCN-224.

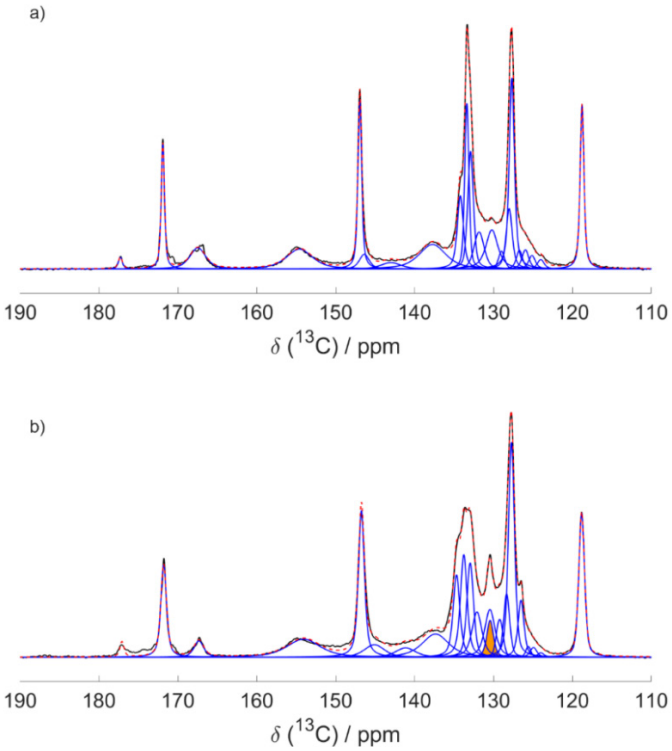

Figure A.29: ^{13}C cross polarization magic angle spinning (CPMAS) NMR deconvoluted with pseudo-Voigt profiles (blue). Spectra of a) experimental PCN-224 and b) MOF_$ZrOCl_2$. The additional signal (colored in orange) at ~130 ppm in (b) is assigned solely to the ortho- and para-CH units of benzoic acid and is used for an estimation of modulator/linker ratio. The ipso carbon and meta-CH groups are superimposed with the ones of tetrakis(4-carboxyphenyl) porphyrin (TCPP). Integration leads to roughly 0.31(1) benzoate ions per TCPP linker and thus to 0.5(2) benzoate ions per cluster.

The most telling region within the ^{13}C MAS NMR spectra for both *d*PCN-224 and PCN-224 is the carboxylic region (165–180 ppm), which contains several signals with maxima around 167.3 and 177.2 ppm centered around a main peak at ≈ 171.9 ppm (Figures 2.6b and A.26). The broad spread observed for the shifts of the carboxylate resonances is indicative of different binding modes between the $Zr_6O_4(OH)_4$ clusters and the carboxylate units of the TCPP linkers combined with a configurational variance on the cluster. DFT calculations for $[Zr_6O_4(OH)_4]Ac_{12}$ clusters (Figure A.30) with configurations that contain Ac ions in bridging coordination only and mixed bridging as well as chelating Ac ions demonstrate, in line with ref. [47], that bridging carboxy groups are high-field shifted by 6–10 ppm with respect to chelating ones, depending on the cluster configuration. On average, and again in agreement with ref. [47] chelating carboxylate groups are less favored by 15–16 kJ/mol. In addition, the majority of the carboxylate groups of the TCPP linkers in PCN-224 are reported to coordinate in a bridging mode.[32] Hence, we assign the central resonance and its high-field region to carboxylates in a bridging motif (Figure 2.6c) and the low-field region (172–176 ppm) to the chelating binding motif (Figure 2.6c). As such, the majority of carboxylate groups is coordinated in a bridging mode for *d*PCN-224 as well, which allowed to refine the

structure model derived from the scattering data further. The broad distribution for the resonances of the μ3-OH groups (≈ 3.3 ppm; Figure 2.6a and A.25), also points towards a configurational variance of bridging and chelating binding motifs, as well as of hydroxy water pairs on the cluster.[48]

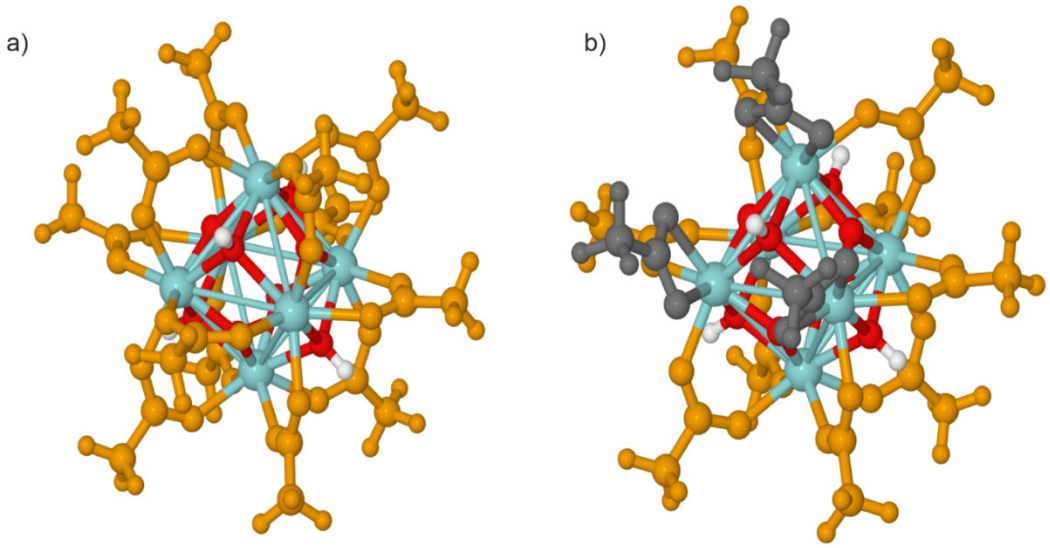

Figure A.30: DFT optimized $[Zr_6O_4(OH)_4]Ac_{12}$ clusters. Optimization with a) only bridging carboxylates and b) with mixed linker environment, where three acetates chelate three Zr atoms of one μ3-OH capped face of the Zr_6 octahedron. The bridging acetates are highlighted in ocher, while the chelating acetates are color-coded in grey. The cluster with mixed linker environment is 0.4855 eV higher in energy.

The distribution of different binding modes is also reflected in the lineshapes of the ^{91}Zr wideline NMR spectra of *d*PCN-224 and ordered PCN-224 (Figure 2.6d) recorded using the (VOCS) approach combined with a quadrupolar Carr-Purcell-Meiboom-Gill (qCPMG) sequence.[13–15,49] Both ^{91}Zr NMR spectra consist of at least four different quadrupolar shapes with non-axial symmetric coupling tensors and coupling constants (C_Q) between 10 and 25 MHz. This proves a markedly more diverse electronic situation for the individual Zr atoms compared to the fully saturated $Zr_6O_4(OH)_4Bz_{12}$[50] used as starting material in one of the *d*PCN-224 syntheses, for which two superimposing quadrupolar lineshapes with coupling constants C_Q of about 14 and 20 MHz were observed (Figure A.31). According to the DFT calculations (Figure A.30) Zr atoms exclusively coordinated by bridging carboxylates exhibit the larger C_Q values compared to those involved in mixed binding modes. The broader variance for *d*PCN-224 and ordered PCN-224 reflects the disorder induced by the hydroxyl ions and water molecules coordinating to the CUS and the strain on the Zr clusters imposed by the framework topology.

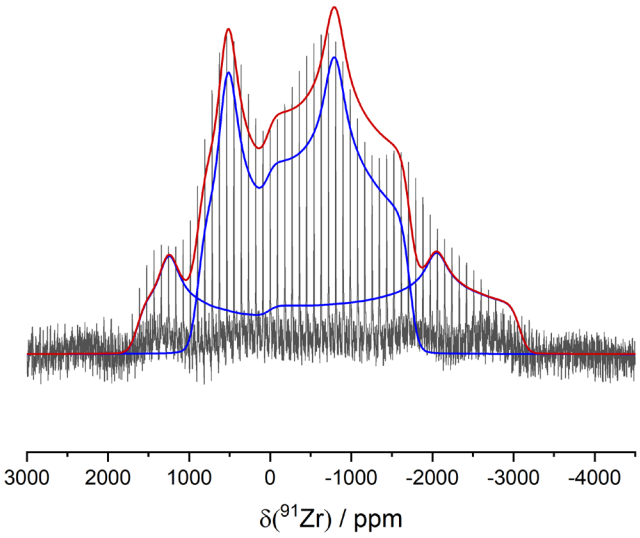

Figure A.31: ^{91}Zr qCPMG NMR VOCS of $Zr_6O_4(OH)_4Bz_{12}$ deconvoluted into two quadrupolar shapes (blue). This is in line with the structure of the cluster proposed in ref. [50] The structure solution consists of 3 chelating and 9 bridging Bz, resulting in two Zr environments. One where only bridging carboxylate groups coordinate and the other where bridging and chelating carboxylate units are mixed.

Table A.11: Refinement parameters of the deconvolution of 91Zr NMR spectrum (Figure A.30) of $[Zr_6O_4(OH)_4]Bz_{12}$ with two second order quadrupolar lineshapes. δiso: isotropic chemical shift, CQ: quadrupolar coupling constant, ηQ: Anistropy of quadrupolar coupling tensor, LB: Lorenzian line broading, GB: Gaussian line broadening.

	1	2
δ_{iso} / ppm	0	0
C_Q / MHz	14	20
η_Q	0.4	0.2
LB / Hz	1000	1000
GB / Hz	10000	10000
Integral /arb. units	0.65	0.35

Table A.12: Refinement parameters of the deconvolution of ^{91}Zr NMR spectrum (Figure 2.6d) of dPCN-224 with four second order quadrupolar lineshapes.

	1	2	3	4
δiso / ppm	408	–142	–780	–600
CQ / MHz	21	19	23	18.5
ηQ	0.5	0.3	1.0	0.6
LB / Hz	1000	1000	1000	1000
GB / Hz	10000	10000	10000	10000
Integral /arb. units	0.31	0.29	0.25	0.15

Table A.13: Refinement parameters of the deconvolution of ^{91}Zr NMR spectrum (Figure 2.6d) of experimental PCN-224 with four second order quadrupolar lineshapes.

	1	2	3	4
δiso / ppm	622	–1850	285	–4000
CQ / MHz	24	14	15	13
ηQ	0.7	1.0	0.0	0.1
LB / Hz	1000	1000	1000	1000
GB / Hz	10000	10000	10000	10000
Integral /arb. units	0.33	0.33	0.24	0.10

A.2.7 Quantum chemical calculations

Zr_8O_6 Cluster

The structure of a Zr_8O_6-Cluster was extracted from the published crystal structure for PCN-221[30]. Using this structure as an initial starting point, the geometry was optimized on PBE0-D3/def2-mSVP[23–26] level of theory. Zr–Zr distances within the initial Zr_8O_6 cluster reside at 2.688 Å, 3.802 Å and 4.656 Å as Zr–Zr distances to the closest, face diagonal and space diagonal neighbor.

All distances expand during the optimization significantly to 6.938 Å, 9.811 Å and 12.016 Å as Zr–Zr distances to the closest, face diagonal and space diagonal neighbor, beyond the distance of bound Zr. These pre-converged results indicate, that the distances within the initial structure of a Zr_8O_6-Cluster are unfeasible.

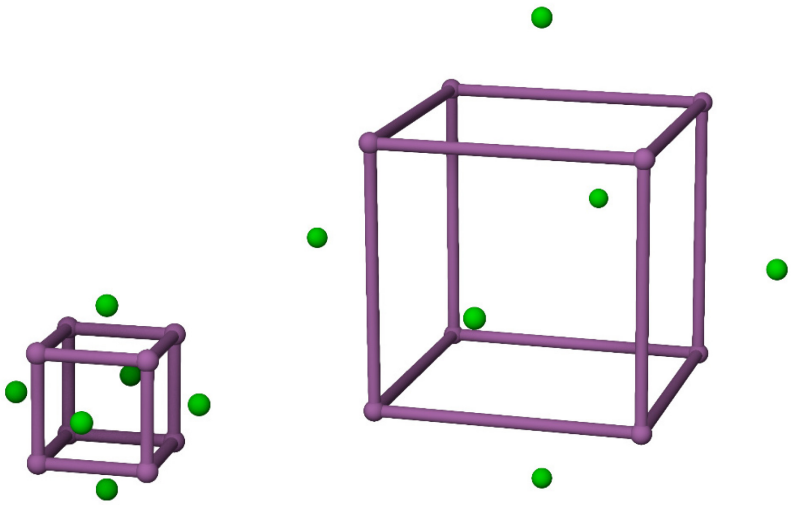

Figure A.32: Structure of the Zr_8O_6 cluster. Left: Initial structure, extracted from the published crystal structure of PCN-221[30]; Right: Pre-Converged structure, obtained on PBE0-D3/def2-mSVP level of theory.

Zr_6O_8 Cluster

The comparison of the optimized Zr_6O_8 cluster obtained on PBE0-D3/def2-mSVP level of theory with the Zr_6O_8 cluster obtained from total scattering pair distribution function (PDF) analysis of *d*PCN-224, shows a good agreement on the position of the zirconium atoms, whereas the position of the modeled oxygen atoms deviate.

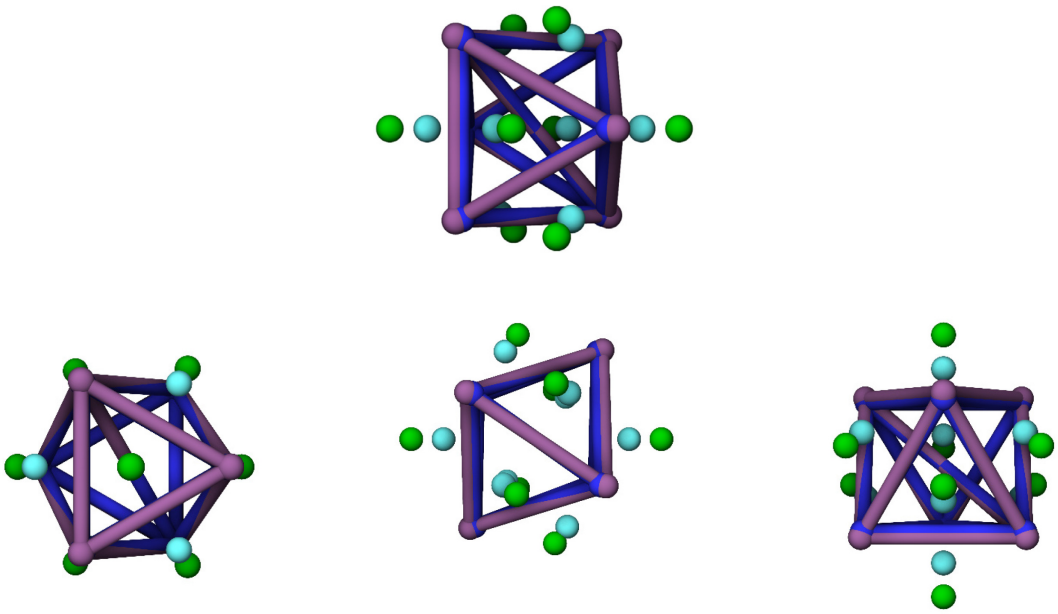

Figure A.33: Overlay of the optimized Zr_6O_8 cluster and cluster structure obtained from total scattering pair distribution function (PDF). The optimized Zr_6O_8 cluster obtained on PBE0-D3/def2-mSVP level of theory is depicted in purple (Zr_6 octahedron) and light blue (oxygen). The Zr_6O_8 cluster structure obtained from (PDF) analysis of *d*PCN-224 is depicted in blue (Zr_6 octahedron) and green (oxygen).

Rotation profile of the TCPP linker

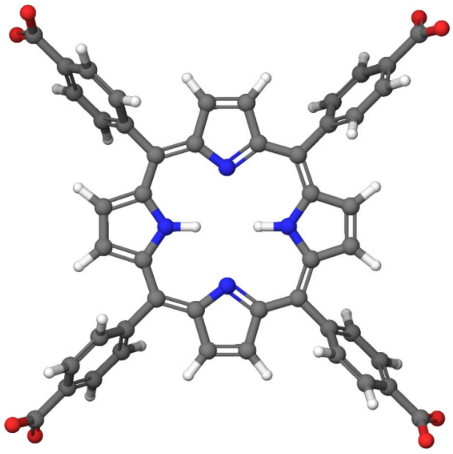

Figure A.34: Optimized geometry of the tetrakis(4-carboxyphenyl) porphyrin linker. Optimized structure obtained on PBE0-D3/def2-TZVP level of theory.

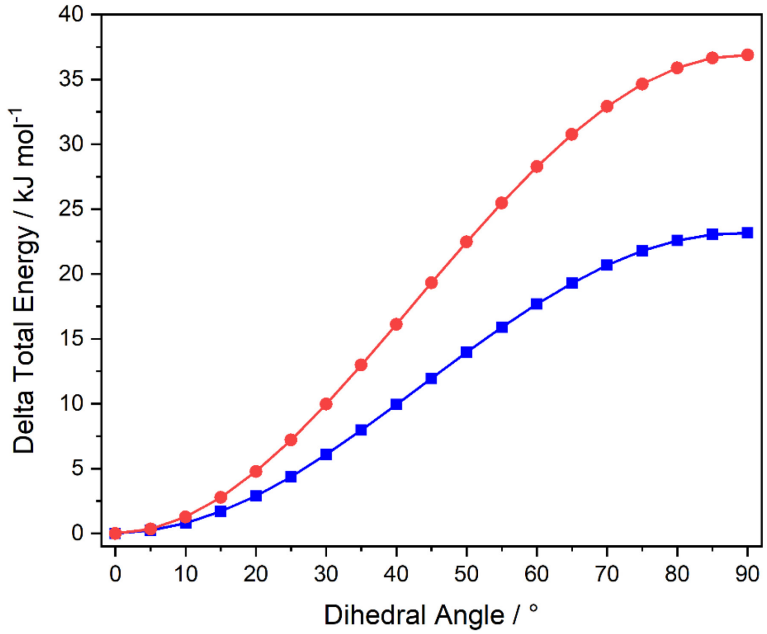

Figure A.35: Rotation profile of the phenyl–carboxylate (PHE-CAR) dihedral angle in tetrakis(4-carboxyphenyl) porphyrin (TCPP). Rotation profile within the optimized geometry of the TCPP linker, obtained on PBE0-D3/def2-TZVP//PBE0-D3/def2-TZVP (blue) and PBE0-D3/def2-mSVP//PBE0-D3/def2-mSVP (red) level of theory. The minimum indicates a preferred dihedral angle of 0°.

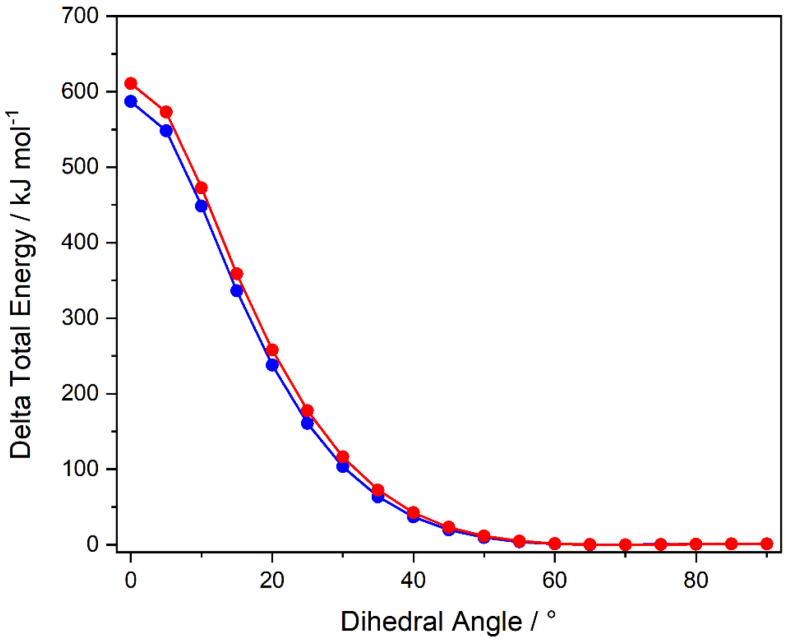

Figure A.36: Rotation profile of the porphyrine–phenyl (POR-PHE) dihedral angle in tetrakis(4-carboxyphenyl) porphyrin (TCPP). Rotation profile within the optimized geometry of the TCPP linker, obtained on PBE0-D3/def2-TZVP//PBE0-D3/def2-TZVP (blue) and PBE0-D3/def2-mSVP//PBE0-D3/def2-mSVP (red) level of theory. The maximum of ~600 kJ/mol at 0° clearly visualizes the preferred planarity of the POR-PHE dihedral angle.

Table A.14: Energies of the rotation of the phenyl–carboxylate (PHE-CAR) dihedral angle of the tetrakis(4-carboxyphenyl) porphyrin linker. The decrease of favorable interactions with increasing dihedral angle is highlighted with a color gradient from green (most favored) to red (least favored).

	PBE0-D3/def2-TZVP			PBE0-D3/def2-mSVP		
Dihedral Angle [°]	Total Energy [H]	Delta Total Energy [H]	Delta Total Energy [kJ/mol]	Total Energy [H]	Delta Total Energy [H]	Delta Total Energy [kJ/mol]
0	-2663.759709	0.000000	0.0	-2662.548636	0.000000	0.0
5	-2663.759623	0.000086	0.2	-2662.548508	0.000128	0.3
10	-2663.759409	0.000300	0.8	-2662.548152	0.000485	1.3
15	-2663.759066	0.000642	1.7	-2662.547581	0.001055	2.8
20	-2663.758608	0.001101	2.9	-2662.546819	0.001818	4.8
25	-2663.758043	0.001665	4.4	-2662.545893	0.002743	7.2
30	-2663.757394	0.002315	6.1	-2662.544840	0.003797	10.0
35	-2663.756679	0.003030	8.0	-2662.543694	0.004943	13.0
40	-2663.755923	0.003785	9.9	-2662.542494	0.006143	16.1
45	-2663.755153	0.004555	12.0	-2662.541276	0.007361	19.3
50	-2663.754389	0.005320	14.0	-2662.540077	0.008560	22.5
55	-2663.753657	0.006051	15.9	-2662.538932	0.009705	25.5
60	-2663.752972	0.006736	17.7	-2662.537868	0.010768	28.3
65	-2663.752360	0.007348	19.3	-2662.536917	0.011719	30.8
70	-2663.751837	0.007872	20.7	-2662.536100	0.012536	32.9
75	-2663.751413	0.008296	21.8	-2662.535444	0.013192	34.6
80	-2663.751109	0.008600	22.6	-2662.534965	0.013672	35.9
85	-2663.750930	0.008778	23.0	-2662.534676	0.013961	36.7
90	-2663.750885	0.008823	23.2	-2662.534589	0.014047	36.9

Table A.15: Energies of the rotation of the porphyrine–phenyl (POR-PHE) dihedral angle of the tetrakis(4-carboxyphenyl) porphyrin linker. The increase of favorable interactions with increasing dihedral angle is highlighted with a color gradient from red (least favored) to green (most favored).

Dihedral Angle [°]	PBE0-D3/def2-TZVP			PBE0-D3/def2-mSVP		
	Total Energy [H]	Delta Total Energy [H]	Delta Total Energy [kJ/mol]	Total Energy [H]	Delta Total Energy [H]	Delta Total Energy [kJ/mol]
0	-2663.535999	0.223507	586.8	-2662.315791	0.232617	610.7
5	-2663.550745	0.208761	548.1	-2662.330214	0.218194	572.9
10	-2663.588667	0.170839	448.5	-2662.368427	0.179981	472.5
15	-2663.631447	0.128059	336.2	-2662.411811	0.136597	358.6
20	-2663.668879	0.090627	237.9	-2662.450161	0.098247	257.9
25	-2663.698310	0.061196	160.7	-2662.480847	0.067561	177.4
30	-2663.720045	0.039461	103.6	-2662.504114	0.044294	116.3
35	-2663.735293	0.024213	63.6	-2662.520845	0.027563	72.4
40	-2663.745481	0.014025	36.8	-2662.532232	0.016176	42.5
45	-2663.751960	0.007546	19.8	-2662.539562	0.008847	23.2
50	-2663.755831	0.003675	9.6	-2662.544031	0.004378	11.5
55	-2663.757998	0.001508	4.0	-2662.546576	0.001832	4.8
60	-2663.759064	0.000442	1.2	-2662.547851	0.000558	1.5
65	-2663.759473	0.000033	0.1	-2662.548342	0.000067	0.2
70	-2663.759506	0.000000	0.0	-2662.548409	0.000000	0.0
75	-2663.759366	0.000140	0.4	-2662.548288	0.000121	0.3
80	-2663.759186	0.000320	0.8	-2662.548120	0.000289	0.8
85	-2663.759060	0.000446	1.2	-2662.547992	0.000416	1.1
90	-2663.759013	0.000493	1.3	-2662.547958	0.000451	1.2

A.2.8 Coordination of tilted Zr_6 cluster in dPCN-224

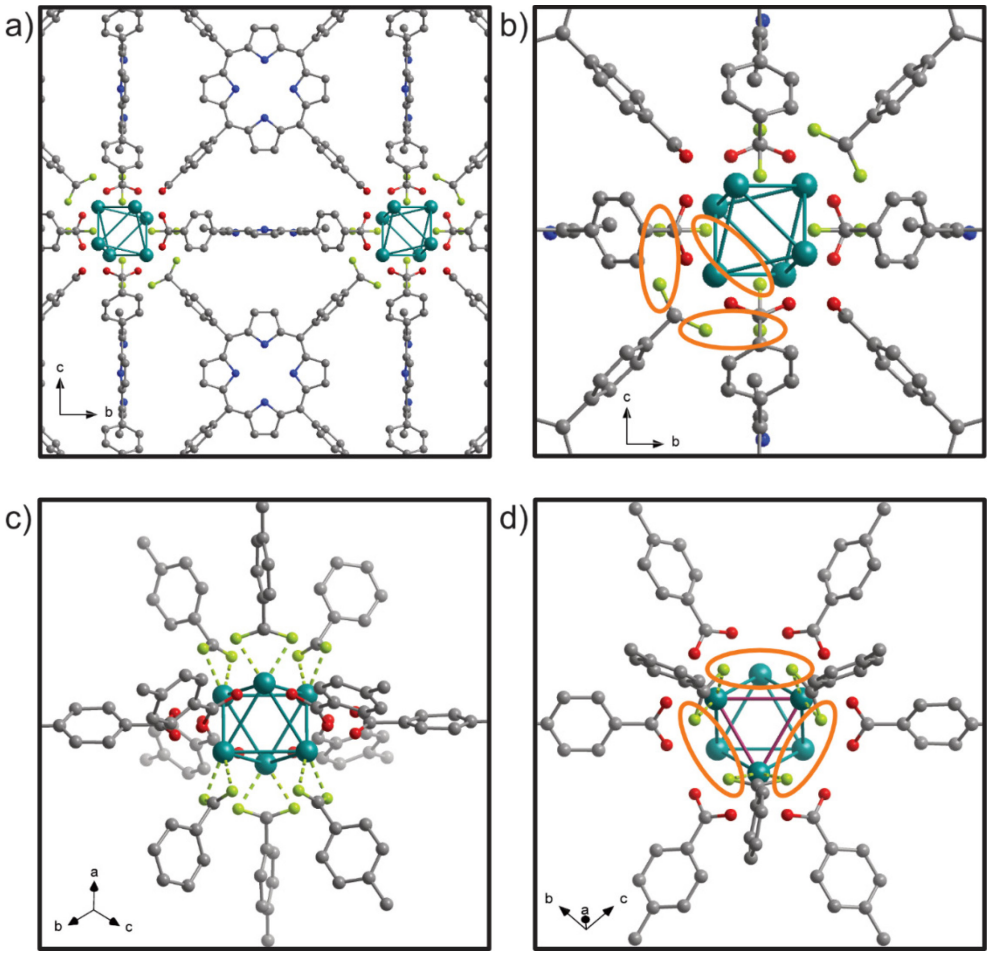

Figure A.37: Coordination of the tilted Zr_6 cluster in dPN-224. a) Two tilted Zr_6 clusters bridged by tetrakis(4-carboxyphenyl) porphyrin in dPCN-224, b) zoom onto the coordination sphere of one tilted cluster with cubic coordination of the linkers, c) coordination of one tilted cluster showing six bridging linkers and six chelating linkers, and d) top-view of the chelating coordinations, showing three Zr–Zr bonds (purple) without bridging coordination. Oxygen involved in a chelating coordination are green and oxygens involved into a bridging coordination in red. Empty, additional bridging coordination sites on the tilted cluster are highlighted in orange showing that no cubic structure with more than six on-average bridging cluster-linker sites can be obtained from tilted Zr_6 cluster.

References

1. R. E. Dinnebier, M. Pink, J. Sieler, P. W. Stephens, *Inorganic Chemistry* **1997**, *36*, 3398-3401.
2. B. A. I. B. Suite, *Version 2019. Bruker AXS Inc.*, Madison, Wi, USA, **2013**.
3. G. M. Sheldrick, *SADABS — Bruker AXS area detector scaling and absorption correction, version 2014/5*, University of Göttingen, Göttingen, Germany, **2014**.
4. G. Sheldrick, *Acta Crystallographica Section A* **2008**, *64*, 112-122.
5. G. Sheldrick, *Acta Crystallographica Section C* **2015**, *71*, 3-8.
6. P. J. Chupas, X. Qiu, J. C. Hanson, P. L. Lee, C. P. Grey, S. J. L. Billinge, *Journal of Applied Crystallography* **2003**, *36*, 1342-1347.
7. A. P. Hammersley, S. O. Svensson, M. Hanfland, A. N. Fitch, D. Hausermann, *High Pressure Research* **1996**, *14*, 235-248.
8. A. Hammersley, *Journal of Applied Crystallography* **2016**, *49*, 646-652.
9. P. Juhas, T. Davis, C. L. Farrow, S. J. L. Billinge, *Journal of Applied Crystallography* **2013**, *46*, 560-566.
10. P. J. Xiaohao Yang, Christopher L. Farrow, Simon J. L. Billinge, xPDFsuite: an end-to-end software solution for high throughput pair distribution function transformation, visualization and analysis, *arXiv* **2014**.
11. M. H. Levitt, *Symmetry-Based Pulse Sequences in Magic-Angle Spinning Solid-State NMR. Encyclopedia of Magnetic Resonance, Vol. 27*, **2007**.
12. P. E. Kristiansen, D. J. Mitchell, J. N. S. Evans, *Journal of Magnetic Resonance* **2002**, *157*, 253-266.
13. F. H. Larsen, H. J. Jakobsen, P. D. Ellis, N. C. Nielsen, *The Journal of Physical Chemistry A* **1997**, *101*, 8597-8606.
14. H. Y. Carr, E. M. Purcell, *Physical Review* **1954**, *94*, 630-638.
15. S. Meiboom, D. Gill, *Review of Scientific Instruments* **1958**, *29*, 688–691.
16. A. Pines, M. G. Gibby, J. S. Waugh, *The Journal of Chemical Physics* **1972**, *56*, 1776-1777.
17. B. M. Fung, A. K. Khitrin, K. Ermolaev, *Journal of Magnetic Resonance* **2000**, *142*, 97-101.
18. S. J. Clark, M. D. Segall, C. J. Pickard, P. J. Hasnip, M. I. J. Probert, K. Refson, M. C. Payne, *Zeitschrift für Kristallographie - Crystalline Materials* **2005**, *220*, 567-570.
19. J. P. Perdew, K. Burke, M. Ernzerhof, *Physical Review Letters* **1996**, *77*, 3865-3868.
20. H. J. Monkhorst, J. D. Pack, *Physical Review B* **1976**, *13*, 5188-5192.
21. A. Tkatchenko, M. Scheffler, *Physical Review Letters* **2009**, *102*, 073005.
22. T. Charpentier, *Solid State Nuclear Magnetic Resonance* **2011**, *40*, 1-20.
23. C. Adamo, V. Barone, *The Journal of Chemical Physics* **1999**, *110*, 6158-6170.
24. M. Ernzerhof, G. E. Scuseria, *The Journal of Chemical Physics* **1999**, *110*, 5029-5036.
25. S. Grimme, J. Antony, S. Ehrlich, H. Krieg, *The Journal of Chemical Physics* **2010**, *132*, 154104.
26. A. Schäfer, H. Horn, R. Ahlrichs, *The Journal of Chemical Physics* **1992**, *97*, 2571-2577.
27. TURBOMOLE V7.3 2018, a development of University of Karlsruhe and Forschungszentrum Karlsruhe GmbH, 1989-2007, TURBOMOLE GmbH, since 2007; available from http://www.turbomole.com.
28. H. Noh, C.-W. Kung, T. Islamoglu, A. W. Peters, Y. Liao, P. Li, S. J. Garibay, X. Zhang, M. R. DeStefano, J. T. Hupp, O. K. Farha, *Chemistry of Materials* **2018**, *30*, 2193-2197.
29. G. Kickelbick, P. Wiede, U. Schubert, *Inorganica Chimica Acta* **1999**, *284*, 1-7.
30. D. Feng, H.-L. Jiang, Y.-P. Chen, Z.-Y. Gu, Z. Wei, H.-C. Zhou, *Inorganic Chemistry* **2013**, *52*, 12661-12667.

31. W. Morris, B. Volosskiy, S. Demir, F. Gándara, P. L. McGrier, H. Furukawa, D. Cascio, J. F. Stoddart, O. M. Yaghi, *Inorganic Chemistry* **2012**, *51*, 6443-6445.
32. D. Feng, W.-C. Chung, Z. Wei, Z.-Y. Gu, H.-L. Jiang, Y.-P. Chen, D. J. Darensbourg, H.-C. Zhou, *Journal of the American Chemical Society* **2013**, *135*, 17105-17110.
33. A. Schaate, P. Roy, A. Godt, J. Lippke, F. Waltz, M. Wiebcke, P. Behrens, *Chemistry – A European Journal* **2011**, *17*, 6643-6651.
34. Z. Hu, I. Castano, S. Wang, Y. Wang, Y. Peng, Y. Qian, C. Chi, X. Wang, D. Zhao, *Crystal Growth & Design* **2016**, *16*, 2295-2301.
35. N. Stock, S. Biswas, *Chemical Reviews* **2012**, *112*, 933-969.
36. D. Feng, Z.-Y. Gu, J.-R. Li, H.-L. Jiang, Z. Wei, H.-C. Zhou, *Angewandte Chemie International Edition* **2012**, *51*, 10307-10310.
37. D. Feng, W.-C. Chung, Z. Wei, Z.-Y. Gu, H.-L. Jiang, Y.-P. Chen, D. J. Darensbourg, H.-C. Zhou, *Journal of the American Chemical Society* **2013**, *135*, 17105-17110.
38. T. Egami, S. Billinge, *Underneath the Bragg peaks: structural analysis of complex materials*, Elsevier, **2012**.
39. E. Lorch, *Journal of Physics C: Solid State Physics* **1969**, *2*, 229-237
40. A. K. Soper, E. R. Barney, *Journal of Applied Crystallography* **2012**, *45*, 1314-1317.
41. C. L. Farrow, P. Juhas, J. W. Liu, D. Bryndin, E. S. Božin, J. Bloch, T. Proffen, S. J. L. Billinge, *Journal of Physics: Condensed Matter* **2007**, *19*, 335219.
42. M.C. Lawrence, C. Schneider, M. J. Katz, *Chemical Communications* **2016**, *52*, 4971–4974.
43. D. Yang, V. Bernales, T. Islamoglu, O. K. Farha, J. T. Hupp, C. J. Cramer, L. Gagliardi, B. C. Gates, *Journal of the American Chemical Society* **2016**, *138*, 15189-15196.
44. T. Steiner, *Angewandte Chemie International Edition* **2002**, *41*, 48-76.
45. H. Grüninger, K. Armstrong, D. Greim, T. Boffa-Ballaran, D. J. Frost, J. Senker, *Journal of the American Chemical Society* **2017**, *139*, 10499-10505.
46. H. Eckert, J. P. Yesinowski, L. A. Silver, E. M. Stolper, *The Journal of Physical Chemistry* **1988**, *92*, 2055-2064.
47. P. Walther, M. Puchberger, F. R. Kogler, K. Schwarz, U. Schubert, *Physical Chemistry Chemical Physics* **2009**, *11*, 3640-3647.
48. J. Hajek, C. Caratelli, R. Demuynck, K. De Wispelaere, L. Vanduyfhuys, M. Waroquier, V. Van Speybroeck, *Chemical Science* **2018**, *9*, 2723-2732.
49. D. Massiot, I. Farnan, N. Gautier, D. Trumeau, A. Trokiner, J. P. Coutures, *Solid State Nuclear Magnetic Resonance* **1995**, *4*, 241-248.
50. G. Kickelbick, U. Schubert, *Chemische Berichte* **1997**, *130*, 473-478.

APPENDIX B: ADDITIONAL INFORMATION FOR CHAPTER 3

B.1 Experimental

B.1.1 Materials

Tetrakis(4-carboxyphenyl)porphyrin (TCPP) was purchased from Tokio Chemical Industry. Zirconyl chloride octahydrate, zirconium(IV) chloride (anhydrous), benzoic acid, and acetone were purchased from Sigma Aldrich. *N,N*-dimethylformamide (DMF) was purchased from VWR. All chemicals were used as received without further purification.

B.1.2 Instruments and methods

Ultrasonication was conducted *via* an ELMASONIC S 100 bath equipped with a high-performance 37 kHz sandwich transducer and state-of-the-art microprocessor. Centrifugation was performed with a benchtop centrifuge *Sigma-3-30K* from SIGMA. For SEM analysis, MOF suspensions were spin-coated onto silicon wafers with a *WS-650S-NPP Lite* device from LAURELL TECHNOLOGY CORPORATION.

Microscope images were taken with a CMOS camera connected to a *DM2500* light microscope from LEICA.

Scanning electron microscopy was performed on a Merlin SEM, Zeiss, with a secondary electron (SE) detector. The particle sizes were measured with the software ImageJ.

^{1}H-NMR spectra were recorded on a JEOL ECZ 400S 400 MHz spectrometer.

Sorption measurements were acquired on a Quantachrome Instruments Autosorb iQ 3 with nitrogen at 77 K. Samples were activated under high vacuum at 120 °C for 12 h before measurement unless stated otherwise. The pore size distribution (PSD) was determined from nitrogen adsorption isotherms using the QSDFT (cylindrical pores, adsorption branch) kernel in carbon for nitrogen at 77 K implemented in the ASiQwin software v 3.01.

Thermogravimetric analysis was performed on a NETZSCH STA 449 F3 Jupiter. Measurements were carried out with 5 mg of sample in an Al_2O_3 crucibles under synthetic air flow in a temperature range between 20 to 800 °C and a heating rate of 5 K/min.

Powder X-ray diffraction patterns were collected at room temperature on a Stoe Stadi-P diffractometer with Cu Kα_1 radiation (λ = 1.540596 Å) or Co-Kα_1 radiation (λ = 1.78896 Å), a Ge(111) Johann monochromator, and a DECTRIS Mythen 1K detector in Debye-Scherrer geometry. The samples were loaded into 0.5 mm inner diameter glass capillaries and measured over a range of 2θ = 2.000–30.695˚, with 0.015˚ step size and 50 s counting time per step when using Cu Kα_1 radiation and a range of 2θ = 0.500–115.325˚, with 0.015˚ step size and 200 s counting time per step when using Co-Kα_1 radiation.

Rietveld refinements were performed with TOPAS v6[1]. Refinements were performed using a 2θ offset correction, full axial model, and Lorentzian and Gaussian crystallite size broadening convolutions to correct for instrumental and morphological peak-shape effects. The background was described using Chebychev polynomials with a suitable number of terms, typically from 3rd to 11th order, and a One_on_X term to describe increased low angle background scattering. Scale factors, lattice parameters, and an isotropic atomic displacement parameter were refined. Additional pseudoatoms with a very large atomic displacement parameter were included to describe missing diffuse electron density due to pore content located near the cluster surface in the smaller pores of the framework.

Total scattering measurements were carried out using P02.1, the Powder Diffraction and Total Scattering Beamline, at PETRA III of the Deutsches Elektronen-Synchrotron (DESY). The rapid acquisition PDF method (RAPDF)[2] was used with a large-area 2D PerkinElmer detector (2048×2048 pixels, 200×200 μm^2 each) and sample-to-detector distance of 481.242 mm. The incident energy of the x-rays was 59.795 keV (λ = 0.20735 Å). Samples were loaded into 0.7 borosilicate or 1 mm inner diameter glass capillaries. An empty capillary was measured as background and subtracted, and a LaB_6 standard was measured at room temperature for calibration. Calibration, polarization correction, and azimuthal integration to 1D diffraction patterns were performed using the software pyFAI. [3-4]

Further correction and normalization of the 1D diffraction intensities were carried out to obtain the total scattering structure function, $F(Q)$, which was Fourier transformed to obtain the PDF, $G(r)$ using PDFgetX3 within xPDFsuite. [5-7] The maximum Q value used in the Fourier transform of the total scattering data was 20.0 Å^{-1}. A Lorch function was used in the data processing to reduce termination ripples present due to truncation.[8] Simulated PDFs were generated from respective models using Diffpy-CMI. [9]

Electron diffraction data were collected on a Thermofisher Titan ‘cubed’ transmission electron microscope operated at 300 kV and at room temperature. Dry polycrystalline powder was gently

crushed between two glass slides and transferred onto a continuous-carbon copper grid. The grid was loaded onto a Fischione 2020 tomography holder and inserted into the TEM without further treatment.

Electron beam-defining settings included C2 lens excitation corresponding to spot size nr. 9 and a C2 aperture of 20 µm. Data collections were conducted using a custom-made script allowing for a stepwise tilt and acquisition of diffraction patterns by a Gatan Ultra Scan 1000 CCD camera.Diffraction data sets were acquired using a oscillation step of 0.25° and processed by the software pets2 version 2.1.20211012.1037.[10]

Elemental analysis of carbon, hydrogen, and nitrogen was carried out *via* an UNICUBE Elementar Analysensysteme GmbH Langenselbold instrument. The zirconium content was determined *via* ICP-OES using a Vista Pro Simultaneous ICP-OES spectrometer equipped with an CCD detector from Agilent Technologies. The evaluation of the data was conducted using the ICP-Expert software.

B.1.3 Synthesis procedures

Synthesis from different $ZrCl_4$ sources

Synthesis was carried out from neat $ZrCl_4$ from the glovebox ($ZrCl_4$_GB), $ZrCl_4$_GB that was left in air for 1 d ($ZrCl_4$_GB_1d), $ZrCl_4$_GB that was left in air for 3 d ($ZrCl_4$_GB_3d), and $ZrCl_4$ that was left in air over several months ($ZrCl_4$_lab). In a typical synthesis, $ZrCl_4$ (120 mg, 0.510 mmol), benzoic acid (1.60 g, 13.1 mmol), and TCPP (40.0 mg, 0.0506 mmol mg) were dissolved in DMF (8 mL) in a 20 mL microwave vial by sonication for 2 min. The mixture was heated in an oven for 24 h at 120 °C. After cooling, the product was collected by centrifugation and washed with DMF (three times, 16k rpm/20 min/16 °C) and acetone (twice, 16k rpm/8 min/16 °C). The product was soaked in acetone overnight, washed with acetone once, and dried with supercritical CO_2.

Synthesis from ZrCl4_GB with addition of water

$ZrCl_4$_GB (120 mg, 0.510 mmol), benzoic acid (1.60 g, 13.1 mmol), and TCPP (40.0 mg, 0.0506 mmol) were dissolved in DMF (8 mL) in a 20 mL microwave vial by sonication for 2 min. 20 or 50 µL of water was added and the mixtures were heated in an oven for 24 h at 120 °C. After cooling, the products were collected by centrifugation and washed with DMF and acetone following the procedure described above. Centrifugation (16k rpm/5 min/16 °C) and supercritical CO_2 drying yielded $ZrCl_4$_GB_20µL and $ZrCl_4$_GB_20µL as purple powders.

Time dependent synthesis from $ZrCl_4$_GB and $ZrCl_4$_lab

$ZrCl_4$_GB or $ZrCl_4$_lab (120 mg, 0.510 mmol), benzoic acid (1.60 g, 13.1 mmol), and TCPP (40.0 mg, 0.0506 mmol) were dissolved in DMF (8 mL) in a 20 mL microwave vial by sonication for 2 min. The mixtures were heated in an oven for varying lengths of time at 120 °C (see Table B.1 for more information). The products were immediately collected by centrifugation, washed with DMF and acetone following the procedure described above and dried with supercritical CO_2.

Table B.1: Sample description and reaction times of time-dependent synthesis study from $ZrCl_4$_GB and $ZrCl_4$_lab.

Sample	$ZrCl_4$	Time	Sample	$ZrCl_4$	Time
MOF_$ZrCl_4$_GB_2min	$ZrCl_4$_GB	2 min	MOF_$ZrCl_4$_lab_2min	$ZrCl_4$_lab	2 min
MOF_$ZrCl_4$_GB_1h	$ZrCl_4$_GB	1 h	MOF_$ZrCl_4$_lab_1h	$ZrCl_4$_lab	1 h
MOF_$ZrCl_4$_GB_24h	$ZrCl_4$_GB	24 h	MOF_$ZrCl_4$_lab_2h	$ZrCl_4$_lab	2 h
MOF_$ZrCl_4$_GB_48h	$ZrCl_4$_GB	48 h	MOF_$ZrCl_4$_lab_6h	$ZrCl_4$_lab	6 h
MOF_$ZrCl_4$_GB_4d	$ZrCl_4$_GB	4 d	MOF_$ZrCl_4$_lab_18h	$ZrCl_4$_lab	18 h
MOF_$ZrCl_4$_GB_20d	$ZrCl_4$_GB	20 d	MOF_$ZrCl_4$_lab_24h	$ZrCl_4$_lab	24 h

Time dependent synthesis from $ZrOCl_2 \cdot 8H_2O$

$ZrOCl_2 \cdot 8H_2O$ (120 mg, 0.372 mmol), TCPP (40.0 mg, 0.0506 mmol) and benzoic acid (1.30 g, 10.6 mmol) were dissolved in DMF (8 mL) in a 20 mL microwave vial *via* sonication. The solution was heated in an oven at 120 °C for varying reaction times (see Table B.2), washed with DMF (three times, 16k rpm/15 min/ 16 °C) and resuspended in DMF (10 mL). The reaction mixture was activated with HCl (8M, 0.50 mL) in an oven (15 h, 100 °C). The suspension was washed with DMF (twice, 16k rpm/20 min/16 °C) and acetone (twice, 16k rpm/8 min/16 °C). The mixture was soaked in acetone overnight and washed once with acetone. The product was obtained as purple powder.

Table B.2: Sample description and reaction times of time dependent synthesis study from $ZrOCl_2 \cdot 8H_2O$.

Sample	Time
MOF_$ZrOCl_2$_15min	15 min
MOF_ $ZrOCl_2$ _30min	30 min
MOF_ $ZrOCl_2$_60min	60 min
MOF_ $ZrOCl_2$_90min	90 min
MOF_ $ZrOCl_2$_4h	4 h
MOF_ $ZrOCl_2$_24h	24 h

B.2 Results and discussion

B.2.1 Powder X-ray diffraction analysis

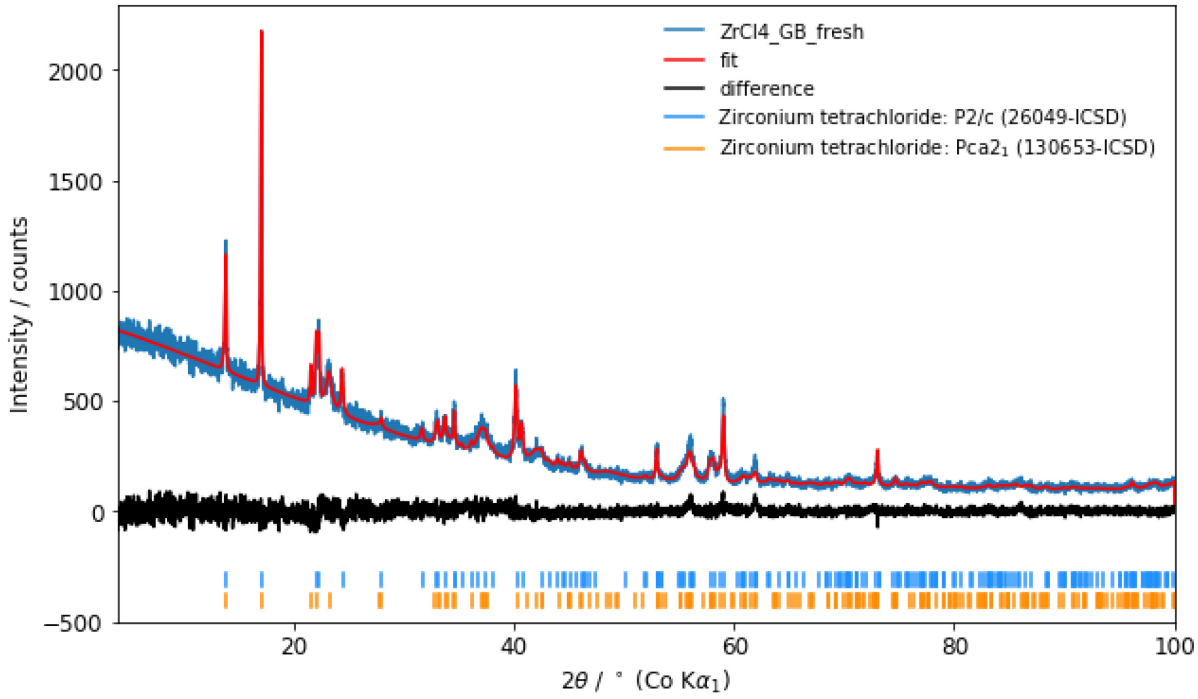

Figure B.1: Rietveld refinement of neat $ZrCl_4$_GB that was stored in the glovebox gives a phase mixture of two modifications of zirconium tetrachloride: 39.7(6)% $P2/c$[11] and 60.3(6)% $Pca2_1$[12].

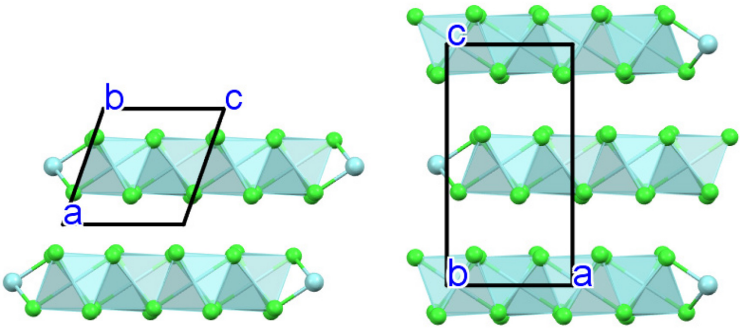

Figure B.2: Both structures consist of 1D $ZrCl_4$ chains with different stacking modifications in the directions perpendicular to the direction of chain propagation. Comparison of stacking patterns in (left) $P2/c$[11] (AA stacking) and (right) $Pca2_1$[12] (ABAB stacking).

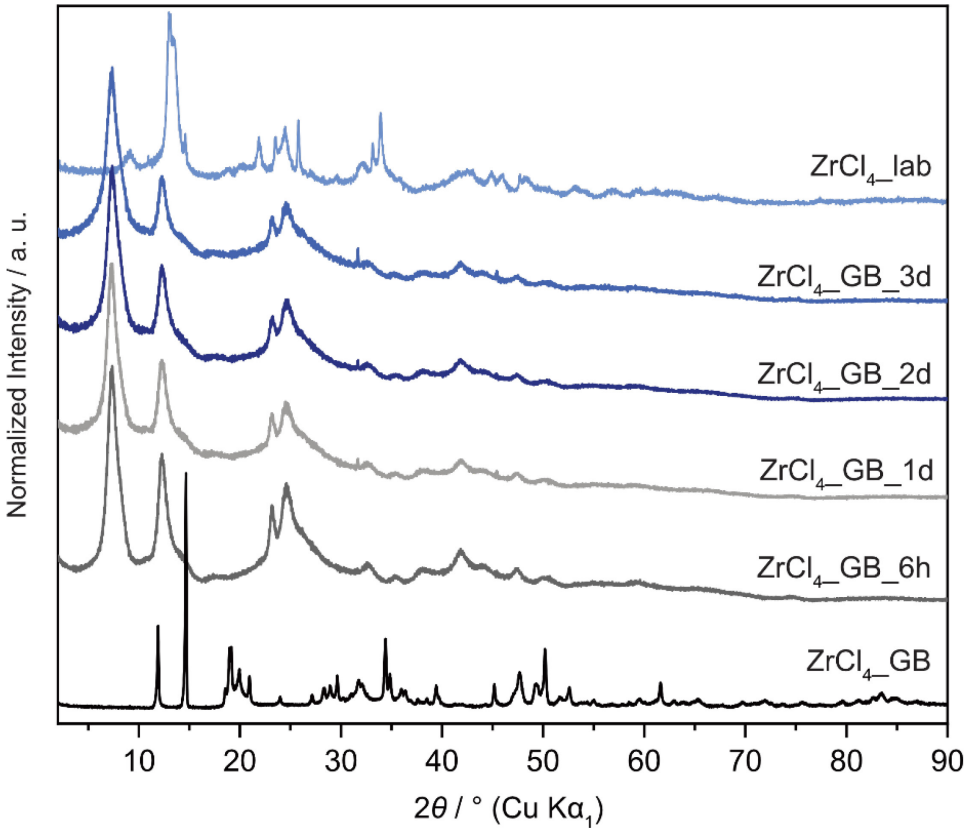

Figure B.3: PXRD patterns of $ZrCl_4$ _GB, $ZrCl_4$ _GB_6h, $ZrCl_4$ _GB_1d, $ZrCl_4$ _GB_2d, and $ZrCl_4$_GB_3d, that were left in air for 6 h, 1 d, 2 d, and 3 d, respectively, as well as $ZrCl_4$ _lab stored in the lab under ambient conditions showing that $ZrCl_4$ hydrolyses when exposed to air.

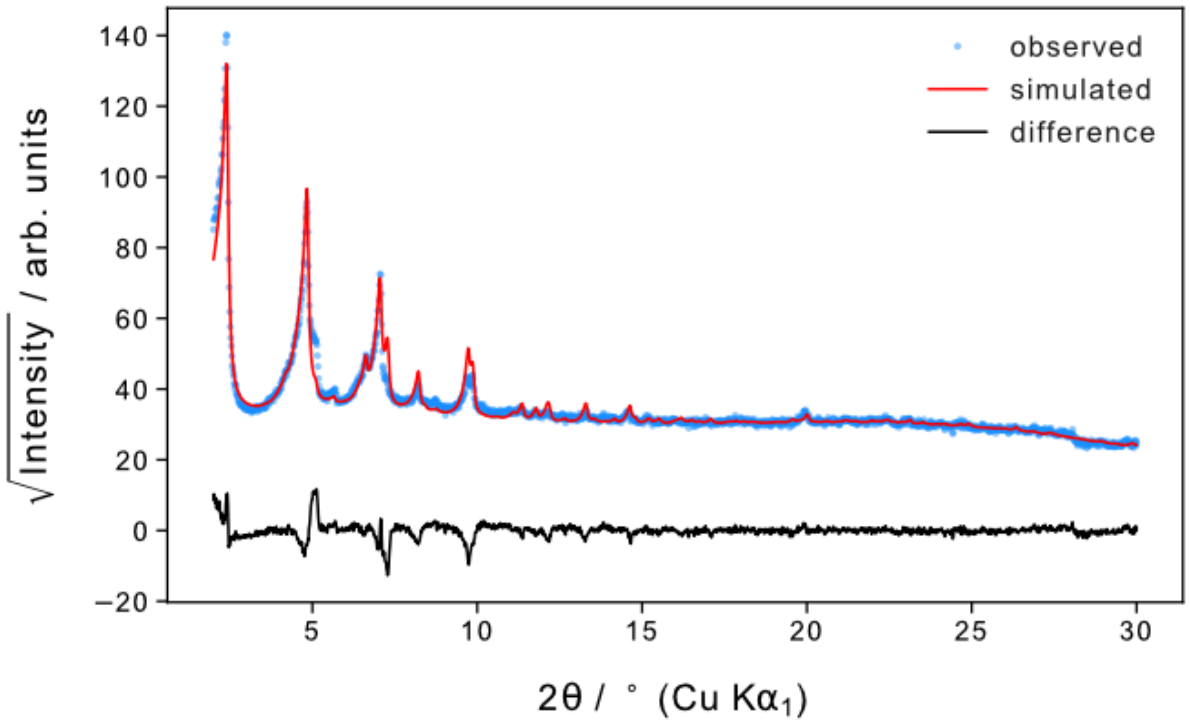

Figure B.4: Rietveld refinement of PCN-222[13] and NU-902[14] against the observed XRD pattern of the product obtained from $ZrCl_4$_1d after 24 h reaction.

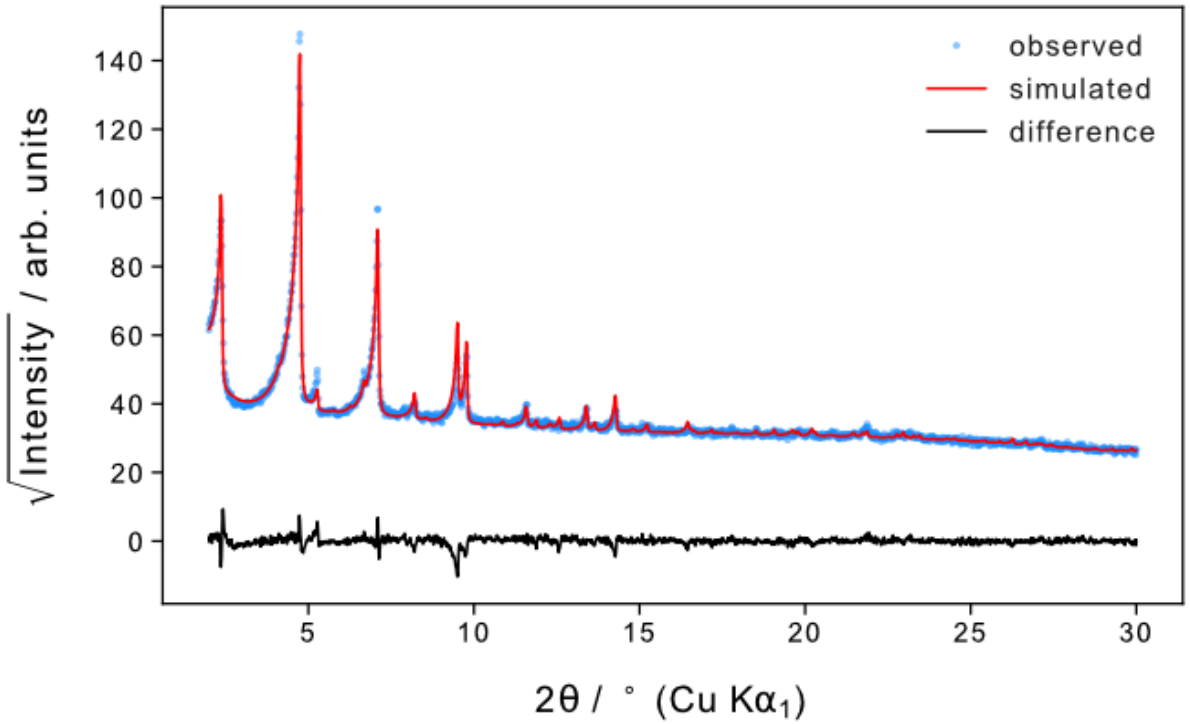

Figure B.5: Rietveld refinement of PCN-222[13] and dPCN-224[15] against the observed XRD pattern of the product obtained from $ZrCl_4$_GB under addition of 20 µL water after 24 h reaction.

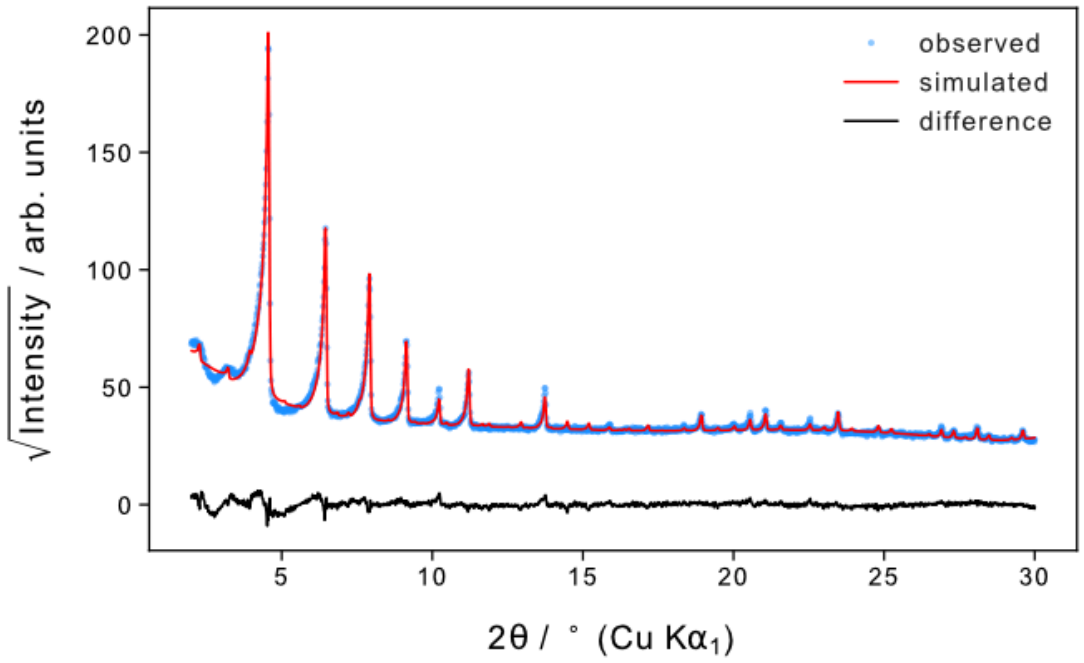

Figure B.6: Rietveld refinement of dPCN-224[15] against the observed pattern of the product obtained from $ZrCl_4$_GB under addition of 50 µL water after 24 h reaction.

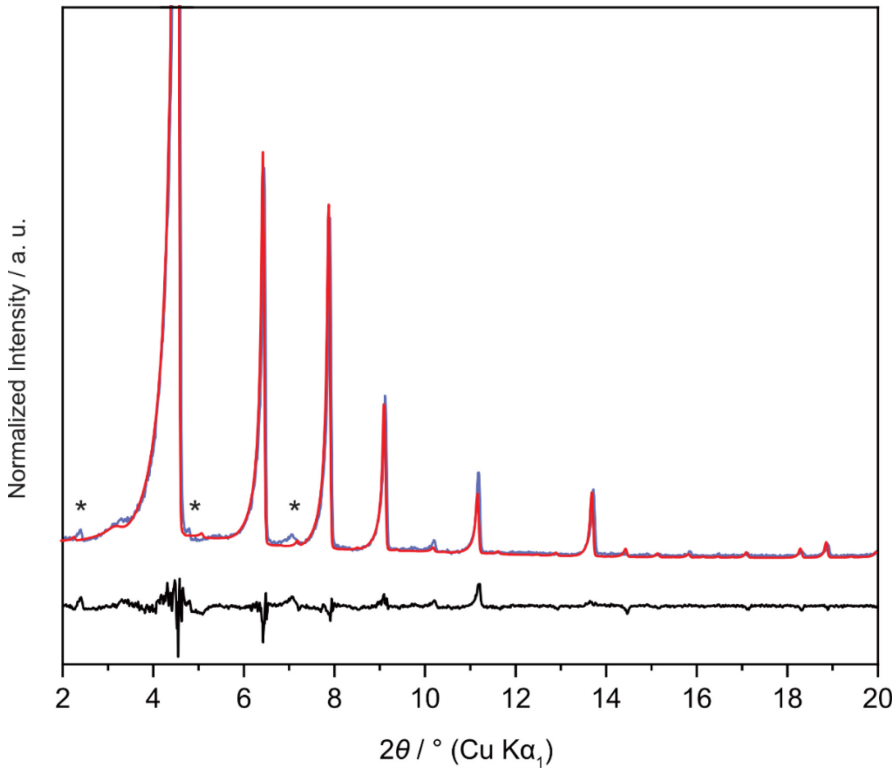

Figure B.7: Rietveld refinement of dPCN-224[15] to the observed pattern of the product obtained after 90 min reaction during synthesis from $ZrOCl_2 \cdot 8H_2O$. The asterisk (*) highlight small amounts of PCN-222[13] like impurities.

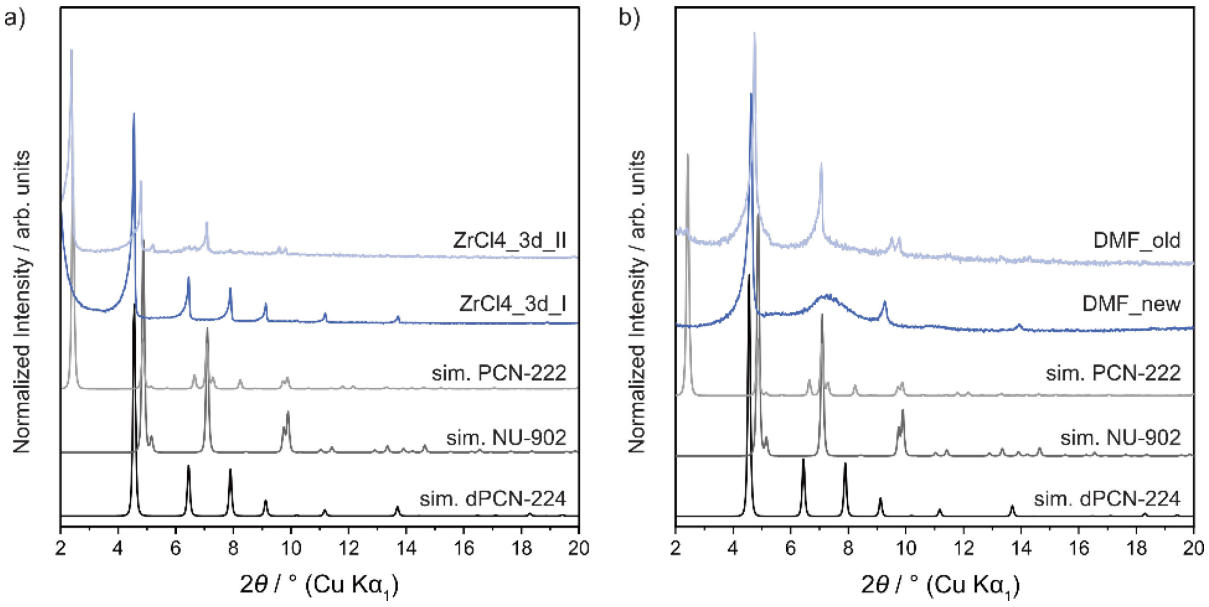

Figure B.8: a) PXRD of the products obtained after 24 h reaction when employing $ZrCl_4$_3d that was left to age for 3 days before synthesis compared to simulated (sim.) patterns of PCN-222[13] and NU-902[14], and dPCN-224[15]. While one synthesis from $ZrCl_4$_3d ($ZrCl_4$_3d _I) yielded phase-pure dPCN-224, another synthesis from $ZrCl_4$_3d performed on another day ($ZrCl_4$_3d_II) yielded a NU-902-like product suggesting slower formation of dPCN-224 due to smaller amounts of water in the reaction. b) PXRD of the products obtained after 24 h reaction from $ZrCl_4$_GB in DMF from a newly opened bottle (DMF_new) and in DMF from the same bottle after standing in air for a month (DMF_old) compared to simulated (sim.) patterns of PCN-222[13] and NU-902[14], and dPCN-224[15]. While synthesis from new DMF did not yield a crystalline MOF, synthesis from DMF_old yielded a NU-902 like product.

B.2.2 Additional SEM images

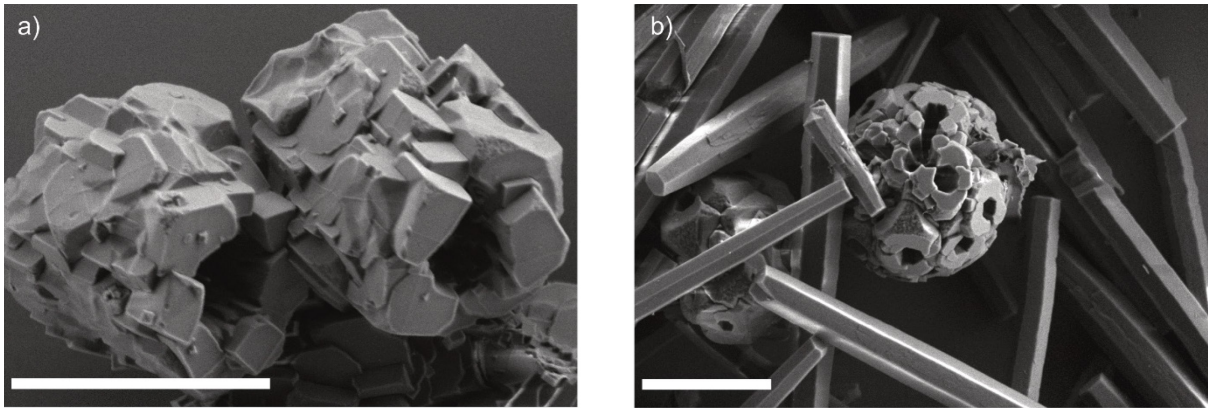

Figure B.9: SEM images of dPCN-224 particles during synthesis with a) $ZrOCl_2 \cdot 8H_2O$ and b) $ZrCl_4$_lab. Scale bar = 5 µm. The holes results from dissolution of the metal–organic rod intermediates.

B.2.3 Sorption analysis

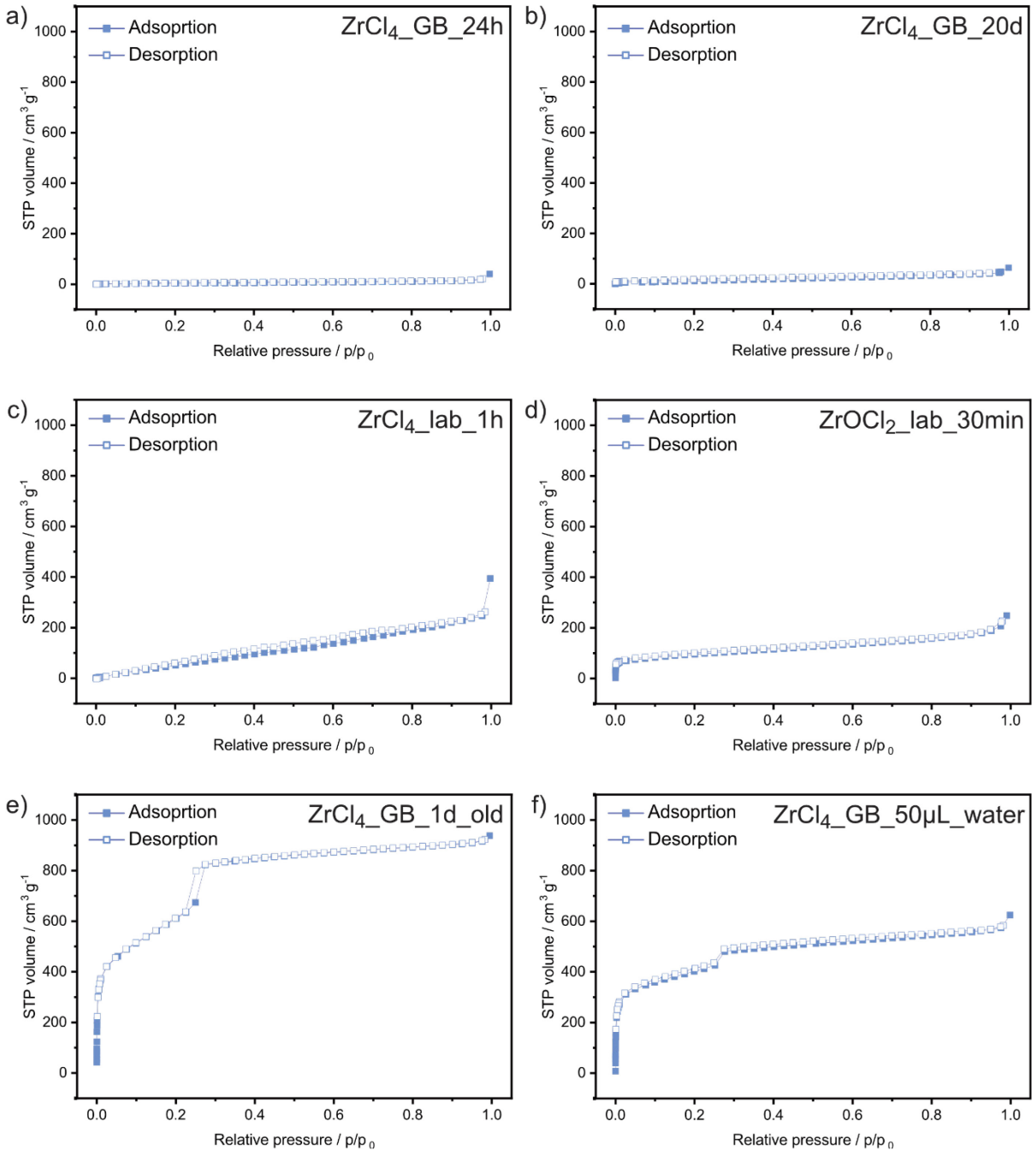

Figure B.10: Nitrogen sorption isotherm (77 K) of a) $ZrCl_4$_GB_24, b) $ZrCl_4$_GB_20d, c) $ZrCl_4$_lab_1h, d) $ZrOCl_2$_30min, e) $ZrCl_4$_1d_old, and f) $ZrCl_4$_GB_50µL_water.

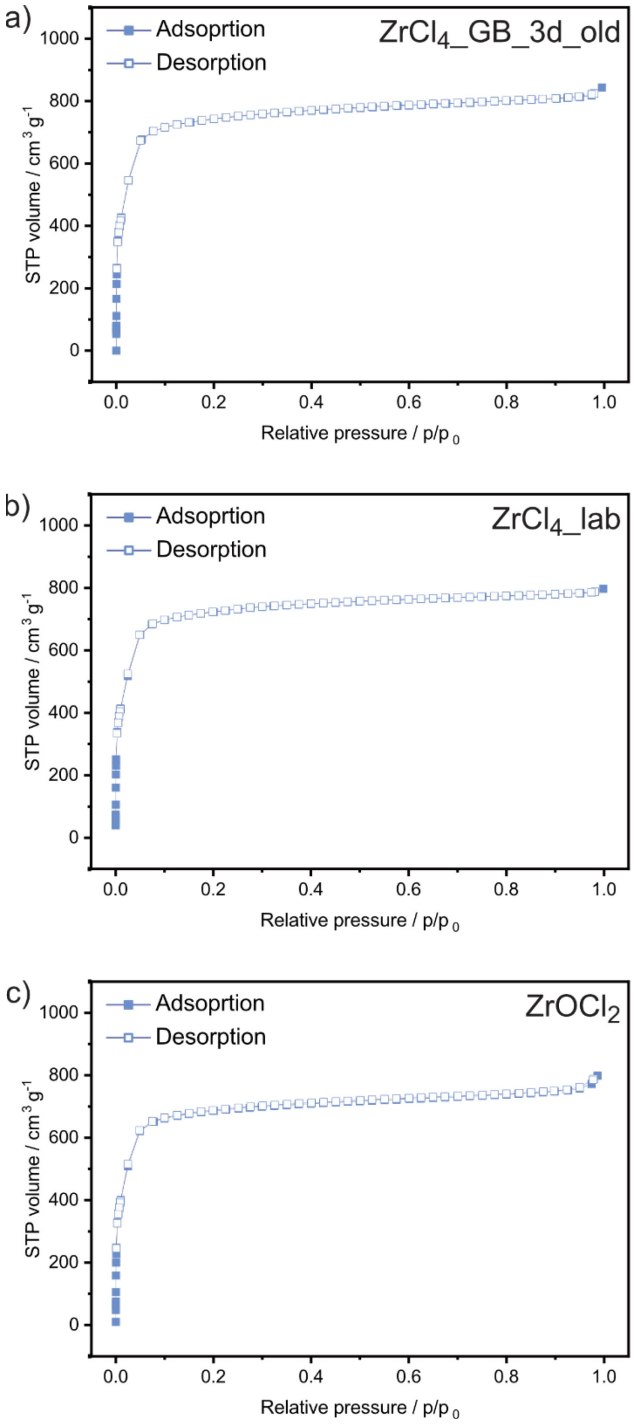

Figure B.11: Nitrogen sorption isotherm (77 K) of the products obtained after 24 h reaction from a) $ZrCl_4$_3d ($ZrCl_4$_GB_3d_old), b) $ZrCl_4$_lab, and c) $ZrOCl_2 \cdot 8H_2O$ ($ZrOCl_2$).

B.2.4 TGA analysis

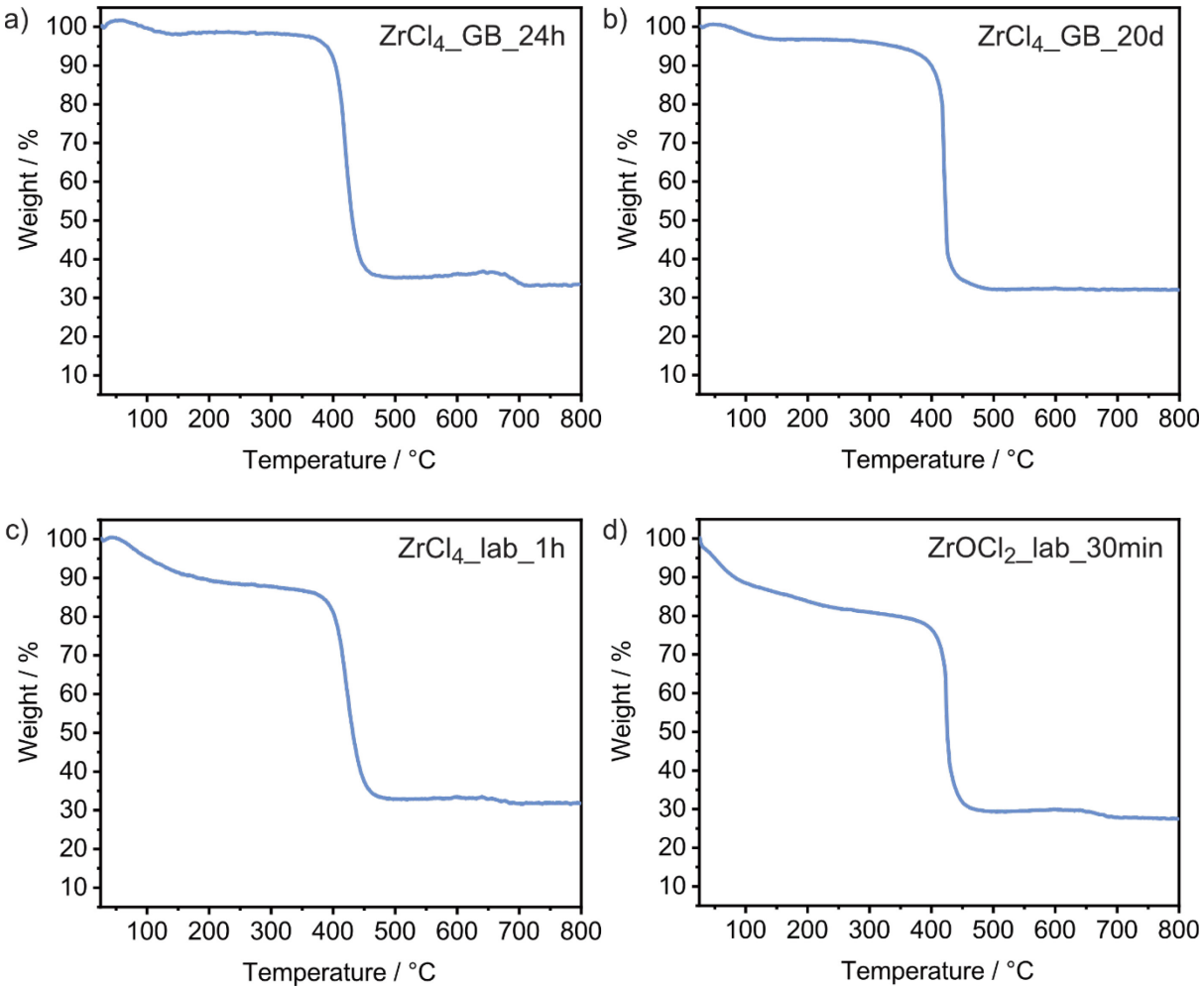

Figure B.12: Thermogravimetric analysis of a) $ZrCl_4$_GB_24, b) $ZrCl_4$_GB_20d, c) $ZrCl_4$_lab_1h, and d) $ZrOCl_2$_30min.

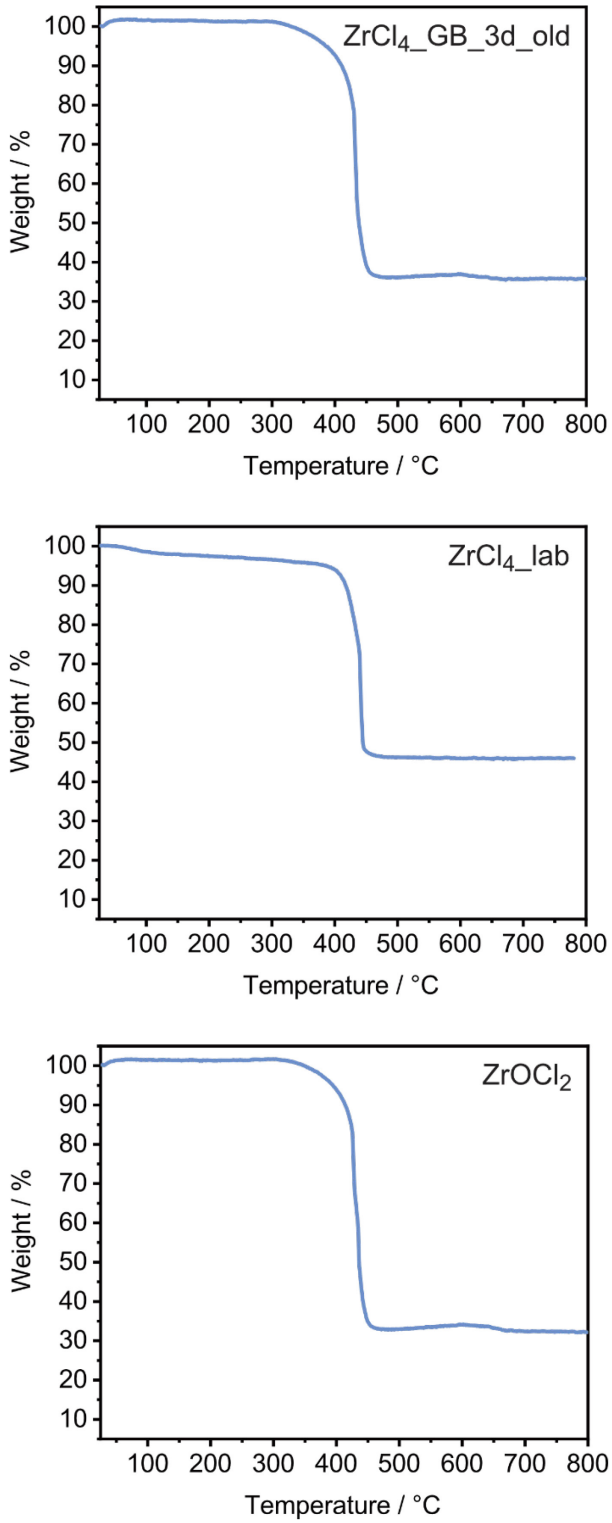

Figure B.13: Thermogravimetric analysis of the products obtained after 24 h reaction from a) $ZrCl_4$_3d ($ZrCl_4$_GB_3d_old), b) $ZrCl_4$_lab, and c) $ZrOCl_2 \cdot 8H_2O$ ($ZrOCl_2$).

B.2.5 Elemental analysis

Table B.3: Zr, C, H, and N content determined from elemental analysis.

Sample	Zr (wt%)	C (wt%)	H (wt%)	N (wt%)
$ZrCl_4$_GB_1h	0.427	60.36	4.69	5.70
$ZrCl_4$_GB_24h	16.52	48.77	4.07	4.72
$ZrCl_4$_GB_20d	19.34	48.20	4.06	3.57
$ZrCl_4$_lab_1h	15.04	40.30	4.88	3.87
$ZrCl_4$_lab_24h	22.84	46.25	3.09	4.74
$ZrCl_4$_GB_1d	20.27	52.14	3.48	4.42
$ZrCl_4$_GB_3d	20.39	51.00	3.42	3.99
$ZrCl_4$_GB_20µL	15.83	47.65	4.62	6.09
$ZrCl_4$_GB_20µL	15.83	47.65	4.62	6.09
$ZrOCl_2$_30min	27.54	40.97	4.00	3.88
$ZrOCl_2$_24h	22.28	49.94	3.33	3.65

B.2.6 Energy dispersive X-ray analysis

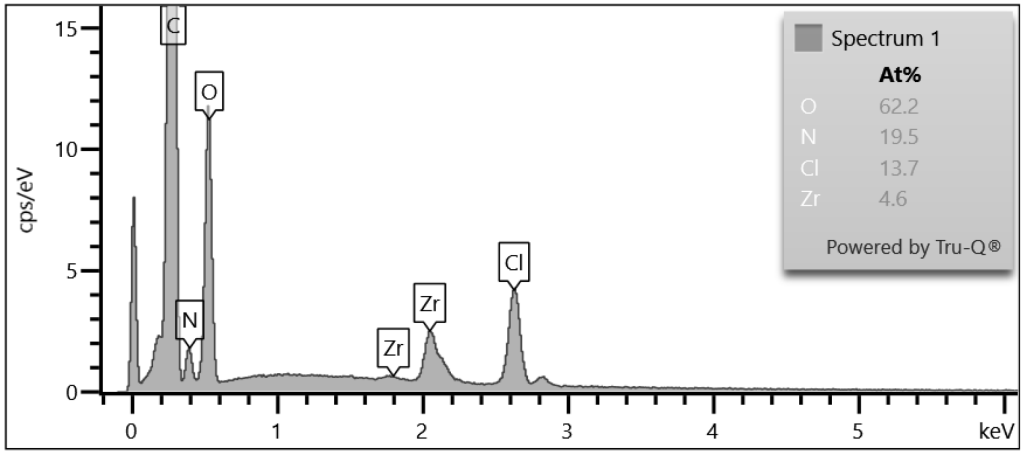

Figure B.14: EDX spectrum of the product obtained from $ZrCl_4$_lab after 2 min reaction time.

B.2.7 NMR spectroscopy

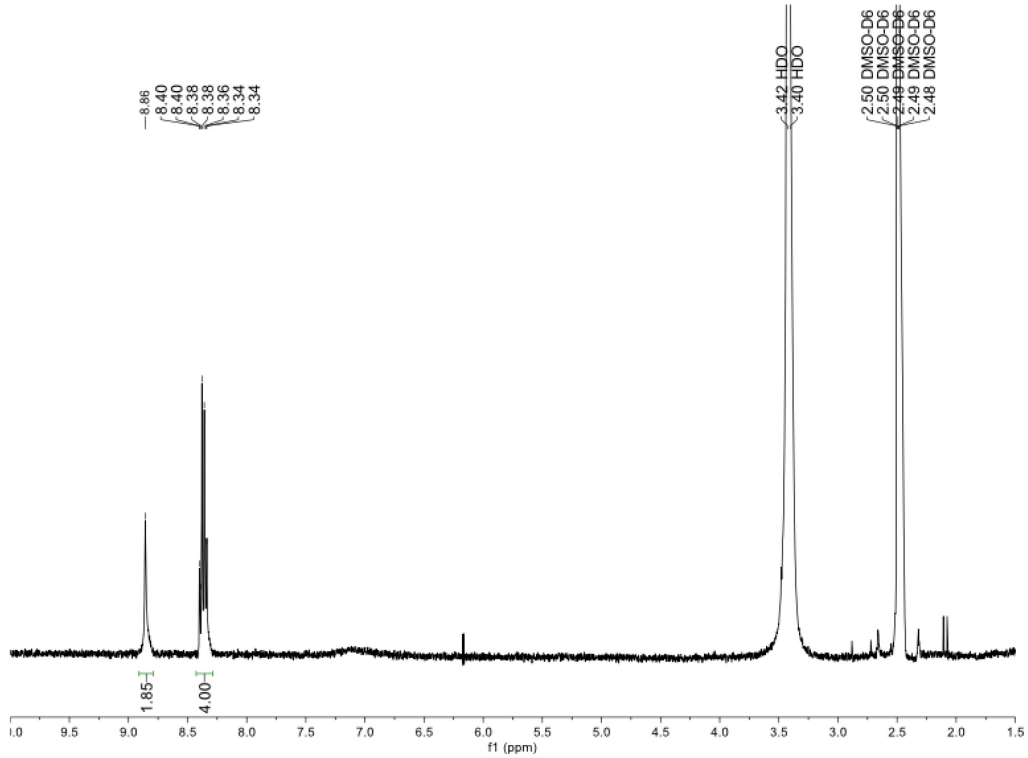

Figure B.15: ^{1}H NMR of organic intermediate obtained after 2 min reaction from $ZrCl_4$_GB showing that the product only contains TCPP (measured in DMSO).

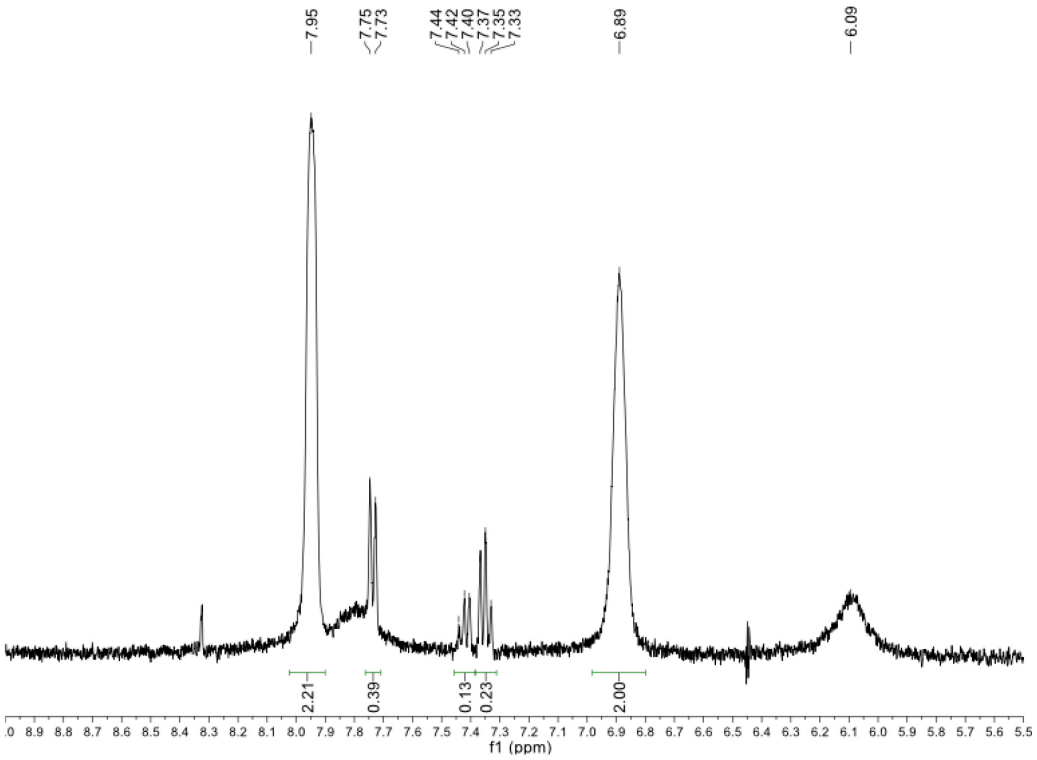

Figure B.16: ^{1}H NMR of the metal–organic intermediate after obtained after 24 h reaction from $ZrCl_4$_GB after NaOH digestion showing that the product contains TCPP and benzoic acid (measured in D_2O).

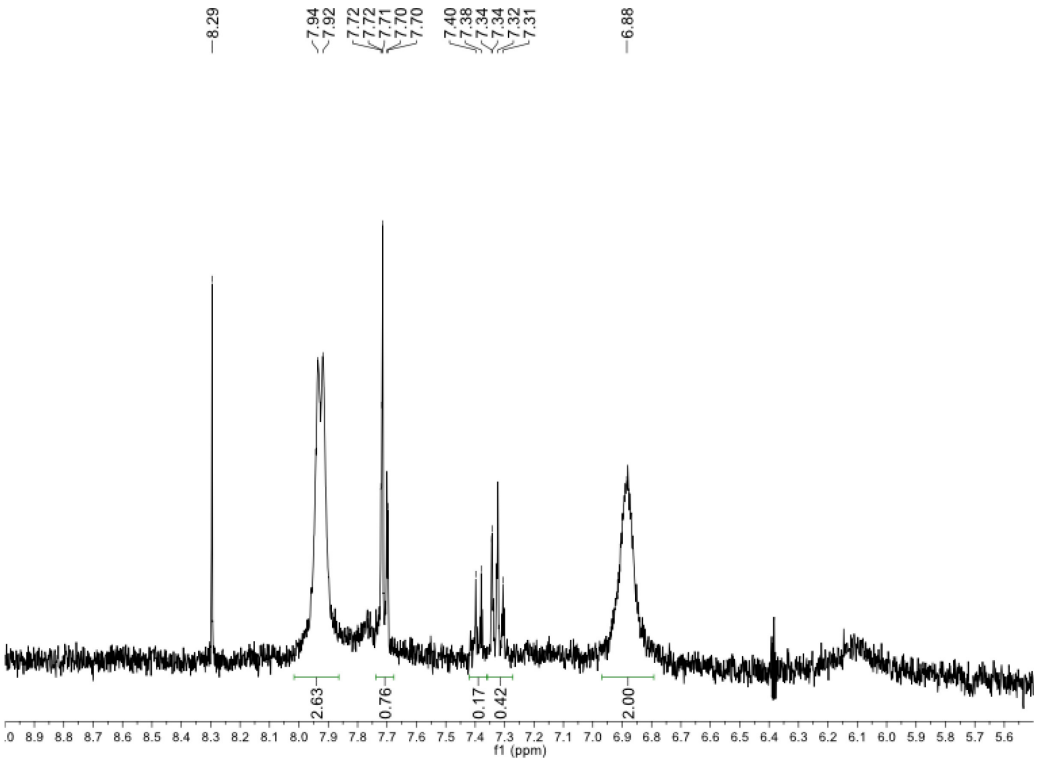

Figure B.17: ^{1}H NMR of the metal–organic intermediate $ZrCl_4$_lab_1h obtained after 1 h reaction from $ZrCl_4$_lab after NaOH digestion showing that the product contains TCPP and benzoic acid (measured in D_2O).

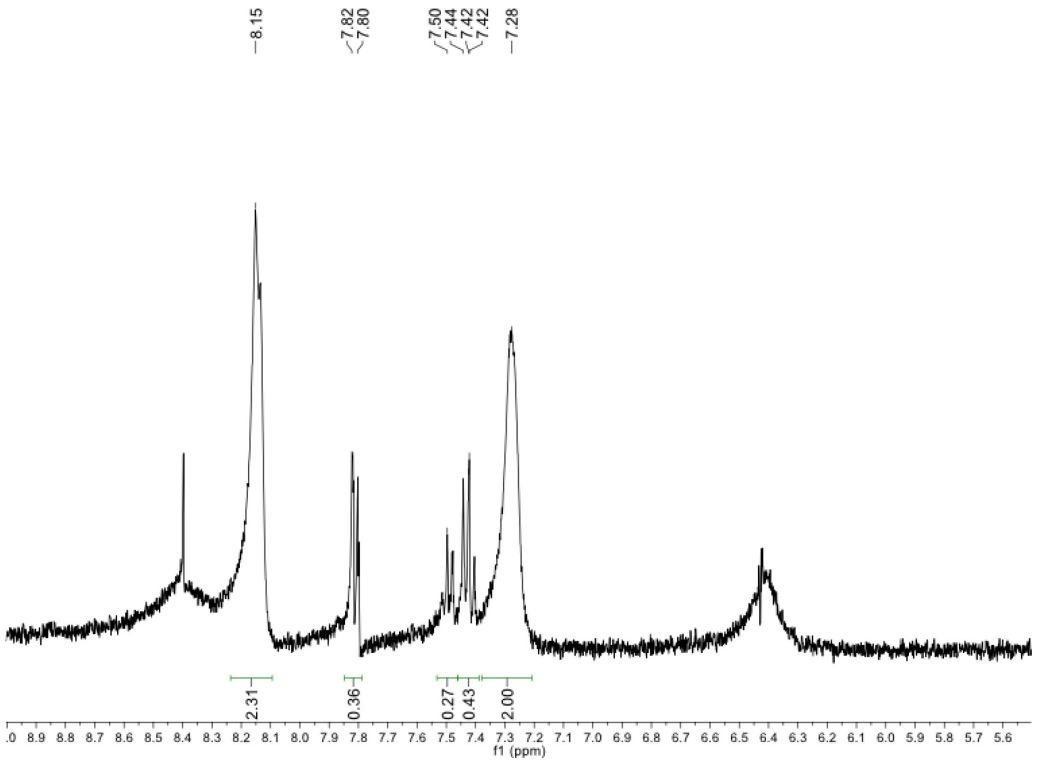

Figure B.18: ^{1}H NMR of the metal–organic intermediate $ZrOCl_2$_30min obtained after 30 min reaction from $ZrOCl_2 \cdot 8H_2O$ after NaOH digestion showing that the product contains TCPP and benzoic acid (measured in D_2O).

B.2.8 Photo of organic intermediate

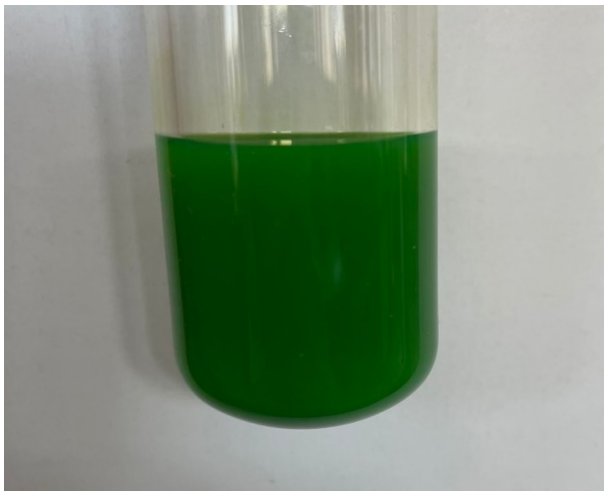

Figure B.19: Green, organic intermediate formed during synthesis from $ZrCl_4$_GB after 1 h reaction indicating that the TCPP linker is protonated to dicationic TCPP (H_4TCPP^{2+}).

B.2.9 TEM

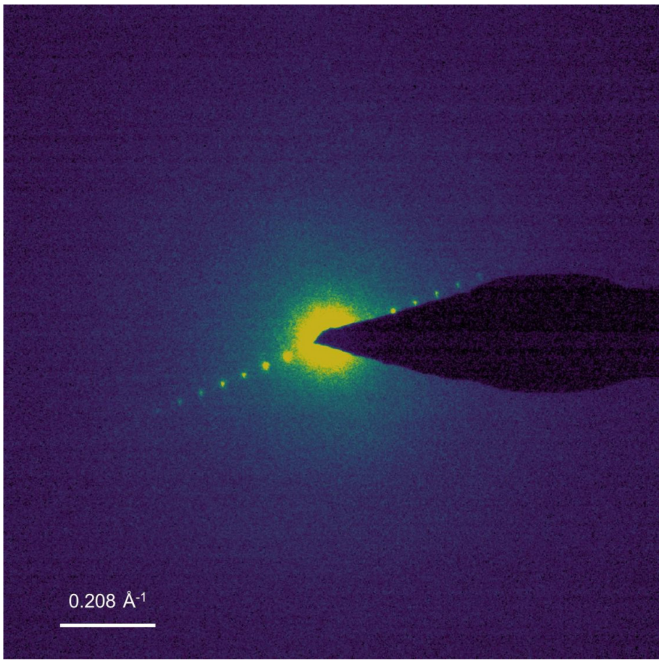

Figure B.20: Diffraction image of metal–organic intermediate obtained during reaction from $ZrOCl_2$ $8H_2O$ showing periodicity along one direction.

B.2.10 Simulated pair distribution functions of Zr-oxo node models

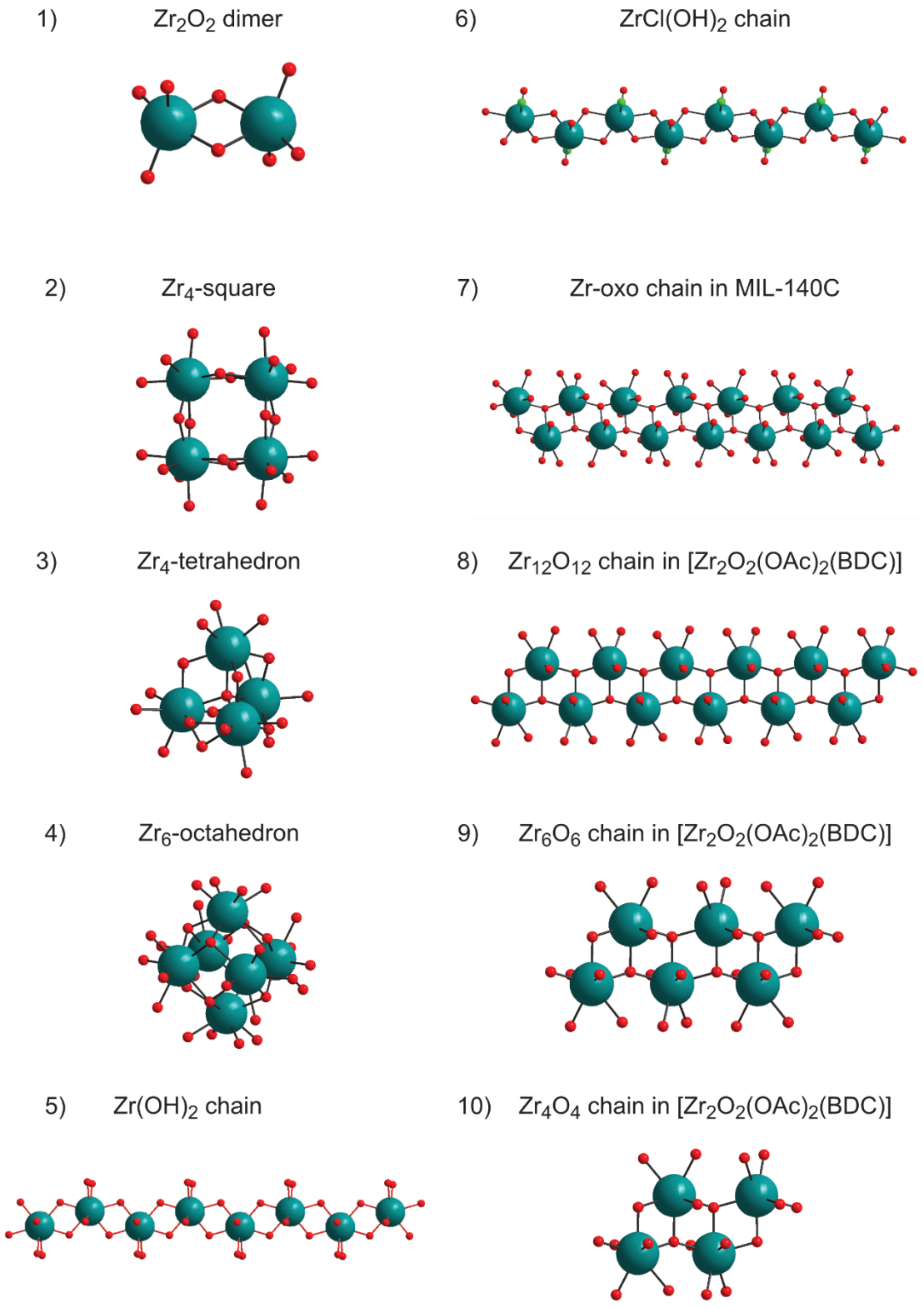

Figure B.21: Employed Zr-oxo nodes for PDF simulations in Figure B.22–B.25.

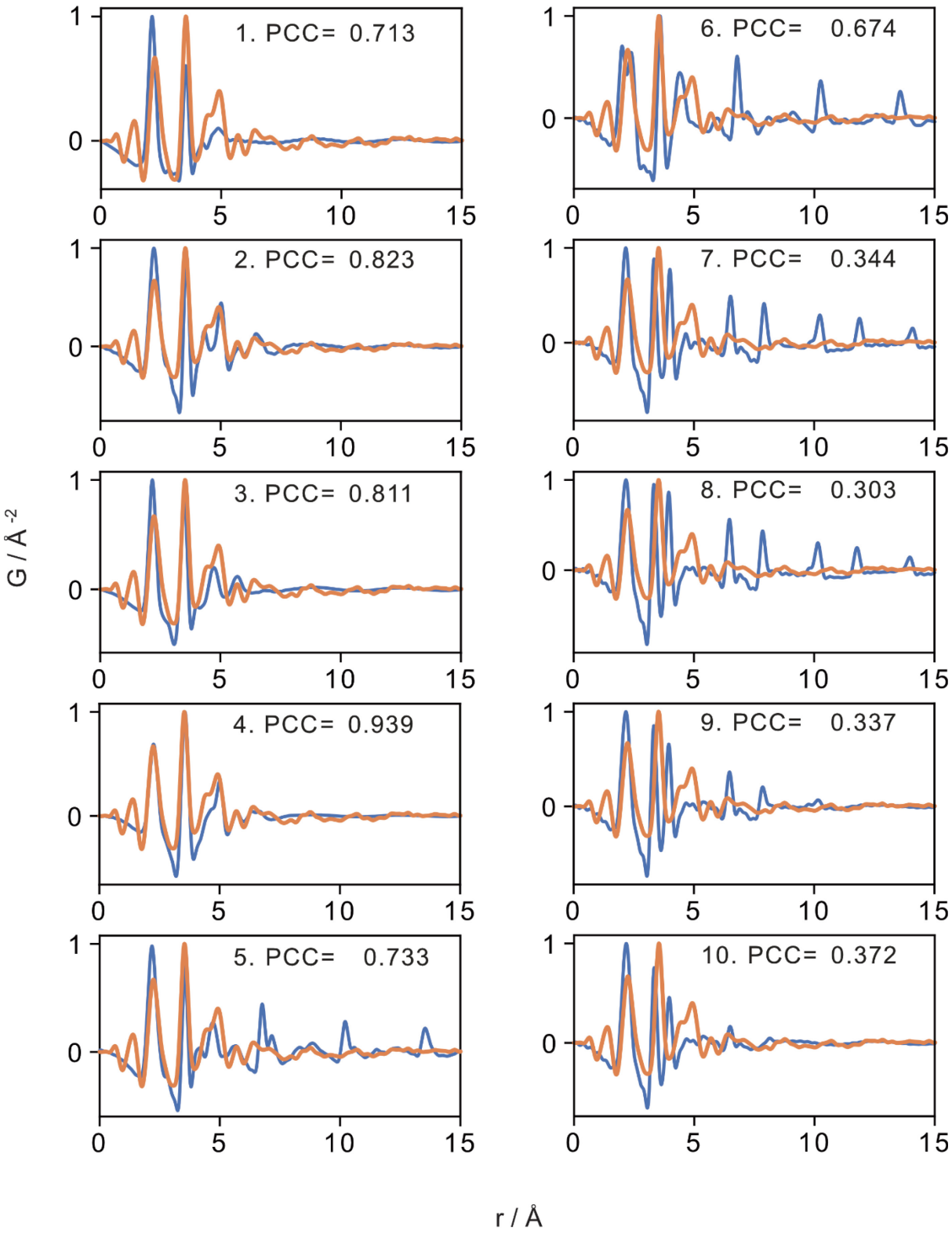

Figure B.22: Experimental PDFs of the metal–organic intermediate $ZrCl_4$_lab_1h synthesized from $ZrCl_4$_lab after 1 h reaction time compared to the simulated PDFs of the Zr-oxo nodes represented in Figure B.21.

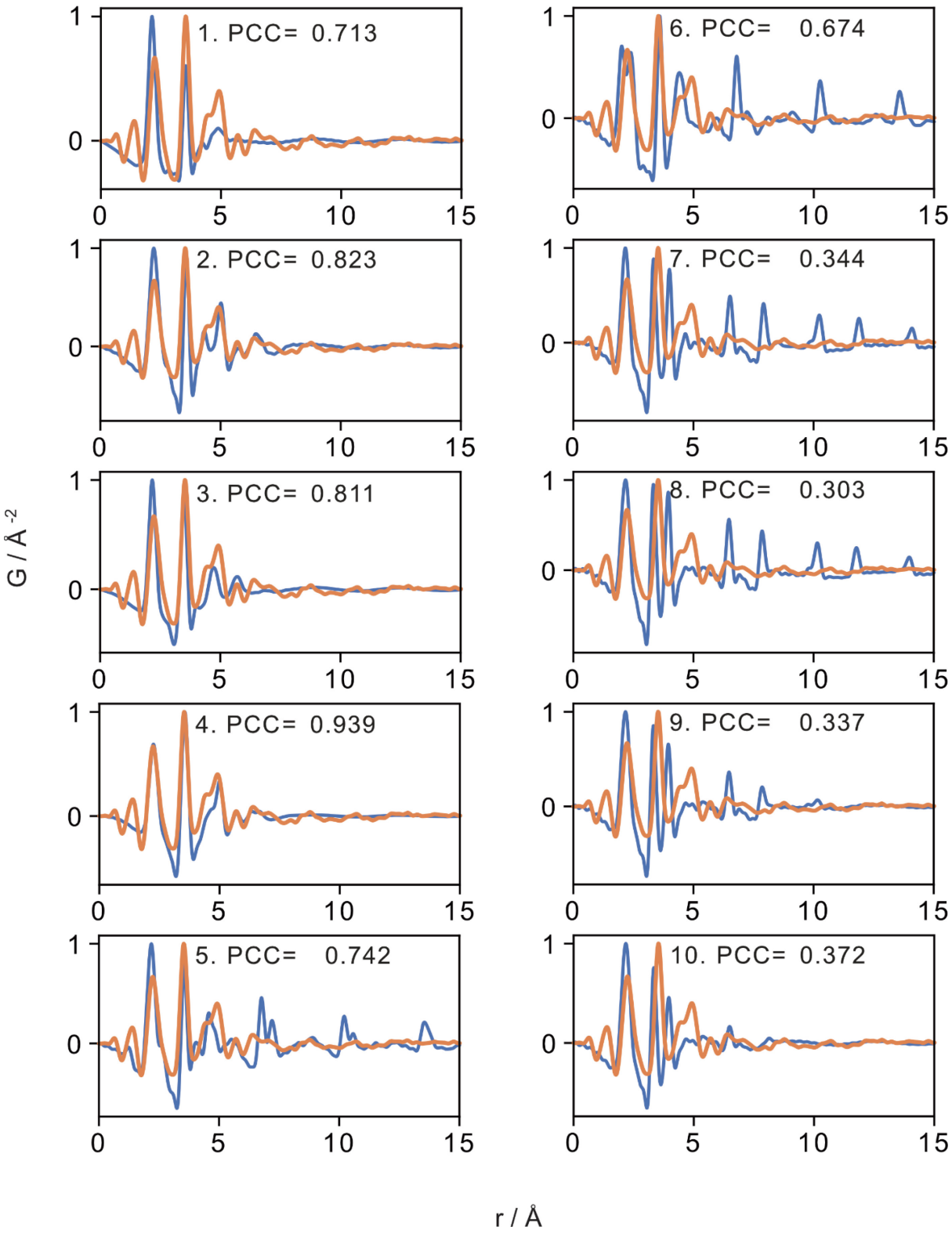

Figure B.23: Experimental PDFs of the metal–organic intermediate $ZrOCl_2$_30min synthesized from $ZrOCl_2 \cdot 8H_2O$ after 30 min reaction time compared to the simulated PDFs of the Zr-oxo nodes represented in Figure B.21.

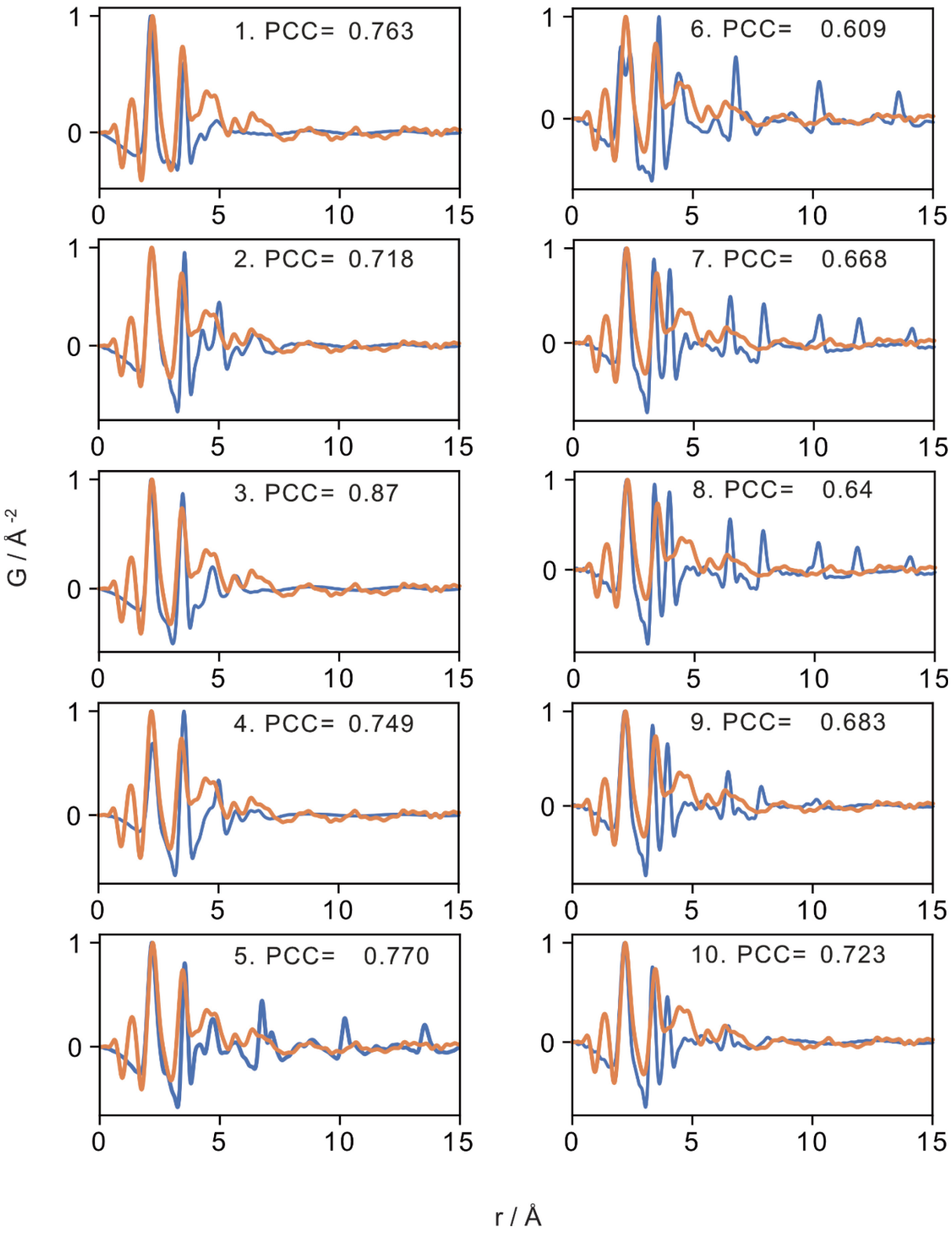

Figure B.24: Experimental PDFs of the metal–organic intermediate $ZrCl_4$_GB_24h synthesized from neat $ZrCl_4$_GB after 24 h reaction time compared to the simulated PDFs of the Zr-oxo nodes represented in Figure B.21.

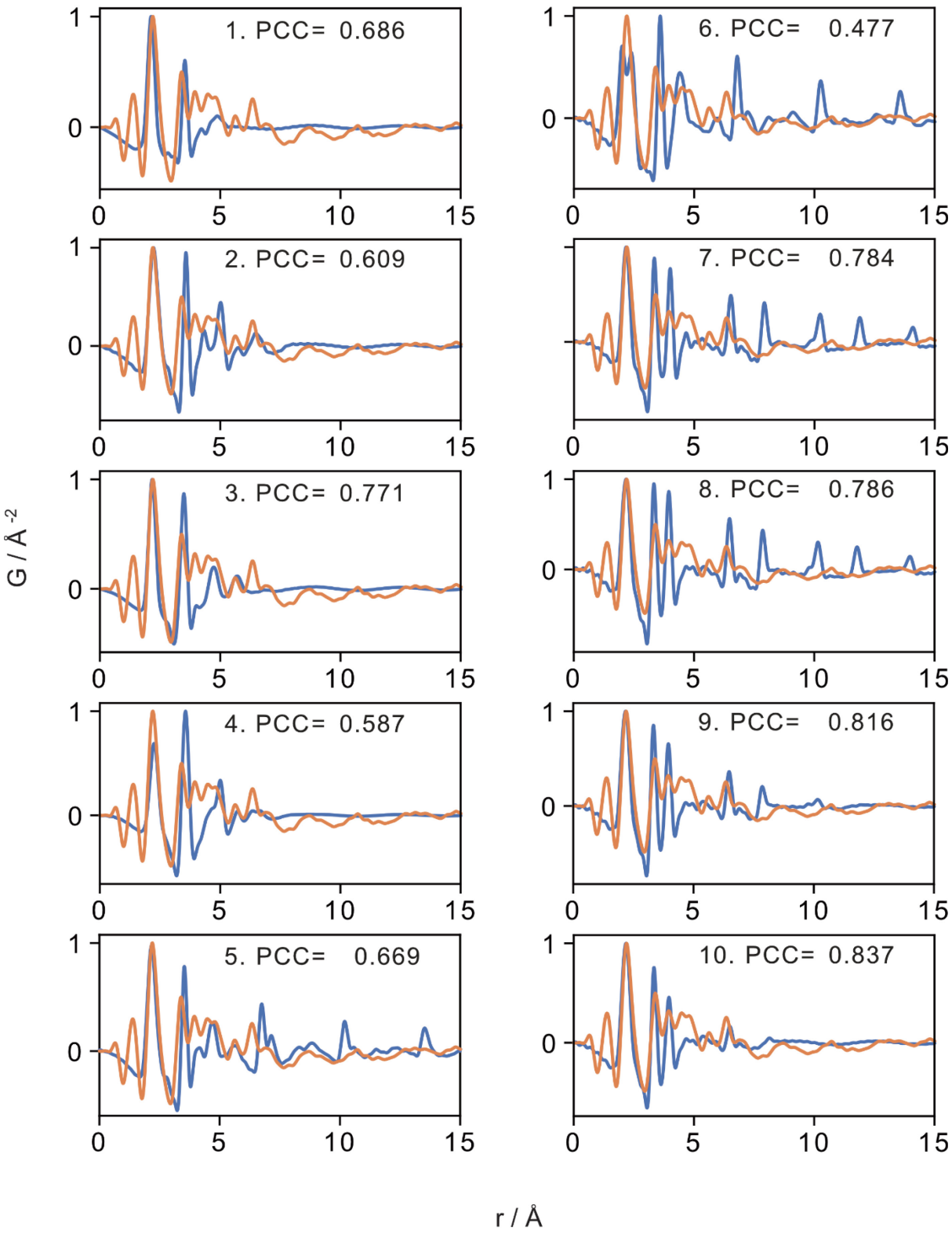

Figure B.25: Experimental PDFs of the metal–organic intermediate $ZrCl_4$_GB_20d synthesized from neat $ZrCl_4$_GB after 20 d reaction time compared to the simulated PDFs of the Zr-oxo nodes represented in Figure B.21.

B.2.11 $Zr_6O_4(OH)_4$-TCPP models

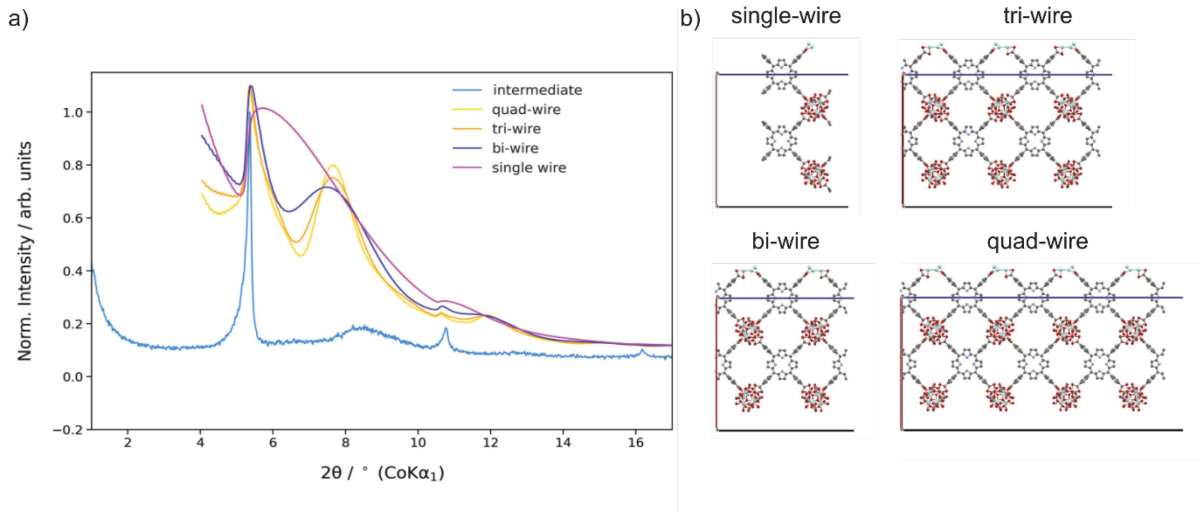

Figure B.26: a) Simulated PXRD patterns of b) $Zr_6O_4(OH)_4$-TCPP single-, bi-, tri-, and quadwire models with periodicity along one direction. The simulations suggest bi-wire-like arranged Zr-nodes and TCPP linkers in the metal–organic intermediate formed during dPCN-224 synthesis from $ZrCl_4$_lab.

References

1. A. Coelho, *Journal of Applied Crystallography* **2018**, *51*, 210-218.
2. P. J. Chupas, X. Qiu, J. C. Hanson, P. L. Lee, C. P. Grey, S. J. L. Billinge, *Journal of Applied Crystallography* **2003**, *36*, 1342-1347.
3. J. Kieffer, V. Valls, N. Blanc, C. Hennig, *Journal of Synchrotron Radiation* **2020**, *27*, 558-566.
4. G. Ashiotis, A. Deschildre, Z. Nawaz, J. P. Wright, D. Karkoulis, F. E. Picca, J. Kieffer, *Journal of Applied Crystallography* **2015**, *48*, 510-519.
5. P. Juhas, T. Davis, C. L. Farrow, S. J. L. Billinge, *Journal of Applied Crystallography* **2013**, *46*, 560-566.
6. X. a. J. Yang, Pavol and Farrow, Christopher L. and Billinge, Simon J. L., *xPDFsuite: an end-to-end software solution for high throughput pair distribution function transformation, visualization and analysis*, arXiv, **2014**.
7. S. J. L. Billinge, C. L. Farrow, *Journal of Physics: Condensed Matter* **2013**, *25*, 454202.
8. E. Lorch, *Journal of Physics C: Solid State Physics* **1969**, *2*, 229-237.
9. P. Juhas, C. L. Farrow, X. Yang, K. R. Knox, S. J. L. Billinge, *Acta Crystallographica Section A* **2015**, *71*, 562-568.
10. L. Palatinus, *PETS-program for analysis electron diffraction data*, Institute of Physics of the AS CR, Prague, Czechia, **2011**.
11. B. Krebs, *Zeitschrift fur Anorganische und Allgemeine Chemie* **1970**, *378*, 263-272.
12. R. Borjas Nevarez, S. M. Balasekaran, E. Kim, P. Weck, F. Poineau, *Acta Crystallographica Section C* **2018**, *74*, 307-311.
13. D. Feng, Z.-Y. Gu, J.-R. Li, H.-L. Jiang, Z. Wei, H.-C. Zhou, *Angewandte Chemie International Edition* **2012**, *51*, 10307-10310.
14. P. Deria, D. A. Gómez-Gualdrón, I. Hod, R. Q. Snurr, J. T. Hupp, O. K. Farha, *Journal of the American Chemical Society* **2016**, *138*, 14449-14457.
15. C. Koschnick, R. Stäglich, T. Scholz, M. W. Terban, A. von Mankowski, G. Savasci, F. Binder, A. Schökel, M. Etter, J. Nuss, R. Siegel, L. S. Germann, C. Ochsenfeld, R. E. Dinnebier, J. Senker, B. V. Lotsch, *Nature Communications* **2021**, *12*, 3099.

APPENDIX C: ADDITIONAL INFORMATION FOR CHAPTER 4

C.1 Experimental

C.1.1 Materials

4',4'',4''',4''''-methanetetrayltetrabiphenyl-4-carboxylic acid (MTBC) was purchased from Alfa Chemistry. Zirconium(IV) chloride (anhydrous), Hafnium(IV) chloride (anhydrous), benzoic acid, acetone, and *N,N*-dimethylacetamide (DMA) were purchased from Sigma Aldrich. *N,N*-diethylformamide (DEF) was purchased from Alfa Aesar. All chemicals were used as received without further purification.

C.1.2 Instruments and methods

Ultrasonication was conducted via an ELMASONIC S 100 bath equipped with a high-performance 37 kHz sandwich transducer and state-of-the-art microprocessor. Centrifugation was performed with a benchtop centrifuge *Sigma-3-30K* from SIGMA. For SEM analysis MOF suspensions were spin-coated onto silicon wafers with a *WS-650S-NPP Lite* device from LAURELL TECHNOLOGY CORPORATION.

Microscope images were taken with a CMOS camera connected to a *DM2500* light microscope from LEICA.

Scanning electron microscopy (SEM; Vega TS 5130 MM, Tescan) was performed with a secondary electron (SE) detector with a Merlin SEM (Zeiss). Particle sizes were measured with the software ImageJ.

Powder X-Ray diffraction patterns were collected at room temperature on a Stoe Stadi-P diffractometers with Cu-Kα_1 radiation (λ = 1.540596 Å) or Co-Kα_1 radiation (λ = 1.78896 Å), a Ge(111) Johann monochromator, and a DECTRIS Mythen 1K detector in Debye-Scherrer geometry. The samples were loaded into 0.5 mm inner diameter polyimide capillaries and measured over a range of 2θ = 2.000–30.695°, with 0.015° step size and 50 s counting time per step when using Cu-Kα_1 radiation and a range of 2θ = 0.500–115.325°, with 0.015° step size and 200 s counting time per step when using Co-Kα_1 radiation.

Rietveld refinements were performed with TOPAS v6.[1] Diffraction data collected using Co-Kα_1 radiation were used for pure phase cubic and tetragonal phase refinements. A 2θ offset correction, simple axial model, Lorentzian and Gaussian crystallite size broadening convolutions, and the Stephens model for strain were used to correct for instrumental and morphological peak-shape effects. The background was described using Chebychev polynomials of 17th to 19th order. Scale factors, lattice parameters, and isotropic atomic displacement parameters were refined. Additional pseudoatoms with a very large atomic displacement parameter were included to describe missing diffuse electron density due to pore content located near the cluster surface. Refinements of mixed phase models used data collected from Cu-Kα_1 radiation. For these refinements, a smaller number of terms were used for the background along with the One_on_X term for increased low angle background. Only scale factors and lattice parameters were refined for the respective phases. A second set of refinements was performed using spherical harmonics corrections of 4th or 6th order for majority phases to account for mismatched relative peak intensities.

Pair distribution function analysis was carried out using P02.1, the Powder Diffraction and Total Scattering Beamline, at PETRA III of the Deutsches Elektronen-Synchrotron (DESY). The rapid acquisition PDF method (RAPDF)[2] was used with a large-area 2D PerkinElmer detector (2048×2048 pixels, 200×200 μm^2 each) and sample-to-detector distance of 481.242 mm. The incident energy of the x-rays was 59.795 keV (λ = 0.20735 Å). Samples were loaded into 1 mm inner diameter glass capillaries. An empty capillary was measured as background and subtracted, and a LaB6 standard was measured at room temperature for calibration of the setup. Calibration, polarization correction, and azimuthal integration to 1D diffraction patterns were performed using the software pyFAI.[3-4]

Additional total scattering measurements were performed on the same samples in-lab using a Stoe Stadi-P diffractometer with Mo Kα_1 radiation (λ = 0.7093 Å), a Ge(111) Johann monochromator, and a DECTRIS Mythen 1K detector in Debye-Scherrer geometry. Measurements were carried out over a range of 2θ = 0.405–110.565˚ and 40.50–110.565˚ with 0.405˚ step size and 150 s count time per step, and 81.00–110.565˚ with 300 s count time. Data ranges were then combined and directly corrected for the 2θ offset of the instrument and polarization.

Further correction and normalization of the 1D diffraction intensities were carried out to obtain the total scattering structure function, $F(Q)$, which was Fourier transformed to obtain the PDF, $G(r)$ using PDFgetX3 within xPDFsuite.[5-7] The maximum value used in the Fourier transform of the total scattering data was 21.0 Å^{-1} for the synchrotron and 14.5 Å^{-1} for the Mo-Kα_1 laboratory data. Simulated PDFs were generated from respective models using code from Diffpy-CMI.[8]

Single crystal X-Ray diffraction data collections for c-(4,12)MTBC-Zr_6, t-(4,12)MTBC-Zr_6, c-(4,12)MTBC-Hf_6, and t-(4,12)MTBC-Hf_6 were conducted at the Bessy Synchrotron facility of the Helmholtz Zentrum Berlin (Beamline 14.2). Suitable crystals were isolated and mounted on a MiTeGen loop in a droplet of a perfluoropolyether oil. Diffraction data were acquired using a monochromatic 0.799897 Å radiation at a temperature of 100K, using a cold dry nitrogen stream produced with an Oxford Cryostream [Oxford Cryosystems Ltd., Oxford, United Kingdom]. The crystal was placed directly under the Cryostream at 100K without any temperature ramp in going from room temperature to cryogenic conditions. Frames were collected on a Pilatus3S 2M, running a phi scan with oscillation 0.2° and covering an angular range of 360°. The data have been processed using the software XDS [Kabsch, W. XDS. Acta Cryst. D66, 125-132 (2010)], which included indexing, intensities integration and empirical absorption correction. Structure solution and refinement were conducted by using the software suite Olex2 v1.5[9], using the programs ShelXT (intrinsic phasing) and ShelXL (Least squares) respectively.[10-11]

As far as structure modelling for refinement is concerned, a few restraints helped maintaining chemically sound bond distances and molecular geometries during the modelling of structural disorder. Specifically, phenyl rings were constrained to a flat hexagonal geometry by AFIX66, and carboxylate moieties of the linkers were modelled in reference geometries using DFIX and DANG commands. Similarly, ISOR and SIMU ADP constraints were used to guide misbehaving displacement parameters towards more physically sound values, as it was observed that free refinement of displacement ellipsoids led to behaviour inconsistent with a meaningful physically sound situation. Furthermore, hydrogen atoms belonging to OH groups on the clusters or aromatic CH groups were fixed by appropriate ShelX commands and were not refined freely.

Every sample was found as a single crystal, and no twinning was detected in the data or in the reciprocal space maps. In the final stages of the refinement, the tool “Mask” of Olex2 (alternative to SQUEEZE which is implemented in Platon) was used to account for solvent molecules, assumed as *N,N*-dimethylformamide, which were not possible to recognise and model satisfactorily in the residual densities.

Symmetry-independent building blocks were refined with free occupancies to account for missing-building-block defects. When occupancy factors exceeded unity, they were fixed to full occupancy. Additional details for each single crystal are reported below in dedicated sections. Partial linker occupancies in the cubic phases were found to coincide with the presence of unaccounted electron density residues in proximity to metal centres, consistent with the presence of water molecules and OH- groups to ensure overall charge balance of the framework. Therefore, these species were modelled and their occupancy was set to complement those of the linker molecules, so that the sum

of the occupancies of linkers and H_2O-OH pairs ensures full occupancy on each coordination position around the metal clusters.

Difference Fourier maps were computed by using the software Vesta[12] by following the routine as follows.

1) A complete model including structure disorder was refined until convergence, until the structure used for deposition into the Cambridge Structural Database is obtained, which includes the use of solvent mask.

2) The disordered atoms relative to the electron density of interest are removed.

3) A single least square ShelXL refinement cycle is ran, using the command list3 in the ".ins" file, which allows to obtain a ".fcf" file compatible with Vesta.

4) The structure model is loaded in vesta, and the Fourier difference map is generated by the function "Fourier synthesis" and the option "Fo-Fc".

5) Positive residues only are selected in the graphical options, and multi-level isosurfaces are coloured to obtain an informative and clear qualitative picture of the electron density residues due to unmodelled disordered building blocks.

C.1.3 Synthesis procedures

Synthesis of cubic Zr-MTBC according to literature

Zr-MTBC was synthesized according to a procedure published by Ji *et al.*[13] $ZrCl_4$ (18.2 mg, 0.0781 mmol), MTBC (16.0 mg, 0.020 mmol), and benzoic acid (554 mg, 4.54 mmol)) were ultrasonically dissolved in DEF (3.2 mL) in a 5 mL microwave vial. The mixture was heated in an Al-block (24 h, 120 °C) under stirring. The product was collected by centrifugation and washed with DEF (three times, 16k rpm/15 min/16 °C) and acetone (twice, 16k rpm/15 min/16 °C). The mixture was soaked in acetone over night and washed with acetone once. Supercritical CO_2 drying yielded a white powder as product.

Adapted synthesis of cubic and trigonal (4,12)-MTBC-Zr_6 and (4,12)-MTBC-Hf_6 for SCXRD analysis

$ZrCl_4$ (18.2 mg, 0.0781 mmol), MTBC (16.0 mg, 0.020 mmol), and benzoic acid (554 mg, 4.54 mmol) were ultrasonically dissolved in DEF (3.2 mL) in a 20 mL pyrex vial. The mixture was heated in an oven at 120 °C for 24 h. The formed crystals were washed with DEF twice and acetone three times (soaked in acetone over night during last washing step). The crystals were dried using supercritical CO_2. Single crystals of cubic and trigonal (4,12)-MTBC-Hf_6 were obtained analogously by reacting $HfCl_4$ (25.0 mg, 0.781 mmol) instead of $ZrCl_4$ for 48 h or 7 d in an oven.

Screening of reaction conditions

$ZrCl_4$, MTBC, and benzoic acid (see Table C.1 for more details) were ultrasonically dissolved in DEF or DMA (3.2 mL) in a 20 mL pyrex vial. The solution was heated in an oven at 100 or 120 °C for 24 h to 7d. In the case of MOF_supernatant, the supernatant obtained after 24 h reaction was further reacted at 120 °C for 72 h. For all reactions, the formed crystals were washed with DEF or DMA twice and acetone three times (soaked in acetone over night during last washing step). The crystals were dried using supercritical CO_2.

Table C.1: Amount of $ZrCl_4$, MTBC, and benzoic acid (BzA), as well as solvent, reaction time, and reaction temperature (temp.) employed during the screening of reaction conditions.

Sample	$ZrCl_4$	MTBC	BzA	Solvent	Time	Temp.
MOF_100	18.2 mg, 0.0781 mmol	16.0 mg, 0.020 mmol	554 mg, 4.54 mmol	DEF	48 h	100 °C
MOF_120	18.2 mg, 0.0781 mmol	16.0 mg, 0.020 mmol	554 mg, 4.54 mmol	DEF	24 h	120 °C
MOF_less_MTBC	18.2 mg, 0.0781 mmol	10.4 mg 0.013 mmol	554 mg, 4.54 mmol	DEF	24 h	120 °C
MOF_ less_$ZrCl_4$+MTBC	9.0 mg 0.039 mmol	8.0 mg 0.010 mmol	554 mg, 4.54 mmol	DEF	5 d	120 °C
MOF_7d	18.2 mg, 0.0781 mmol	16.0 mg, 0.0200 mmol	554 mg, 4.54 mmol	DEF	7 d	120 °C
MOF_supernatant	18.2 mg, 0.0781 mmol	16.0 mg, 0.0200 mmol	554 mg, 4.54 mmol	DEF	24 h (1) 72 h (2)	120 °C
MOF_DMA_24h	18.2 mg, 0.0781 mmol	16.0 mg, 0.0200 mmol	554 mg, 4.54 mmol	DMA	24 h	120 °C
MOF_DMA_48h	18.2 mg, 0.0781 mmol	16.0 mg, 0.0200 mmol	554 mg, 4.54 mmol	DMA	48 h	120 °C

C.2 Results and discussion

C.2.1 SEM images

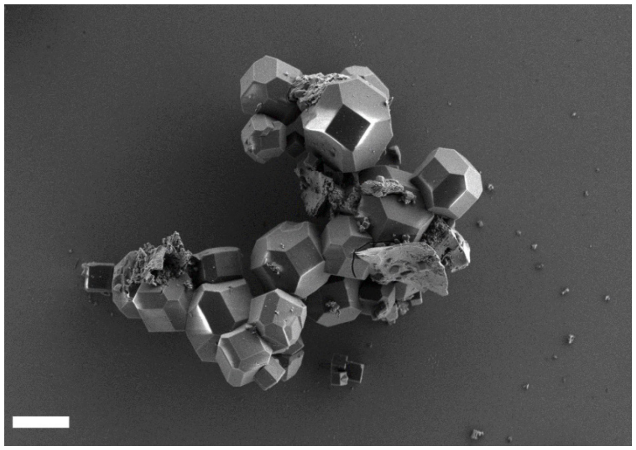

Figure C.1: Scanning electron microscopy image of Zr-MTBC particles synthesized according to literature. Scale bar = 5 µm.

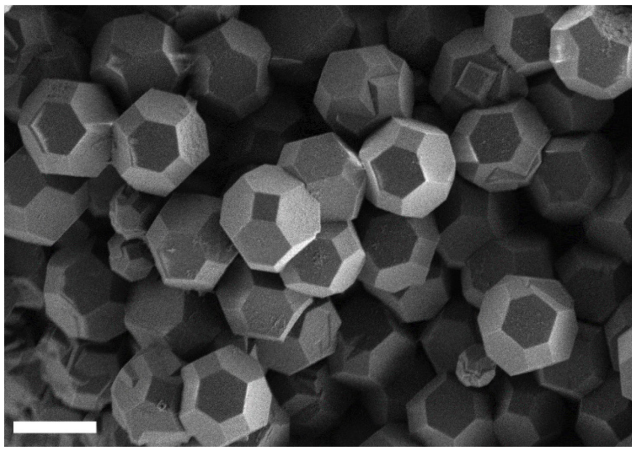

Figure C.2: Scanning electron microscopy image of c-(4,12)MTBC-Zr_6 particles synthesized at 100 °C (MOF_100). Scale bar = 5 µm.

C.2.2 Microscope images of single crystals

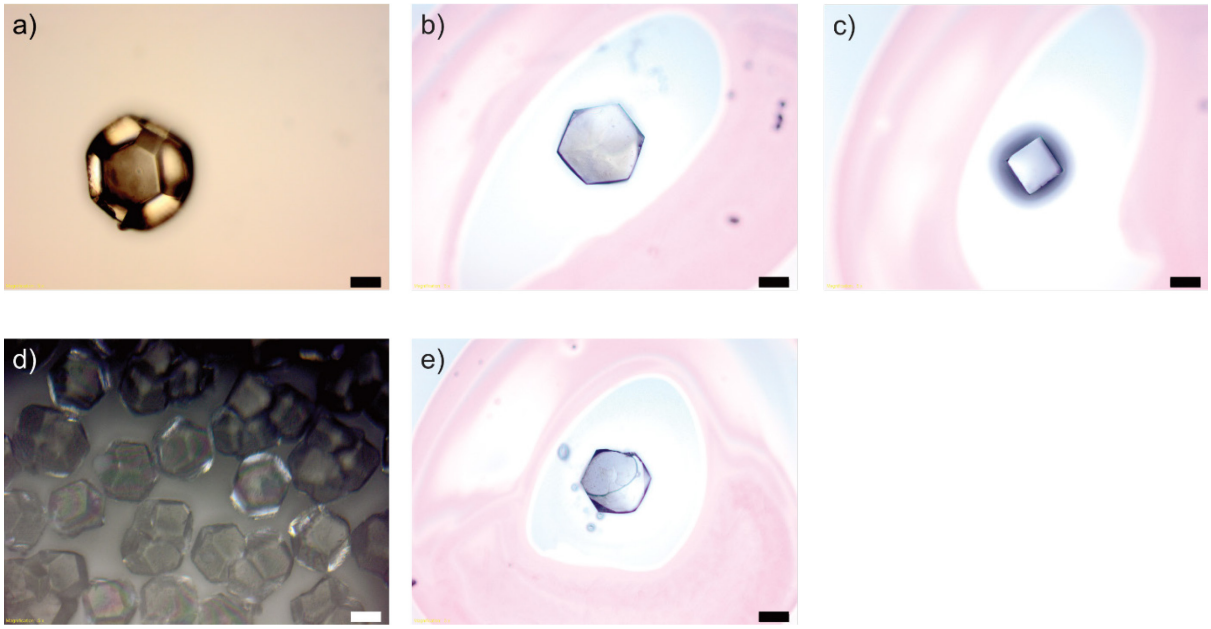

Figure C.3: Microscope image of a) cuboctahedral c-(4,12)MTBC-Zr_6, b) trigonal t-(4,12)MTBC-Zr_6, c) cubic c-(4,12)MTBC-Zr_6, d) cuboctahedral c-(4,12)MTBC-Hf_6, and e) trigonal t-(4,12)MTBC-Hf_6 singles crystals. Scale bar = 100 µm.

C.2.3 Powder X-Ray diffraction analysis

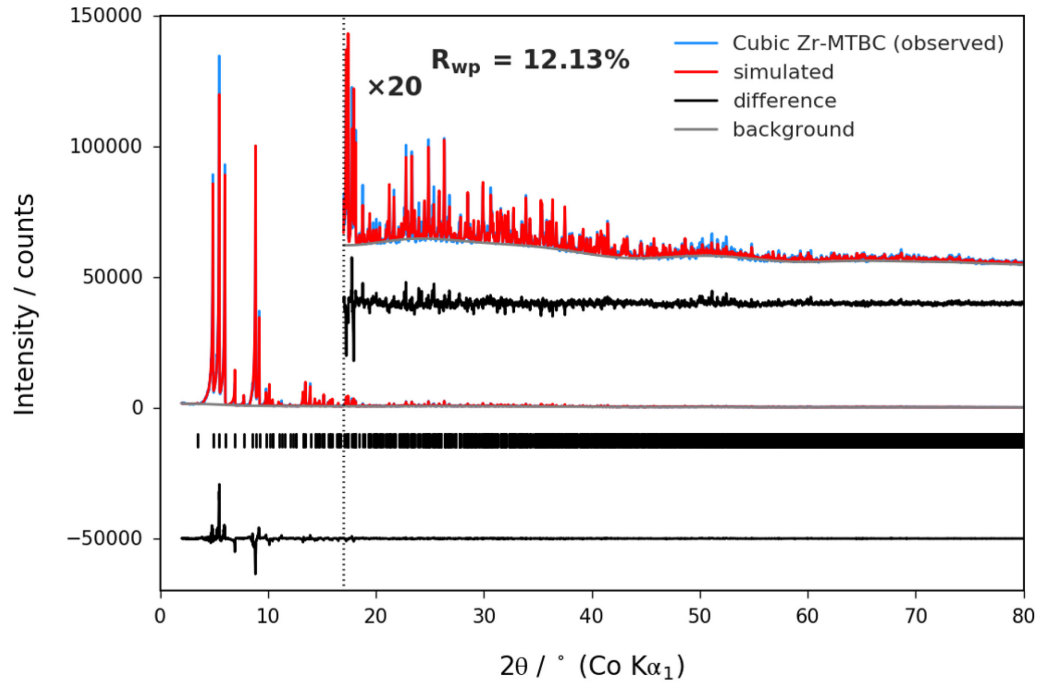

Figure C.4: Rietveld refinement of the new c-(4,14)MTBC-Zr_6 structure model against the observed pattern of experimental cuboctahedral c-(4,14)MTBC-Zr_6.

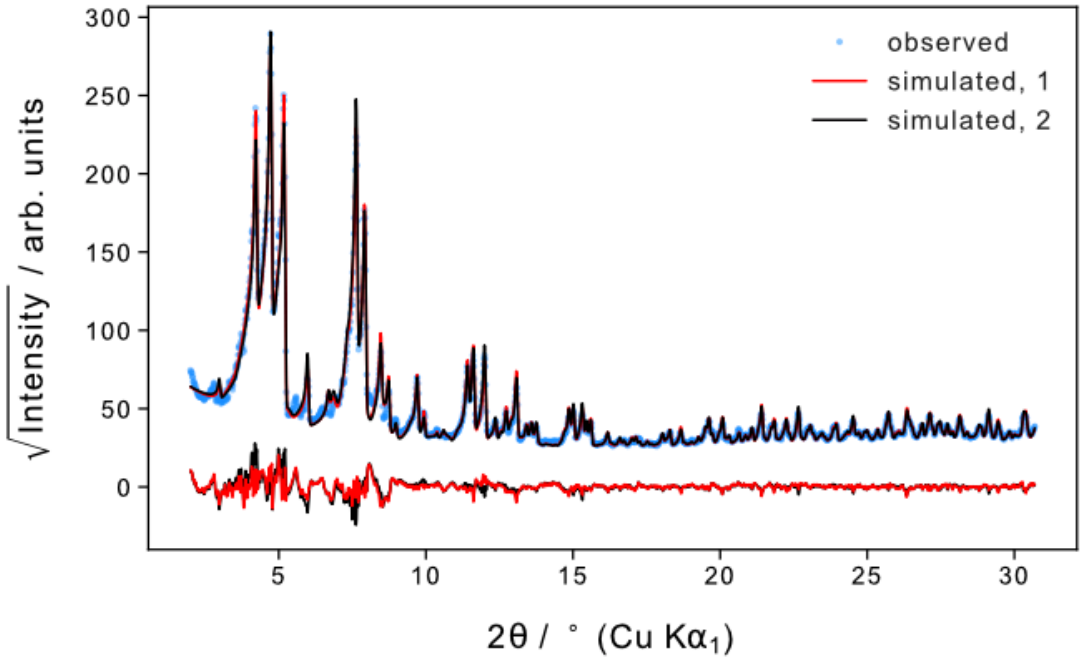

Figure C.5: Rietveld refinement allowing for reflexes of cubic, trigonal, and tetragonal MTBC-Hf_6 against observed PXRD pattern of the product obtained from $HfCl_4$ from synthesis at 120 °C after 48 h reaction time. Simulation 1 includes spherical harmonics corrections of 4-6th order on the predominant phases to account for mismatched relative peak intensities, while simulation 2 does not. Refined composition: 91 % c-(4,12)MTBC-Hf_6 and 9 % t-(4,12)MTBC-Hf_6.

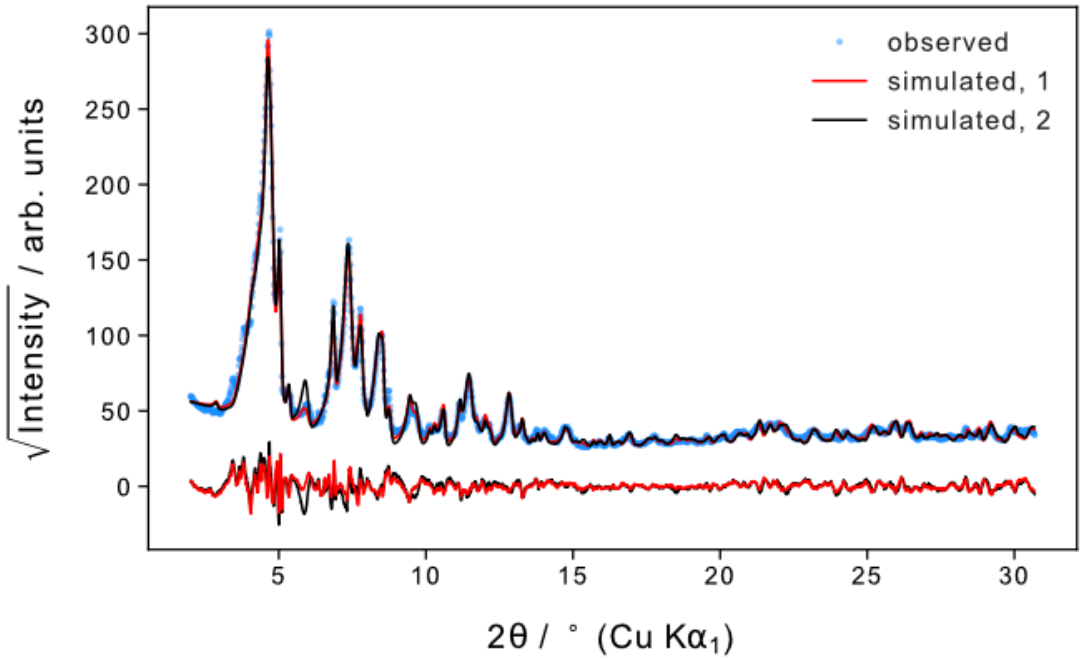

Figure C.6: Rietveld refinement allowing for reflexes of cubic (c), trigonal (t), and tetragonal MTBC-Hf_6 against observed PXRD pattern of the product obtained from $HfCl_4$ from synthesis at 120 °C after 7 d reaction time. Simulation 1 includes spherical harmonics corrections of 4-6th order on the predominant phases to account for mismatched relative peak intensities, while simulation 2 does not. Refined composition: 50 % tetragonal MTBC-Hf_6 (PCN-523), 43 % t-(4,12)MTBC-Hf_6, and 16 % c-(4,12)MTBC-Hf_6.

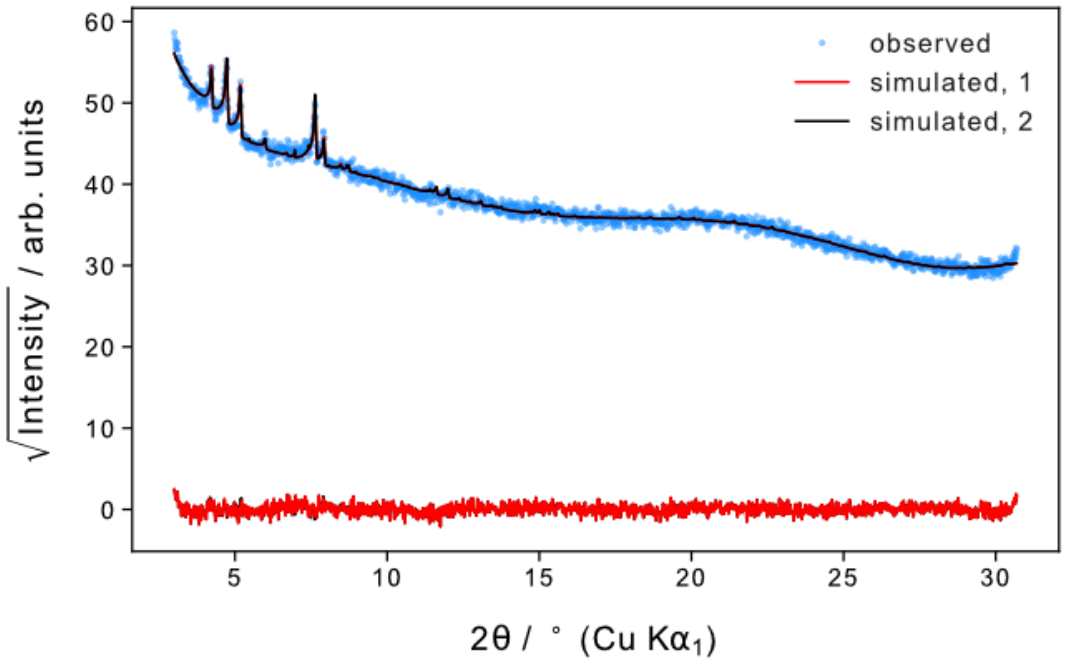

Figure C.7: Rietveld refinement allowing for reflexes of cubic, trigonal, and tetragonal MTBC-Zr_6 against observed PXRD pattern of the product obtained from synthesis at 100 °C. Simulation 1 includes spherical harmonics corrections of 4-6th order on the predominant phases to account for mismatched relative peak intensities, while simulation 2 does not. Refined composition is given in Table C.2.

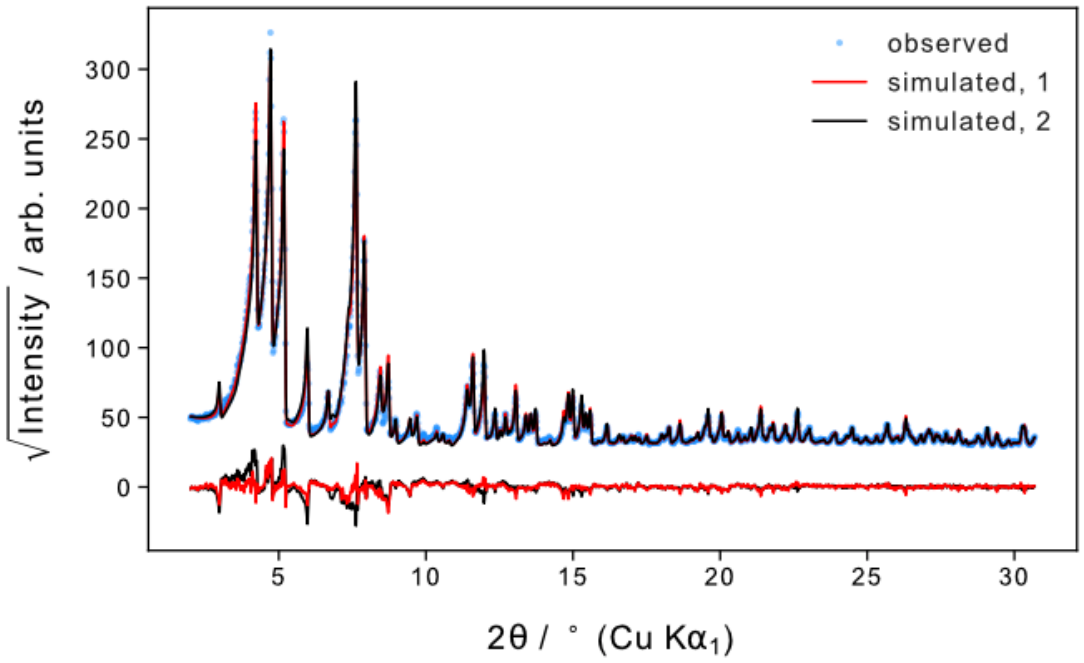

Figure C.8: Rietveld refinement allowing for reflexes of cubic, trigonal, and tetragonal MTBC-Zr_6 against observed PXRD pattern of the product obtained from synthesis at 120 °C. Simulation 1 includes spherical harmonics corrections of 4-6th order on the predominant phases to account for mismatched relative peak intensities, while simulation 2 does not. Refined composition is given in Table C.2.

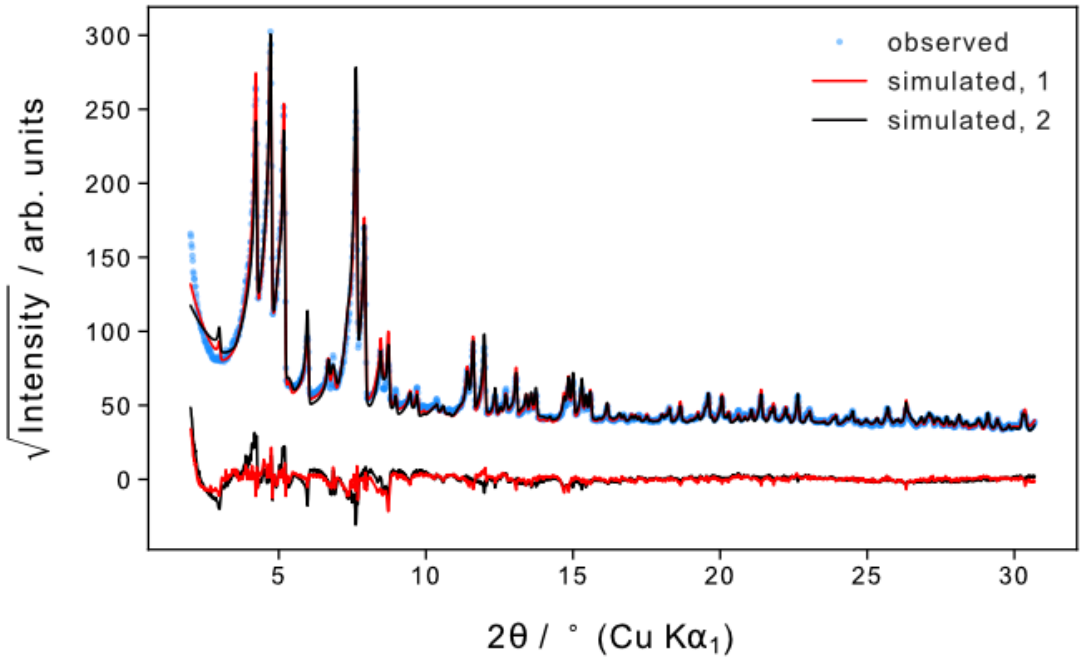

Figure C.9: Rietveld refinement allowing for reflexes of cubic, trigonal, and tetragonal MTBC-Zr_6 against observed PXRD pattern of the product obtained from synthesis with reduced MTBC-concentration (MOF_MTBC_reduced). Simulation 1 includes spherical harmonics corrections of 4-6th order on the predominant phases to account for mismatched relative peak intensities, while simulation 2 does not. Refined composition is given in Table C.2.

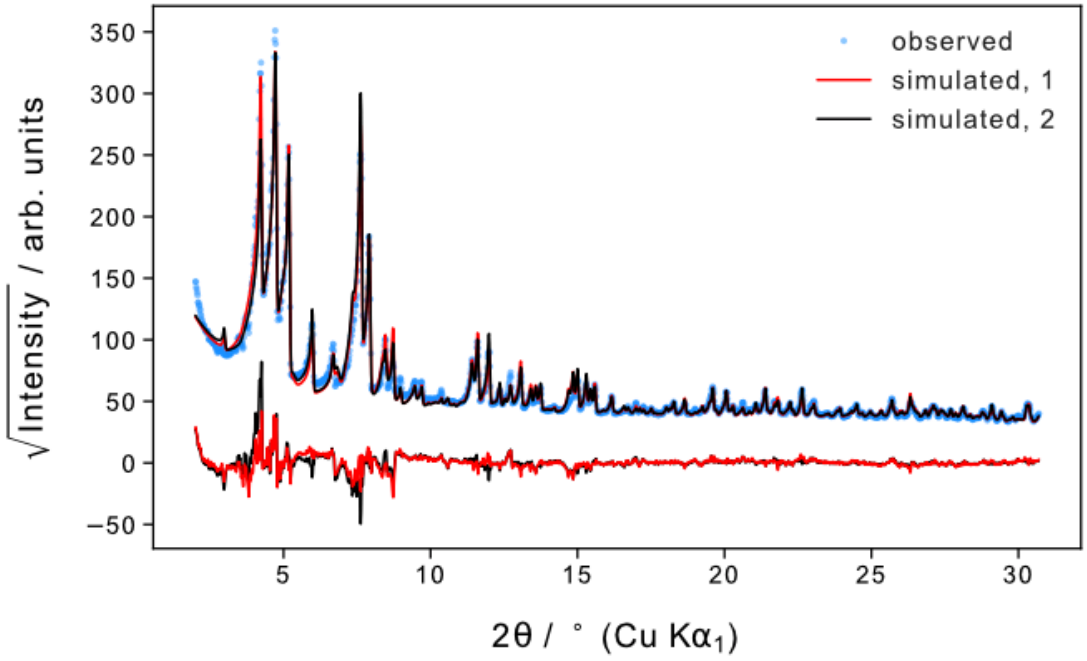

Figure C.10: Rietveld refinement allowing for reflexes of cubic, trigonal, and tetragonal MTBC-Zr_6 against observed PXRD pattern of the product obtained from synthesis with reduced $ZrCl_4$- and MTBC-concentration (MOF_$ZrCl_4$+MTBC_reduced). Simulation 1 includes spherical harmonics corrections of 4-6th order on the predominant phases to account for mismatched relative peak intensities, while simulation 2 does not. Refined composition is given in Table C.2.

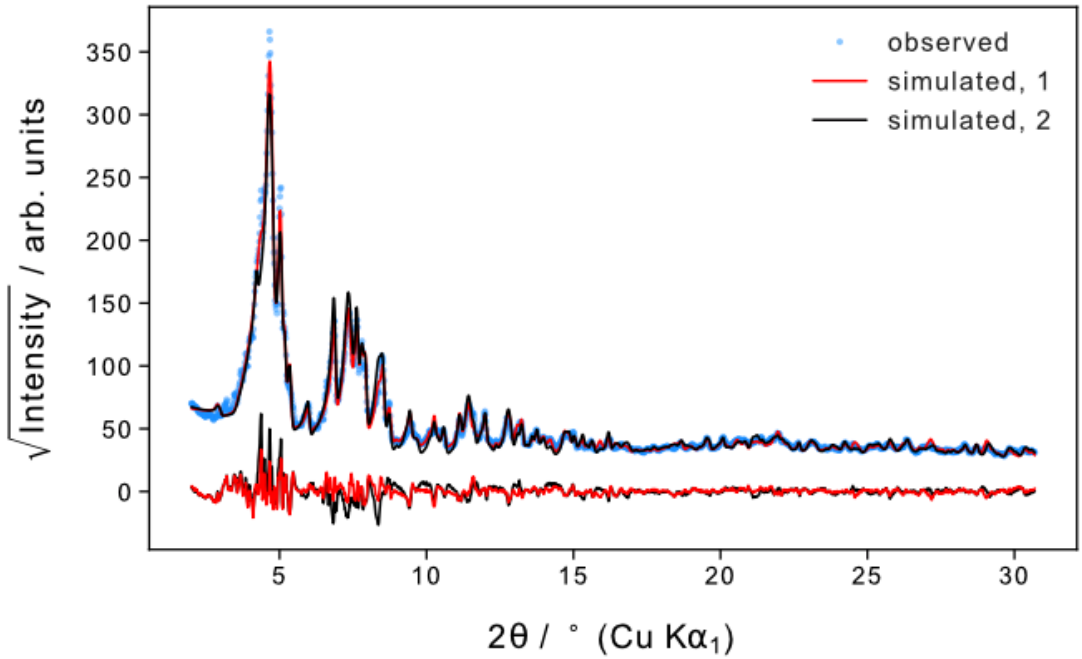

Figure C.11: Rietveld refinement allowing for reflexes of cubic, trigonal, and tetragonal MTBC-Zr_6 against observed PXRD pattern of the product obtained from product after 7d reaction at 120 °C (MOF_7d). Simulation 1 includes spherical harmonics corrections of 4-6th order on the predominant phases to account for mismatched relative peak intensities, while simulation 2 does not. Refined composition is given in Table C.2.

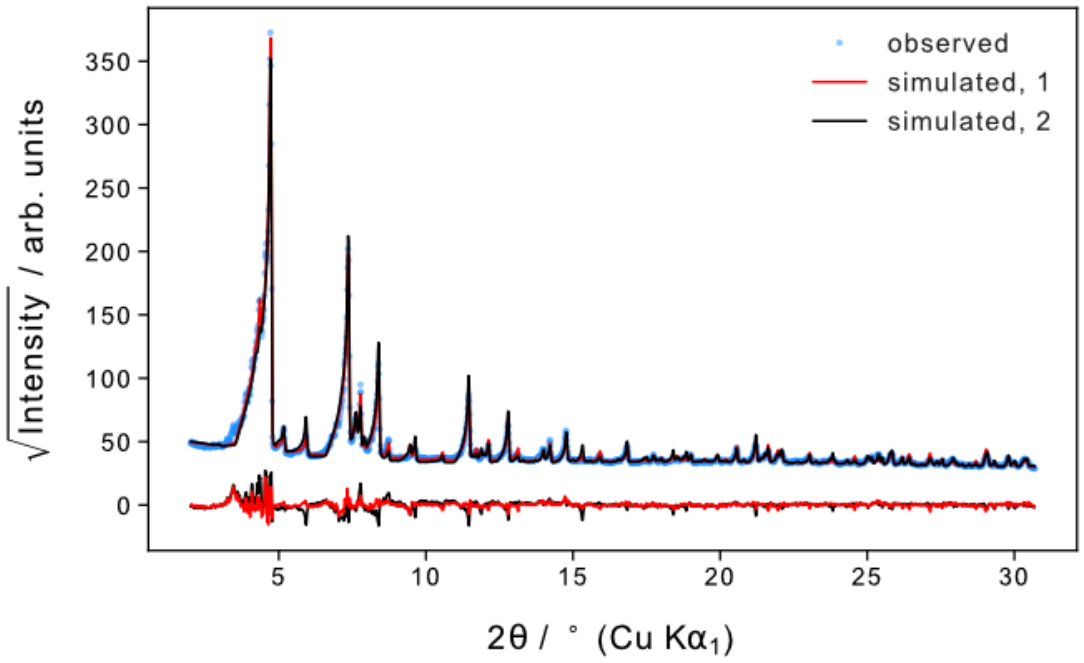

Figure C.12: Rietveld refinement allowing for reflexes of cubic, trigonal, and tetragonal MTBC-Zr_6 against observed PXRD pattern of the product obtained from product after further reaction of the supernatant (MOF_supernatant). Simulation 1 includes spherical harmonics corrections of 4-6th order on the predominant phases to account for mismatched relative peak intensities, while simulation 2 does not. Refined composition is given in Table C.2.

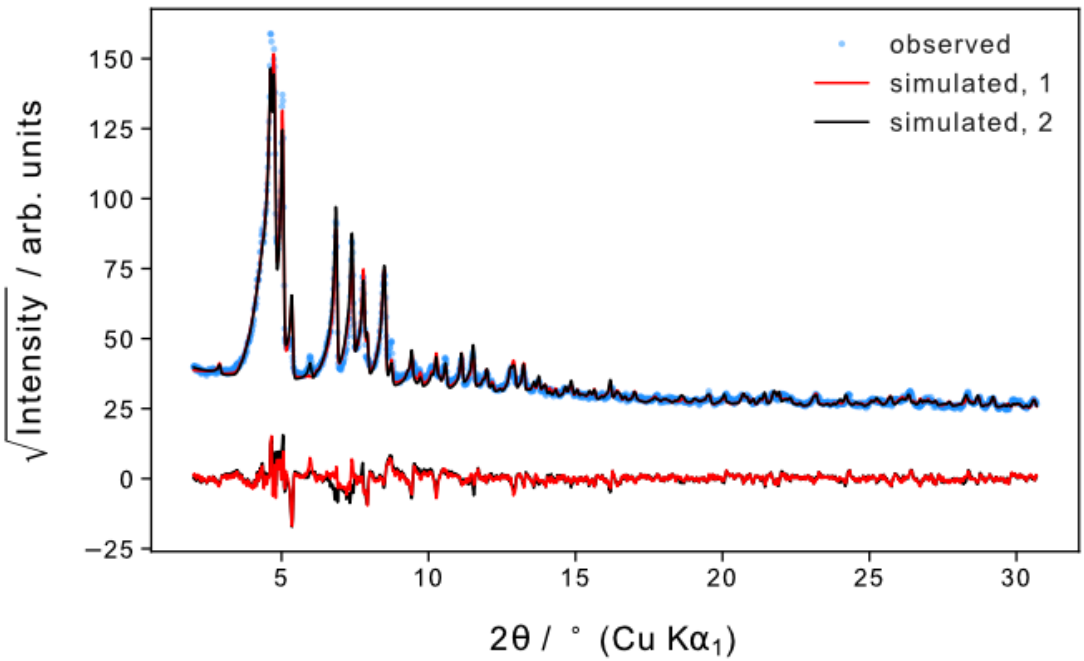

Figure C.13: Rietveld refinement allowing for reflexes of cubic, trigonal, and tetragonal MTBC-Zr_6 against observed PXRD pattern of the product obtained from product from synthesis in DMA for 24 h (MOF_DMA_24h). Simulation 1 includes spherical harmonics corrections of 4-6th order on the predominant phases to account for mismatched relative peak intensities, while simulation 2 does not. Refined composition is given in Table C.2.

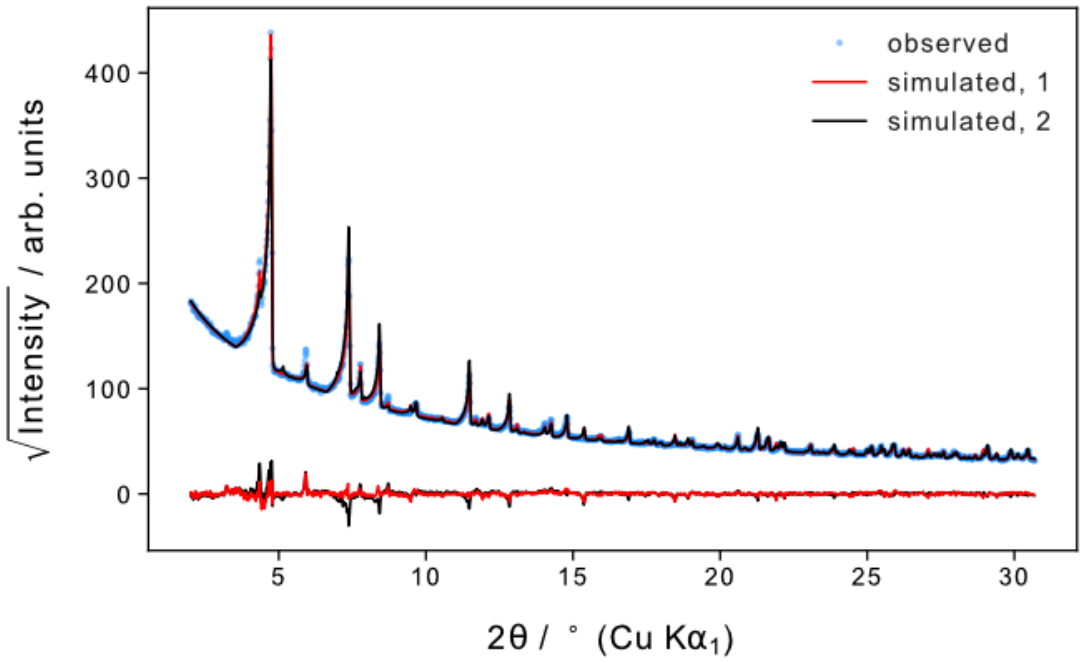

Figure C.14: Rietveld refinement allowing for reflexes of cubic, trigonal, and tetragonal MTBC-Zr_6 against observed PXRD pattern of the product obtained from product from synthesis in DMA for 48 h (MOF_DMA_48h). Simulation 1 includes spherical harmonics corrections of 4-6th order on the predominant phases to account for mismatched relative peak intensities, while simulation 2 does not. Refined composition is given in Table C.2.

Table C.2: Composition of tetragonal, cubic, and trigonal (4,12)MTBC-Zr_6 obtained from Rietveld refinements (Figure C.7–C.14) of from MOF products synthesized under variable reaction conditions.

	100 °C	**120 °C**	**less MTBC**	**less $ZrCl_4$+MTBC**	**7d**	**Super-natant**	**DMA 24h**	**DMA 48h**
no spherical harmonics correction								
Tetragonal	2.19	2.2	1.41	4.38	36.18	90.4	31.46	94.73
Cubic	90.16	92.91	86.06	86.55	20.09	8.16	3.31	4.03
Trigonal	7.65	4.89	12.54	9.07	43.73	1.44	65.24	1.24
spherical harmonics correction								
Tetragonal	2.44	3.38	2.19	4.44	40.28	93.57	30.78	99.78
Cubic	92.33	94.51	90.89	88.64	19.69	6.09	0.95	0
Trigonal	5.24	2.11	6.92	6.92	40.03	0.34	68.27	0.22
average								
Tetragonal	2	3	2	4	38	92	31	97
Cubic	91	94	88	88	20	7	2	2
Trigonal	6	4	10	8	42	1	67	1
standard deviation								
Tetragonal	0.4	2	1	0.08	6	4	1	7
Cubic	3	2	7	3	1	3	3	6
Trigonal	3	4	8	3	5	2	4	1

C.2.4 Multiphase behavior of Zr-MTBC-based MOFs

Although $Zr_6O_4(OH)_4$ cluster based MOFs have been intensively studied since 2008, the control over MOF phases remains challenging. Oftentimes, multiple MOF topologies with different catalytic activities and gas sorption properties can be built from the same linker and Zr-cluster.[14-17] We identified three MOF phases, cubic, tetragonal, and trigonal Zr-MTBC to form from $ZrCl_4$ and MTBC when using benzoic acid as modulator. The phase composition of the product was found to vary depending on the reaction conditions (Figure C.15). Changing the reaction time, temperature, concentration of reactant, solvent, and water content during synthesis from $ZrCl_4$ lead to several observations worth mentioning. (1) Both reaction temperature as well as concentrations of linker and $ZrCl_4$ did not significantly affected the composition of MOF phases formed, all yielding cubic Zr-MTBC as main product. As discussed above, decreasing both MTBC and $ZrCl_4$ concentration, however, remarkably slowed down particle growth (24 h vs 5 d) and yielded cubic instead of cuboctahedral particles with higher crystallinity. (2) Increasing the reaction time, in turn, inversed the phase ratios in the product and more tetragonal and trigonal Zr-MTBC were formed. (3) Similarly, the addition of water to the reaction, which is known to accelerate $Zr_6O_4(OH)_4$ cluster formation and MOF particle growth, reduced the amount of cubic Zr-MTBC in the product in favor of tetragonal and trigonal Zr-MTBC. (4) Importantly, separation of the supernatant after 24 h reaction and further reaction of the supernatant mostly yielded the tetragonal phases. This suggests, that at the beginning of the reaction cubic and trigonal Zr-MTBC form while tetragonal Zr-MTBC growth later in the reaction. (5) When employing DMA as solvent instead of DEF, no cubic Zr-MTBC was formed. Interestingly, 24 h reaction yielded a mixture of the trigonal and tetragonal phase whereas reaction for 48 h mainly yielded the tetragonal MOF suggesting a phase transformation from the trigonal to tetragonal phase.

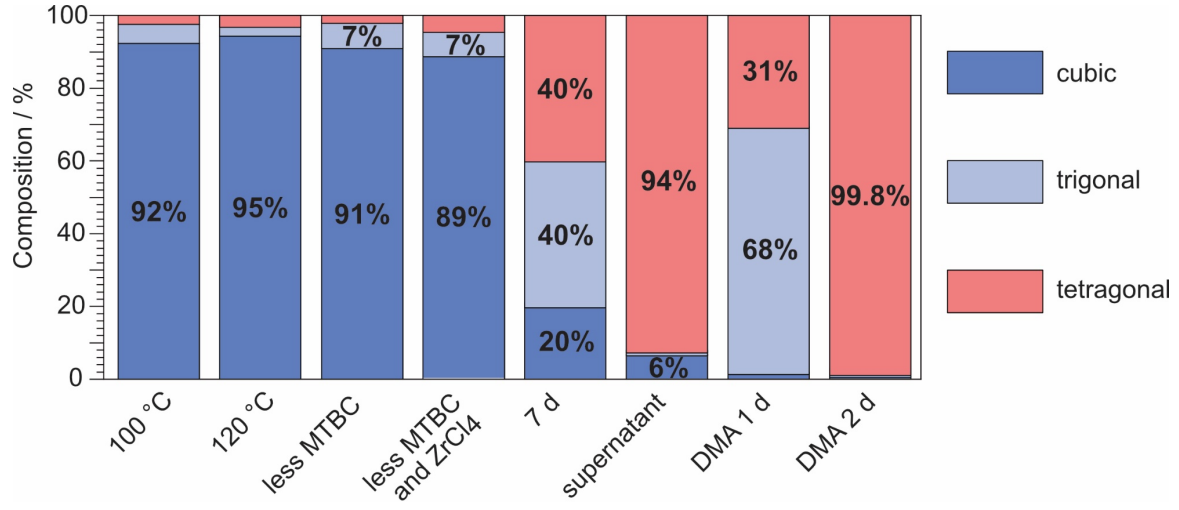

Figure C.15: Phase compositions of cubic, trigonal, and tetragonal Zr-MTBC depending on the employed reaction conditions.

C.2.5 Pair distribution function analysis of cuboctahedral c-(4-12)MTBC-Zr_6 SC

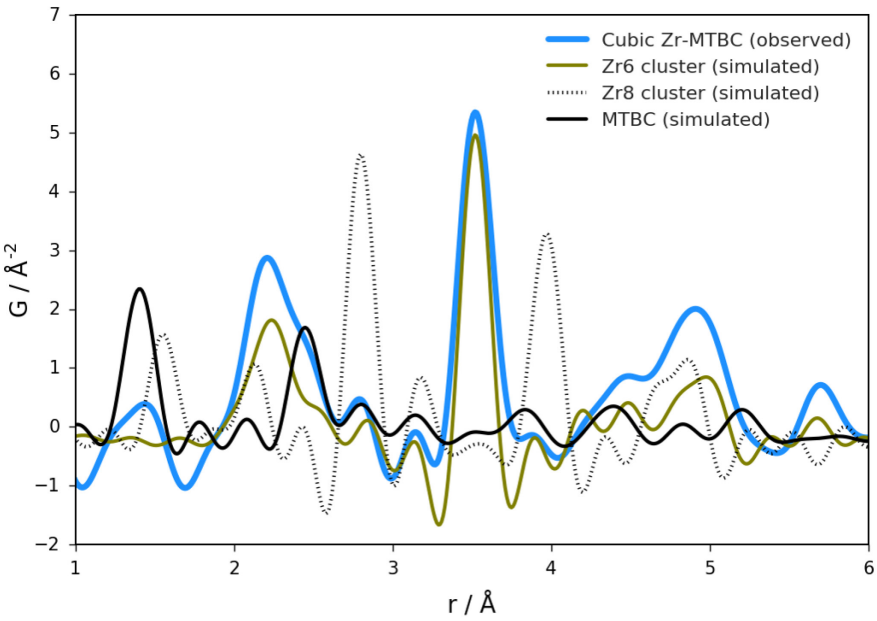

Figure C.16: Comparison of the pair distribution functions (PDFs) of sample c-(4,14)MTBC-Zr_6 (cubic Zr-MTBC) to PDFs simulated for Zr_6 cluster, Zr_8 cluster, and the MTBC linker.[13]

C.2.6 Single crystal X-ray diffraction: refinement details

Cuboctahedral c-(4,12)MTBC-Zr_6 crystal nr.1

Linker occupancy: 0.901(3)
Ordered cluster occupancy: 1
Disordered cluster occupancy: 0.25

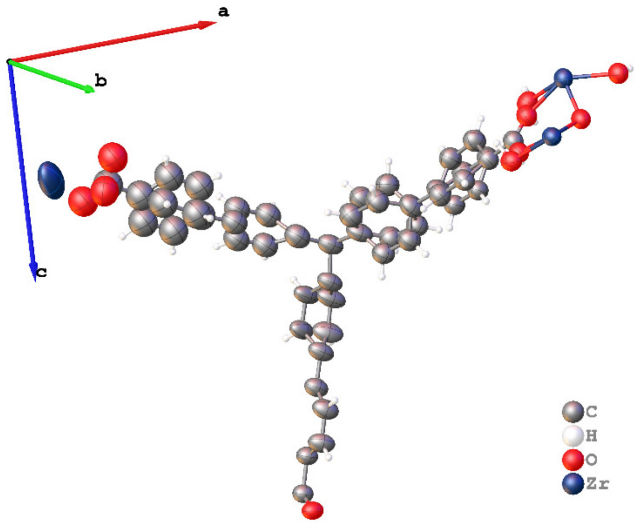

Figure C.17: Asymmetric unit of cuboctahedral c-(4,12)MTBC-Zr_6 crystal nr.1 (ellipsoids corresponding to 30% probability).

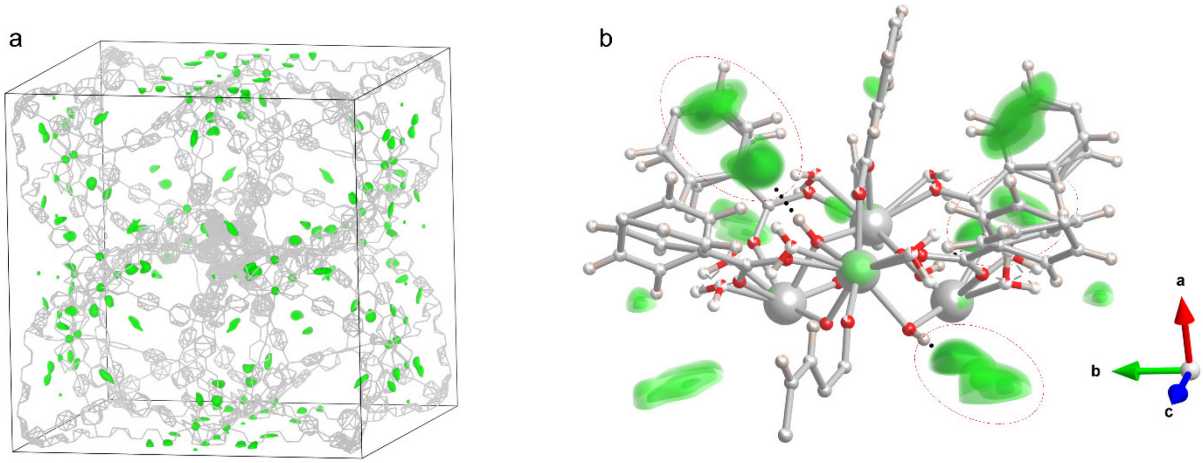

Figure C.18: Difference electron density maps (Fobs-Fcalc) obtained by using the option "Fourier Synthesis" of the software Vesta, based on the ".fcf" file produced by structure refinements without solvent mask. In detail, (a) view of the electron density residues in the unit cell (isosurface level = 1 $e^-/Å^3$), and (b) main location where these densities are found, i.e., around the ordered metal clusters (isosurface levels = 0.8, 1, and 1.2 $e^-/Å^3$). Note the circled areas, where density maxima suggest the presence of solvent molecules interacting with the cluster's OH groups via hydrogen bonding (dotted black line; H–density maximum distance: 1.939(4) Å).

Solvent masking accounted for electron density peaks that were not possible to assign to discrete solvent molecules without deteriorating the quality of the refinements, due to the overlap of symmetry-equivalent positions of solvent species (likely *N,N*-dimethylformamide). Difference Fourier maps were computed for displaying the density residues, as shown in Figure C.18.

Table C.3: Crystal data and structure refinement for cuboctahedral c-(4,12)MTBC-Zr_6 crystal nr.1.

Empirical formula	$C_{143.3}H_{88.3}O_{28.82}Zr_6$
Formula weight	2818.44
Temperature/K	100.00
Crystal system	cubic
Space group	Pm-3n
a/Å	41.510(10)
b/Å	41.510(10)
c/Å	41.510(10)
α/°	90
β/°	90
γ/°	90
Volume/$Å^3$	71525(52)
Z	8
$\rho_{calc}g/cm^3$	0.523
μ/mm^{-1}	0.270
F(000)	11349.0
Crystal size/mm^3	0.15 × 0.15 × 0.15
Radiation	synchrotron (λ = 0.79999)
2Θ range for data collection/°	3.124 to 64.352
Index ranges	$-55 \leq h \leq 54$, $-55 \leq k \leq 55$, $-55 \leq l \leq 55$
Reflections collected	992517
Independent reflections	15063 [R_{int} = 0.0516, R_{sigma} = 0.0099]
Data/restraints/parameters	15063/368/519
Goodness-of-fit on F^2	1.256
Final R indexes [I>=2σ (I)]	R_1 = 0.0979, wR_2 = 0.3051
Final R indexes [all data]	R_1 = 0.1156, wR_2 = 0.3497
Largest diff. peak/hole / e $Å^{-3}$	1.77/-0.71

Cuboctahedral c-(4,12)MTBC-Zr_6 crystal nr.2

Linker occupancy: 0.946(3)
Ordered cluster occupancy: 1
Disordered cluster occupancy: 0.2365(7)

Solvent masking produced electron densities without significant differences compared to those shown for crystal nr.1 in Figure C.18.

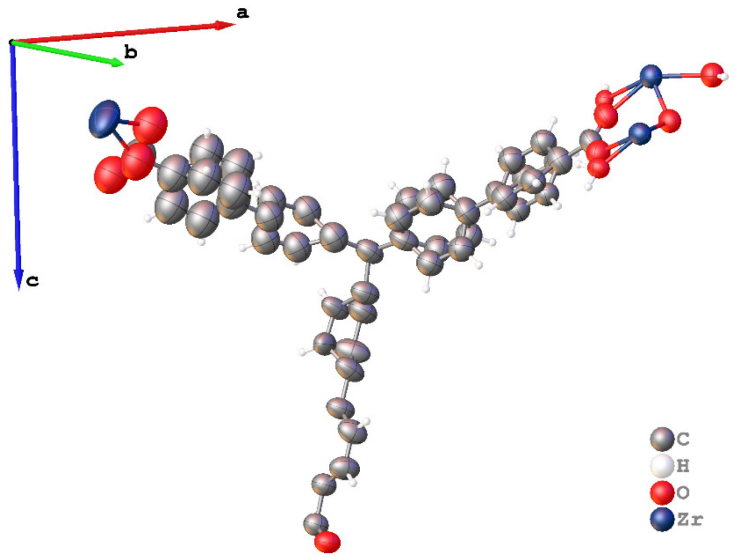

Figure C.19: Asymmetric unit of cuboctahedral c-(4,12)MTBC-Zr_6 crystal nr.2 (ellipsoids corresponding to 30% probability).

Table C.4: Crystal data and structure refinement for cuboctahedral c-(4,12)MTBC-Zr_6 crystal nr.2.

Empirical formula	$C_{150.39}H_{94.78}O_{29.35}Zr_{5.92}$
Formula weight	2911.27
Temperature/K	100.00
Crystal system	cubic
Space group	Pm-3n
a/Å	41.48(5)
b/Å	41.48(5)
c/Å	41.48(5)
α/°	90
β/°	90
γ/°	90
Volume/$Å^3$	71344(258)
Z	8
$\rho_{calc}g/cm^3$	0.542
μ/mm^{-1}	0.269
F(000)	11750.0
Crystal size/mm^3	0.15 × 0.15 × 0.15
Radiation	Synchrotron (λ = 0.79999)
2Θ range for data collection/°	2.708 to 64.4
Index ranges	$-52 \leq h \leq 52$, $-55 \leq k \leq 55$, $-55 \leq l \leq 55$
Reflections collected	1001027
Independent reflections	14973 [R_{int} = 0.0560, R_{sigma} = 0.0111]
Data/restraints/parameters	14973/383/522
Goodness-of-fit on F^2	1.260
Final R indexes [I>=2σ (I)]	R_1 = 0.1066, wR_2 = 0.3287
Final R indexes [all data]	R_1 = 0.1318, wR_2 = 0.3831
Largest diff. peak/hole / e $Å^{-3}$	1.79/-0.76

Cubic c-(4,12)MTBC-Zr_6 crystal nr.1

Linker occupancy: 0.932(2)

Ordered cluster occupancy: 1
Disordered cluster occupancy, Zr3: 0.1810(16)
Disordered cluster occupancy, Zr4: 0.167(3)
The two Zr occupancies were refined to have an overall occupancy of the disordered cluster of 1, since free occupancy refinements resulted in an overall site occupancy >1.

Solvent masking produced electron densities without significant differences compared to those shown for crystal nr.1 in Figure C.18.

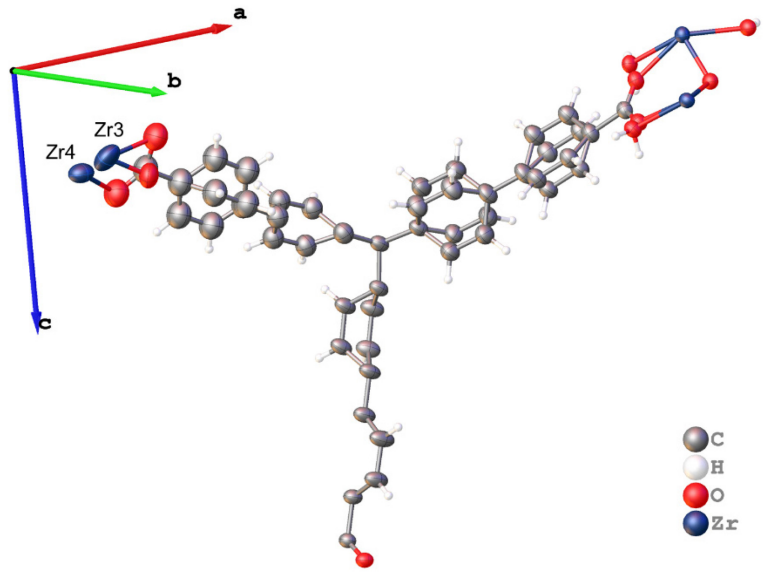

Figure C.20: Asymmetric unit of cubic c-(4,12)MTBC-Zr_6 crystal nr.1 (ellipsoids corresponding to 30% probability).

Table C.5: Crystal data and structure refinement for cubic c-(4,12)MTBC-Zr_6 crystal nr.1.

Empirical formula	$C_{148.23}H_{93.72}O_{29.19}Zr_{6.08}$
Formula weight	2898.41
Temperature/K	100
Crystal system	cubic
Space group	Pm-3n
a/Å	41.630(10)
b/Å	41.630(10)
c/Å	41.630(10)
α/°	90
β/°	90
γ/°	90
Volume/$Å^3$	72147(52)
Z	8
$\rho_{calc}g/cm^3$	0.534
μ/mm^{-1}	0.272
F(000)	11687.0
Crystal size/mm^3	0.15 × 0.15 × 0.15
Radiation	Synchrotron (λ = 0.79999)
2Θ range for data collection/°	2.698 to 64.426
Index ranges	$-52 \leq h \leq 52$, $-55 \leq k \leq 55$, $-55 \leq l \leq 55$
Reflections collected	1022290
Independent reflections	15138 [R_{int} = 0.0431, R_{sigma} = 0.0083]
Data/restraints/parameters	15138/816/561
Goodness-of-fit on F^2	1.067
Final R indexes [I>=2σ (I)]	R_1 = 0.0736, wR_2 = 0.2417
Final R indexes [all data]	R_1 = 0.0793, wR_2 = 0.2570
Largest diff. peak/hole / e $Å^{-3}$	1.68/-1.86

Cubic c-(4,12)MTBC-Zr_6 crystal nr.2

Linker occupancy: 0.931(2)
Ordered cluster occupancy: 1
Disordered cluster occupancy, Zr3: 0.1851(16)
Disordered cluster occupancy, Zr4: 0.167(3)
The two Zr occupancies were refined to have an overall occupancy of the disordered cluster of 1, since free occupancy refinements resulted in an overall site occupancy >1.

Solvent masking produced electron densities without significant differences compared to those shown for crystal nr.1 in Figure C.18.

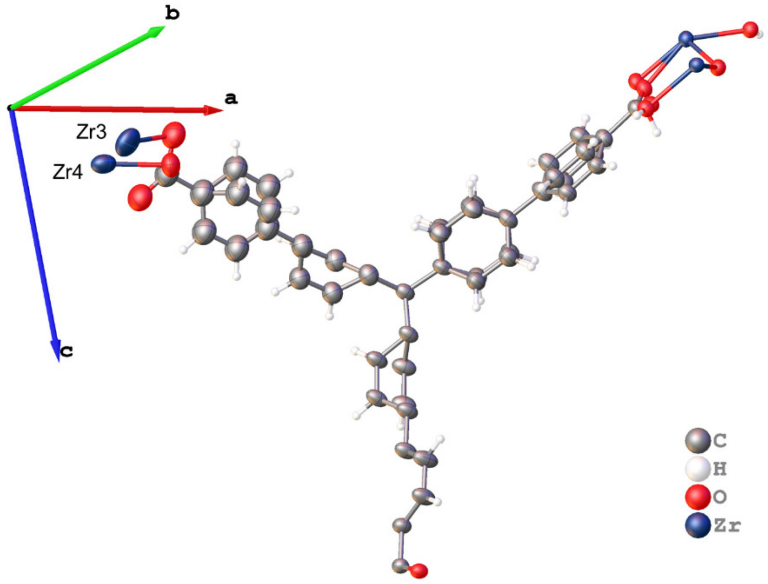

Figure C.21: Asymmetric unit of cubic c-(4,12)MTBC-Zr_6 crystal nr.2 (ellipsoids corresponding to 30% probability).

Table C.6: Crystal data and structure refinement for cubic c-(4,12)MTBC-Zr_6 crystal nr.2.

dentification code	c-ZrMTBC_cubes_354x01
Empirical formula	$C_{148.47}H_{93.83}O_{29.2}Zr_{5.88}$
Formula weight	2881.03
Temperature/K	100.00
Crystal system	cubic
Space group	Pm-3n
a/Å	41.646(4)
b/Å	41.646(4)
c/Å	41.646(4)
α/°	90
β/°	90
γ/°	90
Volume/$Å^3$	72232(22)
Z	8
$\rho_{calc}g/cm^3$	0.530
μ/mm^{-1}	0.264
F(000)	11627.0
Crystal size/mm^3	0.15 × 0.15 × 0.15
Radiation	Synchrotron (λ = 0.79999)
2Θ range for data collection/°	2.696 to 64.422
Index ranges	$-52 \leq h \leq 52$, $-55 \leq k \leq 55$, $-55 \leq l \leq 55$
Reflections collected	1004180
Independent reflections	15024 [R_{int} = 0.0398, R_{sigma} = 0.0085]
Data/restraints/parameters	15024/816/561
Goodness-of-fit on F^2	1.068
Final R indexes [I>=2σ (I)]	R_1 = 0.0724, wR_2 = 0.2354
Final R indexes [all data]	R_1 = 0.0777, wR_2 = 0.2493
Largest diff. peak/hole / e $Å^{-3}$	1.60/-1.94

Cuboctahedral c-(4,12)MTBC-Hf_6 crystal nr.1

Linker occupancy: 0.885(5)
Ordered cluster occupancy: 1
Disordered cluster occupancy: 0.25
Solvent masking produced electron densities without significant differences compared to those shown for crystal nr.1 in Figure C.18.

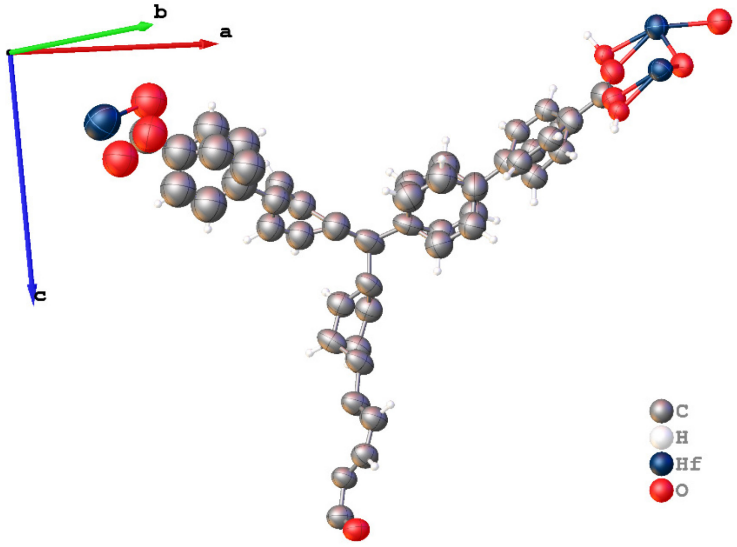

Figure C.22: Asymmetric unit of cuboctahedral c-(4,12)MTBC-Zr_6 crystal nr.1 (ellipsoids corresponding to 30% probability).

Table C.7: Crystal data and structure refinement for cuboctahedral c-(4,12)MTBC-Hf_6 crystal nr.1.

Empirical formula	$C_{145.16}H_{92.21}Hf_{6.02}O_{28.96}$
Formula weight	3374.63
Temperature/K	100.00
Crystal system	cubic
Space group	Pm-3n
a/Å	41.41(5)
b/Å	41.41(5)
c/Å	41.41(5)
α/°	90
β/°	90
γ/°	90
Volume/$Å^3$	71030(247)
Z	8
$\rho_{calc}g/cm^3$	0.631
μ/mm^{-1}	2.406
F(000)	13028.0
Crystal size/mm^3	0.15 × 0.15 × 0.15
Radiation	Synchrotron (λ = 0.79999)
2Θ range for data collection/°	2.712 to 47.082
Index ranges	$-40 \leq h \leq 40$, $-41 \leq k \leq 41$, $-41 \leq l \leq 41$
Reflections collected	445098
Independent reflections	6136 [R_{int} = 0.0477, R_{sigma} = 0.0102]
Data/restraints/parameters	6136/872/544
Goodness-of-fit on F^2	1.526
Final R indexes [I>=2σ (I)]	R_1 = 0.0843, wR_2 = 0.2911
Final R indexes [all data]	R_1 = 0.0923, wR_2 = 0.3239
Largest diff. peak/hole / e $Å^{-3}$	2.17/-1.23

Cuboctahedral c-(4,12)MTBC-Hf_6 crystal nr.2

Linker occupancy: 0.872(3)
Ordered cluster occupancy: 1
Disordered cluster occupancy: 0.25
Solvent masking produced electron densities without significant differences compared to those shown for crystal nr.1 in Figure C.18.

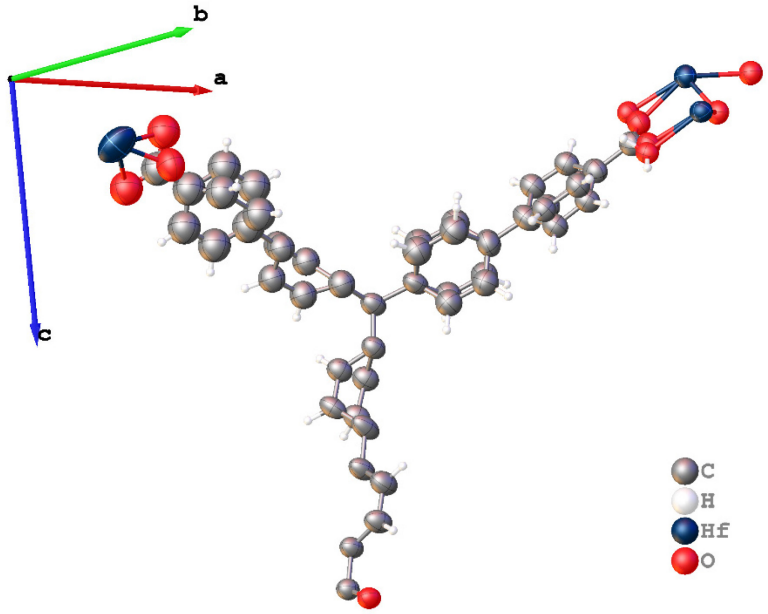

Figure C.23: Asymmetric unit of cuboctahedral c-(4,12)MTBC-Zr_6 crystal nr.2 (ellipsoids corresponding to 30% probability).

Table C.8: Crystal data and structure refinement for cuboctahedral c-(4,12)MTBC-Hf_6 crystal nr.2.

Empirical formula	$C_{138.65}H_{89.02}Hf_6O_{28.46}$
Formula weight	3281.48
Temperature/K	100.00
Crystal system	cubic
Space group	Pm-3n
a/Å	41.46(6)
b/Å	41.46(6)
c/Å	41.46(6)
α/°	90
β/°	90
γ/°	90
Volume/$Å^3$	71257(320)
Z	8
$\rho_{calc}g/cm^3$	0.612
μ/mm^{-1}	2.388
F(000)	12646.0
Crystal size/mm^3	0.15 × 0.15 × 0.15
Radiation	Synchrotron (λ = 0.79999)
2Θ range for data collection/°	3.128 to 59.942
Index ranges	$-51 \leq h \leq 51$, $-51 \leq k \leq 51$, $-51 \leq l \leq 51$
Reflections collected	856804
Independent reflections	11997 [R_{int} = 0.0436, R_{sigma} = 0.0077]
Data/restraints/parameters	11997/824/553
Goodness-of-fit on F^2	1.052
Final R indexes [I>=2σ (I)]	R_1 = 0.0587, wR_2 = 0.1961
Final R indexes [all data]	R_1 = 0.0721, wR_2 = 0.2283
Largest diff. peak/hole / e $Å^{-3}$	1.11/-1.01

t-(4,12)MTBC-Zr_6

The structure is affected by disorder in the form of two alternative framework structures, whose combination is observed in the average structure. Consistently, reciprocal space reconstructions reported in Figure C.24 show streaks and additional intensities along a* and b*, attributable to loss of periodicity in the ab plane of the crystal.

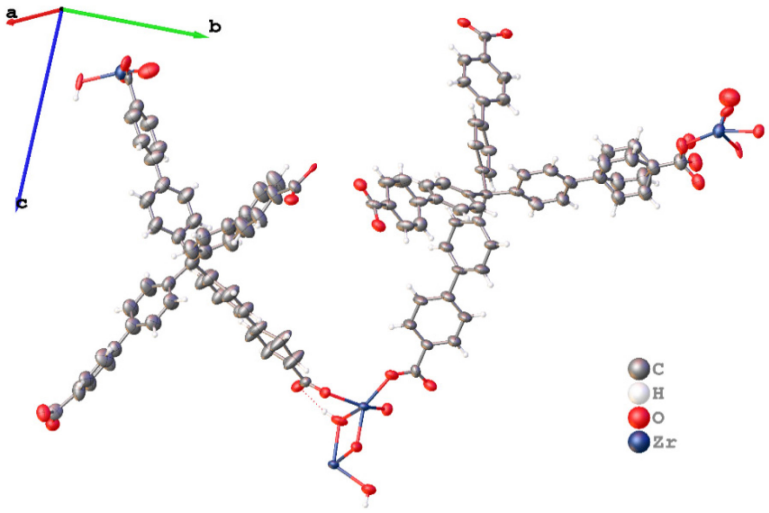

Figure C.24: Asymmetric unit of trigonal t-(4,12)MTBC-Zr_6 (ellipsoids corresponding to 30% probability).

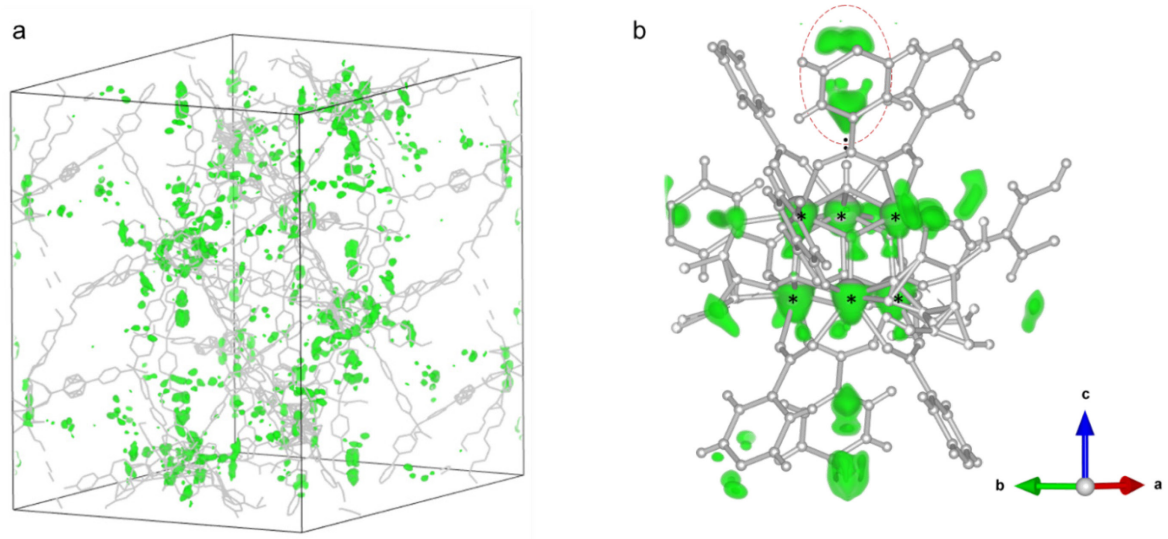

Figure C.25: Difference electron density maps (Fobs-Fcalc) obtained by using the option "Fourier Synthesis" of the software Vesta, based on the ".fcf" file produced by structure refinements without solvent mask. In detail, (a) view of the electron density residues in the unit cell (isosurface level = 1 $e^-/Å^3$), and (b) main location where these densities are found, i.e., around the ordered metal clusters (isosurface levels = 1, 1, and 1.3 $e^-/Å^3$). Note the circled area, where density maxima suggest the presence of solvent molecules interacting with the cluster's OH groups via hydrogen bonding (dotted black line; H–density maximum distance: 1.95(2) Å).

Table C.9: Crystal data and structure refinement for t-(4,12)MTBC-Zr_6.

Empirical formula	$C_{159}H_{97}O_{33.5}Zr_6$
Formula weight	3090.68
Temperature/K	293(2)
Crystal system	trigonal
Space group	P-3c1
a/Å	34.3901(4)
b/Å	34.3901(4)
c/Å	49.4392(4)
α/°	90
β/°	90
γ/°	120
Volume/$Å^3$	50637.1(12)
Z	6
$\rho_{calc}g/cm^3$	0.608
μ/mm^{-1}	0.291
F(000)	9354.0
Crystal size/mm^3	0.15 × 0.15 × 0.04
Radiation	Synchrotron (λ = 0.79999)
2Θ range for data collection/°	3.854 to 56.142
Index ranges	$-40 \leq h \leq 40$, $-37 \leq k \leq 37$, $-58 \leq l \leq 58$
Reflections collected	507581
Independent reflections	28787 [R_{int} = 0.0930, R_{sigma} = 0.0251]
Data/restraints/parameters	28787/570/1074
Goodness-of-fit on F^2	1.697
Final R indexes [I>=2σ (I)]	R_1 = 0.1343, wR_2 = 0.3955
Final R indexes [all data]	R_1 = 0.1671, wR_2 = 0.4440
Largest diff. peak/hole / e $Å^{-3}$	4.58/-1.40

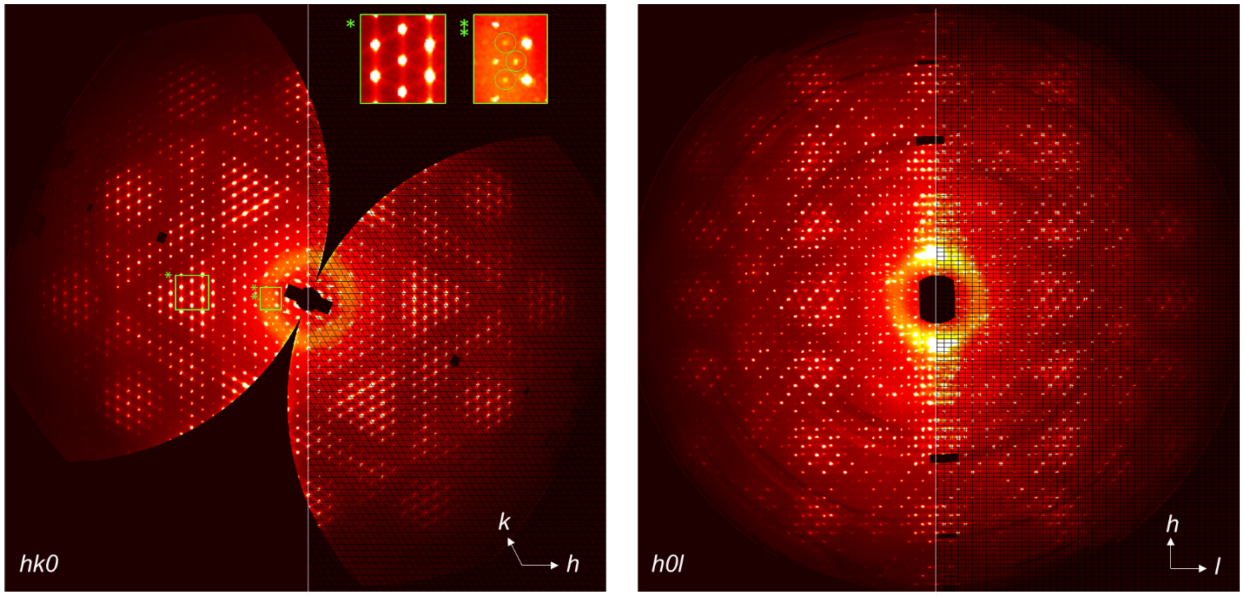

Figure C.26: Reciprocal space reconstructions of the hk0 and h0l planes of t-(4,12)MTBC-Zr_6. Showing diffuse streaks along h and k (*) due to loss of periodicity across the ab plane of the crystal, violation of systematic absences attributable to substitutional disorder (**), and a peculiar Bragg peaks distribution which does not match perfectly the unit cell metric, akin to an incommensurately modulated structure.

t-(4,12)MTBC-Hf_6

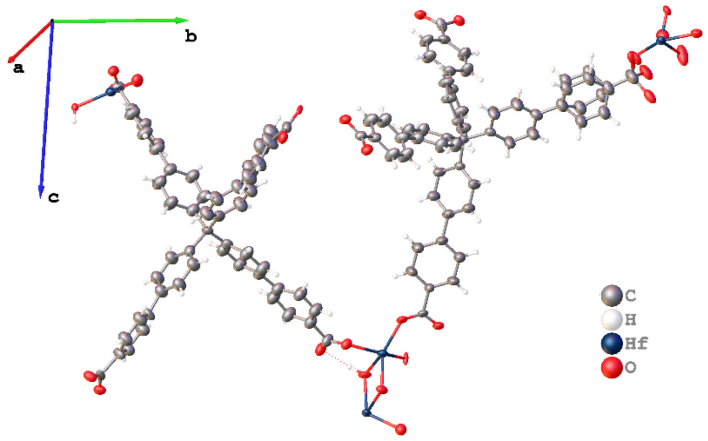

Figure C.27: Asymmetric unit of trigonal t-(4,12)MTBC-Hf_6 (ellipsoids corresponding to 30% probability).

Table C.10: Crystal data and structure refinement for t-(4,12)MTBC-Hf_6.

Empirical formula	$C_{159}H_{98.33}Hf_6O_{34}$
Formula weight	3623.64
Temperature/K	100.00
Crystal system	trigonal
Space group	P-3c1
a/Å	35.0368(4)
b/Å	35.0368(4)
c/Å	48.7688(4)
α/°	90
β/°	90
γ/°	120
Volume/$Å^3$	51846.7(13)
Z	6
$\rho_{calc}g/cm^3$	0.696
μ/mm^{-1}	0.897
F(000)	10538.0
Crystal size/mm^3	0.15 × 0.15 × 0.04
Radiation	Synchrotron (λ = 0.534)
2Θ range for data collection/°	2.948 to 38.992
Index ranges	$-43 \leq h \leq 43$, $-42 \leq k \leq 43$, $-60 \leq l \leq 60$
Reflections collected	685321
Independent reflections	35355 [R_{int} = 0.0807, R_{sigma} = 0.0299]
Data/restraints/parameters	35355/1290/1151
Goodness-of-fit on F^2	1.034
Final R indexes [I>=2σ (I)]	R_1 = 0.0654, wR_2 = 0.1769
Final R indexes [all data]	R_1 = 0.1003, wR_2 = 0.2126
Largest diff. peak/hole / e $Å^{-3}$	2.40/-1.65

References

1. A. Coelho, *Journal of Applied Crystallography* **2018**, *51*, 210-218.
2. P. J. Chupas, X. Qiu, J. C. Hanson, P. L. Lee, C. P. Grey, S. J. L. Billinge, *Journal of Applied Crystallography* **2003**, *36*, 1342-1347.
3. J. Kieffer, V. Valls, N. Blanc, C. Hennig, *Journal of Synchrotron Radiation* **2020**, *27*, 558-566.
4. G. Ashiotis, A. Deschildre, Z. Nawaz, J. P. Wright, D. Karkoulis, F. E. Picca, J. Kieffer, *Journal of Applied Crystallography* **2015**, *48*, 510-519.
5. P. Juhas, T. Davis, C. L. Farrow, S. J. L. Billinge, *Journal of Applied Crystallography* **2013**, *46*, 560-566.
6. X. a. J. Yang, Pavol and Farrow, Christopher L. and Billinge, Simon J. L., *xPDFsuite: an end-to-end software solution for high throughput pair distribution function transformation, visualization and analysis*, arXiv, **2014**.
7. S. J. L. Billinge, C. L. Farrow, *Journal of Physics: Condensed Matter* **2013**, *25*, 454202.
8. P. Juhas, C. L. Farrow, X. Yang, K. R. Knox, S. J. L. Billinge, *Acta Crystallographica Section A* **2015**, *71*, 562-568.
9. O. V. Dolomanov, L. J. Bourhis, R. J. Gildea, J. A. K. Howard, H. Puschmann, *Journal of Applied Crystallography* **2009**, *42*, 339-341.
10. G. Sheldrick, *Acta Crystallographica Section C* **2015**, *71*, 3-8.
11. C. B. Hubschle, G. M. Sheldrick, B. Dittrich, *Journal of Applied Crystallography* **2011**, *44*, 1281-1284.
12. K. Momma, F. Izumi, *Journal of Applied Crystallography* **2011**, *44*, 1272-1276.
13. P. Ji, K. Manna, Z. Lin, A. Urban, F. X. Greene, G. Lan, W. Lin, *Journal of the American Chemical Society* **2016**, *138*, 12234-12242.
14. B. Karadeniz, D. Žilić, I. Huskić, L. S. Germann, A. M. Fidelli, S. Muratović, I. Lončarić, M. Etter, R. E. Dinnebier, D. Barišić, N. Cindro, T. Islamoglu, O. K. Farha, T. Friščić, K. Užarević, *Journal of the American Chemical Society* **2019**, *141*, 19214-19220.
15. X. Gong, H. Noh, N. C. Gianneschi, O. K. Farha, *Journal of the American Chemical Society* **2019**, *141*, 6146-6151.
16. V. Bon, I. Senkovska, I. A. Baburin, S. Kaskel, *Crystal Growth & Design* **2013**, *13*, 1231-1237.
17. Y. Bai, Y. Dou, L.-H. Xie, W. Rutledge, J.-R. Li, H.-C. Zhou, *Chemical Society Reviews* **2016**, *45*, 2327-2367.

APPENDIX D: ADDITIONAL INFORMATION FOR CHAPTER 5

D.1 Experimental

D.1.1 Materials

Tetrakis(4-carboxyphenyl) porphyrin (TCPP) was purchased from Tokio Chemical Industry. Zirconyl chloride octahydrate (>98%), zirconium(IV) chloride (not stored in glovebox), benzoic acid, [6,6]-Phenyl C61 butyric acid methyl ester, and acetone were purchased from Sigma Aldrich. Iodine was purchased from Merck. *N,N*-dimethylformamide (DMF) was purchased from VWR. Acetic acid and hydrochloric acid were purchased from Carl Roth. All chemicals were used as received without further purification.

D.1.2 Instruments and methods

Ultrasonication was conducted *via* an ELMASONIC S 100 bath equipped with a high-performance 37 kHz sandwich transducer and state-of-the-art microprocessor. An *Initiator Classic* from BIOTAGE was used for microwave-assisted synthesis. Centrifugation was performed with a benchtop centrifuge *Sigma-3-30K* from SIGMA. For SEM analysis, MOF suspensions were spin-coated onto silicon wafers with a *WS-650S-NPP Lite* device from LAURELL TECHNOLOGY CORPORATION. For the fabrication of thin MOF film the suspensions (ca. 2 wt%) were spin-coated onto silicon wafers (60 µL per layer) with a *WS-650S-NPP Lite* device from LAURELL TECHNOLOGY CORPORATION at 4k rpm rotation and 4k rpm acceleration.

Scanning electron microscopy was performed on a Merlin SEM, Zeiss, with a secondary electron (SE) detector.

Powder X-ray diffraction patterns were collected at room temperature on a Stoe Stadi-P diffractometers with Cu $K\alpha_1$ radiation (λ = 1.540596 Å), a Ge(111) Johann monochromator, and a DECTRIS Mythen 1K detector in Debye-Scherrer geometry. The samples were loaded into 0.3 mm inner diameter polyimide capillaries and measured over a range of 2θ = 2.000–30.695°, with 0.015° step size and 50 s counting time per step. The software package WinXPOW was used to analyze all obtained data and to simulate theoretical diffraction patterns.

The photoluminescence decay experiments were recorded on a double monochromator spectrofluorometer (Edinburgh FLS980). The PL decay was collected over a 1 nm spectral window centered at λ = 720 nm. The time-resolved PL were fitted with a combination of a δ function and a Γ function, as described previously.[1-2] MOF suspensions with concentrations of 1 mg mL^{-1} in DMF were used for measurements.

Elemental analysis of carbon, hydrogen, and nitrogen was carried out *via* an UNICUBE Elementar Analysensysteme GmbH Langenselbold instrument. The zirconium content was determined *via* ICP-OES using a Vista Pro Simultaneous ICP-OES spectrometer equipped with an CCD detector from Agilent Technologies. The evaluation of the data was conducted using the ICP-Expert software.

Cyclic voltammetry experiments were conducted on a Metrohm-Autolab MULTISTAT M204 potentiostat. The measurements were conducted *via* a three-electrode electrochemical setup with an FTO substrate spin-coated with the sample as the working electrode, a platinum wire as the counter electrode, and an Ag/AgCl electrode as the reference (RE) in varying potential windows and scan rates. The active area of the tested working electrodes was 0.70 cm^2. Perchloric acid solution (0.1 M) in ultrapure water (Barnstead™ MicroPure™, Thermofisher Scientific) was employed as the electrolyte.

Energy-dispersive X-ray analysis was performed on a TESCAN Vega TS 5130 MM instrument and evaluated using the AZTEC Oxford software.

Impedance measurements were performed at room temperature using a Novocontrol Alpha A with alternating voltage and 100 mV amplitude (frequency from 1 MHz to 100 mHz). The measurements were conducted *via* a two-point setup for which two circular gold electrodes were applied on an FTO substrate spin-coated with the sample.

D.1.3 Synthetic procedures

MOF samples for additional time-dependent study

PCN-224 was synthesized based on the PCN-224 procedure described in Appendix A Section A.1.3 with 16 h, 24 h, and 52 h reaction time yielding PCN-224_16h, PCN-224_24h, and PCN-224_52h. Synthesis of dPCN-224 in the microwave was performed based on the MOF_$ZrOCl_2$_(II) procedure described in Appendix B, Section B.1.3, with 30 min and 90 min reaction time yielding dPCN-224_MW_30min and dPCN-224_MW_90min.

MOF samples for study on photoluminescence lifetimes

PL was measured on products obtained from Chapter 2 and 3. The samples PCN-224, dPCN-224_$ZrOCl_2$_MW were synthesized according to the procedures of PCN-224 and MOF_$ZrOCl_2$_(I), respectively, described in Appendix A Section A.1.3, without HCl activation. The samples dPCN-224_$ZrOCl_2$_oven, dPCN-224_$ZrCl_4$_lab_oven, and dPCN-224_$ZrCl_4$_3d_oven correspond to $ZrOCl_2$_24h, $ZrCl_4$_lab_24h, and $ZrCl_4$_1d, respectively, described in Appendix B Section B.1.3.

dPCN-224 for PSM

dPCN-224 was synthesized according to the procedure described in Section B.1.3. After washing with DMF, the product was resuspended in DMF (10 mL). The suspension was activated with HCl (8M, 0.20 mL) in an oven (15 h, 100 °C). The product was collected by centrifugation and washed with DMF (three times, 16k rpm/20 min/16 °C) and acetone (twice, 16k rpm/8 min/16 °C). The mixture was soaked in acetone overnight and washed once with acetone. Centrifugation (16k rpm/5 min/16 °C) and supercritical CO_2 drying yielded a purple powder as product.

PCBA

PCBA was synthesized *via* saponification of and [6,6]-Phenyl C61 butyric acid methyl ester (PCBM) based on a published procedure by Gupta *et al.*[3] PCBM (50 mg, 0.056 mmol) was dissolved in chlorobenzene (10 mL). Glacial acetic acid (10 mL) and concentrated hydrochloric acid (3 mL) were added. The resulting reaction mixture was heated to reflux (132 °C) overnight. It was cooled to 23 °C and the two phases were separated. The organic phase was evaporated under reduced pressure and the thus recovered solid dried under vacuum. PCBA was obtained as black powder (49 mg, 0.055 mmol, 98 %). The measured ^{1}H NMR spectra are in agreement with previous literature reports.[4]

^{1}H NMR (400 MHz, CS_2, 23°C, *d*-DMSO): δ=11.7 (s br, 1H, COOH), 7.95 (d, ^3J (H,H)=8 Hz, 2H; *o*-Ar-H), 7.57 (t, ^3J (H,H)=8 Hz, 2H; *m*-Ar-H), 7.50 (t, ^3J (H,H)=8 Hz, 1H; *p*-Ar-H); 2.92 (m, 2H; CH_2), 2.40 (t, ^3J (H,H)=7 Hz, 2H; CH_2), 2.14 ppm (m, 2H; CH_2).

I@dPCN-224

dPCN-224 was modified with iodine based on a published procedure by Hao *et al.*[5] Iodine (15.0 mg, 0.059 mmol) was dissolved in acetonitrile (3 mL) and the resultant solution was added to CO_2 dried dPCN-224 (35.0 mg, 0.0178 mmol). The mixture was sonicated for 5 min and left at

23 °C for 48 h. The suspension was centrifuged (16k rpm, 20 min, 16 °C), washed with acetonitrile (four times, 16k rpm/20 min/16 °C) and soaked in acetonitrile overnight. After washing with acetone (three times, 16k rpm/20 min/16 °C) the product was left to soak in acetone overnight, washed once with acetone, and stored in acetone.

PCBA@dPCN-224

PCBA (23.4 mg, 0.0261 mmol) was dissolved in *o*-dichlorobenzene (20 mL) and the resulting solution was added to CO_2-dried dPCN-224 (12.5 mg, 0.00636 mmol). The mixture was heated in an aluminium heating block at 100 °C while stirring overnight. After cooling, the suspension was washed with *o*-dichlorobenzene (four times, 16k rpm/20 min/16 °C) and left to soak in *o*-dichlorobenzene for 65 h. After washing with acetone (three times, 16k rpm/20 min/16 °C) the product was left to soak in acetone overnight, washed once with acetone, and stored in acetone.

D.2 Results and discussion

D.2.1 Particle growth of MOFs

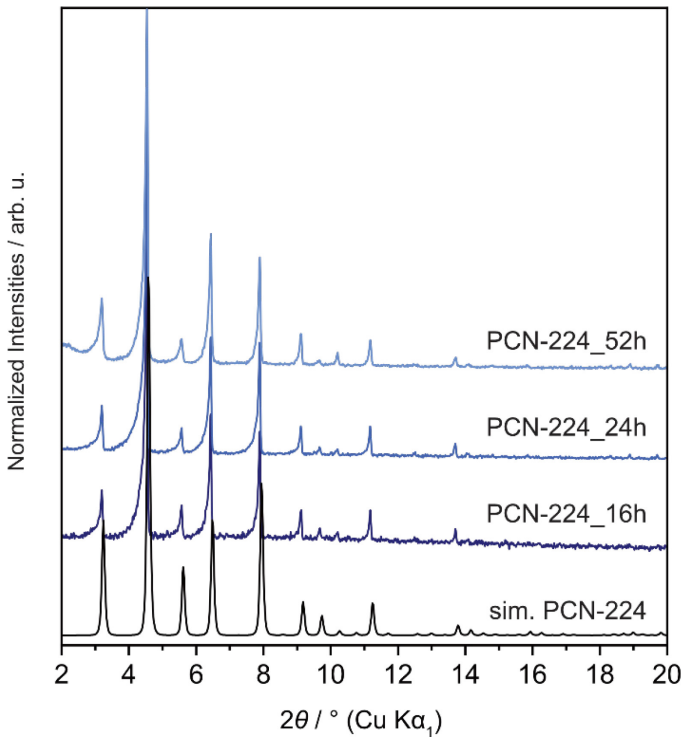

Figure D.1: PXRD patterns of the PCN-224 products obtained after 16 h, 24 h, and 52 h reaction time in an oven compared to the simulated (sim.) pattern of PCN-224.[6]

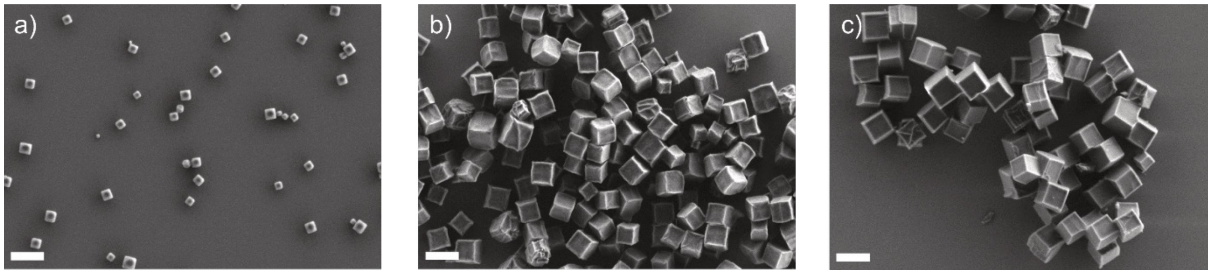

Figure D.2: SEM images of PCN-224 particles after a) 16 h, b) 24 h, and c) 52 h reaction time in an oven. Scale bar = 1 µm.

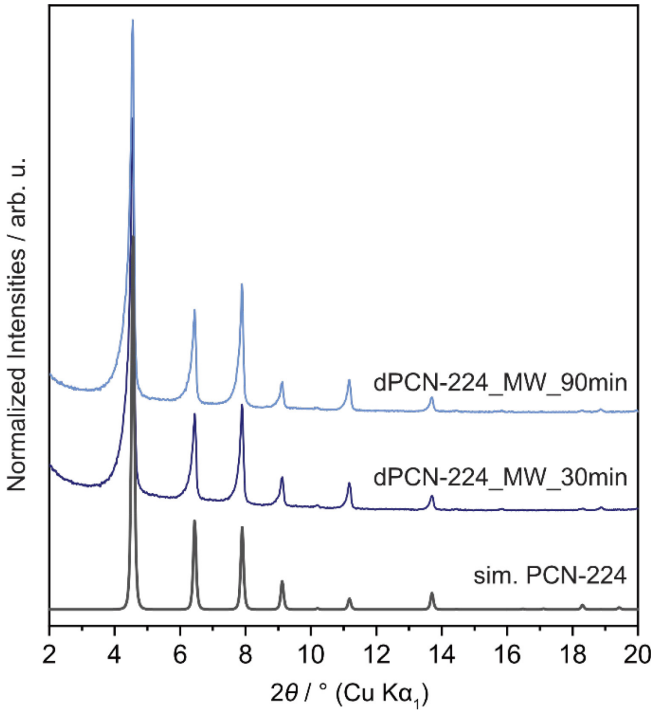

Figure D.3: PXRD patterns of the dPCN-224 products obtained after 30 min and 90 min reaction time in a microwave (MW) compared to the simulated (sim.) pattern of dPCN-224.[7]

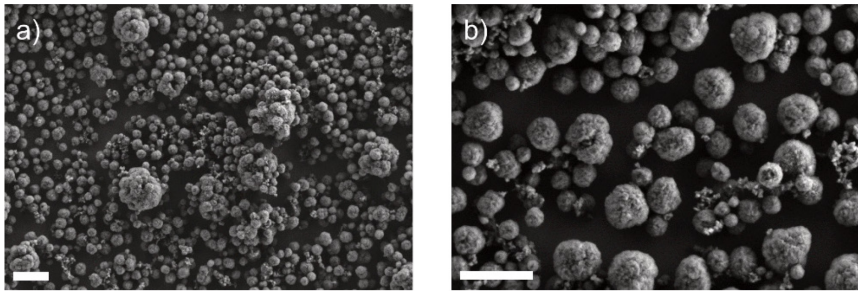

Figure D.4: SEM images of dPCN-224 synthesized from $ZrOCl_2.H_2O$ in the microwave after a) 30 min and b) 90 min reaction time. Scale bar = 1 µm.

D.2.2 Photoluminescence decay

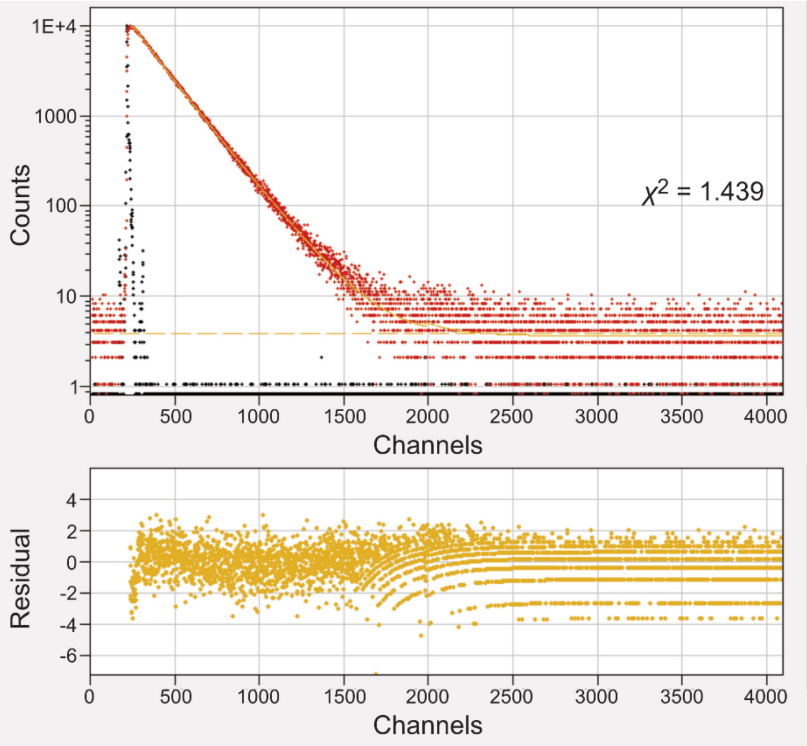

Figure D.5: PL lifetime measurement and fitting of dPCN-224_$ZrOCl_2$_MW.

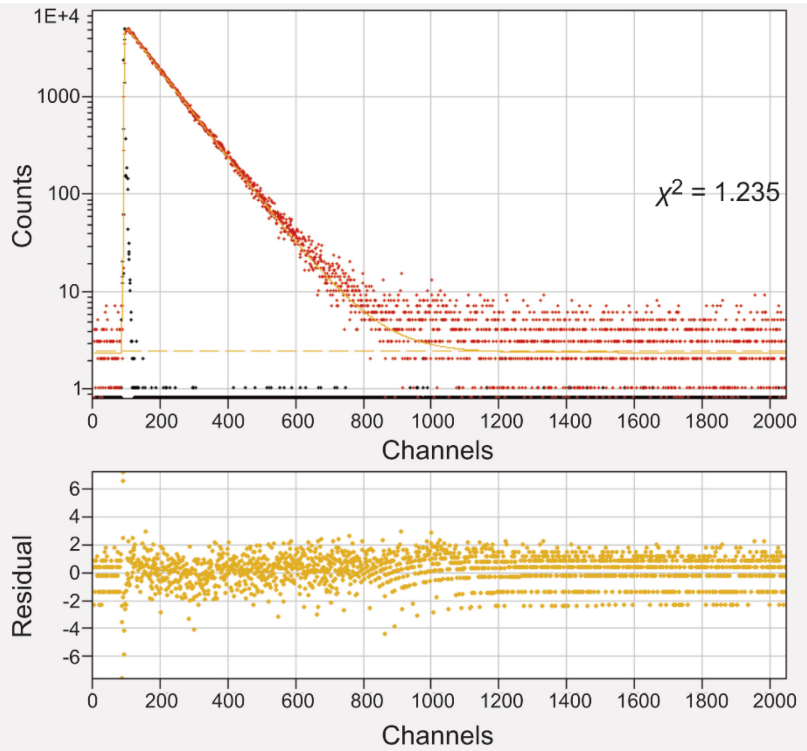

Figure D.6: PL lifetime measurement and fitting of dPCN-224_$ZrOCl_2$_oven.

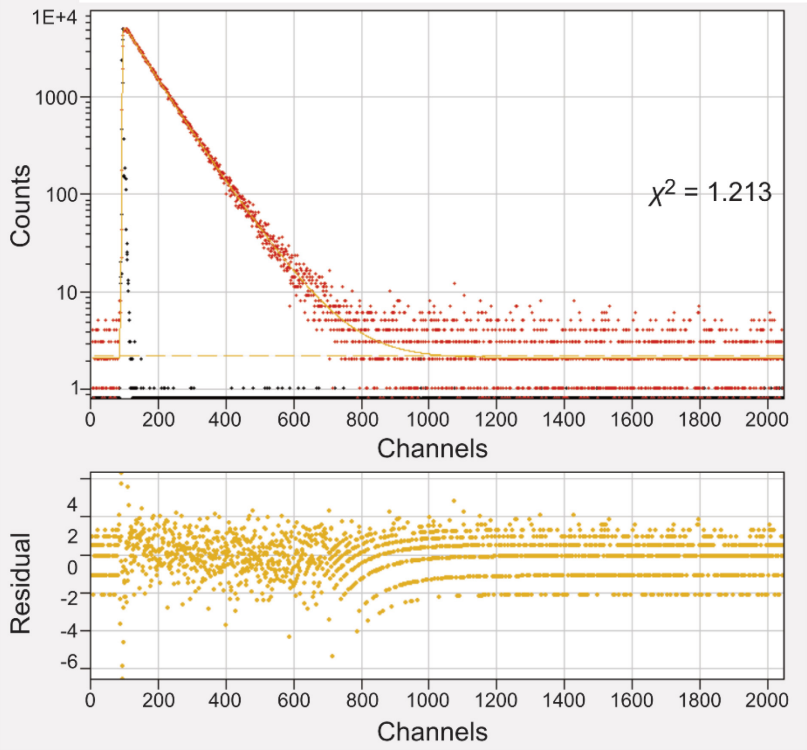

Figure D.7: PL lifetime measurement and fitting of dPCN-224_$ZrCl_4$_3d_oven.

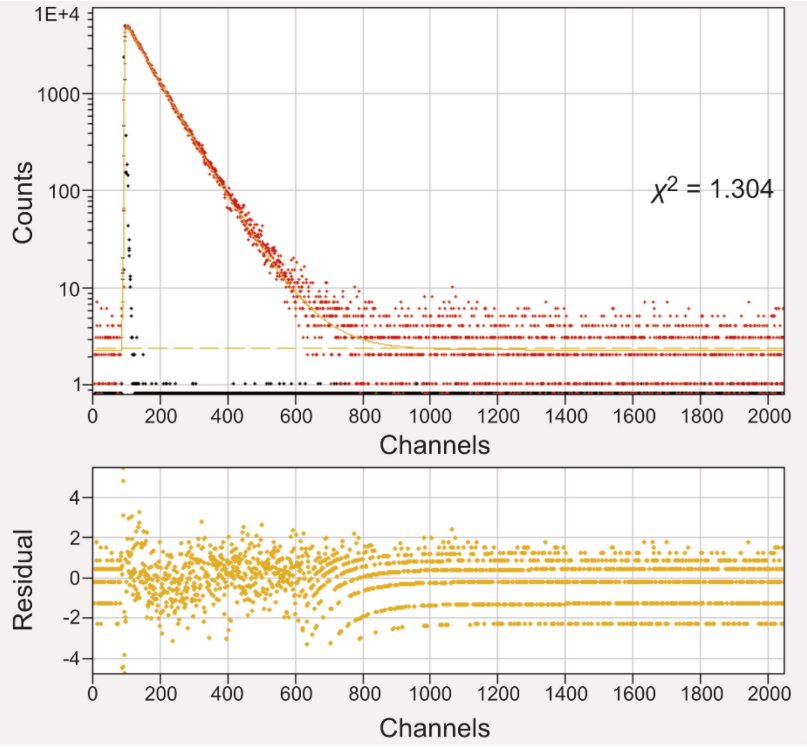

Figure D.8: PL lifetime measurement and fitting of dPCN-224_$ZrCl_4$_lab_oven.

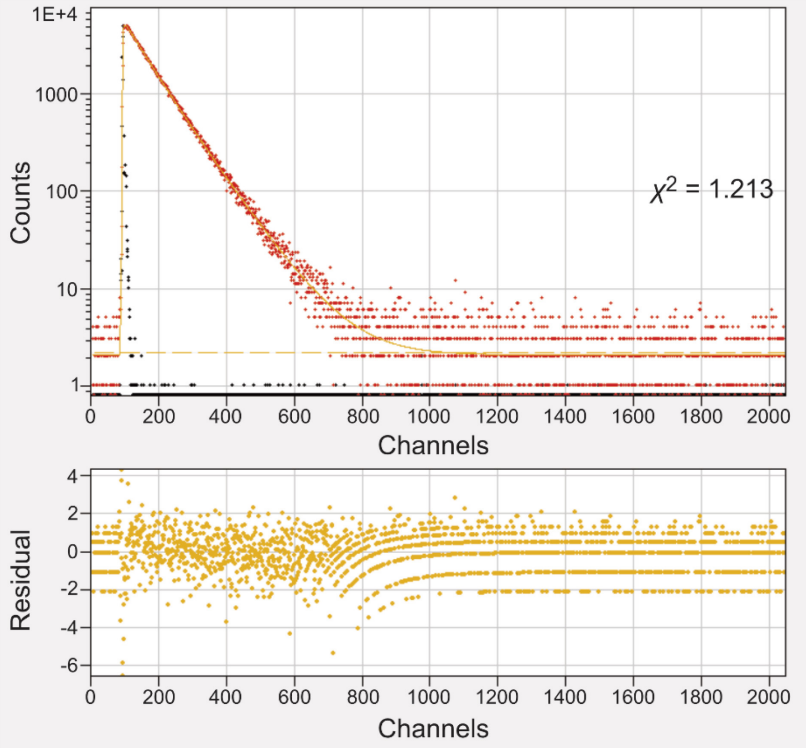

Figure D.9: PL lifetime measurement and fitting of PCN-224.

D.2.3 Post-synthetic modifications

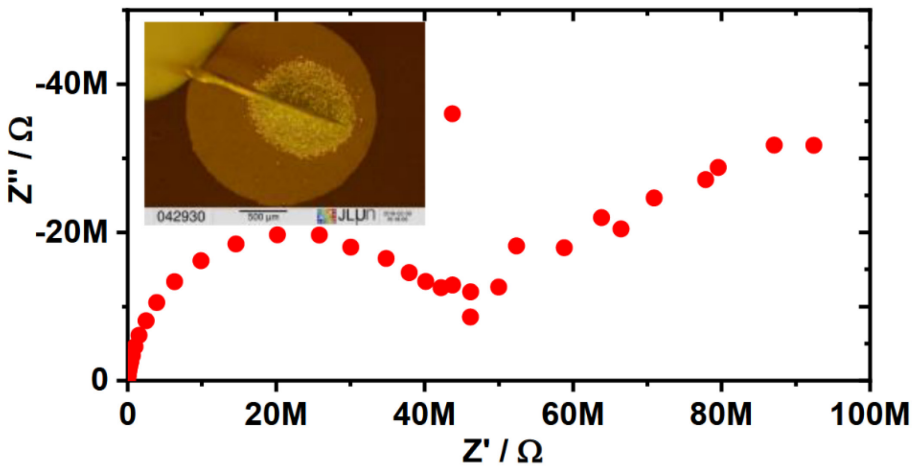

Figure D.10: Impedance measurement of dPCN-224 thin film on FTO substrate.

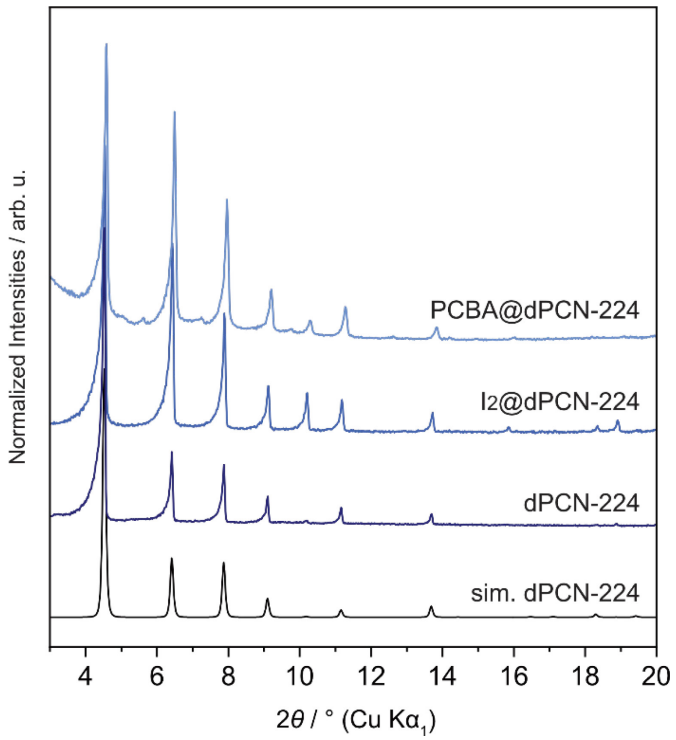

Figure D.11: PXRD patterns of pristine dPCN-224, I_2@dPCN-224, and PCBA@dPCN-224 compared to the simulated (sim.) pattern of dPCN-224.[7]

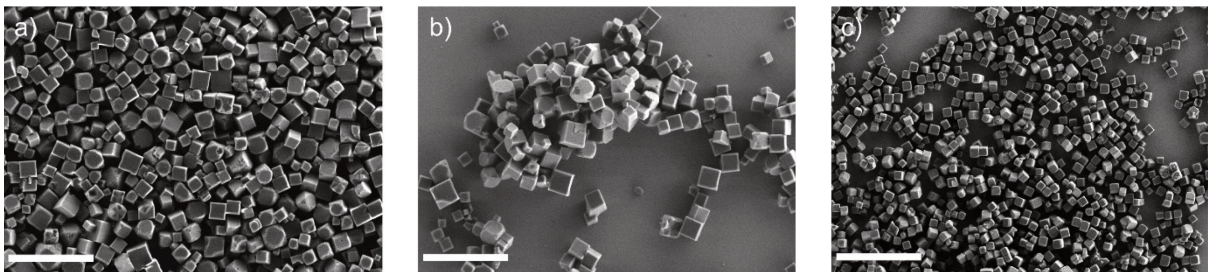

Figure D.12: SEM images of a) pristine dPCN-224, b) I_2@dPCN-224, and c) PCBA@dPCN-224. Scale bar = 5 µm.

Table D.1: C, H, and N content before and after PCBA modification determined from elemental analysis.

Sample	C (wt%)	H (wt%)	N (wt%)
dPCN-224	46.25	3.09	4.74
PCBA@dPCN-224	62.04	3.27	2.58

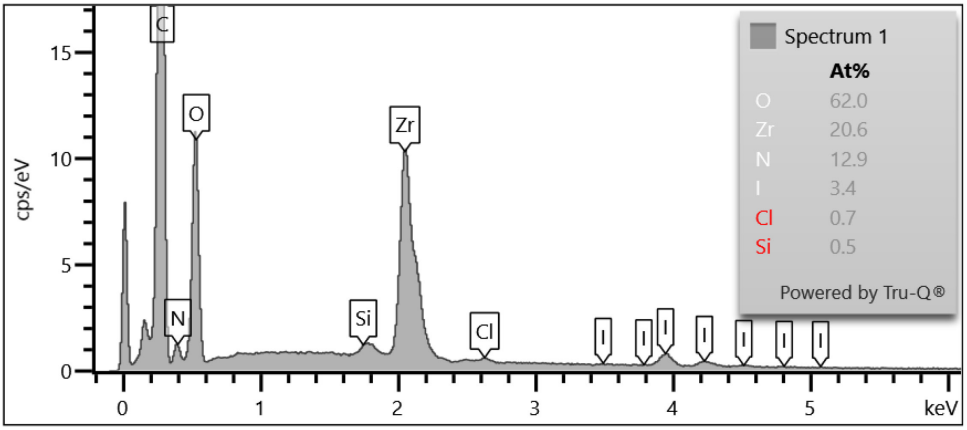

Figure D.13: EDX spectrum of I_2@dPCN-224.

Acknowledgements

The author acknowledges Viola Duppel for performing SEM images and EDX analysis, Daniel Zink and Matthias Elm for performing impedance measurements, Marie-Luise Schreiber for performing elemental analysis, Andreas Gouder and Ana Mateos for help with CV measurements, and Alberto Jiménez-Solano for help with photoluminescence lifetime measurements.

References

1. A. C. Fogarty, A. C. Jones, P. J. Camp, *Physical Chemistry Chemical Physics* **2011**, *13*, 3819-3830.
2. J. Kröger, A. Jiménez-Solano, G. Savasci, P. Rovó, I. Moudrakovski, K. Küster, H. Schlomberg, H. A. Vignolo-González, V. Duppel, L. Grunenberg, C. B. Dayan, M. Sitti, F. Podjaski, C. Ochsenfeld, B. V. Lotsch, *Advanced Energy Materials* **2021**, *11*, 2003016.
3 N. Gupta, S. Naqvi, M. Jewariya, S. Chand, R. Kumar, *Journal of Physical Organic Chemistry* **2017**, *30*, 1-11.
4. J. C. Hummelen, B. W. Knight, F. LePeq, F. Wudl, *The Journal of Organic Chemistry* **1995**, *60*, 532-538.
5. Z. Hao, G. Yang, X. Song, M. Zhu, X. Meng, S. Zhao, S. Song, H. Zhang, *Journal of Materials Chemistry A* **2014**, *2*, 237-244.
6. D. Feng, W.-C. Chung, Z. Wei, Z.-Y. Gu, H.-L. Jiang, Y.-P. Chen, D. J. Darensbourg, H.-C. Zhou,*Journal of the American Chemical Society* **2013**, *135*, 17105-17110.
7. C. Koschnick, R. Stäglich, T. Scholz, M. W. Terban, A. von Mankowski, G. Savasci, F. Binder, A. Schökel, M. Etter, J. Nuss, R. Siegel, L. S. Germann, C. Ochsenfeld, R. E. Dinnebier, J. Senker, B. V. Lotsch, *Nature Communications* **2021**, *12*, 3099.